University of Cambridge
Department of Engineering

Matthew T. Cole
St John's College

Dry-Transfer of Chemical Vapour Deposited Nanocarbon Thin Films

A Dissertation submitted for the Degree of Doctor of Philosophy
to the Department of Engineering, Cambridge University.

Sept. 2011

"Sine labore nihil"- Annon.

"Opportunity is missed by most people because it's dressed in overalls & looks like work" - Edison (*ca.* 1900)

*To those who never stopped supporting me…*

Declaration

This thesis is submitted in fulfilment of the requirements for the Degree of Doctor of Philosophy as stipulated by the Department of Engineering, University of Cambridge. This report herein was wholly written by the author and contains original work by the author, except where references are made and due credit is given in the acknowledgements. This work has not been submitted in whole, or in part, for any other degree or diploma.

Permission is granted to consult or copy the information and results contained herein for the purpose of private study only and not for publication.

In accordance with Cambridge University regulations, this report contains less than 65,000 words and 100 figures.

Matthew T. Cole
Dept. of Engineering, Cambridge University

....
(1ˢᵗ Sept. 2011)
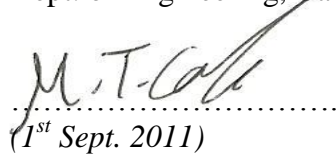
Acknowledgements

This work was made possible through the encouragement and support of countless individuals whom I wish to express my sincere appreciation.

First and foremost I would like to thank my supervisor, **Prof. Bill Milne**, for his ever positive guidance and inspiration, as well as the continuous support he has provided over this past three years. Although being an exceptionally busy man he has always made time for me whenever possible, albeit as a result of regular onslaughts of emails. Our meetings have been, without a doubt, some of the most efficient use of my time. He has allowed me to control the direction of my research with limited restraint; and as a consequence I have found my research to be exceptionally rewarding, interesting and most importantly, enjoyable.

The continued support of **Dr Mark Mann** and **Dr Yan Zhang** is greatly appreciated, without whom much of this work would not have been possible. I would especially like to thank them for their sustained patience throughout. Assistance has also been provided by **Dr David Hasko**, to whom I am exceptionally appreciative for his, what appears to be, unending insight and his ever-willingness to engage in debates regarding my ideas. I am also grateful to my advisor, **Dr Stephan Hofmann** for his persistence, drive, general helpfulness and argumentativeness. I would also like to acknowledge the on-going efforts of **Dr Chi Li** and **Dr Kai Hou** for their enthusiasm and support.

Thanks to **Dr Ken Teo (Aixtron Nanoinstruments)** for the equipment and all of the doors he has opened for me. Many thanks to **Prof. Andrea Ferrari** for generously allowing me access to his Raman facilities.

I am very grateful to the following collaborators who have provided expert help throughout. For assistance in; laser equipment and measurement I thank **Dr Xiulia Xu**, high resolution transmission electron microscopy - **Dr Caterina Ducati**, **Mr Sai Shivareddy** and **Dr Jamie Warner (Oxford University)** and assistance with supercapacitor manufacturing and measurement - **Mr** (soon to be Dr, hopefully) **Pritesh Hiralal**. I also extend my gratitude to **Prof. Hyung Gyu Park (ETH Zurich)** and **Dr Jie Sun (Chalmers University)** for their help, insight and general outstanding collaborative skills in the optimisation of the graphene growth. Much gratitude is given to **Mr Matthew Doherty (Queen's University, Belfast)** for his speedy assistance and our productive discussion in developing the nanotube membrane polariser and enhanced electric field models. I would also like to thank **Mr Bernhard Bayer**, **Mr Piran Kidambi**, **Mr Robert Weatherup** and **Mr Kai Ying** for their (always speedy) helpfulness.

I am decidedly appreciative of the concerted efforts of **Mr Ric Gillams (Southampton Univ.)** and **Prof. Mike Kelly** (the transient next door neighbour) for all their painful hours spent proof reading this thesis.

I am indebted to **Anthony Barrett** and **Adrian Gin** – possibly the best set of technicians any research student could hope for. Thank you for your time, experience and general good-willed banter - long may it last.

I would also like to thank my parents, **Geoffrey** and **Denise**, and my sister, **Stacy** for putting up with me, my endless struggles and my academia for all these years. It seems now that I will "get a real job". Thank you for your continued support and encouragement in everything I do. I would not be where I am today if it were not for you.

To my partner **Karen**. Never have I meet someone as strong and supportive. Thank you for tolerating me, my recent thesis-induced weight gain and my ridiculously late nights. Your steadfast love, affection and perseverance have unquestionably driven me.

Finally, I would like to thank all the past and present members of the Electronic Devices & Materials group who have proved to be an invaluable asset throughout and who have shown much kindness, support and friendship - a sentiment made no less genuine for its anonymity. I would similarly like to express my gratitude to all those individuals from the various other departments, faculties, institutions and research groups within Cambridge University and further afield, for the time they have devoted to training me and allowing me to grow both personally and academically, my thanks go out to you.

M T Cole
(Sept. '11)

Dry-Transfer of Chemical Vapour Deposited Nanocarbon Thin Films

By M T Cole
(Sept. '11)

This thesis presents the development of chemical vapour deposited (CVD) graphene and multi-walled carbon nanotubes (MWCNTs) as enabling technologies for flexible transparent conductors offering enhanced functionality. The technologies developed could be employed as thin film field emission sources, optical sensors and substrate-free wideband optical polarisers.

Detailed studies were performed on CVD Fe and Ni catalysed carbon nanotubes and nanofibres on indium tin oxide, aluminium and alumina diffusion barriers. Activations energies of 0.5 and 1.5 eV were extracted supporting surface diffusion limited catalysis for CNTs and CNFs. For the first time an activation energy of 2.4 eV has been determined for Cu-catalysed growth of CVD graphene. Graphene was shown to deviate significantly from the more traditional rate-limited surface diffusion and suggests carbon-atom-lattice-integration limited catalysis.

An aligned dry-transferred MWCNT thin film fabrication technique was developed using MWCNTs of varied lengths to control the optical transparency and conductivity. A process based on the hot-press lamination of bilayer CVD graphene (HPLG) was also developed. Transport studies revealed that these thin films behave, in a macroscopic sense, similar to traditional *c*-axis conductive graphite and deviate toward tunnel dominated conduction with increasing degrees of network disorder.

Various MWCNT-based thin film field emitters were considered. Solution processing was shown to augment the surface work function of the MWCNTs resulting in reduced turn-on electric fields. Integrated zinc oxide nanowires were investigated and were shown to ballast the emission, thereby preventing tip burn out, and offered lower than expected turn-on fields due to the excitation of a hot electron population. To obviate nearest neighbour electrostatic shielding effects an electrochemical catalyst activation procedure was developed to directly deposit highly aligned sparse carbon nanofibres on stainless steel mesh.

Highly-aligned free-standing MWCNT membranes were fabricated through a solid-state peeling technique. Membranes were spanned across large distances thereby offering an ideal platform to investigate the unambiguous photoresponse of MWCNTs by removing all extraneous substrate interfaces, charge traps and nanotube-electrode Shottky barriers as well as using pure, chemically untreated material. Oxygen physisorbtion was repeatedly implicated through *in-situ* lasing and *in-situ* heated EDX measurements, FT-IR and low-temperature transport and transfer measurements.

A MWCNT membrane absorptive polariser was fabricated. Polarisers showed wideband operation from 400 nm to 1.1 μm and offered operation over greater spectral windows than commercially available polymer and glass-support dichroic films. *Ab-initio* simulations showed excellent agreement with the measured polarisation attributing the effect to long-axis selective absorption.

Symbols & Abbreviations

S.I. units have been used throughout this thesis, except in the case of gas flow rates, which are quoted in standard cubic centimeters per minute (1 sccm = 1.67×10^{-8} m^3/s) and pressure (mbar, 1 mbar = 100 Pa).

In the first instance, all abbreviations are written in the text and are denoted in the parenthesis immediately following the first usage.

Unless stated otherwise the notation and symbols have the following meanings;

%T	- Optical Transmission (%)	λ_D	- Debye length (m)
a.u	- Arbitrary Units	*L*	- Characteristic length (m)
A	- Emission Area (m^2)	n_e	- Electron density (m^{-3})
A*	- Effective emission area (m^2)	*P*	- Pressure (mbar)
β	- Field enhancement factor	*R*	- Growth rate (nm/s)
c	- Speed of light	*Re*	- Reynolds number
δ	- Polariser rotation (^{o})	*S*	- (plasma) Sheath width (m)
e	- Electronic charge	*Str37*	- SPIP Image Analysis software Steridian 37 function.
E	- Energy (eV)		
E_g	- Band gap (eV)	*τ*	- Time decay constant (s)
ε	- Strain (%)	*t*	- Time (s)
ε_o	- Permittivity of free space	*T*	- Temperature (^{o}C, K)
E_a	- Activation Energy (eV)	*θ*	- (plasma) Power (W)
E_f	- Fermi level (eV)	*U*	- Free stream velocity (m/s)
F	- Electric field (V/μm)	V_o	- Cathode potential (V)
h	- Planck's constant	V_p	- Glow potential (V)
I	- Current (A)	*υ*	- Frequency (Hz)
J	- Current density (A/cm^2)	*Y*	- Kinematic viscosity (kg/s.m)
k	- Boltzmann's Constant	*z*	- Position (m)
λ	- Wavelength (nm)		

Abbreviations used throughout this thesis have the following meanings.

a-C	- Amorphous carbon	*DI*	- Deionised (water)
AFM	- Atomic force microscopy	*DLC*	- Diamond-like carbon
APTES	- Aminopropyl triethoxysilane	*EDX*	- Energy dispersive x-ray (spectroscopy)
CNTs	- Carbon nanotubes		
CVD	- Chemical vapour deposition	*EDLC*	- Electric double layer cell
DC	- Direct current	*ESR*	- Equivalent series resistance

FN	- Fowler-Nordheim (field emission)	*r-GO*	- Reduced graphene oxide
		RF	- Radio frequency
FT-IR	- Fourier transform infra-red (spectroscopy)	*rpm*	- Revolutions per minute
		ss-mesh	- Stainless steel mesh
HPLG	- Hot press laminated graphene	*SAM*	- Self assembled monolayer
ITO	- Indium tin oxide	*SDBS*	- Sodium dodecylbenzenesulfonate
MCE	- Mixed cellulose ester (membrane)	*TEM*	- Transmission electron microscope
MWCNTs	- Multi-walled carbon nanotubes	*T-CVD*	- Thermal CVD
NIR	- Near infra-red	*TCO*	- Transparent conducting oxide
PET	- Poly(ethylene terephthalate)	*TFCs*	- Transparent flexible conductors
PVD	- Physical vapour deposition	*UV*	- Ultraviolet
PE-CVD	- Plasma enhanced chemical vapour deposition	*Vis*	- Visible
		XRD	- X-ray diffractometry
PMMA	- Poly(methylmethacrylate)		

Publications *(Oct. '08-Sept '11)*

[1] J. Chen, C. Li, D. W. Zhao, W. Lei, Y. Zhang, D. P. Chu, **M. T. Cole**, X. W. Sun, B. P. Wang, & W. I. Milne, "A Quantum Dot Sensitized Solar Cell Based on Vertically Aligned Carbon Nanotube Templated ZnO Arrays", *Electrochem. Commun.*, 12 (2010) pp. 1432–1435.

[2] W. I. Milne, C. Li, Y. Zhang, D. G. Hasko, P. Hiralal, M. Mann, H. Emrah Unalan, G. A. J. Amaratunga, **M. T. Cole**, D. Chu, W. Lei, D. Pribat, J. Jang, & B. Wang, "Optimisation of CNTs & ZnO Nanostructures for Electron Sources", *IEEE T. Nanotech. Proc.*, 2010, 62.

[3] J. Sun, N. Lindvall, **M. T. Cole**, K. B. K. Teo & A. Yurgens, "Large-Area Uniform Graphene-like Thin Films Grown by Chemical Vapour Deposition Directly on Silicon Nitride", *Appl. Phys. Letts.*, 98, 252107 (2011).

[4] J. Sun, N. Lindvall, **M. T. Cole**, K. B. K. Teo, K. T. T. Angel, D. H. C. Chua, & A. Yurgens, "Low Partial Pressure Chemical Vapour Deposition of Graphene on Copper", *IEEE T. Nanotech.*, Accepted June 2011.

[5] **M. T. Cole**, W. I. Milne, M. Mann, Y. Zhang, C. Li, X. Qing & K. B. K. Teo, Symposium of Nanodevices & Nanofabrication, *ICMAT2011 Conference Proceedings*, Singapore (Pan Stanford Publishing), July 2011.

[6] **M. T. Cole**, W. I. Milne, M. Mann, Y. Zhang, C. Li, X. Qing & K. B. K. Teo, "Field Emission & Surface-Conduction Electron-Emitter Displays", *Handbook of Digital Imaging* (Wiley & Sons Ltd.), In-print Oct. 2011.

[7] **M. T. Cole**, J. T. H. Tsai, Y. T. Chiao, C. Li, & Y. Zhang, "Multi-walled carbon nanotube conductivity enhancement and band gap widening via rapid pulsed thermal annealing", Accepted *J. Mater. Sci. Tech.*, Aug. 2011.

[8] K. Celebik, **M. T. Cole**, K. B. K. Teo & H. G. Park, "Observations of Early Stage Graphene Growth on Copper", Accepted *Electrochem. Sol. Sat. Letts.* Sept. 2011.

[9] **M. T. Cole**, K. Hou, C. Li, K. B. K Teo & W. I. Milne, "*In-situ* deposition of vertically aligned carbon nanotubes on electrolyzed stainless steel mesh", Submitted to *Dia. Relat. Mater.*, July 2011.

[10] J. Sun, N. Lindvall, **M. T. Cole**, T. Wang, T. Booth, P. Boggild, K. B. K. Teo, J. Liu & A. Yurgens, "Controllable Chemical Vapor Deposition of Large Area Nanocrystalline Graphene Directly on Silicon Dioxide", Submitted to Carbon, Sept. 2011.

[11] **M. T. Cole**, P. Hiralal, Y. Zhang, C. Li, K. B. K. Teo & W. I. Milne, " Flexible dry-processed Multi-Walled Carbon Nanotube Thin Films" Submitted to *J. Nanomat.*, Sept. 2011

[12] J. Sun, **M. T. Cole**, N. Lindvall, K. B. K. Teo & A. Yurgens, "Noncatalytic chemical vapor deposition of graphene on high-temperature substrates for transparent electrodes", Submitted to *Appl. Phys. Letts.*, Aug. 2011.

[13] S. A. Ahmed, J. Sun, **M. T. Cole**, O. Bäcke, T. Ive, M. Löffler, E. Olsson, N. Lindvall, K. B. K. Teo, A. Yurgens & Å. Haglund, "Direct Chemical Vapor Deposition of large-area graphene-like thin films on Gallium Nitride for Transparent Electrodes", Submitted to *Appl. Phys. Letts.*, Aug. 2011.

Conference Presentations *(Oct. '08-Sept '11)*

[1]   **M. T. Cole**, X. Xiulia, D. G. Hasko, C. Duncati, Y. Zhang, C. Li, K. Ying, K. B. K. Teo & W. I. Milne (Oral). Suspended, Horizontally Aligned Multi-Walled Carbon Nanotube Arrays for Broad Spectrum Optical Detection. International Conference on Materials & Advanced Technologies. Suntec, Singapore, 2011.

[2]   P. Hiralal, Y. Liu, **M. T. Cole**, H. Wang, H.E. Unalan, D. Wei, P. Andrew, G. A. J. Amaratunga (Oral). Effect of Design Architecture on the Performance of CNT Supercapacitors. Nanotube. Cambridge, UK, 2011.

[3]   **M. T. Cole**, D.G. Hasko, P. Kidambi, K. Ying, K. B. K. Teo & W. I. Milne (Oral). Conduction Mechanisms in Discrete Carbon Structures – A Comparative Study of Suspended Horizontal Carbon Nanotubes & Multi-domain Hot-Press Laminated Graphene. International Conference on Materials & Advanced Technologies. Suntec, Singapore, 2011.

[4]   **M. T. Cole**, K. Ying, M. S. Haque, K. B. K. Teo & W. I. Milne (Poster). Generalisation of the Schottky Barrier Postulate at Carbon-Metal Interfaces for Pure, Aligned, Suspended Horizontal Carbon Nanotubes and Hot-press Laminated Graphene Thin Films. Imaginenano. Bilbao, 2011.

[5]   W. I. Milne, C. Li, Y. Zhang, P. Hiralal, M. Mann, **M. T. Cole**, L. Wei, J. Jang & B. Wang (Oral) CNT & CNT/ZnO Nanostructures for Electron Source. Nanocarbon & International Vacuum Electron Sources Conference. Nanjing, China, 2010.

[6]   **M. T. Cole**, M. Mann & W. I. Milne (Poster). Planar Growth of Parallel Carbon Nanotube Networks by Plasma Enhanced Chemical Vapour Deposition. CNT@Cambridge. Cambridge, UK, 2010.

[7]   P. Hiralal, Y. Liu, **M. T. Cole**, H. Wang, H.E. Unalan, D. Wei, P. Andrew, G. A. J. Amaratunga (Oral). Effect of Design Architecture on the Performance of CNT Supercapacitors. Nanocarbon & International Vacuum Electron Sources Conference. Nanjing, China, 2010.

[8]   W.I. Milne, C. Li, Y. Zhang, D.G. Hasko, P. Hiralal, M. Mann, H.E. Unalan, G.A.J. Amaratunga, **M. T. Cole**, D. Chu, W. Lei, D. Pribat, J. Jang & B. Wang (Oral). Optimization of CNTs & ZnO Nanostructures for Electron Sources. IEEE Nano. Korea, 2010.

[9]   **M. T. Cole**, Y. Zhang, C. Li, P. Hiralal, K. B. K. Teo & W. I. Milne (Plenary Session Oral). Planar CNT Networks: Highly Conductive, Flexible & Transparent Electrodes, Field Emitters & IR Sensors. Trends in Nanotechnology. Braga, Portugal, 2010.

[10]   W. I. Milne, C. Li, Y. Zhang, P. Hiralal, M. Mann, **M. T. Cole**, L. Wei, J. Jang & B. Wang (Plenary Session Oral). Carbon Nanotubes & Zinc Oxide Based Nanostructures as Electron Sources. NanoSMAT. Reims, France, 2010.

[11]   **M. T. Cole**, Y. Zhang, W. I. Milne (Oral). Carbon Nanotube Based Electronic Devices. Cambridge Nano Showcase. Cambridge, UK, 2010.

[12]   **M. T. Cole**, M. Mann, W. I. Milne (Poster). Electric-Field Aligned Horizontal Synthesis of Carbon Nanotubes by Plasma Enhanced Chemical Vapour Deposition. Materials Research Society Spring Meeting. San Francisco, USA, 2010.

[13]   Y. Zhang, **M. T. Cole**, H. E. Unalan, P. Hiralal, S. Dalal, G. Aramatunga & W. I. Milne (Oral). Hybrid CMOS Devices Utilizing Zinc Oxide Nanowire & Single Walled Carbon Nanotube Network Transistors. Materials Research Society Spring. San Francisco, USA, 2010.

[14]   **M. T. Cole**, M. Mann & W. I. Milne (Poster). Electric-Field Aligned Horizontal Synthesis Plasma Enhanced Chemical Vapour Deposition. CNT@Cambridge. Cambridge, UK, 2009

Contents

List of Figures & Tables

Chapter I

Introduction

1.   Motivation

We interact with an incredibly large number of electronic devices on a daily basis. From computers and television displays, touch screens on mobile phones, to energy storage technologies such as solar cells, as well as sensors and light emitting devices. Conductors, particularly those offering optically transparent functionality, pervade almost all technologies to a certain degree or another, as well as a wide variety of other electronic devices, as illustrated in Figure 1.1. For this very reason new conductive materials, that simultaneously offer transparency and conductivity, have been the focus of considerable attention.

Trends in materials science and engineering are intimately related to the functionality of the end-market product and the end-user defined requirements. In recent years one such new requirement has come to light; flexibility. Disposable, low-cost, light weight and flexible substrates are attractive for many applications and the ultimate challenge has been, for some time, to combine both transparency and flexibility in a single conductive material[*].

It was not until 1995, when various families of conductive polymers were discovered, that serious applications exploiting flexible and transparent conductive materials were truly considered. The concurrent development of numerous soft-lithography techniques and improvements in micro ink-jet and gravure printing improved processability making a number of exciting new applications, such as electronic-skin and electronic–paper, accessible for the first time. Unfortunately, these conductive polymers were, and still are highly resistive. Finding materials with suitable combinations of flexibility, transparency and conductivity has proven difficult and the envisaged flexible and highly transparent touch screens, energy storage, sensors, and flexible displays are still some way off. Nonetheless, various candidate materials have been identified.

Metals, whilst being excellent conductors in their mechanically relaxed state, become poorly conducting when strained. Moreover, metals become optically opaque at thicknesses greater than 5 nm, whilst for thickness less than this their conductance drastically reduces[17]. Elastomer-embedded Au ribbons and pre-strained metal bridges have made some progress

---

[*] There are several [13] [14] [18] excellent reviews that consider transparent conductors, flexible conductors and flexible transparent conductors. All provide a good account on the current status of the field.
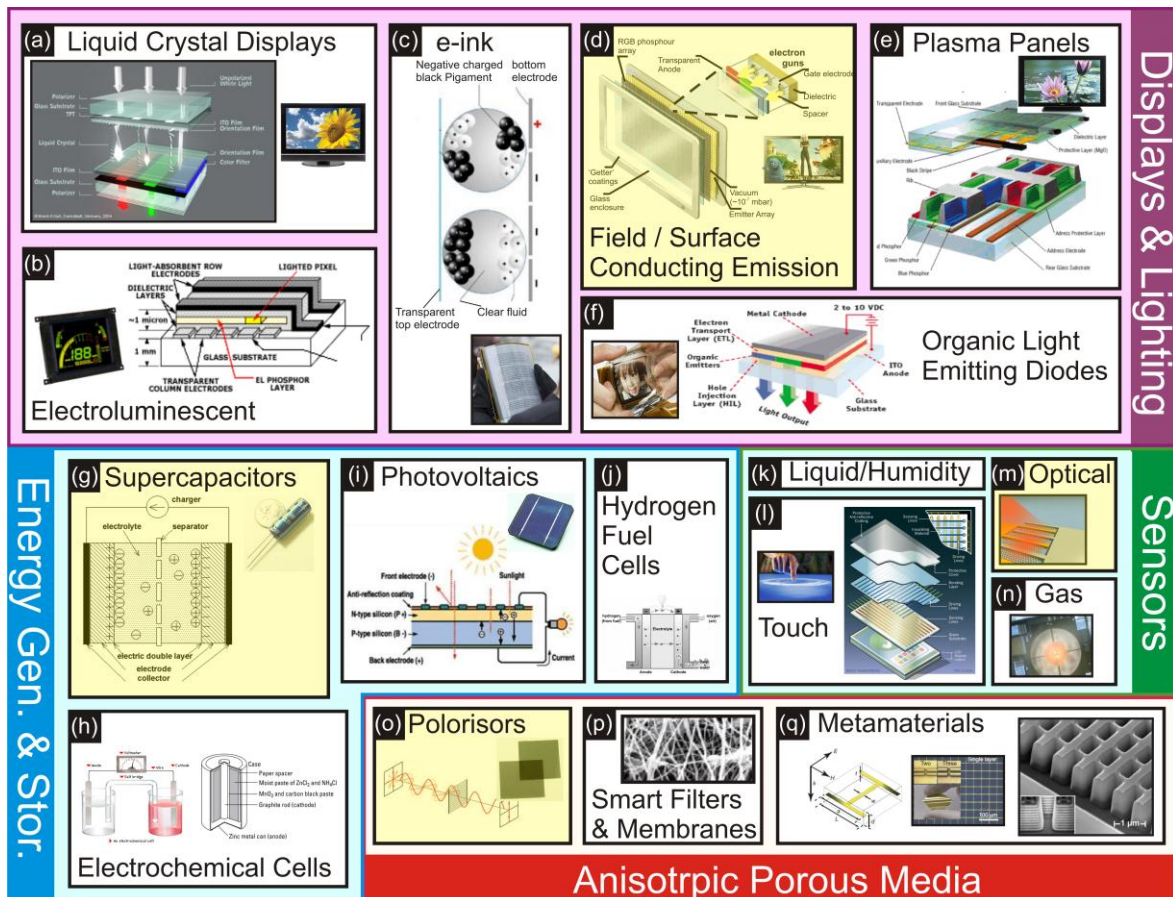
Figure 1.1 | Application of TFC nanostructured thin films. (a-f) Display and lighting, **(g-j)** energy storage and generation, **(k-n)** sensors and **(o-q)** anisotropic porous media are some of the many applications of flexible and/or transparent conductors. **(d)** Field emission sources, **(g)** supercapacitors, **(o)** optical polorisors and **(m)** optical sensors are highlighted as they have been developed during the work presented in this thesis work. Images from [1-5] [12] [8] [9] [10] [11] [14, 22] [26] [27] [30] [31] [32] [34].

toward enhancing the flexibility performance (Figure 1.2(a))[19, 20] but little can be done by way of increasing their optical transparency. Furthermore, these long wire-like structures cannot be easily processed into thin films – a major hindrance to practical integration and device development. Micro-crack formation ultimately limits the mechanical

robustness regardless of the patterning or host substrate[24].

Transparent conducting metal oxides (TCO), such as flourine doped tin oxide and (the increasingly expensive) indium tin oxide (ITO), have dominated the flat-panel display market for over three decades[28, 29] with little or no competition. Indeed, references to ITO have been made as far back as 1947 (US Patent #2564707) and indium, tin, antimony and fluorine alloys have been around since the 1930s[13]. Other more recently developed TCOs include aluminium, gallium and indium doped zinc oxides. Today, almost all electronic devices that require transparent conductors employ TCOs because of their excellent optical transparency

across the visible spectrum, large-area compatibility and high conductivity. The flat panel display market, which has an estimated net-worth of £61 billion per annum[35], accounts for the majority of TCO usage and has been the root cause of the steep rise in indium demand in recent years. All TCOs have poor flexibility performance, even patterned 'strain resistant' TCOs fail under modest flexing due to micro-crack formation (Figure 1.2(b)). Clearly, the successful use of conventional materials, like physical vapour deposited metals and TCOs, in exotic and pre-strained structures is costly, time-consuming and generally limited in broadness of application. A complementary approach is to develop whole new families of materials and to structure and pattern them in more conventional ways.

Conductive polymers including poly(aniline), untreated, poly(ethyl glycol) (PEG)[37] and 2′ -thiodiethanol (TDE) [40] enhanced poly(3, 4 -ethylenedioxythiophene) : poly(styrenesulfonate) (PEDOT : PSS) and its derivatives are highly flexible, relatively inexpensive, environmentally friendly and relatively conductive (Figure 1.2(j)). Nonetheless, they have undesirable hues and sheet resistances that are still too high for many applications[42, 43]. The minimum industry standard for display applications is an optical transmission > 90% and sheet resistance < 100 Ω/sq.[45]. Nevertheless the exact opto-electronic performance is largely application dependent. For example, displays require highly transparent and highly conductive electrodes, whilst touch screens and sensors can be far less transparent, less conductive but must offer higher flexibility. Few materials have reached the industry opto-electronic standard, notwithstanding any flexibility issues. Metal nanowires, specifically silver nanowires (Figure 1.2(c)), offer the highest electrical conductivity for a given transparency[45, 48]. However, whilst functionally attractive, they are largely inflexible and rather expensive[49].

A material with simultaneously high optical transparency, high flexural tolerance and high electrical conductivity is the ultimate goal. Thin films consisting of low-dimensional carbon nanomaterials offer a viable solution. These 'nanocarbons' come in variety of metallic and semiconducting forms (Figure 1.2(d,g-p)) and have shown, time and again, to outperform the competing technologies across a variety of industry important metrics. Furthermore, the structural anisotropy of the composite nanocarbons promises multi-functional transparent flexible conductors (TFCs). The various competing technologies are summarised in terms of their flexibility, transparency and conductivity in Figure 1.2. Clearly the nanocarbons, specifically graphene and carbon nanotube thin films, are well placed due to their high and

Figure 1.2 | Materials for TFCs.
(a) Metal serpentines, **(b)** metal-doped tin and zinc oxide derivatives dominate the transparent conductor market. **(c)** metal nanowires, **(e, f)** metallic and semiconducting nanowires are viable alternatives. **(j)** organic / polymers. **(d)** Graphene and **(g-I, k-p)** carbon nanotubes are shown to offer some of the highest flexibility performance (CNTs) and highest transparency performance (graphene) whilst maintaining low sheet resistances. M and S denote metallic and semiconducting materials. Adapted from [6-12] [15] [14, 16] [21] [23] [25] [19] [33] [36] [38] [39] [41] [44] [46] [47].

NEXT GEN. DISPLAYS & DEVICES

Nanocarbons (1,2,3,....-layer Graphene)

M/S   >700 Ω/sq.

Metal Doped Oxides

20 Ω/sq.

Ag Nanowires

15-1000 Ω/sq.

Flexible Photovoltaics

M/S   SI NANO

Nanocarbons (SW & MWCNTs) 2 - >1000 Ω/sq.

e-skin

e-paper

Conformal Sensors

Wearable electronics.

M/S

Touch Screens

Semicon. Nanowires (Si/GaN/ZnO/In₂O₃/MnO₂)

Organics - PEDOT:PSS, Pentacene, etc. >5 kΩ/sq.

M/S

STATE-OF-THE-ART DISPLAYS & DRIVERS

Metal serpentines

1 Ω/sq.

Micro-processors

Low   Transparency   High

Low   Flexibility   High

wide-ranging transparency (2.3 % per graphene layer), high flexibility and broad range of conductivity. Nanotubes, being more opaque, accommodate higher conductivities and higher flexibilities.

This thesis documents the authors work on the development of dry-processed graphene and multi-walled carbon nanotube TFCs offering *enhanced functionality* over more traditional and currently available materials. The thin films developed throughout this work have been evaluated in terms of their functional performance as supercapacitors, field emitting electron sources, optical sensors and optical polarisers and were fabricated through dry-processing techniques. That is to say that no wet chemistry has been used. Wet processing damages the as-grown materials and reduces the size and crystallinity of the composite nanocarbons which degrades the electronic performance. The structure and the electronic properties of the nanocarbons are intimately related through the degree of crystallographic disorder. Similarly, surfactants have been avoided in all cases. The performance of the dry-processed films has been compared where appropriate to their *chemi douche* equivalent in an attempt to understand some of the more important implications of wet processing and network alignment.

Materials such as pentacene and porous networks of silicon, gallium nitride and zinc oxide nanowires offer flexible and transparent semiconductivity. However, it is important to note that the carbon nanotubes and graphene, although semi-metallic in this study, can also be semiconducting by simple adjustment of the chemical vapour deposition (CVD) parameters. Combining metallic and semi-metallic carbon electronics promises a viable technological route toward next-generation flexible transparent displays for handheld devices that are compatible across a range of display platforms, including: liquid crystal, field emission, plasma, and even electroluminescent. In all cases it is the driver electrodes that enforce the structural stiffness of the display. Consideration of flexible transparent semiconducting thin films is outside the scope of this thesis.

1.1 Objectives

The objectives of this thesis are to understand, develop and employ the underlying thermal CVD growth mechanisms and functionality of TFCs based on large-area graphene and multi-walled carbon nanotube (MWCNTs). The major challenges throughout to understand the

CVD growth mechanism, develop appropriate transfer techniques and evaluate the transport and opto-electronic performance of the nanostructured carbon thin films.

1.2 Thesis Structure

This thesis charts the authors' work on the development and understanding of CVD synthesised MWCNTs and graphene thin films for transparent and flexible electronics applications; specifically polymer-supported TFCs, field emitters, and free-standing optical polarisers and optical sensors.

Chapter 2 introduces the reader to the range and history of the various nanocarbon derivatives and synthesis techniques, with specific emphasis on the chemical vapour deposition of carbon nanotubes and graphene. To elucidate the underlying chemical vapour deposition mechanisms and to draw generalisations between nanotube and graphene synthesis, the authors work on determining the activation energies of indium tin oxide and alumina supported iron and nickel catalysed MWCNTs and copper catalysed graphene have been investigated and compared. The analysis presented suggests that transition metal catalysed nanotube and nanofibre growth are surface-diffusion limited whilst Cu-catalysed graphene growth is atom-integration-limited.

The development of nanotube and graphene dry-transfer techniques is detailed in Chapter 3. A MWCNT physical rolling process and a hot-pressed graphene lamination process is presented. The films' opto-electronic performances are evaluated through UV-Vis spectrophotometry and sheet resistance measurements. Processability, functionality (as supercapacitor electrodes) and flexibility issues are also considered. A generalised macroscopic transport mechanism for large area bilayer graphene and MWCNT thin films is proposed based on c-axis conduction combined with strong tunnelling artefacts, determined by low-temperature transport measurements. Decreasing disorder was shown to increase the deviation from a purely tunnelling model.

The field emission performance of rolled, vacuum filtrated and screen printed nanotube thin films is examined in Chapter 4. Models are proposed to account for the reduced turn-on potential for vacuum filtrated films compared to their untreated counterpart. The field emission performance and characteristics of zinc oxide nanowire ballasted dry-processed

nanotube films are discussed in addition to those of *in-situ* grown carbon nanotubes on electrolysed stainless steel mesh.

MWCNTs are structurally anisotropic and as such offer TFCs of enhanced functionality if macroscopic films can be developed to exploit this anisotropy. Chapter 5 describes various *in-situ* and *ex-situ* dry-processing routes to nanotube alignment. A mechanical extrusion technique, promising process scalability and high degrees of alignment, is exploited to form optical polarisers and optical sensors. The latter offering the perfect platform to study and unambiguously determine the photoresponse of multi-walled carbon nanotubes. Experiments into the photoresponse of such films are described to determine the root cause of the photoresponse. A model based on the surface migration of weakly bound gas species is proposed to account for the measured variation in conductivity. Nanotube polarisers with extinction coefficients well into the near infra-red were developed, outperforming common dichroic films by some 400 nm. No absorption edge was identified. The limit of this study was 1.1 μm. A generalised model describing the polarisability is also explained.

The conclusions, technological outlook and planned future work are described in Chapter 7.

References

1. Image: Plasma Display Panels - http://www-star.stanford.edu (/~vlf/plasma_display/index.htm).
2. Image: Samsung Nano TV using Field Emission Display - http://led-fever.blogspot.com (/2010/10/samsung-nano-tv-using-field-emission.html).
3. Image: Organic Light Emitting Diode - http://www.audioholics.com (/news/industry-news/panasonic-oleds-2011/image_view_fullscreen).
4. Image: Planar. Electroluminescent Display Technology - http://www.planarembedded.com (/technology/el/).
5. Image: Electrochemical Cells; Flashlight Cells - http://www.dummies.com (/how-to/content/electrochemical-cells-flashlight-cells.html).
6. McAlpine, M. C., Ahmad, H., Wang, D.& Heath, J. R. (2007). Highly ordered nanowire arrays on plastic substrates for ultrasensitive flexible chemical sensors, *Nat. Mater.*, **6**, pp. 379-384.
7. Image: IEEE Spectrum. Watching the Nanotube - http://spectrum.ieee.org (/semiconductors/optoelectronics/watching-the-nanotube/0).
8. Image: e-ink displays - http://www.eink.com/.
9. Image: Supercapitor - http://www.sparkfun.com (/products/746).
10. Image: Photovoltaics; Electricity direct from sunlight - http://benes-ltd.com (/cms/index.php?option=com_content&view=article&id=19&Itemid=27).
11. Image: Poarizer - http://en.wikipedia.org (/wiki/File:Wire-grid-polarizer.svg).
12. Image: What is a Hydrogen Fuel Cell? - http://biodiesel.environmentalactiongroup.org (/hydrogen.html).
13. Hecht, D. S., Hu, L.& Irvin, G. (2011). Emerging transparent electrodes based on thin films of carbon nanotubes, graphene, and metallic nanostructures, *Adv. Mater.*, **23**, pp. 1482-1513.

14. Sun, J., Zhang, B.& Katz, H. E. (2011). Materials for printable, transparent, and low-voltage transistors, *Adv. Funct. Mater.*, **21**, pp. 29-45.

15. Chen, P.-C., Shen, G., Chen, H., Ha, Y.-g., Wu, C., Sukcharoenchoke, S., Fu, Y., Liu, J., Facchetti, A., Marks, T. J., Thompson, M. E.& Zhou, C. (2009). High-Performance Single-Crystalline Arsenic-Doped Indium Oxide Nanowires for Transparent Thin-Film Transistors and Active Matrix Organic Light-Emitting Diode Displays, *ACS Nano*, **3**, pp. 3383-3390.

16. Cao, Q., Zhu, Z. T., Lemaitre, M. G., Xia, M. G., Shim, M.& Rogers, J. A. (2006). Transparent flexible organic thin-film transistors that use printed single-walled carbon nanotube electrodes, *Appl. Phys. Lett.*, **88**, pp. 1-3.

17. Lacour, S. P., Huang, Z., Suo, Z.& Wagner, S. (2002). Deformable interconnects for conformal integrated circuits, *Mat. Res. Soc. Symp. Proc.*, **736**, pp. 183-188.

18. De, S., Lyons, P. E., Sorel, S., Doherty, E. M., King, P. J., Blau, W. J., Nirmalraj, P. N., Boland, J. J., Scardaci, V., Joimel, J.& Coleman, J. N. (2009). Transparent, Flexible, and Highly Conductive Thin Films Based on Polymer−Nanotube Composites, *ACS Nano*, **3**, pp. 714-720.

19. Rogers, J. A., Someya, T.& Huang, Y. (2010). Materials and Mechanics for Stretchable Electronics, *Science*, **327**, pp. 1603-1607.

20. Lacour, S. P., Jones, J., Suo, Z.& Wagner, S. (2004). Design and performance of thin metal film interconnects for skin-like electronic circuits, *IEEE Electr. Device L.*, **25**, pp. 179-181.

21. Baca, A. J., Ahn, J.-H., Sun, Y., Meitl, M. A., Menard, E., Kim, H.-S., Choi, W. M., Kim, D.-H., Huang, Y.& Rogers, J. A. (2008). Semiconductor wires and ribbons for high-performance flexible electronics, *Angewandte Chemie*, **47**, pp. 5524-5542.

22. Image: Invisibility metamaterials research breakthrough - http://www.gizmag.com (/3d-metamaterials-invisibility/9804/).

23. Xu, H., Chen, L., Hu, L.& Zhitenev, N. (2010). Contact resistance of flexible, transparent carbon nanotube films with metals, *Appl. Phys. Lett.*, **97**, pp. 1-3.

24. Lacour, S. P., Chan, D., Wagner, S., Li, T.& Suo, Z. (2006). Mechanisms of reversible stretchability of thin metal films on elastomeric substrates, *Appl. Phys. Lett.*, **88**, pp. 1-3.

25. Sun, Y.& Rogers, J. A. (2007). Inorganic semiconductors for flexible electronics, *Adv. Mater.*, **19**, pp. 1897-1916.

26. Choi, M., Lee, S. H., Kim, Y., Kang, S. B., Shin, J., Kwak, M. H., Kang, K. Y., Lee, Y. H., Park, N.& Min, B. (2011). A terahertz metamaterial with unnaturally high refractive index, *Nature*, **470**, pp. 369-373.

27. Image: What are Touch Screens? - http://whatistouchscreen.com/.

28. Gerhardinger, P.& Strickler, D. (2008). Fluorine doped tin oxide coatings - Over 50 years and going strong, *Key Eng. Mater.*, **380**, pp. 169-178.

29. Image: Cambridge CMOS Sensors - http://www.ccmoss.com/.

30. Image: How the iPhone Works - http://electronics.howstuffworks.com (/iphone2.htm).

31. Image: SolarGen - http://www.solargenuk.com (/3asolarpv.html).

32. Image: View Beyond LCD DID Innovation - http://www.flatsoftglobal.com (/12-07-2009/view-beyond-lcd-did-innovation.html).

33. Ishikawa, F. N., Chang, H.-K., Ryu, K., Chen, P.-C., Badmaev, A., De Arco, L. G., Shen, G.& Zhou, C. (2009). Transparent Electronics Based on Transfer Printed Aligned Carbon Nanotubes on Rigid and Flexible Substrates, *ACS Nano*, **3**, pp. 73-79.

34. Image: Flexible, full-color OLED display - http://pinktentacle.com (/2007/05/flexible-full-color-organic-el-display/).

35. Qaurterly Worldwide FRD Forecast Report , Q3 2009 - www.displaysearch.com

36. Jung, Y. J., Kar, S., Talapatra, S., Soldano, C., Viswanathan, G., Li, X. S., Yao, Z. L., Ou, F. S., Avadhanula, A., Vajtai, R., Curran, S., Nalamasu, O.& Ajayan, P. M. (2006). Aligned carbon nanotube-polymer hybrid architectures for diverse flexible electronic applications, *Nano Lett.*, **6**, pp. 413-418.

37. Wang, T., Qi, Y., Xu, J., Hu, X.& Chen, P. (2005). Effects of poly(ethylene glycol) on electrical conductivity of poly(3,4-ethylenedioxythiophene)-poly(styrenesulfonic acid) film, *Appl. Surf. Sci.*, **250**, pp. 188-194.

38. Lee, Y., Bae, S., Jang, H., Jang, S., Zhu, S.-E., Sim, S. H., Song, Y. I., Hong, B. H.& Ahn, J.-H. (2010). Wafer-Scale Synthesis and Transfer of Graphene Films, *Nano Lett.*, **10**, pp. 490-493.

39. Bae, S., Kim, H., Lee, Y., Xu, X. F., Park, J. S., Zheng, Y., Balakrishnan, J., Lei, T., Kim, H. R., Song, Y. I., Kim, Y. J., Kim, K. S., Ozyilmaz, B., Ahn, J. H., Hong, B. H.& Iijima, S. (2010). Roll-to-roll production of 30-inch graphene films for transparent electrodes, *Nat. Nanotechnol.*, **5**, pp. 574-578.

40. Admassie, S., Zhang, F., Manoj, A. G., Svensson, M., Andersson, M. R.& Inganäs, O. (2006). A polymer photodiode using vapour-phase polymerized PEDOT as an anode, *Sol. Energ. Mat. Sol. C.*, **90**, pp. 133-141.

41. Madaria, A. R., Kumar, A., Ishikawa, F. N.& Zhou, C. (2010). Uniform, Highly Conductive, and Patterned Transparent Films of a Percolating Silver Nanowire Network on Rigid and Flexible Substrates Using a Dry Transfer Technique, *Nano Res.*, **3**, pp. 564-573.

42. Tehrani, P., Isaksson, J., Mammo, W., Andersson, M. R., Robinson, N. D.& Berggren, M. (2006). Evaluation of active materials designed for use in printable electrochromic polymer displays, *Thin Solid Films*, **515**, pp. 2485-2492.

43. Jönsson, S. K. M., Birgerson, J., Crispin, X., Greczynski, G., Osikowicz, W., Denier van der Gon, A. W., Salaneck, W. R.& Fahlman, M. (2003). The effects of solvents on the morphology and sheet resistance in poly(3,4-ethylenedioxythiophene)-polystyrenesulfonic acid (PEDOT-PSS) films, *Synth. Met.*, **139**, pp. 1-10.

44. Cairns, D. R.& Crawford, G. P. (2005). Electromechanical properties of transparent conducting substrates for flexible electronic displays, *Proc. IEEE*, **93**, pp. 1451-1458.

45. De, S.& Coleman, J. N. (2010). Are there fundamental limitations on the sheet resistance and transmittance of thin graphene films?, *ACS Nano*, **4**, pp. 2713-2720.

46. OLED/PLED technology

47. Sankir, N. D. (2008). Selective deposition of PEDOT/PSS on to flexible substrates and tailoring the electrical resistivity by post treatment, *Circuit World*, **34**, pp. 32-37.

48. Lee, J. Y., Connor, S. T., Cui, Y.& Peumans, P. (2008). Solution-processed metal nanowire mesh transparent electrodes, *Nano Lett.*, **8**, pp. 689-692.

49. Yu, Z., Zhang, Q., Li, L., Chen, Q., Niu, X., Liu, J.& Pei, Q. (2011). Highly flexible silver nanowire electrodes for shape-memory polymer light-emitting diodes, *Adv. Mater.*, **23**, pp. 664-668.

Chapter II

The Nanocarbons &
Chemical Vapour Deposition
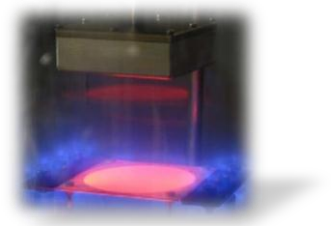
2.   Introduction

Carbon is a hugely diverse element. It can be conducting, semiconducting or insulating, chemically inert or extremely reactive, incredibly soft or one of the hardest materials known and even optically opaque or transparent. The most common carbons forms are diamond and graphite - two profoundly different materials.

2.1   Carbon & it's Nano Derivatives

Very few other materials in nature enjoy the allotropic diversity of carbon. The reason for which stems from carbons affinity toward atomic orbital hybridisation which allows it to assume several distinct types of valence bonds. Carbon, a group 14 non-metal, has six electrons; four in its outermost valence shell ($2s^2 2p^2$) and two strongly bound core ($1s^2$) electrons. Chemical bonds form when the atomic orbitals of the constituent atoms overlap to produce molecular orbitals. When two atomic orbitals combine, to form two molecular orbitals, one of the molecular orbitals has a lower energy (the bonding) and the other has higher energy (the anti-bonding). When a single carbon atom bonds with a neighbouring carbon atom, to maximise orbital overlap their orbitals hybridise via the mixing of the electrons wave functions. Hybridisation involves the combination of atomic orbitals to produce hybrid atomic orbitals which interact with one another to produce augmented molecular orbitals. The *s* orbital is spherical and the three *p* orbitals align orthogonally in the x, y, and z directions (p_x, p_y and p_z). The promotion of a *2s* electron to the *2p* orbital induces one of three possible orbital hybridisations. *p*-mixing produces planar sets of hybrid molecular orbitals where the third *p* orbital remains unchanged giving rise to two-dimensional confinement. The one-to-one, *2s-2p*, interaction produces two sp^2 orbitals. The resulting two σ and two π bonds are common to the hydrocarbons, typically found in alkynes like acetylene. The remaining two hybridisation types are important to diamond and graphite and the crystallites. In the crystalline phase the *2s*, *2p_x*, *2p_y* and *2p_z* orbitals are central in producing strong covalent bonds common to all nanostructured carbons, diamond and graphite. In the case of diamond, the *2s* electron orbital interacts with three *2p* orbitals. The four sp^3 bound carbon atoms tetrahedrally arrange, as this is the lowest energy arrangement, in a face-centred cubic lattice via single covalent σ bonds. The carbon-carbon bond angle and length are 109.5$^\text{o}$ and 1.55±0.1 Å, respectively. The amorphous carbons (*a*-C), such as
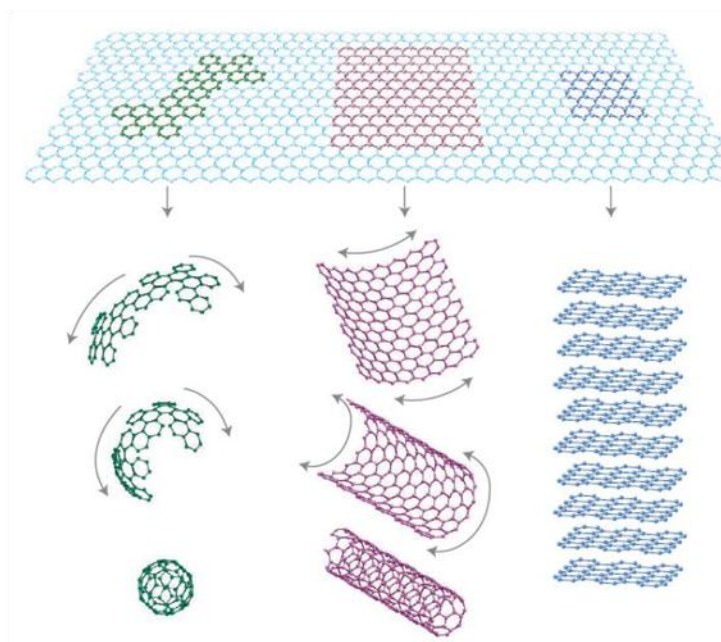
Figure 2.1 │ The graphene building block. Schematic representation of the various types of nanocarbon formation based on the graphene unit. Graphene can be wrapped to form the 0D fullerenes (left), rolled into 1D nanotubes (centre) and stacked into 3D graphite (right). From[9, 10].

tetrahedral *a*-C / diamond-like carbon, are random assortments of sp^2 and sp^3. Diamond, an sp^3 hybridised allotrope, is amongst the hardest materials known and has a density of 3.51 g/cm^3. It is highly transparent, has a wide band gap (5.5 eV) and is an extremely poor conductor due to the lack of free-electrons. In contrast, graphite is a soft opaque material, has a density of 2.26 g/cm^3, and is an excellent conductor. Graphite falls into the fourth hybridisation type. Three sp^2 orbitals are formed from a *2s* orbital interacting with two *2p* orbitals. The resulting hexagonal lattice is maintained by σ bonds in the basal plane and has a bond angle and length of 120° and 1.42 Å, respectively. π stacking increases the inter plane (separated by 3.34 Å) Van der Waals forces (temporary electrostatic interactions) and allow these planes to slide freely making graphite an excellent solid lubricant. These stacks can be arranged in a variety of ways, including ABAB[28] (Bernal), alpha[29] (hexagonal), beta[30] (rhombohedral) or turbostratic[32] (unaligned / uncorrelated with respect to one another) configurations – all of which, in the 3D limiting case, show similar electronic properties. Each carbon atom is covalently bonded to three others. Each carbon contributes a loosely bound delocalised π electron which makes graphite a good conductor in the *c*-axis (in-plane).

In the past three decades an increasing number of exotic low-dimensional nanostructured carbon allotropes have been discovered. In order of descending dimensionality these include

artificial diamond (3D), graphene (2D), carbon nanotubes (1D) and the fullerenes (0D). Such self-assembly across multiple dimensionalities and over such huge length scales: from the centimetre-scale diamond to the nanoscopic nanotube, is unique to carbon. Graphene, a single atomic plane of graphite, is the fundamental unit of the fullerenes, nanotubes and graphite and can be wrapped, rolled and stacked accordingly to form each, as illustrated in Figure 2.1.

2.2   The History of the Nanocarbons

Owing to the intriguing size-dependent optical, mechanical, magnetic and electronic properties of many materials, combined with the development of electron microscopes of ever finer resolution, the field of nanotechnology[α] was spawned in the mid-1950s and has burgeoned ever-since. The term 'nanotechnology' refers to "the creation of useful materials (and) devices through (the) control of matter at the nanometre (10^{-9} m) length scale and the exploitation of (the) novel properties and phenomena developed at (this) scale[*],[34]. The strong association between carbon and nanotechnology began with the auspicious discovery of carbon fibres, the macroscopic analogue of the carbon nanotube.

 The history of carbon as an engineering material has been closely coupled to our ability to isolate, albeit synthetically derive or naturally source, its various forms. One of the earliest and most profound instances of exploiting engineered carbon, specifically filamentous carbon, was by the pioneer T. Eddison who successfully integrated pyrolysed carbon filaments into early incandescent light bulbs. These filaments where ohmically heated to produce light. Unfortunately their fame was short-lived as they were soon superseded by the more robust tungsten filament we all know today. Consequently carbon research stagnated for some years and any on-going research progressed at a reserved pace. The demand for light weight, stiff and strong composites by the automobile and aeronautics industries stimulated the field once again in the early 1950s. Indeed, it seems that throughout history the development of the various nanocarbons has been largely stimulated by our desire to find and develop new and enhanced composite materials to imbed in polymeric hosts. It was such composite applications that sparked the detailed seminal investigations into the growth of carbon fibres, specifically through the use of polymer-precursor CVD. During CVD synthesis the then well-known carbon fibres were, very occasionally, combined with a small number of

---

[α] Nano *(ηαηοσ)* – From the Latin (nānus) meaning 'dwarf', today describes structures smaller than < 100 nm.
[*] N. Taniguchi
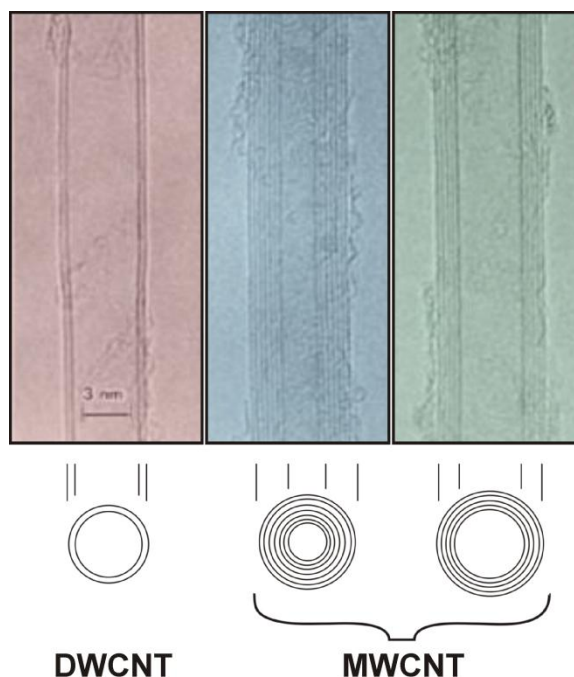
Figure 2.2 | The nanotube. (left to right). A 4.7 nm diameter double-walled CNT, a seven-walled multi-walled (MW) CNT (6.5 nm in diameter), and a 6.7 nm five-walled MWCNT[6-8]. (Scale bar 3 nm)

sub-micron fibres. In the mid-1970s, Baker *et al.*[35-38] conjectured that the underlying growth mechanism of these carbon nanofibres (CNFs) was a combination of hydrocarbon precursor pyrolysis on the transition metal catalysts, carbon diffusion and precipitation. The catalysts were deemed essential to CNF growth. The first fibres produced consisted of graphitic walls aligned in an assortment of directions relative to fibre axis. Baker *et al.* were not the first, by any means, to observe such sub-micron fibres. Some very early, and largely unnoticed works go back to 1952, by Radushkevich *et al.*[39] and Tesner *et al.*[40]. The synthesis of the first sub-50 nm diameter fibres must really be attributed to M. Endo, A. Oberlin and T. Koyama[41] who, in 1976, reported hollow tubes, with diameters ranging from 2 to 50 nm formed from concentrically nested graphitic planes aligned parallel to the tubes long axis. These so-called "filamentous carbons", now known as carbon nanotubes (CNTs), unknown to them at the time, were to be an incredibly rich source of fascinating science over the next three decades. Unfortunately the lack of repeatable and macro-scale synthesis processes inhibited further progress for some time and nanotubes did not return to prominence until 1991.

The early-1990s saw a year of renewed interest. The new field of nanotechnology had been stirred by the independently published electron microscopy studies of Iijima *et al.*[6] (Figure 2.2) and Bethune *et al.*[42], who, like many in the field, were primarily working on diamond-

like carbon at the time. Consequently, and rather unfortunately, the accolade of 'nanotube discoverer' is repeatedly and incorrectly awarded to Iijima *et al.*[43] due to the sheer impact of their studies. The individual who coined the now famous term 'carbon nanotube' has faded into history whilst the nanotubes themselves have gone on to achieve equal amounts of fame and notoriety in a variety of physical, biological and engineering fields.

Rather unexpectedly, the first nanotube-based commercial products, based on conducting nanotube-polymer composites, have only recently been released into the market by Hyperion[44] and others[45], some 20 years after their discovery. Other viable applications include heat sink materials, advanced filtration media, atomic force and scanning electron microscope tips, field effect transistor channels and electrodes, field emitting displays and environmental lighting, integrated circuit interconnects, optoelectronics components, supercapacitor electrodes, nanoelectromechanical devices, and chemical, biological and physical sensing materials that can be optimised by chemical functionalization. This list, although it may seem so, is not exhaustive.

The discovery of the fullerenes (self-terminated spheres formed from 20-100 trigonally bonded carbon atoms – the most famous of which being the C_{60} Buckminster fullerene; a 60 atom truncated isocahedron 7.1 Å in diameter), six years earlier than the work of Iijima *et al.*[43], by H. W. Kroto *et al.*[46], set the scene for the nanotubes. However, the nanocarbon group was incomplete. The zero-dimensional fullerenes had been discovered, isolated and even grown. So too had the one-dimensional nanotubes, although controlled growth and understanding of the structures electronic properties were still under heated discourse. Graphite accounted for the three-dimensional form and was readily available from nature. However, no two-dimensional allotrope had yet been isolated despite the fact that its properties had been understood and widely utilised for over 70 years as an academic tool to predict the electronic properties of other carbon materials, including both the fullerenes and the nanotubes. Isolation of these 2D crystals had been deemed a natural uncertainty. In the 1934, the theorists Landau and Peierls and later, Mermin, argued that 2D crystals would be impossible to isolate at finite temperatures, regardless of their constituents, due to lattice thermodynamic instabilities[47-49]. For this reason any significant attempts at direct synthesis were few and far between and were often hampered before any significant progress could be made. Graphene remained, for a long time, a purely academic material[9]. It would be another 13 or so years before graphene would become a truly realisable, rather than a purely
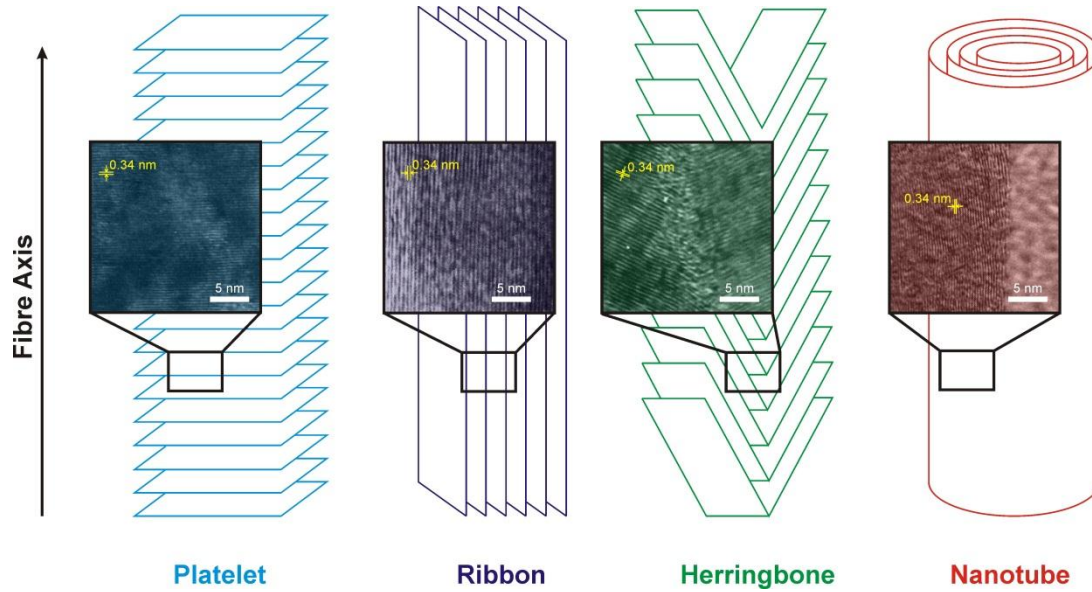
Figure 2.3 | **The filamentous graphitic carbons.** Adapted from Rodriguez *et al.*[2, 4, 5].

hypothetical, engineering material. In the meantime nanotube research was developing at a break-neck pace.

Nanotubes exist within a subset of the filamentous graphitic nanofibres (Figure 2.3). The group is broken-down depending on the orientation of the graphitic planes and consists of the platelets (or stacked), ribbons, herringbones and nanotubes. Platelet fibres are composed of graphitic planes that lie perpendicular to the long axis. Ribbons are composed of graphitic planes that lie parallel to the long axis. Herringbone fibres are an intermediary between the ribbons and platelets. The graphitic planes form at angles to the fibre axis. The herringbone and platelet types are often >50 nm in diameter and are referred to as bamboo-like due to their, typically nitrogen containing, compartmentalised structure. Herein these wide diameter and crystallographically defective fibres are referred to simply as 'nanofibres'. Nanofibres are typically used in energy storage applications, such as electrodes in lithium cells[50] because of their highly defective crystal lattices which allow small ions and molecules to intercalate, thereby offering incredibly high active surface areas. Nanotubes are the fourth member of the set. They have the smallest diameter of all the filaments, the record being 0.4 nm[51], and are very similar in their graphitic alignment to the ribbons. The ribbon structure is less thermodynamically stable than the cylindrical nanotube structure due to the large number of edge-state dangling (undefined) bonds. Although cylinder formation imparts high levels of internal strain energy it is, nonetheless, energetically favourable.   A similar argument

explains why the nanotube ends are capped by bisected / semi-fullerene structures. Internal strain perturbs the sp^2 molecular orbitals which augments the electronic character. Nanotubes can be single-walled (SWCNTs) or multi-walled and can be anywhere from less than a few, to several tens of nanometers in diameter and up to a few millimeters in length[52]. MWCNTs are composed of a series of coaxial, hollow uncorrelated shells[53].

Graphene, as an engineering material, has had a much more enigmatic and even sporadic developmental history and it was not until 2004 that free-standing graphene was successfully isolated by mechanical exfoliation[54, 55]. Contrary to popular belief at the time, this was not the first instance of engineered graphene production. The early experiments between 1930 and 1960 of Dresselhaus *et al.*[31], Hofmann *et al.*[56] and others[57-61] on graphite chemical exfoliation using intercalates - compounds developed to swell, expand and even separate graphite crystals - had already isolated graphene, albeit extremely small flakes in low quantities. However, intercalation compounds were of little interest to many. Although the intercalates could be removed by post-processing rinsing, process variability and the inability to isolate significant amounts of truly individual graphene flakes limited its commercial and even scientific value[9]. Since then various approaches to graphene synthesis have been developed with CVD being one of the most promising. Figure 2.4 illustrates some of the key steps in the development of graphene processing.

Figure 2.4 | **Graphene isolation.** Adapted from [3] [25] [27] [20] [19] [18] [10].

1) Graphite intercalation[17, 31] **(a,b)** Intercalation equipment and solution dispersed graphite flakes. **(c)** An expanded intercalated graphite crystal.

2) Mechanical exfoliation **(d,e)** Schematic and optical micrograph of a bi-layer channel transistor. **(f)** Atomic resolution scanning tunnelling micrograph of an exfoliated flake.

3) Silicon carbide (SiC) sublimation **(g)** A SiC facet illustrating graphene nucleation during thermal restructuring. **(h)** SiC crystal structure. **(i)** Atomic force micrograph (AFM) of a graphene/SiC substrate clearly showing characteristic plateaus. *Insert*: AFM cross-section line-scan of the plateau. **(j)** Optical micrograph of SiC 1-3 layered graphene.

4) Chemical Vapour Deposition **(k)** SEM micrograph[8]. *Insert:* Aberration-corrected annular dark-field scanning TEM image showing flake boundaries (500 nm scale bar). Select area diffraction pattern[33]. **(l)** TEM of multi-layer graphene[8]. **(m,n)** Optical micrographs of 1-4 layer large-area films[8]. **(o)** Raman spectra of 1-4 layer films[8]. **(p-t)** Spatially mapped Raman spectra (D, G, G', G/D and G'/G ratios)[16]. **(u)** Raman spectra of 1-3 layer flakes[16].

2.3 Properties of Graphene & Carbon Nanotubes

The strength of the hybridised sp^2 bonds, which are incidentally nearly as strong as the sp^3 bonds of diamond, impart graphene and the nanotubes with their exceptional and unparalleled thermal, electronic and mechanical properties. Long-range crystallographic order and covalent bonding make them excellent conductors that are extremely resilient to atomic diffusion and electromigration effects and, as a result, are technologically important in applications such as electronics interconnects, power electronics and thermal management systems. Current carrying densities $>10^9$ A/cm^2[62], three orders of magnitude greater than copper deposited by the Damascene process, and near ballistic electron transport at room temperature have been reported[63, 64]. Young's moduli five times greater than steel are common, producing extremely robust materials that have attractive combinations of strength and flexibility. The low number of dangling bonds in the bulk impart nanotubes and graphene with high inertness to various gas species and resistance in strongly acidic and basic environments. Rather than chemically reacting with their environments reactants tend to physically adsorb. Paradoxically this bulk inertness is combined with high chemical reactiveness at the edge dangling bonds which promises ultra-high single-molecular sensitivity in various biological sensing applications.

Nanotubes and graphene have proven to be exceptionally rich scientific platforms for condensed matter physicists due to their intrinsic spatial confinement. Phenomena associated with two-dimensional confinement, in one-dimensional nanostructures, have been accessed using nanotubes and have ranged from the Kondo effect[65] to the optical Stark effect[66] and Rabi oscillations[67]. In (two-dimensional) graphene, the electrons are confined in one-dimension and allowed to move freely in the remaining two dimensions. In such two-dimensional electron gas systems the electrons behave like relativistic particles with a zero rest mass (massless Dirac Fermions) and rather extraordinarily have permitted table-top studies of phenomena such as the Klein Paradox[68] and the quantised anomalous quantum Hall effect - observations normally resigned to more complex, and certainly more costly experimentation[69, 70]. Graphene and nanotubes have high electron mobility at room temperature[71, 72], long mean free paths (>1 µm)[73, 74] are superconductors[75, 76] (as is graphite when intercalated with potassium-containing compounds) and have long spin-relaxation times[77, 78].

		Al	MWCNTs	GRAPHENE	*Ref.*
MECHANICAL	Young's Modulus (GPa)	70	200-1,200	>1,000	[79-81]
	Ultimate Tensile Strength (GPa)	0.09	11-150	130	[82]
	Failure Strain (%)	60	12-23	12	[83, 84]
	Structural Anisotropy	Low (3D)	High (1D)	Medium (2D)	/
OPTICAL	Band Gap (meV)	0	<100	<100, Tuneable	[15, 85]
	Absorption @ 550nm (%)	/	~20	2.3	[86]
THERMAL	Thermal Conductivity* (W/mK)	250	30-3,000	5,300	[87, 88]
	Specific Heat (mJ/gK) @ RT	962	200-600	200-750	[89, 90]
	Coeff. Lin. Therm. Expansion (K^{-1})	10^{-5}	10^{-6}	5×10^{-6}	[91-93]
	Thermoelectric power (µV/K)	2.5	65	90	[92, 94, 95]
ELECTRICAL	Resistivity (Ωm)	10^{-8}	10^{-4}	10^{-7}	[96, 97]
	Max. Current Density (A/cm^2)	~10^6	10^9	2×10^9	[97-99]
	Quantised Conductance (kΩ^{-1})	/	$(6.5)^{-1}$	$(6.5)^{-1}$	[100]
	Mobility (cm^2/Vs)	/	/	15,000-200,000	[9, 71]

Table 1 | **Physical properties.** Comparison between Aluminium, multi-walled (MW) CNTs and Graphene[2, 7, 33] (*At room temperature).

Table 1 summarises some of the more interesting properties of MWCNTs and graphene compared to aluminium, one of the most widely used materials in the electronics industry.

SWCNTs are rolled graphene flakes. The flake structure, roll angle (known as the chiral angle) and nanotube diameter are all intimately related to, and are critically important in determining the nanotubes electronic properties. Evidently an understanding of graphene is fundamental to an understanding of nanotubes.

A section of the real space honeycomb, densely-packed, graphene lattice, each unit cell consisting of two carbon atoms, is shown in grey in Figure 2.5(a). Figure 2.5(a) shows the reciprocal-space graphene lattice (red). The electronic band structure, first predicted by P. R. Wallace in 1947[101], depends on the interactions between the spatially localised orbitals of the two crystallographically inequivalent sub-lattices associated with adjacent atoms, each having a cosine-like dependence of energy (E) on momentum (k). Sets of wave functions constructed from tight-binding approximations of the superimposed orbitals give rise to the pseudo-three dimensional E-k dispersion diagram for the bonding (π) and anti-boding (π*)-bands in the first Brillouin zone, illustrated in Figure 2.5(b). The points at which the valence and conduction bands touch are the so-called Dirac point(s) and are denoted by the high symmetry K and K'. Graphene owes its semi-metallic character to this band touching (Figure 2.5(b) / Figure 2.6(a)). For energies close to the Fermi level (within ~1 eV) the dispersion relationship is linearly conical (Figure 2.5(c)). In more traditional electron systems and
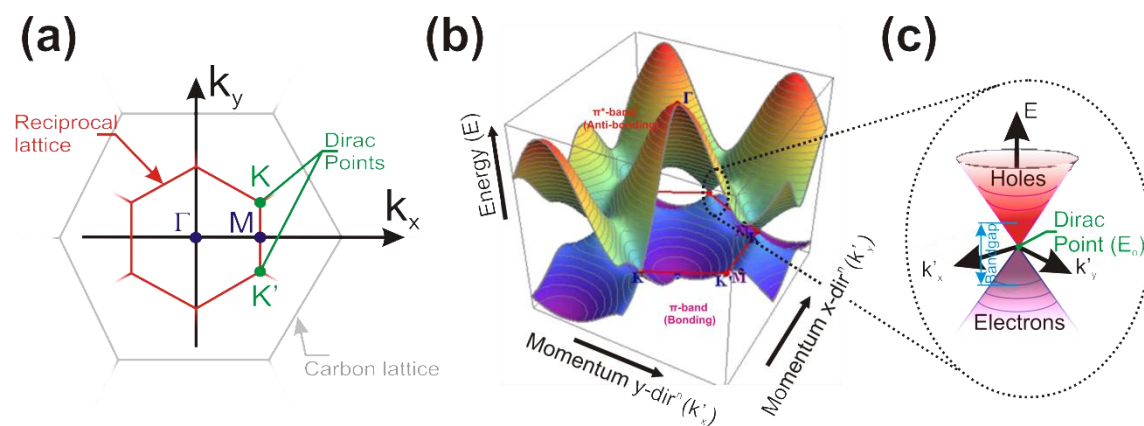
Figure 2.5 | The band structure of graphene. (a) The Brillouin zone with the carbon lattice in grey and the reciprocal lattice in red. Γ and M denote the high symmetry points and K / K' the Dirac points. **(b)** Pseudo-3D energy (E)-momentum (k) dispersion diagram for the bonding (π) and anti-boding (π*) bands. **(c)** Linear dispersion relation (Fermi level located at 0 eV). For doped and gated graphene the Fermi level shifts along the ordinate accordingly. Adapted from[22].
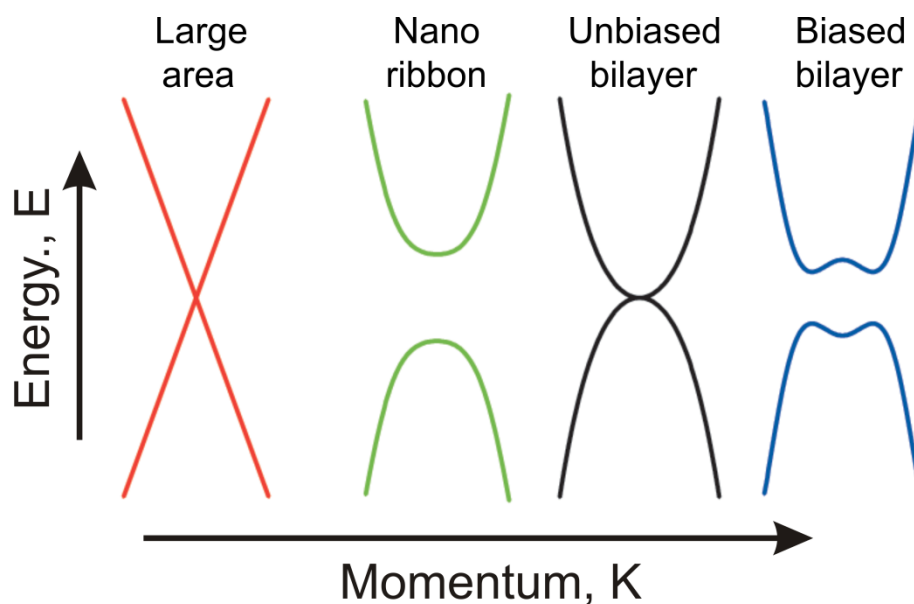
Figure 2.6 | The evolving band gap of graphene. The dispersion relations of **(a)** large area, **(b)** nanoribbon, **(c)** bilayer and **(d)** gated bilayer graphene (200-250 meV at F= 1-3x10^7 V/cm). Adapted from[13].

materials the near-ubiquitous quadratic dispersion relation, predicted by the Scrödinger equation, is most often valid. An important consequence of linear dispersion is that the electrons effective mass, given by the second order derivative of the dispersion relation, is zero. The electrons are said, therefore, to be massless. This dispersion relation is largely valid for mono and bilayer graphene (to a first approximation). Adding subsequent graphene layers drastically augments the electronic band structure. As the number of layers approaches ten the electronic structure becomes increasingly complex and tends toward that of turbostratic

graphite[102]. The stacking type and width (typically < 10 nm) of the graphene also affect the band structure[103]. Graphene is easily doped which also adjusts its band structure. Many compounds have been implicated including various photo and electron beam resists, metal etchants, metal contacts and nitrogen in Hall bar, Van der Pauw, transmission line and two and four terminal transport studies[104-107]. Figure 2.6 illustrates the general, undoped dispersion relations for large area, nanoribbon, bilayer and gated bilayer graphene. The band gap of bilayer graphene has been electrically tuned using dual-gated field effect transistor (FET) structures and operates as an analogue semiconductor with a continuously tunable gap and carrier doping concentration. In these bilayer FETs the electrons appear more massive when electrostatically gated - an effect directly probed by the degree of infra-red absorption during gating[108].

The graphene lattice can be conceptually rolled up to form a SWCNT (Figure 2.7(a)). The nanotubes chiral vector and chiral angle describe how the graphene lattice rolls. The chiral vector ($\vec{C}_h$), illustrated in Figure 2.7(b), is defined as;

$$\vec{C}_h = n_1\hat{a}_1 + n_2\hat{a}_2 \equiv (n_1, n_2) \tag{2.1}$$

where the lattice unit vectors are;

$$\hat{a}_1 = \left(\frac{\sqrt{3}}{2}a, \frac{1}{2}a\right), \quad \hat{a}_2 = \left(\frac{\sqrt{3}}{2}a, -\frac{1}{2}a\right) \tag{2.2}$$

and n_1 and n_2 are integer values. The corresponding nanotube diameter as a function of chiral angle is given by;

$$d = \left(\frac{l}{\pi}\right), \quad l = |C_h| = \sqrt{C_h.C_h} = a\sqrt{n_1^2 + n_2^2 + n_1 n_2} \tag{2.3}$$

where l defines the nanotubes circumference and a is the lattice constant and is given by;

$$a = \sqrt{(\hat{a}_1.\hat{a}_1)} = \sqrt{(\hat{a}_2.\hat{a}_2)} = \sqrt{2(\hat{a}_1.\hat{a}_2)} = 1.42\overset{o}{\text{A}} \times \sqrt{3} = 2.46\overset{o}{\text{A}} \tag{2.4}$$

The carbon-carbon bond length, $a_{c-c} = 1.42\overset{o}{\text{A}}$. The chiral angle, θ (Figure 2.7(b)) is, as a result, given by;

$$\theta = \tan^{-1}\left(-\frac{\sqrt{3}n_2}{2n_1 + n_2}\right) \tag{2.5}$$

Three SWCNT chirality configurations can be constructed depending on the chiral angle (Figure 2.7(c)). For $0^o \leq \theta \leq 30^o$. For zig-zag (n, 0) nanotubes $\theta = 0^o$, whilst for armchair (n, n)
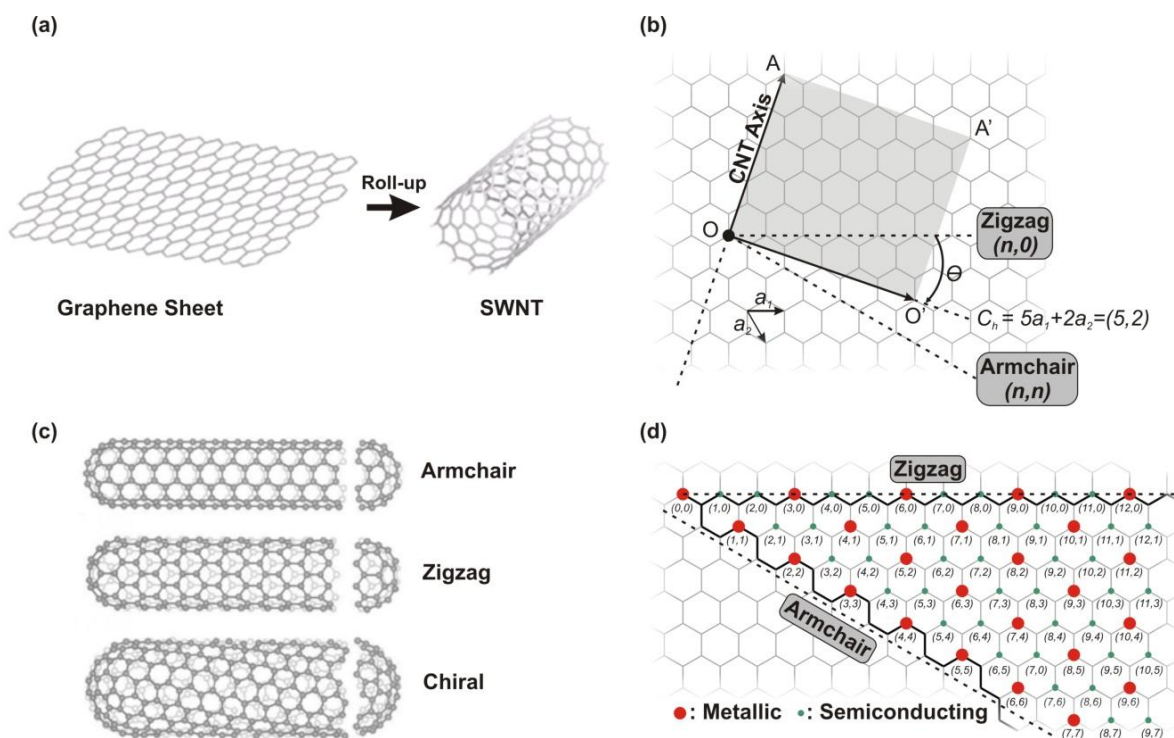
Figure 2.7 | **The (academic) construction of SWCNTs from graphene. (a)** ASWCNT formed from a rolled graphene sheet. SWCNTs are uniquely characterised in terms of their chiral vector, $\vec{C}_h$ and a chiral angle, θ, as illustrated in **(b)**. $\vec{C}_h$ is typically expressed in terms of the unit vectors $\hat{a}_1$ and $\hat{a}_2$ and the integers n_1 and n_2. **(c)** SWCNTs can be subdivided into three principle groups. When $n_1 = n_2 = n$, then $\theta = 30°$ and the SWCNTs are referred to as *armchair* (n,n), for $n_1 = n$ and $n_2 = 0$ then $\theta = 0°$ and the SWCNTs are *zigzag*. Intermediary cases $(0° < \theta < 30°)$ are referred to as *chiral*, or twisted. An example of a $(5,2)$ chiral SWCNT is shown in (b). A partially chiral map is depicted in **(d)**. Here metallic (red) and semiconducting (green) SWCNTs have been highlighted. Adapted from[10, 14-21].

nanotubes θ=30°. For intermediate θ values, where 0°<θ<30°, the nanotubes are referred to as chiral. SWCNTs are semiconducting except when n_1-n_2 is divisible by three. Such SWCNTs are metallic (E$_g$ ~0 eV). All armchair and one-third of all zig-zag nanotubes show this property. Similarly, all chiral and two-thirds of all zig-zag SWNTs are semiconducting (E$_g$ ~0.4-0.7 eV). Figure 2.7(d) shows an abridged chiral map of possible semiconducting and metallic chiral vectors. Chiral identification is achieved using scanning tunnelling electron microscopy. However strong Van der waals interactions results in nanotube aggregation and bundling which can make accurate chiral discrimination difficult[109]. Separation of SWCNT by chiral type has proven challenging. Only recently have a few post-synthesis wet chemistry post-growth filtration techniques become available[110]. No one has grown predominately single chiral samples.

Just as graphene can be stacked to form bilayer, multi-layer, and ultimately graphite - all of which have differing electronic properties - SWCNTs can be concentrically nested to form incommensurate MWCNTs which too have differing properties from their single-walled counterparts. Recent studies have shown that the inter-shell spacing in fact ranges from 0.34-0.39 nm and decreases with increasing nanotube diameter[111, 112]. Nonetheless, the uncorrelated graphitic planes in MWCNTs have an inter-plane separation approximately equal to that of bulk graphite (0.335 nm) and as a result tend to exhibit similar properties to turbostratic graphite[14]. All MWCNTs are conducting. In the case of SWCNTs the energy band gap associated with the nanotube structure is approximately inversely proportional to its diameter ($E_g \propto 1/d$)[113]. Only the outermost shell of the MWCNT is typically in direct contact with the electrodes and as a result conduction has been found to take place predominately in this shell [114] with only weak inter-shell interactions being reported[115]. All MWCNTs exhibit semi-metallic characteristics, in-part due to their large diameter which results in demonstrable room-temperature band gaps approaching that of graphite. Work function dependent Schottky barrier formation at metal electrodes also impart apparent FET functionality[116]. Due to their complex structure the detailed transport mechanisms in MWCNTs are still poorly understood and the debate is still open as to whether they are a zero-band gap material. In practice MWCNTs are coined as quasi-metallic due to their low, but non-negligible band gaps. MWCNTs have been used throughout the work presented in this thesis.

Single- and multi-walled nanotubes can be distinguished from one another using a variety of techniques, the most common of which are transmission and scanning electron microscopy (TEM / SEM), atomic force microscopy (AFM), electronic transport measurements, UV-Vis optical spectrophotometry and Raman spectroscopy. Raman spectroscopy is repeatedly used throughout the presented work and as a result warrants some discussion.

Raman spectroscopy is an important technique as it provides quantitative data, in a non-destructive manner, on the degree of crystallographic disorder in carbon materials. All carbon allotropes share two common spectral peaks: a G peak at 1580–1600 cm^{-1} and a D peak at 1350 cm^{-1}, as illustrated in Figure 2.8. Ferrari and Robertson defined the G peak as the first order scattering of the E$_{2g}$ phonon at the Brillouin zone centre of sp^2 carbon bonds[117-119]. Whilst the defect induced D peak was defined as the C-C breathing modes of six-fold rings of K-point phonons of A$_{1g}$ symmetry[117, 119].
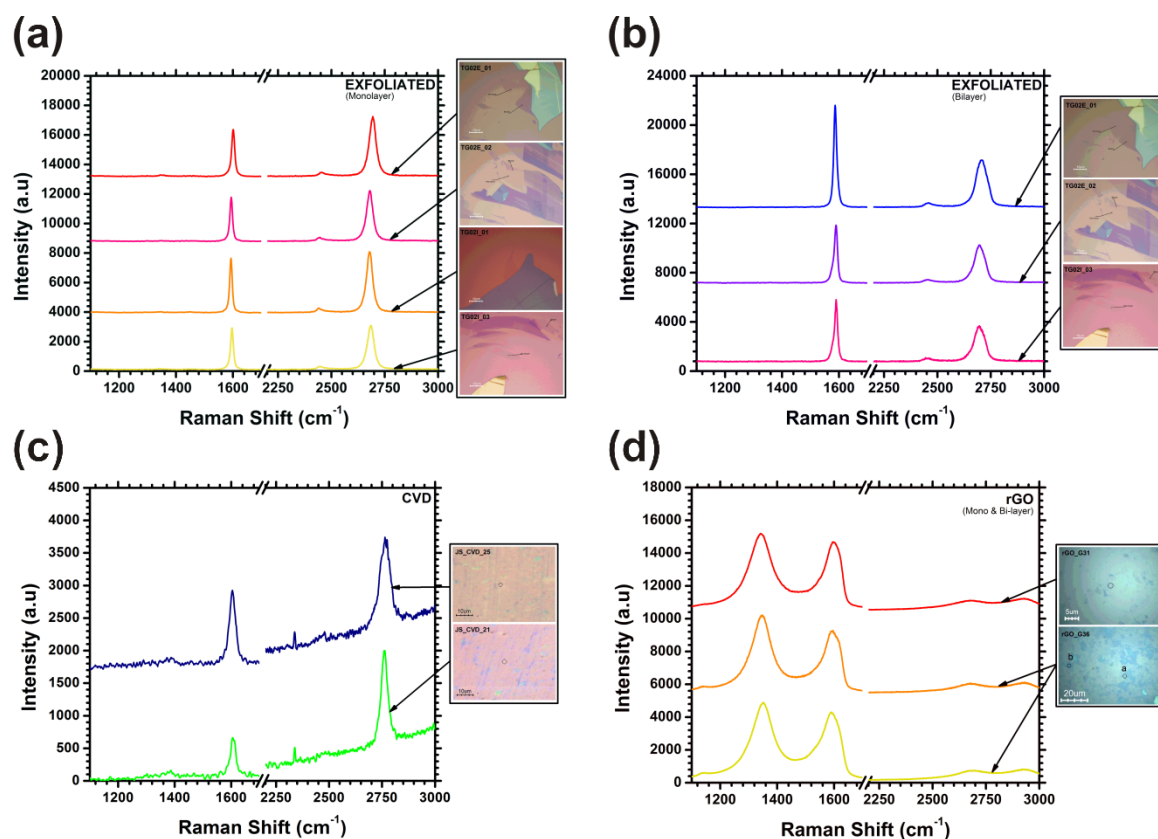
Figure 2.8 | Top-down Vs. bottom-up graphene. Raman spectra (514 nm, 3mW) of high quality exfoliated **(a)** highly crystalline mono- and **(b)** bi-layer graphene samples. **(c)** Cu-catalysed (and supported) CVD graphene (this work). The linear increase in the intensity after 2250 cm^{-1} is a result of substrate optical excitation. Raman spectra retained their high quality when PMMA transferred to Si/SiO$_2$. **(d)** Highly defective reduced graphene oxide (rGO) (Courtesy of G. Eda, Imperial College, London). *Inserts:* Optical Micrographs of the synthesised graphene illustrating the high uniformity of CVD graphene compared to the mechanically (a,b) and chemically (d) exfoliated samples. D, G and 2D peaks are denoted for clarity.

The ratio of the G to D peak intensities (I$_D$/ I$_G$) gives a measure of how disordered a graphitic lattice is and as such is widely used to quantify the degree of disorder in nanotubes and graphene. Strong D peaks suggest nanocrystallites and lattice defects such as distortion and vacancies as well as possible lattice straining. Spectra of graphene show a third peak, historically denoted as the G' as it is the second largest peak. However this G' peak, located at ~2700 cm^{-1}, is in fact related to the second order of the D peak and is herein referred to as the 2D peak for convenience. The D, G and 2D peaks are illustrated in Figure 2.8.

Exfoliated graphite is exceptionally crystalline which accounts for the lack of a defect (D) peak (Figure 2.8(a,b)). The number of graphene layers can be estimated from the number of fitted Lorentzians distributions to the 2D peak[119]. As the number of layers increases the 2D peak position positively shifts and increasing numbers of Lorenztians must be used to fit it.

Monolayers fit a single Lorentzian, whilst bilayers require four[3, 119]. Similarly, the I_{2D}/I_G ratio can also be used to approximate the number of graphene layers. For graphene monolayers 2D peak enhancement results in I_{2D}/I_G >1-4[120] (Figure 2.8(a)), whilst for bilayer and few-layer I_{2D}/I_G ≤1 (Figure 2.8(b)). The I_{2D}/I_G ratio continues to decrease as the number of layers increases. A number of relationships have also been derived to estimate the crystal size based on the peak position, peak intensities and integrated peak intensities[121, 122].

The Raman spectra of nanotubes also have a third region of interest. The radial breathing mode (RBM) phonon, for SWCNTs, occurs when the nanotube radially expands and contracts in-phase[123]. RBMs occur at 100-500 cm^{-1} and provide a convenient means to estimate the diameter. MWCNTs do not exhibit RBMs because of incoherent shell interactions. Raman measurements were performed using a multi-wavelength (70 mW-4.1 W), Ar (100 mW) and He-Ne (30 mW) class 4 and 3B laser-supported Renishaw InVia system with fused-silica optics operated at 457 nm (Cu supported graphene), 514 nm (Si/SiO$_2$ supported graphene) or 633 nm (CNTs) at variable powers (<10 mW). Various wavelengths have been used to obviate substrate electroluminescence and to optimise the measured signals. Triplicate accumulations and 50 times optical apertures were used throughout. The spot size was approximately 1.2 µm in diameter.

Another important technique repeatedly used throughout the work presented in this thesis is in quantifying the degree of nanotube alignment. Other techniques[124, 125] have been developed to quantify the degree of alignment, however the simplest is to image process SEM micrographs to extract a quantative measure of the alignment. This was achieved using the steradian 37 (Str37) function in SPIP^{TM} image analysis software as demonstrated elsewhere[126-128]. Str37 is defined as the ratio of the in-plane distance between the real autocorrelation centre and the boundary at which the height of the image has decayed to 37% of the depth-range at said autocorrelation centre. An autocorrelation is applied to the images depth-range to infer this position. The decay in the depth-range in all directions is evaluated and the Str37 value calculated[127, 129]. For perfectly aligned arrays Str37=0, whilst for disordered networks with exhibit no directional preference, Str37=1.
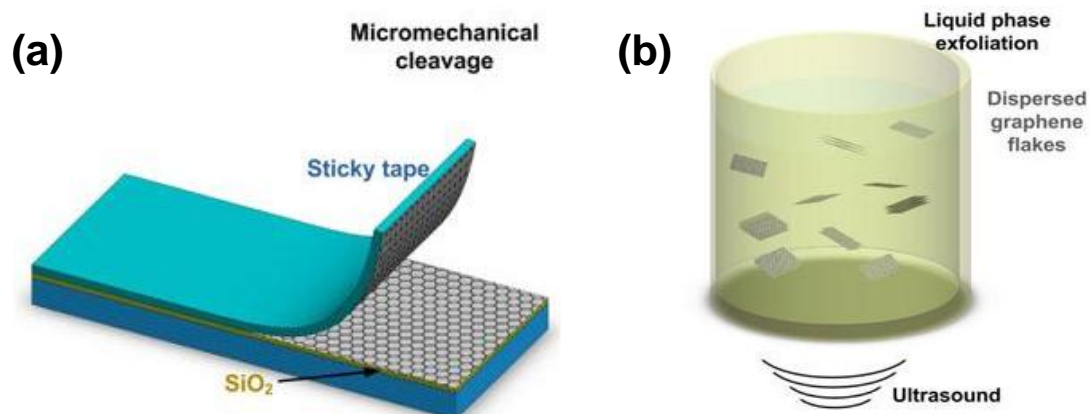
Figure 2.9 | **Top-down routes to graphene isolation. (a)** Mechanical and **(b)** liquid phase exfoliation. From[12].

2.4   Synthesis Techniques: Top-Down Vs. Bottom-Up

In the strictest sense, nanostructures can be synthesised in one of two ways: top-down (the successive removal of material) or bottom-up (the self-assembly of single atomic or molecular units). Their complex structure means nanotubes cannot be synthesised via top-down techniques. Graphene, on the other hand can and it is in fact the preferable means for many researchers. Mechanical exfoliation/cleavage from large graphite crystals (Figure 2.9(a)), is essentially a process of repeatedly breaking down graphite and has been proven extremely successful in producing very high quality flakes[54] (Figure 2.8(a,b)). Liquid phase chemically exfoliated[130] (Figure 2.9(b)) films deposited by Langmuir-Blodgett[131] and drop casting[132] techniques have also demonstrated moderate usefulness though the films are generally of a lower quality. An exfoliation derivative, reduced graphene oxide (rGO), also offers another possible approach. However, the oxidation through acid treatments and damaging ultrasonication limit the usefulness of these wet chemistry approaches. Crystallographically defective flakes are often produced due to edge-dominating effects and small flake sizes (<5 μm) (Figure 2.8(d)). Whilst the simplicity of these top-down approaches is certainly attractive in a processing sense, they are limited to bench-top-scale applications. They are time-consuming and require high levels of skill and costly chemicals. The crystallographic quality is also largely uncontrollable and varies drastically between samples. Large-area, uniform films cannot be processed in this way.
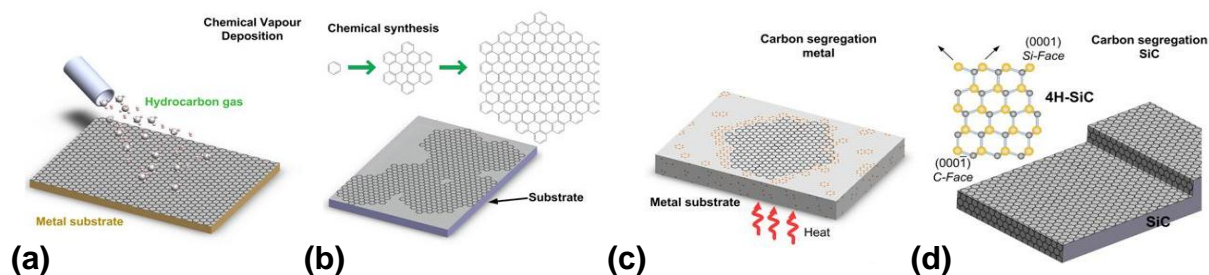
Figure 2.10 | Bottom-up 'growth' of graphene. (a) chemical vapour deposition, **(b)** molecular precursor self-assembly (via benzene derivatives[24]), **(c)** carbon segregation (following ion implantation) and **(d)** host sublimation of carbon containing compounds (such as SiC[26]). Adapted from[12].

This thesis is concerned with bottom-up synthesis. Here the nanostructures self-assemble from molecular or atomic units. High quality graphene has been synthesised in this way (Figure 2.8(c)).

Perhaps the first bottom-up approach to nanocarbon synthesis was reported by D. Huffman *et al.*[133] in the 1970s, who produced what was then termed "graphite smoke" in a rudimentary arc-discharge system. Electric arcs sparked between high voltage graphite electrodes to produce a "smokey" output that undoubtedly contained a myriad of (carcinogens, as well as) carbon nanostructures; mostly fullerenes. Collaborating with Huffman, W. Krätschmer *et al.*[134] developed the concept to increase yield and to produce macroscopic amounts of C_{60}, rather than graphene or nanotubes. Nonetheless, an important step was made. The process had generality. By heating a carbon source, albeit a solid, vapour or even liquid, under the correct atmosphere and in the presence of an appropriate catalyst, crystalline carbon nanostructures could be synthesised.

Despite constituting the fundamental unit of the nanotube the bottom-up synthesis of graphene has paradoxically lagged that of nanotubes, quite profoundly in fact. Only in the last six years or so has it appeared that significant progress has been made. As well as CVD, which will be discussed in some length later, another promising candidate technology is epitaxial growth on silicon carbide (SiC) (Figure 2.10(d)). Pioneered by W. De Heer *et al.*[26], chemically-mechanically polished SiC substrates are heated under ultrahigh vacuum conditions ($<10^{-10}$ mbar) to temperatures in excess of $1300^{\circ}C$. The composite Si sublimes under these extreme conditions leaving surface bound graphene. The technique is important as SiC is an insulator and the ability to deposit high-quality graphene directly onto dielectrics opens up a number of important electronics applications. Extremely costly substrates are
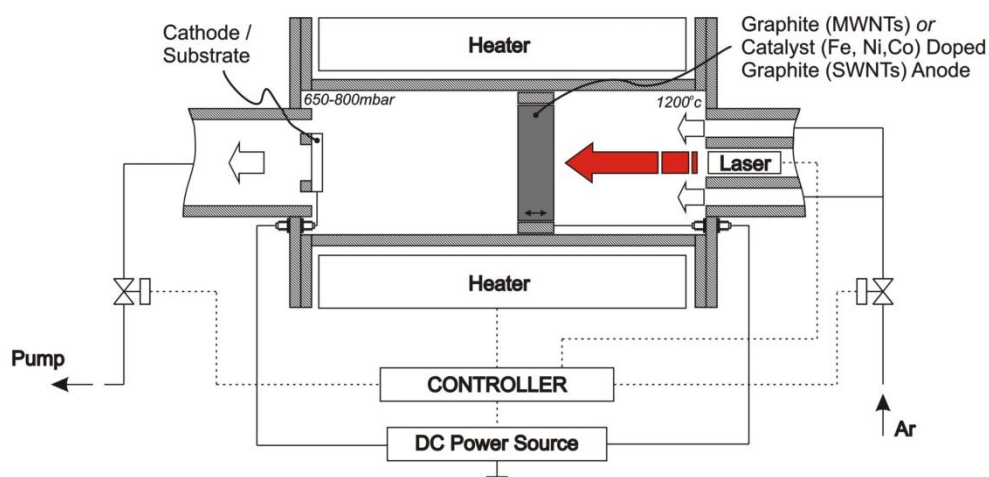
Figure 2.11 | Schematic of typical laser ablation apparatus.[11]

required and the process is energetically demanding. Notwithstanding, very high-quality graphene, of radio frequency (RF) application quality, has been produced[135]. Long annealing durations make the process rather time-consuming. CVD synthesis (Figure 2.10(a)), on the other hand is, most importantly, significantly faster and comparatively inexpensive. A number of other more exotic approaches to graphene synthesis have recently come to light, including flame synthesis[136], nanotube plasma unzipping[3, 137] metal particle carving[138], carbon segregation on carbon-implanted metal supports (Figure 2.10(c)) and organic self-assembly of benzene derivatives (Figure 2.10(b))[27, 139, 140]. However, all are (at this stage at least) bench-top scale and highly uncontrollable. CVD, a process well understood and infrastructurally accommodated by industry, is one of the few truly viable techniques for large area, high quality graphene synthesis.

2.4.1 Bottom-up Synthesis

Nanotubes and graphene can be grown by laser ablation[141], electric arc discharge[142], high-pressure carbon monoxide conversion[143] and catalytic CVD[144]. Arc discharge and laser ablation are classified as high temperature (>3000°C) and short timescale reactions (μs to ms), whereas catalytic CVD is a medium temperature (300-1200°C) long timescale reaction (typically minutes to hours)[145]. Other less common, and certainly non-scalable approaches include ball milling[146] and flame synthesis[136, 147]. This section provides a general overview of the more prominent bottom-up synthesis methods.
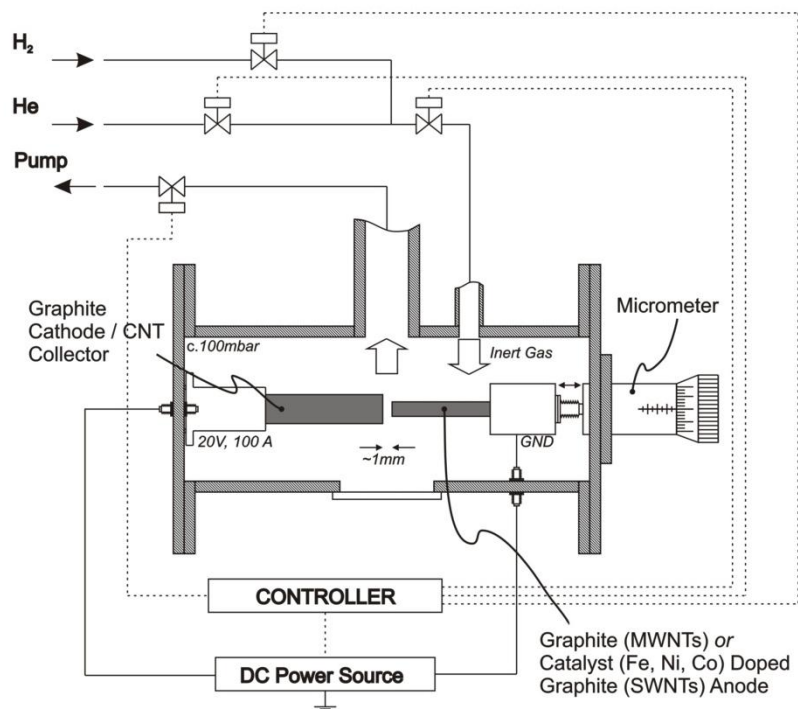
Figure 2.12 | **Schematic of a typical arc discharge chamber.** Adapted from[1-3].

A typical *Laser ablation / evaporation / vaporisation* synthesis reactor is depicted in Figure 2.11. R. Smalley *et al.*[148] were, in 1995, the first to heavily develop and understand this technique, predominantly using it for fullerene synthesis. In an inert atmosphere a continuous wave high powered laser is incident on a solid (or occasionally a liquid) carbon-containing target, which also often contains Co, Fe, or Ni. The carbon target is rapidly heated to temperatures in excess of $1000^{o}C$ which vaporises the carbon-containing target. The ablated[†] graphite sublimes forming plasma which is attracted to a cooler counter-electrode. Here it precipitates to form the nanocarbons. Fullerenes[149], nanotubes[150] or (only recently) graphene[151] synthesis have all been demonstrated using this method. Laser ablation tends to produce high quality, minimally defective structures which are unfortunately accompanied by a wide variety of undesirable carbonaceous species; *a*-C being the most prominent. Aggressive purification and post-synthesis manipulation are frequently required to separate out the nanostructures from the 'soot'.

Arc discharge (Figure 2.12) is similar in many ways to laser ablation insofar as it is a transient sublimation process. A high potential is applied between two closely spaced

---

[†] The surface removal of material via vaporization.

graphite electrodes in a vacuum, inert atmospheres (like He, H_2 and N_2[150, 152, 153]) or liquid environments (such as liquid nitrogen or water[154, 155]). The electrode separation is carefully controlled to induce electrical breakdown between the electrodes. The electric arc passes a current of 50-200 A which rapidly (<1 s) increases the temperature of the anode to >1000°C. The carbon source sublimes and the mobilised stream of free carbon atoms emitted from the anode is carried by the inert atmosphere toward the cooler anode, at which point it condenses to form the nanotubes[150], fullerenes[156] or graphene[157]. As with laser ablation, either pure graphite or catalyst doped graphite anodes can be used to selectively synthesise MWCNTs or SWCNTs. MWCNT and SWCNT growth by arc discharge was first demonstrated by Iijima *et al.*[6] (whilst working at the NEC laboratories) and Bethune *et al.*[42] (then at IBM), in 1993. The nanostructures, as with laser ablation are high quality and defect free as a result of the high synthesis temperatures. Nonetheless, the end product, again, is usually extremely contaminated. In the case of nanotubes, 70-80 wt.% of the material is unwanted and after purification and centrifugation extremely low (<1 wt.%) nanotube yields are not uncommon. 5-35 wt.% account for metal impurities[158].

Chemical vapour deposition (CVD) differs from the preceding approaches due to its high controllability. Figure 2.13 illustrates a typical CVD reactor. CVD systems can be either hot or cold walled. Hot walled systems are globally heated, whilst in cold walled systems smaller thermally-isolated heaters reside within water-cooled chambers. High quality graphene[159], nanotubes[160] and nanofibres[161] have been controllably synthesised via CVD. Rather than a transient solid sublimation process, carbon is sourced by the maintained thermal decomposition (at 500-1200°C) of a carbon contain gas (such as acetylene - C_2H_2[162], methane - CH_4[163], ethylene - C_2H_4[164], and carbon monoxide - CO[165]) which is mixed with a carrier / etching gas, such as NH_3 and H_2, to inhibit *a*-C deposition. Extremely wide ranging feedstock partial pressures, from 10^{-5} to 10^2 mbar, can be used to grow nanotubes. Very little carbon is necessary to grow graphene. Diluted (i.e. low partial pressures, ~10^{-2} mbar[166]) CH_4 and C_2H_4 are commonly used as they are kinetically stable and undergo minimal thermal decomposition at high temperatures (900°C). Other hydrocarbons have been used, although to less success[167]. CVD techniques demonstrate significant promise due to simple automation, high controllability, comparative cheapness, and most-importantly, scalability; all of which are tantamount to successful commercialisation.
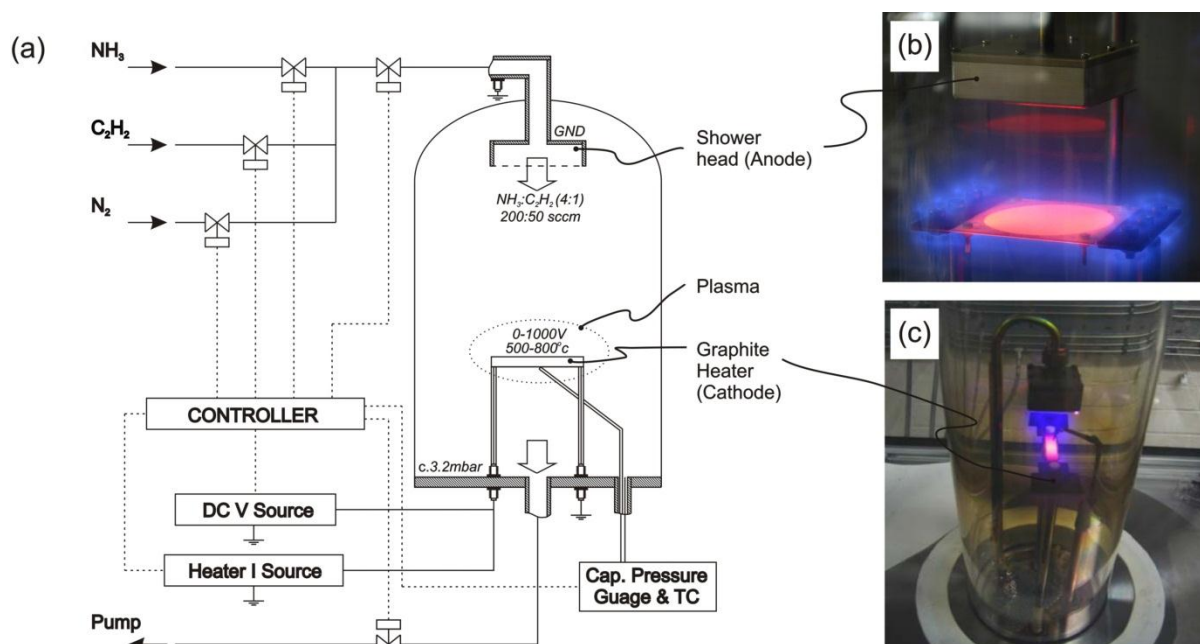
Figure 2.13 | The plasma enhanced / thermal chemical vapour deposition apparatus for nanotube and graphene synthesis, as used throughout this work. (a) System schematic and **(b)-(c)** optical micrographs of the graphite, ohmically heated stage during plasma exposure. Samples are loaded onto the heated stage and exposed to the carbon precursor and etching gases through the shower head[10, 11].

Plasma enhanced chemical vapour deposition (PE-CVD, Figure 2.13(b,c)), a CVD variant, facilitates accurate nanotube directional control by regulating the strength and direction of an applied electric-field, or more correctly, the sheath field. A variety of plasma types have been studied: direct current (DC)[168-170], hot-filament[171-173] aided DC, RF[174] and magnetically enhanced RF[175], microwave[176-178] and inductively coupled[179, 180]. In our hot-filament DC plasma system, ~600 V is applied between a grounded ohmically heated graphite stage (~600°C) and a gas inlet which strikes the plasma. Not only does the plasma heat and surface modify the catalyst[181] but it also plays an important role in nanotube alignment and *a*-C etching[182]. Combined ion bombardment and joule heating produce temperatures in excess of 700°C, at least 200°C of which can be attributed to the plasma alone[183]. PE-CVD is most often used for nanotube growth. Nevertheless, some reports on the PE-CVD of graphene are appearing[184, 185], though harsh plasma environments make high quality graphene synthesis challenging.

Figure 2.14(i)(c,d) illustrates nanotube growth with and without plasma. PE-CVD synthesised nanotubes are often larger in diameter than their thermal CVD counterparts and
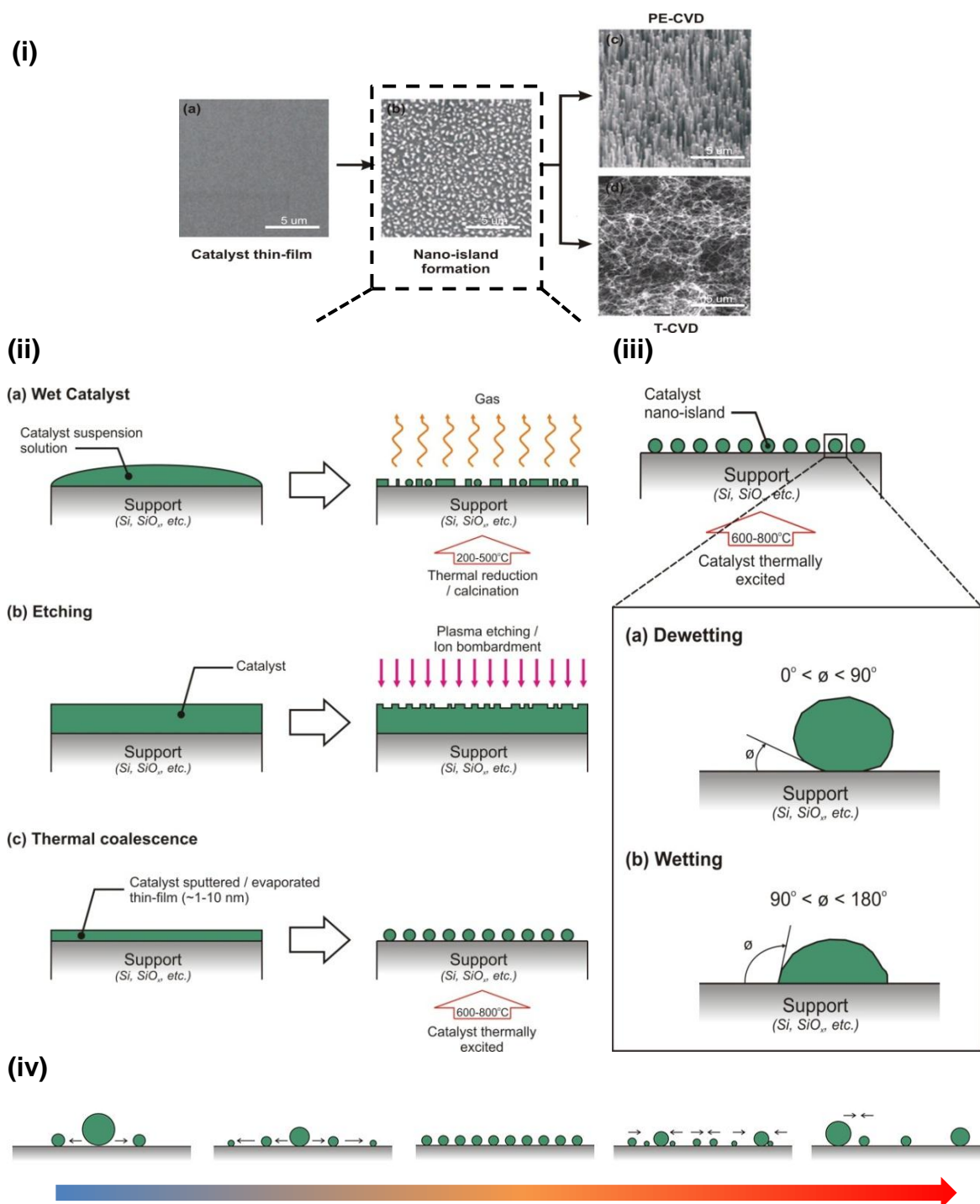
Figure 2.14 | Nanotube catalyst-bed formation. (i) Generalised nanotube growth. **(ii)** Routes to catalyst nanoisland formation; **(a)** Deposition of wet catalyst (e.g. ferritin, metallic salts, ferrocene, etc.). **(b)** Plasma, or wet etching of materials such as steel, or PVD deposited thin films. **(c)** Thermal coalescence of a PVD deposited thin film. **(iii)** Catalyst wetting behaviour. The degree of wetting determines the adopted route or tip growth mechanism. Illustrations of nanoisland **(a)** wetting and **(b)** dewetting. **(iv)** Ostwald ripening[23] - catalyst formation and coalescence occurring during increasing temperatures and / or annealing durations. Gradient arrow indicates either increasing anneal duration or temperature. The orange central region, where uniform catalyst particles are formed, denotes the optimal case[2].

are more correctly referred to as nanofibres (as discussed previously). PE-CVD favours Ni over Fe catalysts as the latter catalyst is usually plasma-etched. Figure 2.13 shows the upgraded AIXTRON Black Magic CVD reactor used throughout this work that can be operated in either plasma (PE-) or thermal (T-) modes. In the case of nanotubes, the relatively low growth temperatures typically result in reduced graphitization[186], though this is not problematic for the applications considered throughout this work, as highly crystalline graphitic samples are not essential. Dia *et al.*[187], Chhowalla *et al.*[188], Robertson *et al.*[189] and Amaratunga *et al.*[190] have all championed the use of CVD, and variants thereof, due to their intrinsic controllability. To the best of the authors knowledge, the lowest-reported CVD growth temperature for nanofibre growth is 270°C, demonstrated by Hofmann *et al.*[191] and 300°C for graphene-like films by Li *et al.*[192]. With continued maturity, CVD is the most promising technique for compatible silicon processing temperatures ($< 300^{o}$C) and a clear understanding of the growth dynamics and catalysis will play important roles in achieving this.

2.4.2 CVD Catalysis of Nanofibres, Nanotubes & Graphene

The general process of nanotube growth is illustrated in Figure 2.14(i). Graphene CVD proceeds in a similar fashion, though the catalyst restructuring is far less obvious.

In a general sense, catalysts can be thermally annealed[161] and/or plasma treated thin films[191], preformed nanoparticles[193], bulk materials that have had their surface topography modified[194] or even floating particles[195]. Nanotube catalysts include[196]; the transition metals (Fe, Ni, Co)-which have shown the highest catalytic activity. Other much less active catalysts include the noble metals (Au[197], Ag[197], Cu[197]), poor metals (Pb[198], In[199]) as well as semiconductors (Ga[199], Ge[200]), oxides (SiO_2[201, 202], ZrO_2[203]) and carbides (SiC[204]). Various metal/metal-oxides including MgO[198], Al_2O_3[205], and TiO_2[198] nanoparticles have all shown varied catalysing capabilities. Binary and tertiary catalysts structures, such as Al_2O_3/Fe[206], Mo/Co[207, 208] and $Mo/Al_2O_3/Fe$[209] increase the yields and growth rates whilst reducing diameter and chiral variations.

Graphene CVD has been demonstrated, both catalytically and non-catalytically, on a wide variety of metal foils and PVD deposited thin films such as Cu, Ni, Co, Pt, Ru and Ir[25, 210, 211] as well as (less efficiently using) numerous alloys[106, 159] and compounds like AlN[212] and

ZnS[213] and even, more recently, oxides[214], nitrides[106] and semiconductors[215] though with substantially lower catalytic activity. There is not, as yet, any clear mechanism as to why oxides catalyse nanocarbon growth. The suggested mechanisms are hotly debated. Many speculate that surface defects nucleate the nanocarbons, whereas others attribute the growth to chamber contamination. In either case, this thesis is primarily interested in the use of metal catalysts due to their superior yields, lattice graphitization and high growth rates. Having said this, the author has completed a significant body of work, none of which is reported in this thesis, in collaboration with Chalmers University, Sweden, on the direct deposition of CVD nanocrystalline graphene on Si/SiO_2[216], Si/Si_3N_4[106], quartz[217], sapphire[217] and GaN[215]. Many materials it would seem catalyse the nanocarbons with varied degrees of activity. For the most part, Fe is frequently employed for nanotubes and Cu for graphene.

An important feature of nanotube growth, second perhaps only to the catalyst selection, is the structural modification of the catalyst prior to carbon precursor exposure. This is not the case for graphene, where catalyst restructuring appears not to affect the growth. Restructured catalyst films template the nanotube growth and control the nanotubes diameter and chirality. Nanoislands can be formed by wet deposition of nanoparticles in aqueous solutions[218] (Figure 2.14(ii)a), plasma etching (Figure 2.14(ii)b) or thermal coalescence (Figure 2.14(ii)c). Accurate catalyst positional control and sub-80 nm patterning have been demonstrated using electron-beam lithography[161] and nanoimprint contact printing[187]. Soluble metal salts (acetates, nitrates, etc.), bicarbonates, biologically derived catalysts (ferritin), organometallic / metallocene compounds (ferrocene)[195] and metallic colloids are all typical examples of wet catalysts which are deposited by dipping, pipetting, spray coating, casting, electrochemical deposition, inkjet printing or microcontact printing methods. Calcination (in ambient atmosphere) at 200-500°C oxidise these catalysts. The resulting metal oxides are then catalytically activated by thermal reduction in H_2 or inert atmospheres. Often samples are finally exposed to mild O_2 plasma to remove remaining organics.

Thermal coalescence of sub-10 nm uniform catalyst PVD deposited (e.g. sputtered or evaporated) thin films is the most common approach to catalyst nanoisland formation (Figure 2.14(ii)c). The catalyst dewets and clusters during thermal (and/or plasma) pre-treatment, due to surface tension and compressive stresses. This minimises the surface free-energy and forms the characteristic globular structures, as depicted in Figure 2.14(i)(b). *In-situ* electron microscopy studies[219, 220] have evidenced that the catalyst need not be liquid, though some
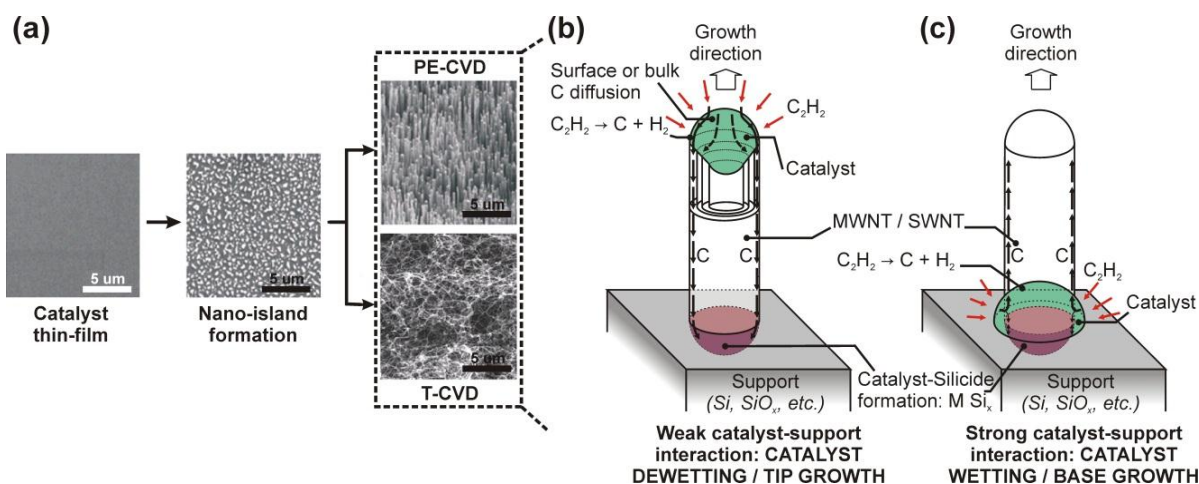
Figure 2.15 | Nanotube and nanofibre growth modes. (a) Generalised nanotube growth showing the catalyst thin film, nano-island formation and nanotube growth with and without plasma. **(b)** Weak catalyst-support interaction leading to catalyst dewetting and a tip growth mode. **(c)** Root growth caused by strong catalyst-support interactions resulting from catalyst wetting upon thermal pre-treatment.

debate still exists. Nanotubes grow at temperatures well below both the catalysts melting and carbide eutectic temperatures and although these temperatures certainly have a size (i.e. Gibbs-Thompsons effect) and pressure dependence the extrapolated temperatures are still higher than the growth temperatures suggesting that catalysts are indeed solid. Ostwald ripening, an inhibitory affect associated with thermal annealing, accounts for the variation in nanoisland size and is extremely prominent on highly hydrophobic supports. Higher energy states exist at the nanoparticles surface, than in the bulk, and it is energetically favourable for the nanoparticles to agglomerate to form ever larger particles, as depicted in Figure 2.14(iv). Lengthy annealing cycles enhance agglomeration and cause unsuitably large nanoislands whilst rapid anneals do not permit complete reduction or surface reconstruction. Evidently recipe optimisation is important in achieving well defined nanostructures.

Following catalyst restructuring, carbon precursors adsorb and dissociate on the catalyst surface and the nanotubes, or graphene, grow via carbon precipitation. This common growth model applies equally well to nanofibre, nanotube and graphene synthesis. Figure 2.15 depicts nanotube tip and root growth modes. The exact growth mode adopted depends on the strength of the catalyst-support interaction. For example, Ni on silica (SiO$_2$)[221] is characterised by a small contact angle (Figure 2.14(iii)a) and has a correspondingly weak interaction which favours tip growth (i.e. the catalyst resides at the tip of the nanotube during carbon precipitation). Correspondingly, a hydrophilic interface, for example in the case of Fe on Si[222], has a large contact angle and favours root growth (Figure 2.14(iii)b). Here the

catalyst particle remains at the substrate interface during carbon extrusion. A vast number of temperature dependent chemical interactions occur at the support-catalyst interface. At high temperatures catalysts can be consumed by the substrate due to uncontrolled diffusion, whilst silicide and carbide formation and alloying inhibit growth and reduce yields. Diffusion barriers such as SiO_2, Al_2O_x and TiN were developed to solve many of these problems[223, 224].

Less obvious catalyst restructuring occurs in the case of Cu-catalysed graphene. Cu grains grow during annealing but retain their planar form. Concurrent high sublimation rates during deposition makes developing a clear understanding of the graphene growth dynamics much more difficult. Nonetheless, the primary processes involved, namely hydrocarbon adsorption, dissociation and carbon diffusion and precipitation, are the same as those for nanofibre and nanotube growth which in themselves provide a useful growth analogue.

2.5   Summary

This chapter presented a comprehensive literature review on the developmental history, physical properties and the principle advantages of isolation and bottom-up growth, with particular emphasis on CVD, of nanofibres, nanotubes and graphene.

References

1.   Saito, Y.& Inagaki, M. (1993). Optical-emission studies on chemical-species in an arc flame of fullerene metallofullerene generator, *Jpn. J. Appl. Phys. 2*, **32**, pp. L954-L957.
2.   Teo, K. B. K. (2002). Aligned Carbon Nanotube Technology for Field Emission Application, *Department of Engineering*, **PhD**, p 34.
3.   Jiao, L. Y. J. L. Y., Zhang, L., Wang, X. R., Diankov, G.& Dai, H. J. (2009). Narrow graphene nanoribbons from carbon nanotubes, *Nature*, **458**, pp. 877-880.
4.   Rodriguez, N. M., Chambers, A.& Baker, R. T. K. (1995). Catalytic engineering of carbon nanostructures, *Langmuir*, **11**, pp. 3862-3866.
5.   Cai, W. W., Zhu, Y. W., Li, X. S., Piner, R. D.& Ruoff, R. S. (2009). Large area few-layer graphene/graphite films as transparent thin conducting electrodes, *Appl. Phys. Lett.*, **95**, pp. 1231151-1231153.
6.   Iijima, S. (1991). Helical microtubules of graphitic carbon, *Nature*, **354**, pp. 56-58.
7.   Carbon Nanotube Fact Sheet - http://nanomac.uq.edu (.au/pdfs/Carbon%20Nanotubes.pdf)
8.   Keun Soo, K., Yue, Z., Houk, J., Sang Yoon, L., Jong Min, K., Kim, K. S., Jong-Hyun, A., Kim, P., Jae-Young, C.& Byung Hee, H. (2009). Large-scale pattern growth of graphene films for stretchable transparent electrodes, *Nature*, **457**, pp. 706-710.
9.   Geim, A. K.& Novoselov, K. S. (2007). The rise of graphene, *Nat. Mater.*, **6**, pp. 183-191.
10.   Chih-Jen, S., Vijayaraghavan, A., Krishnan, R., Sharma, R., Jae-Hee, H., Moon-Ho, H., Zhong, J., Shangchao, L., Paulus, G. L. C., Reuel, N. F., Qing Hua, W., Blankschtein, D.& Strano, M. S. (2011). Bi- and trilayer graphene solutions, *Nat. Nanotechnol.*, **6**, pp. 439-445.
11.   Mann, M. (2007). Carbon Nanotubes as Next Generation Electron Sources, *Department of Engineering*, **PhD**, p 154.
12.   Graphene Technology: Roadmap to Applications - http://ec.europa.eu

13.   Schwierz, F. (2010). Graphene transistors, *Nature Nanotechnol.*, **5**, pp. 487-496.
14.   Dresselhaus& G *Physical Properties of Carbon Nanotubes* eds. (Imperial College Press), pp. 61.
15.   Yuanbo, Z., Tsung-Ta, T., Girit, C., Zhao, H., Martin, M. C., Zettl, A., Crommie, M. F., Shen, Y. R.& Feng, W. (2009). Direct observation of a widely tunable bandgap in bilayer graphene, *Nature*, **459**, pp. 820-823.
16.   Wei, W., Zhihong, L., Jauregui, L. A., Qingkai, Y., Pillai, R., Helin, C., Jiming, B., Chen, Y. P.& Shin-Shem, P. (2010). Wafer-scale synthesis of graphene by chemical vapor deposition and its application in hydrogen sensing, *Sensor Actuat B-Chem*, **150**, pp. 296-300.
17.   Emeleus, H. J.& Sharpe, A. G. (1959). Graphite Intercalation Compounds, *Adv. Inorg. Chem. Radiochem.*, pp. 224-266.
18.   Thermally exfoliated graphite oxide: An alternative to CNTs -
         http://www.princeton.edu (/~cml/html/research/TEGO.html)
19.   Sutter, P. (2009). Epitaxial graphene - How silicon leaves the scene, *Nat. Mater.*, **8**, pp. 171-172.
20.   Park, S.& Ruoff, R. S. (2009). Chemical methods for the production of graphenes, *Nat. Nanotechnol.*, **4**, pp. 217-224.
21.   Ishigami, M., Chen, J. H., Cullen, W. G., Fuhrer, M. S.& Williams, E. D. (2007). Atomic structure of graphene on SiO_2, *Nano Lett.*, **7**, pp. 1643-1648.
22.   Structure of Carbon Nanotubes: Symmetry -
         http://www.szfki.hu (/~kamaras/nanoseminar/Maultzsch_Janina-7-13.pdf)
         Graphene Brillouin Zone and Electronic Energy Dispersion -
         http://demonstrations.wolfram.com (/GrapheneBrillouinZoneAndElectronicEnergyDispersion/)
23.   Oei, S.-P. (2009). Novel Applications of Carbon Nanotubes, *Department of Engineering*, **PhD**, p 187.
24.   Cai, J., Ruffieux, P., Jaafar, R., Bieri, M., Braun, T., Blankenburg, S., Muoth, M., Seitsonen, A. P., Saleh, M., Feng, X., Müllen, K.& Fasel, R. (2010). Atomically precise bottom-up fabrication of graphene nanoribbons, *Nature*, **466**, pp. 470-473.
25.   Reina, A., Jia, X. T., Ho, J., Nezich, D., Son, H. B., Bulovic, V., Dresselhaus, M. S.& Kong, J. (2009). Large area, few-layer graphene films on arbitrary substrates by chemical vapor deposition, *Nano Lett.*, **9**, pp. 30-35.
26.   Berger, C., Song, Z., Li, T., Li, X., Ogbazghi, A. Y., Feng, R., Dai, Z., Alexei, N., Conrad, M. E. H., First, P. N.& De Heer, W. A. (2004). Ultrathin epitaxial graphite: 2D electron gas properties and a route toward graphene-based nanoelectronics, *J. Phys. Chem. B*, **108**, pp. 19912-19916.
27.   Wei, D.& Liu, Y. (2010). Controllable synthesis of graphene and Its applications, *Adv. Mater.*, **22**, pp. 3225-3241.
28.   Bernal, J. D. (1924). *Proc. R. Soc. London, Ser.*, **106**.
29.   Weller, T. E., Ellerby, M., Saxena, S. S., Smith, R. P.& Skipper, N. T. (2005). Superconductivity in the intercalated graphite compounds, *Nature Physics*, **1**, pp. 39-41.
30.   Fahy, S., Louie, S. G.& Cohen, M. L. (1986). Pseudopotential total-energy study of the transition from rhombohedral graphite to diamond, *Phys. Rev. B*, **34**, pp. 1191-1199.
31.   Dresselhaus, M. S.& Dresselhaus, G. (2002). Intercalation compounds of graphite, *Adv. Phys.*, **51**, pp. 1-186.
32.   Zheng, T., Reimers, J. N.& Dahn, J. R. (1995). Effect of turbostratic disorder in graphitic carbon hosts on the intercalation of lithium, *Phys. Rev. B*, **51**, pp. 734-741.
33.   Huang, P. Y., Ruiz-Vargas, C. S., van der Zande, A. M., Whitney, W. S., Levendorf, M. P., Kevek, J. W., Garg, S., Alden, J. S., Hustedt, C. J., Zhu, Y., Park, J., McEuen, P. L.& Muller, D. A. (2011). Grains and grain boundaries in single-layer graphene atomic patchwork quilts, *Nature*, **469**, pp. 389-392.
34.   Dai, L. (2007) *Carbon Nanotechnology: Recent Developments in Chemistry, Physics, Materials Science & Device Applications* eds. Dai, L., (Elsevier).
35.   Baker, F. S., Williams, J.& Osborn, A. R. (1972). Field-emission from carbon fibers - new electron source, *Nature*, **239**, pp. 96-97.
36.   Baker, R. T. K., Barber, M. A., Harris, P. S., Feates, F. S.& Waite, R. J. (1972). Nucleation and growth of carbon deposits from the nickel catalyzed decomposition of acetylene *J. Catal.*, **26**, pp. 51-62.
37.   Baker, R. T. K., Harris, P. S., Thomas, R. B.& Waite, R. J. (1973). Formation of filamentous carbon from iron, cobalt and chromium catalyzed decomposition of acetylene *J. Catal.*, **30**, pp. 86-95.
38.   Baker, R. T. K. (1989). Catalytic growth of carbon filaments, *Carbon*, **27**, pp. 315-323.
39.   V., R. L.& M., L. V. (1952). *Zurn Fisic Chim*.
40.   Tesner, P. A.& Echeistova, A. I. (1952). *Doklady Akad. Nauk (USSR)*, **87**.
41.   Oberlin, A., Endo, M.& Koyama, T. (1976). Filamentous growth of carbon through benzene decomposition, *J. Cryst. Growth*, **32**, pp. 335-349.

42.   Bethune, D. S., Kiang, C. H., Devries, M. S., Gorman, G., Savoy, R., Vazquez, J.& Beyers, R. (1993). Cobalt-catalyzed growth of carbon nanotubes with single-atomic-layer walls, *Nature*, **363**, pp. 605-607.

43.   Iijima, S.& Ichihashi, T. (1993). Single-shell carbon nanotubes of 1-nm diameter, *Nature*, **363**, pp. 603-605.

44.   http://hyperioncatalysis.com/.

45.   Pyrograf Products, Inc. - http://www.pyrografproducts.com/

46.   Kroto, H. W., Heath, J. R., Obrien, S. C., Curl, R. F.& Smalley, R. E. (1985). C-60: Buckminsterfullerene, *Nature*, **318**, pp. 162-163.

47.   Peierls, R. E. (1935). Quelques proprietes typiques des corpses solides, *Ann. I. H. Poincare*, **5**, pp. 177-222.

48.   Landau, L. D. (1937). Zur Theorie der phasenumwandlungen II, *Phys. Z. Sowjetunion*, **11**, pp. 26-35.

49.   Mermin, N. D. (1986). Crystalline order in two dimensions, *Phys. Rev.*, **176**, pp. 250-254.

50.   Yoon, S.-H., Park, C.-W., Yang, H., Korai, Y., Mochida, I., Baker, R. T. K.& Rodriguez, N. M. (2004). Novel carbon nanofibers of high graphitization as anodic materials for lithium ion secondary batteries, *Carbon*, **42**, pp. 21-32.

51.   Li, G. D., Tang, Z. K., Wang, N.& Chen, J. S. (2002). Structural study of the 0.4-nm single-walled carbon nanotubes aligned in channels of AlPO$_4$-5 crystal, *Carbon*, **40**, pp. 917-921.

52.   Huang, S. M., Cai, X. Y.& Liu, J. (2003). Growth of millimeter-long and horizontally aligned single-walled carbon nanotubes on flat substrates, *J. Appl. Chem.*, **125**, pp. 5636-5637.

53.   Yu, M. F., Yakobson, B. I.& Ruoff, R. S. (2000). Controlled sliding and pullout of nested shells in individual multiwalled carbon nanotubes, *J. Phys. Chem. B*, **104**, pp. 8764-8767.

54.   Novoselov, K. S., Geim, A. K., Morozov, S. V., Jiang, D., Zhang, Y., Dubonos, S. V., Grigorieva, I. V.& Firsov, A. A. (2004). Electric field effect in atomically thin carbon films, *Science*, **306**, pp. 666-669.

55.   Novoselov, K. S., Jiang, D., Schedin, F., Booth, T. J., Khotkevich, V. V., Morozov, S. V.& Geim, A. K. (2005). Two-dimensional atomic crystals, *Proc. Natl. Acad. Sci. (U.S.A.)*, **102**, pp. 10451-10453.

56.   Hofmann, U.& Frenzel, A. (1931). *Z. Elektrochem.*, **37**.

57.   Schleede, A.& Wellman, M. (1932). *Z. Phys. Chem.*

58.   Ebert, L. B., Huggins, R. A.& Brauman, J. I. (1974). The nature of the chromium trioxide intercalation in graphite, *Carbon*, **12**, pp. 199-208.

59.   Riley, H. J. (1945). *Fuel Sci. Pract.*, **24**, pp. 43-53.

60.   Hennig, G. R. (1959). *Progr. Inorg. Chem.*, **1**, pp. 125-205.

61.   Rudorff, W. (1959). *Adv. Inorg. Chem. Radiochem.*, **1**, pp. 223-66.

62.   Wei, B. Q., Vajtai, R.& Ajayan, P. M. (2001). Reliability and current carrying capacity of carbon nanotubes, *Appl. Phys. Lett.*, **79**, pp. 1172-1174.

63.   Poncharal, P., Berger, C., Yi, Y., Wang, Z. L.& de Heer, W. A. (2002). Room temperature ballistic conduction in carbon nanotubes, *J. Phys. Chem. B*, **106**, pp. 12104-12118.

64.   Du, X., Skachko, I., Barker, A.& Andrei, E. Y. (2008). Approaching ballistic transport in suspended graphene, *Nature Nanotechnol.*, **3**, pp. 491-495.

65.   Egger, R. (2009). Kondo physics: What the noise is all about, *Nature Physics*, **5**, pp. 175-176.

66.   Song, D., Wang, F., Dukovic, G., Zheng, M., Semke, E. D., Brus, L. E.& Heinz, T. F. (2006). Optical stark effect in semiconducting single-walled carbon nanotubes, pp. 1-2.

67.   Bondarev, I. V.& Lambin, P. (2004). Vacuum-field Rabi oscillations in atomically doped carbon nanotubes, *Phys. Lett.*, **328**, pp. 235-240.

68.   Bai, C.& Zhang, X. (2007). Klein paradox and resonant tunneling in a graphene superlattice, *Phys. Rev. B*, **76**, pp. 0754301-0754307.

69.   Novoselov, K. S., Geim, A. K., Morozov, S. V., Jiang, D., Katsnelson, M. I., Grigorieva, I. V., Dubonos, S. V.& Firsov, A. A. (2005). Two-dimensional gas of massless Dirac fermions in graphene, *Nature*, **438**, pp. 197-200.

70.   Novoselov, K. S., Jiang, Z., Zhang, Y., Morozov, S. V., Stormer, H. L., Zeitler, U., Maan, J. C., Boebinger, G. S., Kim, P.& Geim, A. K. (2007). Room-temperature quantum Hall effect in graphene, *Science*, **315**, p 1379.

71.   Bolotin, K. I., Sikes, K. J., Jiang, Z., Klima, M., Fudenberg, G., Hone, J., Kim, P.& Stormer, H. L. (2008). Ultrahigh electron mobility in suspended graphene, *Sol. State Comms.*, **146**, pp. 351-355.

72.   Dürkop, T., Getty, S. A., Cobas, E.& Fuhrer, M. S. (2004). Extraordinary Mobility in Semiconducting Carbon Nanotubes, *Nano Lett.*, **4**, pp. 35-39.

73.   Berger, C., Song, Z., Li, X., Wu, X., Brown, N., Naud, C., Mayou, D., Li, T., Hass, J., Marchenkov, A. N., Conrad, E. H., First, P. N.& De Heer, W. A. (2006). Electronic confinement and coherence in patterned epitaxial graphene, *Science*, **312**, pp. 1191-1196.

74. Purewal, M. S., Hong, B. H., Ravi, A., Chandra, B., Hone, J.& Kim, P. (2007). Scaling of resistance and electron mean free path of single-walled carbon nanotubes, *Phys. Rev. Lett.*, **98**, pp. 1868081-1868084.

75. Tang, Z. K., Zhang, L., Wang, N., Zhang, X. X., Wen, G. H., Li, G. D., Wang, J. N., Chan, C. T.& Sheng, P. (2001). Superconductivity in 4 angstrom single-walled carbon nanotubes, *Science*, **292**, pp. 2462-2465.

76. Uchoa, B.& Castro Neto, A. H. (2007). Superconducting states of pure and doped graphene, *Phys. Rev. Lett.*, **98**, pp. 1468011-1468014.

77. Tombros, N., Tanabe, S., Veligura, A., Jozsa, C., Popinciuc, M., Jonkman, H. T.& Van Wees, B. J. (2008). Anisotropic spin relaxation in graphene, *Phys. Rev. Lett.*, **101**, pp. 0466011-0466014.

78. Hueso, L. E., Pruneda, J. M., Ferrari, V., Burnell, G., Valdés-Herrera, J. P., Simons, B. D., Littlewood, P. B., Artacho, E., Fert, A.& Mathur, N. D. (2007). Transformation of spin information into large electrical signals using carbon nanotubes, *Nature*, **445**, pp. 410-413.

79. Yu, M. F., Files, B. S., Arepalli, S.& Ruoff, R. S. (2000). Tensile loading of ropes of single wall carbon nanotubes and their mechanical properties, *Phys. Rev. Lett.*, **84**, pp. 5552-5555.

80. Salvetat, J. P., Kulik, A. J., Bonard, J. M., Briggs, G. A. D., Stöckli, T., Méténier, K., Bonnamy, S., Béguin, F., Burnham, N. A.& Forró, L. (1999). Elastic modulus of ordered and disordered multiwalled carbon nanotubes, *Adv. Mater.*, **11**, pp. 161-165.

81. Jang, Y. T., Ahn, J. H., Ju, B. K.& Lee, Y. H. (2003). Lateral growth of aligned mutilwalled carbon nanotubes under electric field, *Sol. State Comms.*, **126**, pp. 305-308.

82. Hone, J., Whitney, M., Piskoti, C.& Zettl, A. (1999). Thermal conductivity of single-walled carbon nanotubes, *Phys. Rev. B*, **59**, pp. 2514-2516.

83. Yu, M. F., Lourie, O., Dyer, M. J., Moloni, K., Kelly, T. F.& Ruoff, R. S. (2000). Strength and breaking mechanism of multiwalled carbon nanotubes under tensile load, *Science*, **287**, pp. 637-640.

84. Lee, C., Wei, X., Kysar, J. W.& Hone, J. (2008). Measurement of the elastic properties and intrinsic strength of monolayer graphene, *Science*, **321**, pp. 385-388.

85. Martel, R., Schmidt, T., Shea, H. R., Hertel, T.& Avouris, P. (1998). Single- and multi-wall carbon nanotube field-effect transistors, *Appl. Phys. Lett.*, **73**, pp. 2447-2449.

86. Tseng, S. H.& Tai, N. H. (2009). Fabrication of a transparent and flexible thin film transistor based on single-walled carbon nanotubes using the direct transfer method, *Appl. Phys. Lett.*, **95**, pp. 2041041-2041043.

87. Yi, W., Lu, L., Zhang, D. L., Pan, Z. W.& Xie, S. S. (1999). Linear specific heat of carbon nanotubes, *Phys. Rev. B*, **59**, pp. 9015-9018.

88. Balandin, A. A., Ghosh, S., Bao, W., Calizo, I., Teweldebrhan, D., Miao, F.& Lau, C. N. (2008). Superior thermal conductivity of single-layer graphene, *Nano Lett.*, **8**, pp. 902-907.

89. Hone, J. (2004) *Encyclopedia of Nanoscience & Nanotechnology - Thermal Properties of Carbon Nanontube* eds. (Marcel Dekker, New York).

90. Zimmermann, J., Pavone, P.& Cuniberti, G. (2008). Vibrational modes and low-temperature thermal properties of graphene and carbon nanotubes: Minimal force-constant model, *Phys. Rev. B*, **78**.

91. Jiang, H., Liu, B., Huang, Y.& Hwang, K. C. (2004). Thermal Exapnsion of Single Wall Carbon Nanotubes, *J. Eng. Mat. Tech.*, **126**, pp. 265-270.

92. Dresselhaus, M. S., Dresselhaus, G., Charlier, J. C.& Hernández, E. (2004). Electronic, thermal and mechanical properties of carbon nanotubes, *Phil. T. Roy. Soc. A*, **362**, pp. 2065-2098.

93. Mounet, N.& Marzari, N. (2005). First-principles determination of the structural, vibrational and thermodynamic properties of diamond, graphite, and derivatives, *Phys. Rev. B*, **71**, pp. 2052141-20521414.

94. Checkelsky, J. G.& Ong, N. P. (2009). Thermopower and Nernst effect in graphene in a magnetic field, *Phys. Rev. B*, **80**, pp. 0814131-0814134.

95. Kim, P., Shi, L., Majumdar, A.& McEuen, P. L. (2001). Thermal transport measurements of individual multiwalled nanotubes, *Phys. Rev. Lett.*, **87**, pp. 2155021-2155024.

96. Thess, A., Lee, R., Nikolaev, P., Dai, H., Petit, P., Robert, J., Xu, C., Lee, Y. H., Kim, S. G., Rinzler, A. G., Colbert, D. T., Scuseria, G. E., Tománek, D., Fischer, J. E.& Smalley, R. E. (1996). Crystalline ropes of metallic carbon nanotubes, *Science*, **273**, pp. 483-487.

97. Murali, R., Brenner, K., Yang, Y., Beck, T.& Meindl, J. D. (2009). Resistivity of graphene nanoribbon interconnects, *IEEE Electr. Device L.*, **30**, pp. 611-613.

98. Schönenberger, C., Bachtold, A., Strunk, C., Salvetat, J. P.& Forró, L. (1999). Interference and interaction in multi-wall carbon nanotubes, *Appl. Phys. A*, **69**, pp. 283-295.

99. De Heer, W. A.& Martel, R. (2000). Industry sizes up nanotubes, *Phys. World*, **13**, pp. 49-53.

100. Frank, S., Poncharal, P., Wang, Z. L.& De Heer, W. A. (1998). Carbon nanotube quantum resistors, *Science*, **280**, pp. 1744-1746.

101.   Wallace, P. R. (1947). The band theory of graphite, *Phys. Rev.*, **71**, pp. 622-634.

102.   Partoens, B.& Peeters, F. M. (2006). From graphene to graphite: Electronic structure around the K point, *Phys. Rev. B*, **74**, pp. 07540401-07540411.

103.   Aoki, M.& Amawashi, H. (2007). Dependence of band structures on stacking and field in layered graphene, *Sol. State Comms.*, **142**, pp. 123-127.

104.   Wang, X., Li, X., Zhang, L., Yoon, Y., Weber, P. K., Wang, H., Guo, J.& Dai, H. (2009). N-doping of graphene through electrothermal reactions with ammonia, *Science*, **324**, pp. 768-771.

105.   Giovannetti, G., Khomyakov, P. A., Brocks, G., Karpan, V. M., Van Den Brink, J.& Kelly, P. J. (2008). Doping graphene with metal contacts, *Phys. Rev. Lett.*, **101**, pp. 0268031-0268034.

106.   Sun, J., Lindvall, N., Cole, M. T., Teo, K. B. K.& Yurgens, A. (2011). Large-area uniform graphene-like thin films grown by chemical vapor deposition directly on silicon nitride, *Appl. Phys. Lett.*, **98**, pp. 2521071-2521073.

107.   Dong, X., Fu, D., Fang, W., Shi, Y., Chen, P.& Li, L. J. (2009). Doping single-layer graphene with aromatic molecules, *Small*, **5**, pp. 1422-1426.

108.   Zhang, Y., Tang, T. T., Girit, C., Hao, Z., Martin, M. C., Zettl, A., Crommie, M. F., Shen, Y. R.& Wang, F. (2009). Direct observation of a widely tunable bandgap in bilayer graphene, *Nature*, **459**, pp. 820-823.

109.   Wildoer, J. W. G., Venema, L. C., Rinzler, A. G., Smalley, R. E.& Dekker, C. (1998). Electronic structure of atomically resolved carbon nanotubes, *Nature*, **391**, pp. 59-62.

110.   Liu, H., Nishide, D., Tanaka, T.& Kataura, H. (2011). Large-scale single-chirality separation of single-wall carbon nanotubes by simple gel chromatography, *Nature Comms.*, **2**, pp. 1-8.

111.   Endo, M., Takeuchi, K., Hiraoka, T., Furuta, T., Kasai, T., Sun, X., Kiang, C. H.& Dresselhaus, M. S. (1997). Stacking nature of graphene layers in carbon nanotubes and nanofibres, *J. Phys. Chem. Sol.*, **58**, pp. 1707-1712.

112.   Kiang, C. H., Endo, M., Ajayan, P. M., Dresselhaus, G.& Dresselhaus, M. S. (1998). Size Effects in Carbon Nanotubes, *Phys. Rev. Lett.*, **81**, pp. 1869-1872.

113.   Odom, T. W., Huang, J. L., Kim, P.& Lieber, C. M. (1998). Atomic structure and electronic properties of single-walled carbon nanotubes, *Nature*, **391**, pp. 62-64.

114.   Bachtold, A., Strunk, C., Salvetat, J. P., Bonard, J. M., Forró, L., Nussbaumer, T.& Schönenberger, C. (1999). Aharonov-Bohm oscillations in carbon nanotubes, *Nature*, **397**, pp. 673-675.

115.   Collins, P. G.& Avouris, P. (2002). Multishell conduction in multiwalled carbon nanotubes, *Appl. Phys. A*, **74**, pp. 329-332.

116.   Yang, M. H., Teo, K. B. K., Milne, W. I.& Hasko, D. G. (2005). Carbon nanotube Schottky diode and directionally dependent field-effect transistor using asymmetrical contacts, *Appl. Phys. Lett.*, **87**, pp. 2531161-2531163.

117.   Ferrari, A. C.& Robertson, J. (2000). Interpretation of Raman spectra of disordered and amorphous carbon, *Phys. Rev. B*, **61**, pp. 14095-14107.

118.   Nemanich, R. J.& Solin, S. A. (1979). First- and second-order Raman scattering from finite-size crystals of graphite, *Phys. Rev. B*, **20**, pp. 392-401.

119.   Ferrari, A. C. (2007). Raman spectroscopy of graphene and graphite: Disorder, electron-phonon coupling, doping and nonadiabatic effects, *Sol. State Comms.*, **143**, pp. 47-57.

120.   Ferrari, A. C., Meyer, J. C., Scardaci, V., Casiraghi, C., Lazzeri, M., Mauri, F., Piscanec, S., Jiang, D., Novoselov, K. S., Roth, S.& Geim, A. K. (2006). Raman spectrum of graphene and graphene layers, *Phys. Rev. Lett.*, **97**, pp. 1874011-1874014.

121.   Caṇado, L. G., Takai, K., Enoki, T., Endo, M., Kim, Y. A., Mizusaki, H., Jorio, A., Coelho, L. N., Magalhães-Paniago, R.& Pimenta, M. A. (2006). General equation for the determination of the crystallite size l_a of nanographite by Raman spectroscopy, *Appl. Phys. Lett.*, **88**, pp. 1631061-1631063.

122.   Lucchese, M. M., Stavale, F., Ferreira, E. H. M., Vilani, C., Moutinho, M. V. O., Capaz, R. B., Achete, C. A.& Jorio, A. (2010). Quantifying ion-induced defects and Raman relaxation length in graphene, *Carbon*, **48**, pp. 1592-1597.

123.   Maultzsch, J., Telg, H., Reich, S.& Thomsen, C. (2005). Radial breathing mode of single-walled carbon nanotubes: Optical transition energies and chiral-index assignment, *Phys. Rev. B*, **72**, pp. 1-16.

124.   Du, F. M., Fischer, J. E.& Winey, K. I. (2005). Effect of nanotube alignment on percolation conductivity in carbon nanotube/polymer composites, *Phys. Rev. B*, **72**, pp. 1214041-1214044.

125.   Fischer, J. E., Zhou, W., Vavro, J., Llaguno, M. C., Guthy, C., Haggenmueller, R., Casavant, M. J., Walters, D. E.& Smalley, R. E. (2003). Magnetically aligned single wall carbon nanotube films: Preferred orientation and anisotropic transport properties, *J. Appl. Phys.*, **93**, pp. 2157-2163.

126.   Zhang, Q., Vichchulada, P.& Lay, M. D. (2010). Length, bundle, and density gradients in spin cast single-walled carbon nanotube networks, *J. Phys. Chem. C*, **114**, pp. 16292-16297.

127. Qinghui, Z., Vichchulada, P.& Lay, M. D. (2010). Effect of deposition conditions on percolation in single-walled carbon nanotube networks, *Phys. Stat. Sol. A*, **207**, pp. 734-738.
128. Fujii, S., Tanaka, T., Nishiyama, S.& Kataura, H. (2011). High performance thin-film transistors using moderately aligned semiconducting single-wall carbon nanotubes, *physica status solidi (b)*, **248**, pp. 2692-2696.
129. Vichchulada, P., Zhang, Q. H., Duncan, A.& Lay, M. D. (2010). Macroscopic electrical properties of ordered single-walled carbon nanotube networks, *ACS Appl. Mater. Interfaces*, **2**, pp. 467-473.
130. Wang, H., Robinson, J. T., Li, X.& Dai, H. (2009). Solvothermal reduction of chemically exfoliated graphene sheets, *J. Am. Chem. Soc.*, **131**, pp. 9910-9911.
131. Li, X., Zhang, G., Bai, X., Sun, X., Wang, X., Wang, E.& Dai, H. (2008). Highly conducting graphene sheets and Langmuir-Blodgett films, *Nature Nanotechnol.*, **3**, pp. 538-542.
132. Choi, H., Kim, H., Hwang, S., Choi, W.& Jeon, M. (2011). Dye-sensitized solar cells using graphene-based carbon nano composite as counter electrode, *Sol. Energ. Mat. Sol. C.*, **95**, pp. 296-300.
133. Day, K. L.& Huffman, D. R. (1973). *Nature Phys. Sci.*, **243**.
134. Kratschmer, W., Lamb, L. D., Fostiropoulos, K.& Huffman, D. R. (1990). Solid C60: a new form of carbon, *Nature*, **347**, pp. 354-358.
135. Lin, Y. M., Dimitrakopoulos, C., Jenkins, K. A., Farmer, D. B., Chiu, H. Y., Grill, A.& Avouris, P. (2010). 100-GHz Transistors from Wafer-Scale Epitaxial Graphene, *Science*, **327**, pp. 662-662.
136. Li, Z., Zhu, H., Xie, D., Wang, K., Cao, A., Wei, J., Li, X., Fan, L.& Wu, D. (2011). Flame synthesis of few-layered graphene/graphite films, *Chem. Commun.*, **47**, pp. 3520-3522.
137. Kosynkin, D. V. K. D. V., Higginbotham, A. L., Sinitskii, A., Lomeda, J. R., Dimiev, A., Price, B. K.& Tour, J. M. (2009). Longitudinal unzipping of carbon nanotubes to form graphene nanoribbons, *Nature*, **458**, pp. 872-877.
138. Datta, S. S., Strachan, D. R., Khamis, S. M.& Johnson, A. T. C. (2008). Crystallographic etching of few-layer graphene, *Nano Lett.*, **8**, pp. 1912-1915.
139. Wu, J., Pisula, W.& Muellen, K. (2007). Graphenes as potential material for electronics, *Chem. Rev.*, **107**, pp. 718-747.
140. Simpson, C. D., Brand, J. D., Berresheim, A. J., Przybilla, L., Rader, H. J.& Mullen, K. (2002). Synthesis of a giant 222 carbon graphite sheet, *Chem. A-EU J.*, **8**, pp. 1424-1429.
141. Scott, C. D., Arepalli, S., Nikolaev, P.& Smalley, R. E. (2001). Growth mechanisms for single-wall carbon nanotubes in a laser-ablation process, *Appl. Phys. A-Mater. Sci. Process.*, **72**, pp. 573-580.
142. Shi, Z., Lian, Y., Zhou, X., Gu, Z., Zhang, Y., Iijima, S., Zhou, L., Yue, K. T.& Zhang, S. (1999). Mass-production of single-wall carbon nanotubes by arc discharge method, *Carbon*, **37**, pp. 1449-1453.
143. Nikolaev, P., Bronikowski, M. J., Bradley, R. K., Rohmund, F., Colbert, D. T., Smith, K. A.& Smalley, R. E. (1999). Gas-phase catalytic growth of single-walled carbon nanotubes from carbon monoxide, *Chem. Phys. Lett.*, **313**, pp. 91-97.
144. Bell, M. S., Teo, K. B. K., Lacerda, R. G., Milne, W. I., Hash, D. B.& Meyyappan, M. (2006). Carbon nanotubes by plasma-enhanced chemical vapor deposition, *Pure Appl. Chem.*, **78**, pp. 1117-1125.
145. Teo, K. B. K., Singh, C., Chhowalla, M.& Milne, W. I. (2003). Catalytic synthesis of carbon nanotubes & nanofibres, *Encyclopedia of Nanoscience & Nanotechnology*, p 22.
146. Pierard, N., Fonseca, A., Konya, Z., Willems, I., Van Tendeloo, G.& Nagy, J. B. (2001). Production of short carbon nanotubes with open tips by ball milling, *Chem. Phys. Lett.*, **335**, pp. 1-8.
147. Yuan, L., Saito, K., Hu, W.& Chen, Z. (2001). Ethylene flame synthesis of well-aligned multi-walled carbon nanotubes, *Chem. Phys. Lett.*, **346**, pp. 23-28.
148. Guo, T., Nikolaev, P., Rinzler, A. G., Tománek, D., Colbert, D. T.& Smalley, R. E. (1995). Self-assembly of tubular fullerenes, *J. Phys. Chem.*, **99**, pp. 10694-10697.
149. Ying, Z. C., Hettich, R. L., Compton, R. N.& Haufler, R. E. (1996). Synthesis of nitrogen-doped fullerenes by laser ablation, *J. Phys. B*, **29**, pp. 4935-4942.
150. Ando, Y., Zhao, X., Inoue, S., Suzuki, T.& Kadoya, T. (2005). Mass production of high-quality single-wall carbon nanotubes by H 2-N2 arc discharge, *Diam. Relat. Mat.*, **14**, pp. 729-732.
151. Dhar, S., Roy Barman, A., Ni, G. X., Wang, X., Xu, X. F., Zheng, Y., Tripathy Ariando, S., Rusydi, A., Loh, K. P., Rubhausen, M., Castro Neto, A. H., Őzyilmaz, B.& Venkatesan, T. (2011). A new route to graphene layers by selective laser ablation *AIP Adv.*, **1**, pp. 0221091-0221098.
152. Hutchison, J. L., Kiselev, N. A., Krinichnaya, E. P., Krestinin, A. V., Loutfy, R. O., Morawsky, A. P., Muradyan, V. E., Obraztsova, E. D., Sloan, J., Terekhov, S. V.& Zakharov, D. N. (2001). Double-walled carbon nanotubes fabricated by a hydrogen arc discharge method, *Carbon*, **39**, pp. 761-770.
153. Shi, Z. J., Lian, Y. F., Zhou, X. H., Gu, Z. N., Zhang, Y. G., Iijima, S., Zhou, L. X., Yue, K. T.& Zhang, S. L. (1999). Mass-production of single-wall carbon nanotubes by arc discharge method, *Carbon*, **37**, pp. 1449-1453.

154. Antisari, M. V., Marazzi, R.& Krsmanovic, R. (2003). Synthesis of multiwall carbon nanotubes by electric arc discharge in liquid environments, *Carbon*, **41**, pp. 2393-2401.
155. Sano, N., Wang, H., Alexandrou, I., Chhowalla, M., Teo, K. B. K., Amaratunga, G. A. J.& Iimura, K. (2002). Properties of carbon onions produced by an arc discharge in water, *J. Appl. Phys.*, **92**, pp. 2783-2788.
156. Ugarte, D. (1992). Morphology and structure of graphitic soot particles generated in arc-discharge C60 production, *Chem. Phys. Lett.*, **198**, pp. 596-602.
157. Subrahmanyam, K. S., Panchakarla, L. S., Govindaraj, A.& Rao, C. N. R. (2009). Simple method of preparing graphene flakes by an arc-discharge method, *J. Phys. Chem. C*, **113**, pp. 4257-4259.
158. Unidym™ Carbon Nanotubes Datasheet - http://www.unidym.com (/files/Unidym_Product_Sheet_SWNT.pdf)
159. Reina, A., Jia, X., Ho, J., Nezich, D., Son, H., Bulovic, V., Dresselhaus, M. S.& Jing, K. (2009). Large area, few-layer graphene films on arbitrary substrates by chemical vapor deposition, *Nano Lett.*, **9**, pp. 30-35.
160. Wirth, C. T., Zhang, C., Zhong, G., Hofmann, S.& Robertson, J. (2009). Diffusion - and reaction - limited growth of carbon nanotube forests, *ACS Nano*, **3**, pp. 3560-3566.
161. Teo, K. B. K., Chhowalla, M., Amaratunga, G. A. J., Milne, W. I., Pirio, G., Legagneux, P., Wyczisk, F., Pribat, D.& Hasko, D. G. (2002). Field emission from dense, sparse, and patterned arrays of carbon nanofibers, *Appl. Phys. Lett.*, **80**, pp. 2011-2013.
162. Teo, K. B. K., Chhowalla, M., Amaratunga, G. A. J., Milne, W. I., Legagneux, P., Pirio, G., Gangloff, L., Pribat, D., Semet, V., Binh, V. T., Bruenger, W. H., Eichholz, J., Hanssen, H., Friedrich, D., Lee, S. B., Hasko, D. G.& Ahmed, H. (2003). Fabrication and electrical characteristics of carbon nanotube-based microcathodes for use in a parallel electron-beam lithography system, *J. Vac. Sci. Technol. B*, **21**, pp. 693-697.
163. Kong, J., Cassell, A. M.& Dai, H. (1998). Chemical vapor deposition of methane for single-walled carbon nanotubes, *Chem. Phys. Lett.*, **292**, pp. 567-574.
164. Cheung, C. L., Kurtz, A., Park, H.& Lieber, C. M. (2002). Diameter-controlled synthesis of carbon nanotubes, *J. Phys. Chem. B*, **106**, pp. 2429-2433.
165. Huang, S., Woodson, M., Smalley, R.& Liu, J. (2004). Growth mechanism of oriented long single walled carbon nanotubes using "fast-heating" chemical vapor deposition process, *Nano Lett.*, **4**, pp. 1025-1028.
166. Sun, J., Lindvall, N., Cole, M. T., Angel, K. T. T., Wang, T., Teo, K. B. K., Chua, D. H. C., Liu, J.& Yurgens, A. (2011). Low partial pressure chemical vapour deposition of graphene on copper, *IEEE. T. Nanotech.*, **1**, pp. 1-6.
167. Lee, Y.-H.& Lee, J.-H. (2010). Scalable growth of free-standing graphene wafers with copper(Cu) catalyst on SiO$_2$/Si substrate: Thermal conductivity of the wafers, *Appl. Phys. Lett.*, **96**, pp. 0831011-0831013.
168. Merkulov, V. I., Lowndes, D. H., Wei, Y. Y., Eres, G.& Voelkl, E. (2000). Patterned growth of individual and multiple vertically aligned carbon nanofibers, *Appl. Phys. Lett.*, **76**, pp. 3555-3557.
169. Merkulov, V. I., Guillorn, M. A., Lowndes, D. H., Simpson, M. L.& Voelkl, E. (2001). Shaping carbon nanostructures by controlling the synthesis process, *Appl. Phys. Lett.*, **79**, pp. 1178-1180.
170. Wei, Y. Y., Eres, G., Merkulov, V. I.& Lowndes, D. H. (2001). Effect of catalyst film thickness on carbon nanotube growth by selective area chemical vapor deposition, *Appl. Phys. Lett.*, **78**, pp. 1394-1396.
171. Tsai, S. H., Chao, C. W., Lee, C. L.& Shih, H. C. (1999). Bias-enhanced nucleation and growth of the aligned carbon nanotubes with open ends under microwave plasma synthesis, *Appl. Phys. Lett.*, **74**, pp. 3462-3464.
172. Teo, K. B. K., Lee, S. B., Chhowalla, M., Semet, V., Binh, V. T., Groening, O., Castignolles, M., Loiseau, A., Pirio, G., Legagneux, P., Pribat, D., Hasko, D. G., Ahmed, H., Amaratunga, G. A. J.& Milne, W. I. (2002). Plasma enhanced chemical vapour deposition carbon nanotubes/nanofibres - how uniform do they grow?, *3rd International Conference on Trends in Nanotechnology*, pp. 204-211.
173. Küttel, O. M., Groening, O., Emmenegger, C.& Schlapbach, L. (1998). Electron field emission from phase pure nanotube films grown in a methane/hydrogen plasma, *Appl. Phys. Lett.*, **73**, pp. 2113-2115.
174. Ho, G. W., Wee, A. T. S., Lin, J.& Tjiu, W. C. (2001). Synthesis of well-aligned multiwalled carbon nanotubes on Ni catalyst using radio frequency plasma-enhanced chemical vapor deposition, *Thin Solid Films*, **388**, pp. 73-77.
175. Ishida, H., Satake, N., Jeong, G. H., Abe, Y., Hirata, T., Hatakeyama, R., Tohji, K.& Motomiya, K. (2002). Experimental study of fullerene-family formation using radio-frequency-discharge reactive plasmas, *Thin Solid Films*, **407**, pp. 26-31.

176. Su, X., Stagarescu, C., Xu, G., Eastman, D. E., McNulty, I., Frigo, S. P., Wang, Y., Retsch, C. C., Noyan, I. C.& Hu, C. K. (2000). Quantitative nanoscale metrology study of Cu/SiO_2 interconnect technology using transmission x-ray microscopy, *Appl. Phys. Lett.*, **77**, pp. 3465-3467.

177. Bower, C., Zhu, W., Jin, S. H.& Zhou, O. (2000). Plasma-induced alignment of carbon nanotubes, *Appl. Phys. Lett.*, **77**, pp. 830-832.

178. Bower, C., Zhou, O., Zhu, W., Werder, D. J.& Jin, S. (2000). Nucleation and growth of carbon nanotubes by microwave plasma chemical vapor deposition, *Appl. Phys. Lett.*, **77**, pp. 2767-2769.

179. Delzeit, L., McAninch, I., Cruden, B. A., Hash, D., Chen, B., Han, J.& Meyyappan, M. (2002). Growth of multiwall carbon nanotubes in an inductively coupled plasma reactor, *J. Appl. Phys.*, **91**, pp. 6027-6033.

180. Matthews, K., Gruden, B. A., Chen, B., Meyyappan, M.& Delzeit, L. (2002). Plasma-enhanced chemical vapor deposition of multiwalled carbon nanofibers, *J. Nanosci. Nanotechno.*, **2**, pp. 475-480.

181. Esconjauregui, S., Bayer, B. C., Fouquet, M., Wirth, C. T., Yan, F., Xie, R., Ducati, C., Baehtz, C., Castellarin-Cudia, C., Bhardwaj, S., Cepek, C., Hofmann, S.& Robertson, J. (2011). Use of plasma treatment to grow carbon nanotube forests on TiN substrate, *J. Appl. Phys.*, **109**, pp. 1143121-11431210.

182. Esconjauregui, S., Fouquet, M., Bayer, B.& Robertson, J. (2010). Carbon nanotubes growth: From entanglement to vertical alignment, *Phys. Stat. Sol. B*, **247**, pp. 38-41.

183. Teo, K. B. K., Hash, D. B., Lacerda, R. G., Rupesinghe, N. L., Bell, M. S., Dalal, S. H., Bose, D., Govindan, T. R., Cruden, B. A., Chhowalla, M., Amaratunga, G. A. J., Meyyappan, M.& Milne, W. I. (2004). The significance of plasma heating in carbon nanotube and nanofiber growth, *Nano Lett.*, **4**, pp. 921-926.

184. Woo, Y., Kim, D. C., Jeon, D. Y., Chung, H. J., Shin, S. M., Li, X. S., Kwon, Y. N., Seo, D. H., Shin, J., Chung, U. I.& Seo, S. (2009). Large-grained and highly-ordered graphene synthesized by radio frequency plasma-enhanced chemical vapor deposition, *Elec. Soc. T.*, **19**, pp. 111-114.

185. Yuan, G. D., Zhang, W. J., Yang, Y., Tang, Y. B., Li, Y. Q., Wang, J. X., Meng, X. M., He, Z. B., Wu, C. M. L., Bello, I., Lee, C. S.& Lee, S. T. (2009). Graphene sheets via microwave chemical vapor deposition, *Chem. Phys. Lett.*, **467**, pp. 361-364.

186. Fan, Y. W., Goldsmith, B. R.& Collins, P. G. (2005). Identifying and counting point defects in carbon nanotubes, *Nat. Mater.*, **4**, pp. 906-911.

187. Cassell, A. M., Franklin, N. R., Tombler, T. W., Chan, E. M., Han, J.& Dai, H. J. (1999). Directed growth of free-standing single-walled carbon nanotubes, *J. Am. Chem. Soc.*, **121**, pp. 7975-7976.

188. Chhowalla, M., Teo, K. B. K., Ducati, C., Rupesinghe, N. L., Amaratunga, G. A. J., Ferrari, A. C., Roy, D., Robertson, J.& Milne, W. I. (2001). Growth process conditions of vertically aligned carbon nanotubes using plasma enhanced chemical vapor deposition, *J. Appl. Phys.*, **90**, pp. 5308-5317.

189. Ducati, C., Alexandrou, I., Chhowalla, M., Amaratunga, G. A. J.& Robertson, J. (2002). Temperature selective growth of carbon nanotubes by chemical vapor deposition, *J. Appl. Phys.*, **92**, p 3299.

190. Amaratunga, G. (2003). Watching the nanotube, *IEEE Spectr.*, **40**, pp. 28-32.

191. Hofmann, S., Ducati, C., Robertson, J.& Kleinsorge, B. (2003). Low-temperature growth of carbon nanotubes by plasma-enhanced chemical vapor deposition, *Appl. Phys. Lett.*, **83**, pp. 135-137.

192. Li, Z., Wu, P., Wang, C., Fan, X., Zhang, W., Zhai, X., Zeng, C., Yang, J.& Hou, J. (2011). Low-temperature growth of graphene by chemical vapor deposition using solid and liquid carbon sources, *ACS Nano*, **5**, pp. 3385-3390.

193. Golovko, V. B., Li, H. W., Kleinsorge, B., Hofmann, S., Geng, J., Cantoro, M., Yang, Z., Jefferson, D. A., Johnson, B. F. G., Huck, W. T. S.& Robertson, J. (2005). Submicron patterning of Co colloid catalyst for growth of vertically aligned carbon nanotubes, *Nanotech.*, **16**, pp. 1636-1640.

194. Vander Wal, R. L.& Hall, L. J. (2003). Carbon nanotube synthesis upon stainless steel meshes, *Carbon*, **41**, pp. 659-672.

195. Ci, L., Wei, J., Wei, B., Liang, J., Xu, C.& Wu, D. (2001). Carbon nanofibers and single-walled carbon nanotubes prepared by the floating catalyst method, *Carbon*, **39**, pp. 329-335.

196. Hermann Rümmeli, M., Bachmatiuk, A., Börrnert, F., Schäffel, F., Ibrahim, I., Cendrowski, K., Simha-Martynkova, G., Plachá, D., Borowiak-Palen, E., Cuniberti, G.& Büchner, B. (2011). Synthesis of carbon nanotubes with and without catalyst particles, *Nano Res. Lett.*, **6**, pp. 1-9.

197. Takagi, D., Homma, Y., Hibino, H., Suzuki, S.& Kobayashi, Y. (2006). Single-walled carbon nanotube growth from highly activated metal nanoparticles, *Nano Lett.*, **6**, pp. 2642-2645.

198. Rümmeli, M. H., Borowiak-Palen, E., Gemming, T., Pichler, T., Knupfer, M., Kalbác, M., Dunsch, L., Jost, O., Silva, S. R. P., Pompe, W.& Büchner, B. (2005). Novel catalysts, room temperature, and the importance of oxygen for the synthesis of single-walled carbon nanotubes, *Nano Lett.*, **5**, pp. 1209-1215.

199. Rao, R., Eyink, K. G.& Maruyama, B. (2010). Single-walled carbon nanotube growth from liquid gallium and indium, *Carbon*, **48**, pp. 3971-3973.

200. Uchino, T., Hutchison, J. L., Ayre, G. N., Smith, D. C., De Groot, K.& Ashburn, P. (2011). Metal-catalyst-free growth of silica nanowires and carbon nanotubes using Ge nanostructures, *Jpn. J. Appl. Phys.*, **50**, pp. 1-18.

201. Liu, B., Ren, W., Gao, L., Li, S., Pei, S., Liu, C., Jiang, C.& Cheng, H. M. (2009). Metal-catalyst-free growth of single-walled carbon nanotubes, *J. Am. Chem. Soc.*, **131**, pp. 2082-2083.

202. Huang, S., Cai, Q., Chen, J., Qian, Y.& Zhang, L. (2009). Metal-catalyst-free growth of single-walled carbon nanotubes on substrates, *J. Am. Chem. Soc.*, **131**, pp. 2094-2095.

203. Steiner Iii, S. A., Baumann, T. F., Bayer, B. C., Blume, R., Worsley, M. A., MoberlyChan, W. J., Shaw, E. L., Schlögl, R., Hart, A. J., Hofmann, S.& Wardle, B. L. (2009). Nanoscale zirconia as a nonmetallic catalyst for graphitization of carbon and growth of single- and multiwall carbon nanotubes, *J. Am. Chem. Soc.*, **131**, pp. 12144-12154.

204. Kusunoki, M., Rokkaku, M.& Suzuki, T. (1997). Epitaxial carbon nanotube film self organized by sublimation decomposition of silicon carbide, *Appl. Phys. Lett.*, **71**, pp. 2620-2622.

205. Liu, H., Takagi, D., Ohno, H., Chiashi, S., Chokan, T.& Homma, Y. (2008). Growth of single-walled carbon nanotubes from ceramic particles by alcohol chemical vapor deposition, *Appl. Phys. Exp.*, **1**, pp. 0140011-0140013.

206. Amama, P. B., Pint, C. L., McJilton, L., Kim, S. M., Stach, E. A., Murray, P. T., Hauge, R. H.& Maruyama, B. (2009). Role of water in super growth of single-walled carbon nanotube carpets, *Nano Lett.*, **9**, pp. 44-49.

207. Goyal, A., Simon, L.& Iqbal, Z. (2005). Kinetic investigations of Co disproportion on Co-Mo/Mgo bimetallic catalyst for single wall carbon nanotubes production, *AIChE* p13993.

208. Ni, L., Kuroda, K., Zhou, L. P., Kizuka, T., Ohta, K., Matsuishi, K.& Nakamura, J. (2006). Kinetic study of carbon nanotube synthesis over Mo/Co/MgO catalysts, *Carbon*, **44**, pp. 2265-2272.

209. Hart, A. J., Slocum, A. H.& Royer, L. (2006). Growth of conformal single-walled carbon nanotube films from Mo/Fe/Al$_2$O$_3$ deposited by electron beam evaporation, *Carbon*, **44**, pp. 348-359.

210. Coraux, J., N'Diaye, A. T., Busse, C.& Michely, T. (2008). Structural coherency of graphene on Ir(111), *Nano Lett.*, **8**, pp. 565-570.

211. de Parga, A. L. V., Calleja, F., Borca, B., Passeggi, M. C. G., Hinarejos, J. J., Guinea, F.& Miranda, R. (2008). Periodically rippled graphene: Growth and spatially resolved electronic structure, *Phys. Rev. Lett.*, **100**, pp. 1-5.

212. Camara, N., Rius, G., Huntzinger, J. R., Tiberj, A., Magaud, L., Mestres, N., Godignon, P.& Camassel, J. (2008). Early stage formation of graphene on the C face of 6H-SiC, *Appl. Phys. Lett.*, **93**, pp. 2631021-2631023.

213. Wei, D., Liu, Y., Zhang, H., Huang, L., Wu, B., Chen, J.& Yu, G. (2009). Scalable synthesis of few-layer graphene ribbons with controlled morphologies by a template method and their applications in nanoelectromechanical switches, *J. Am. Chem. Soc.*, **131**, pp. 11147-11154.

214. Kim, K.-B., Lee, C.-M.& Choi, J. (2011). Catalyst-free direct growth of triangular nano-graphene on all substrates, *J. Phys. Chem. C*, **115**, pp. 14488-14493.

215. Ahmed, S. A., Sun, J., Cole, M. T., Backe, O., Ive, T., Loffler, M., Olsson, E., Lindvall, N., Teo, K. B. K., Larsson, A., Yurgens, A.& Haglund, A. (2011). Direct chemical vapour depositin of large-area graphene-like thin films on gallium nitride for transparent electrodes, *Submitted to Appl. Phys. Lett.*

216. Sun, J., Lindvall, N., Cole, M. T., Wang, T., Booth, T. J., Boggild, P., Teo, K. B. K., Liu, J.& Yurgens, A. (2011). Controllable chemical vapour deposition of large area uniform nanoncrystalline graphene directly on silicon dioxide, *Submitted to Carbon*.

217. Sun, J., Cole, M. T., Lindvall, N., Teo, K. B. K.& Yurgens, A. (2011). Noncatalytic chemical vapor deposition of graphene on high-temperature substrates for transparent electrodes, *Submitted to Appl. Phys. Lett.*

218. Yu, Z., Li, S. D.& Burke, P. J. (2004). Synthesis of aligned arrays of millimeter long, straight single-walled carbon nanotubes, *Chem. Mater.*, **16**, pp. 3414-3416.

219. Hofmann, S., Sharma, R., Ducati, C., Du, G., Mattevi, C., Cepek, C., Cantoro, M., Pisana, S., Parvez, A., Cervantes-Sodi, F., Ferrari, A. C., Dunin-Borkowski, R., Lizzit, S., Petaccia, L., Goldoni, A.& Robertson, J. (2007). In-situ observations of catalyst dynamics during surface-bound carbon nanotube nucleation, *Nano Lett.*, **7**, pp. 602-608.

220. Yoshida, H., Takeda, S., Uchiyama, T., Kohno, H.& Homma, Y. (2008). Atomic-scale in-situ observation of carbon nanotube growth from solid state iron carbide nanoparticles, *Nano Lett.*, **8**, pp. 2082-2086.

221. Takenaka, S., Kobayashi, S., Ogihara, H.& Otsuka, K. (2003). Ni/SiO$_2$ catalyst effective for methane decomposition into hydrogen and carbon nanofiber, *J. Catal.*, **217**, pp. 79-87.

222. Arcos, T., Vonau, F., Garnier, M. G., Thommen, V., Boyen, H.-G., Oelhafen, P., Düggelin, M., Mathis, D.& Guggenheim, R. (2002). Influence of iron-silicon interaction on the growth of carbon nanotubes produced by chemical vapor deposition, *Appl. Phys. Lett.*, **80**, pp. 2383-2385.

223. Kpetsu, J. B. A., Jedrzejowski, P., Côté, C., Sarkissian, A., Mérel, P., Laou, P., Paradis, S., Désilets, S., Liu, H.& Sun, X. (2010). Influence of Ni catalyst layer and TiN diffusion barrier on carbon nanotube growth rate, *Nano Res. Lett.*, **5**, pp. 539-544.

224. Simmons, J. M., Nichols, B. M., Marcus, M. S., Castellini, O. M., Homers, R. J.& Eriksson, M. A. (2006). Critical oxide thickness for efficient single-walled carbon nanotube growth on silicon using thin SiO_2 diffusion barriers, *Small*, **2**, pp. 902-909.

Chapter III

Chemical Vapour Deposition of Carbon Nanofibres, Nanotubes & Graphene
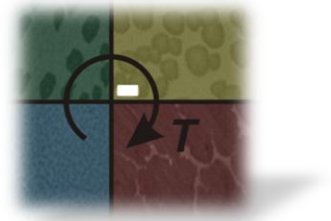
3.   Introduction

The following sections report the authors work on determing the validity of the CNT / CNF diffusion-limited catalysis analogue for graphene synthesis by CVD.

3.1   The Activation Energy of CVD Catalysis: Nanofibre, nanotube & graphene growth – Are they similarly rate-limited?

To accurately control CVD deposition insight into the underlying catalysis is necessary. No general theory of graphitic carbon catalysis via CVD, which spans multiple nanocarbon allotropes, has been proposed or even experimentally considered. The applicability of traditional growth models such as the vapour-liquid-solid[1-3] and vapour-solid-solid[6], applied to more conventional systems such as Si nanowires (where the dissociated silane saturate diffuses through the Ag nanoparticle) have questionable validity in the case of the nanocarbons. In general, dissociative hydrocarbon adsorption on metal surfaces is central to heterogenous catalysis[4]. This experimental framework has not, as yet, been considered in regards to graphene growth. As a result generalisations between nanotube, nanofibre and graphene catalysis, performed in nominally equivalent systems, are missing from the literature and have yet to be demonstrated. Improved levels of catalysis understanding may ultimately lead to reductions in synthesis temperatures and the ensuing energy savings will make CVD processing increasingly commercially attractive. Similarly, a deeper understanding of the underlying catalysis will permit high-quality nanocarbon growth on more exotic substrates, such as plastics for example.

3.2   The Rate-Limiting Step?

CVD is characterised by an activation energy (E_a). This energy is a composite measure of (i) surface hydrocarbon adsorption (mass transfer), (ii) hydrocarbon dissociation via pyrolysis, (iii) carbon diffusion (into the bulk or surface) of the catalyst and (iv) carbon precipitation and structural incorporation. Figure 3.1(a,b) illustrates CVD in the case of metal catalysed nanotubes/fibres and graphene, respectively. Note that both nanofibres and nanotubes are considered in the following study and that the strict distinctions between nanofibres and
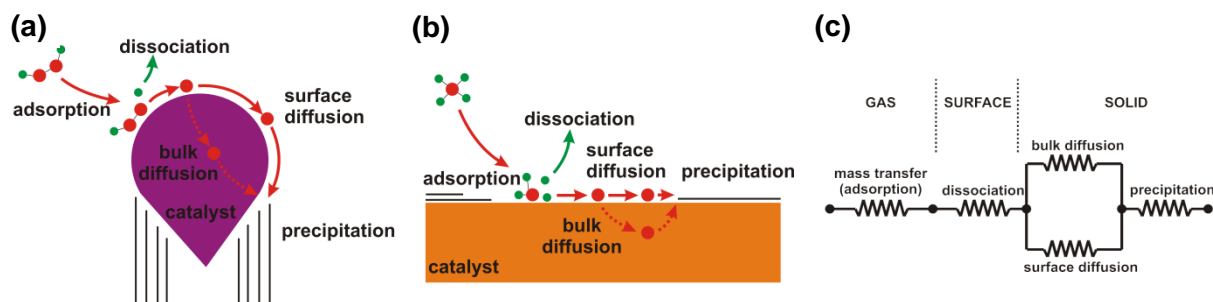
Figure 3.1 | **CVD growth.** Both **(a)** nanotube and **(b)** graphene growth can be modelled in conceptually similar ways. In particular; *(i)* hydrocarbon adsorption and *(ii)* dissociation, *(iii)* carbon diffusion and *(iv)* precipitation. Adapted from [4]. **(c)** Scheme representing the various potential rate-limiting steps during CVD growth[8].

nanotubes were made in earlier sections. Figure 3.1(c) depicts a generalised scheme illustrating the various possible rate-limiting processes. Vertically aligned nanofibres were grown by plasma enhanced chemical vapour deposition (PE-CVD) to investigate the catalytic activity of Fe and Ni on equivalent indium tin oxide (ITO) diffusion barriers. To investigate the effect of the support barrier, Al and Al_2O_x barriers, for equivalent 1 nm Fe catalysts, have been employed during thermal chemical vapour deposition (T-CVD). The growth rates of as-grown nanofibres, nanotubes and graphene are presented based on C_2H_2/NH_3 (PE-CVD), C_2H_2/H_2 (T-CVD) and $C_2H_4/H_2/Ar$ (T-CVD), respectively. The corresponding activation energies have been determined for each and discussed to elucidate the catalysis rate-limiting step in an attempt to determine the validity of a nanotube analogue for graphene growth.

To accurately measure the nanofibre diameters, and to consider the growth implications of patterning, dot arrays with a pitch of 2 μm and diameter of 80 nm were written by electron-beam lithography on <100> *p*-type, boron doped (0.015 Ωcm), 200 (±20) nm thermally oxidized Si substrates. 25-nm-ITO diffusion barriers and 6 nm Ni (99.5%, Advent) or Fe (99.5%, Advent) films were sequentially deposited by DC magnetron sputtering. For the nanotubes either a 10-nm-Al or 10-nm-Al_2O_3 (99.99%, Lesker) film was RF magnetron sputtered, air exposed and coated with 1 nm Fe by thermal evaporation (Lesker PVD75, 99.95%). For cleanliness, base-pressures below 10^{-5} mbar were ensured for all depositions. As-received 25 μm Cu foils (99.99%, Advent) and PVD deposited Cu thin films (~ 900 nm) were used to catalyse graphene growth. All catalyst samples were degreased in a 65°C acetone bath for 1 h prior to growth.
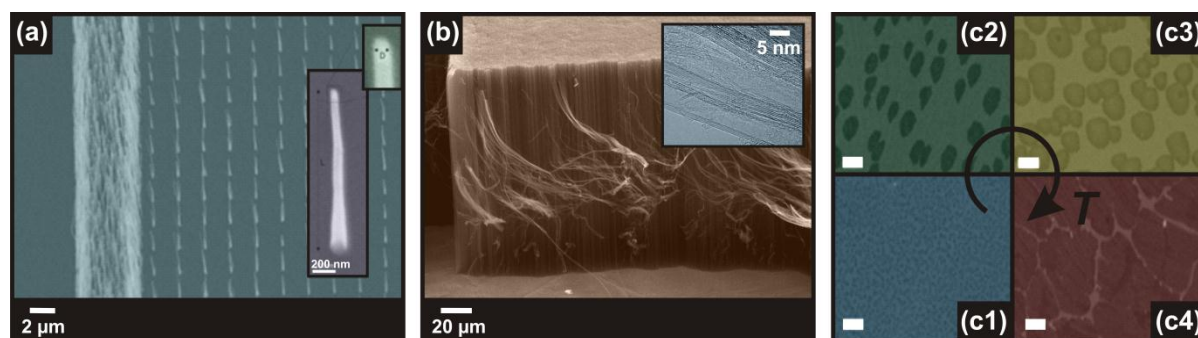
Figure 3.2 | **CVD nanofibres, multi-walled carbon nanotubes and graphene.** SEM micrographs of **(a)** vertically aligned nanofibres (~2 μm separation), **(b)** MWCNTs (*Insert*: HR-TEM micrograph showing the nanotubes graphitic walls) and **(c)** monolayer graphene. Graphene was grown for 5 min at **(1)** $800^{o}C$, **(2)** $850^{o}C$, **(3)** $900^{o}C$ and **(4)** $950^{o}C$ and PMMA-transferred to Si/SiO$_2$ (300 nm). (Scale bar 2 μm).

All nanofibre, nanotube and graphene samples were grown in a commercially available CVD reactor (AIXTRON, Black Magic). Aligned nanofibres were grown by PE-CVD. Nanotubes and graphene were grown by T-CVD. For each the growth temperatures were varied to investigate the corresponding activation energies. Nanofibres were grown by thermally annealing the ITO-supported samples for 60 s in NH$_3$ (grade 3.8) and subsequent exposure, for 1200 s, to plasma (620 V / 35 W) under a 200:50 sccm flow of NH$_3$:C$_2$H$_2$ (dissolved, grade 1.5) at 3.2 mbar. Nanotubes were grown by loading the alumina-supported samples into the room temperature reactor under a C$_2$H$_2$ (8 sccm):H$_2$ (192 sccm) flow (26.0 mbar). The low-mass graphite heater was then thermally ramped at $5^{o}C$/s and maintained at the growth temperature ($700^{o}C$) for 300 s. Graphene was grown by ethylene-based Cu-catalysis. Cu foils were annealed at $850^{o}C$ (measured by surface IR interferometry) for 30 mins in a 20:1500 sccm (H$_2$:Ar) atmosphere. Growth was initiated by introducing 7 sccm ethylene (C$_2$H$_4$, 99.92% purity) under maintained H$_2$ (99.98% purity) and Ar (99.998% purity) dilution. Graphene growth was halted after 300 s prior to flake coalescence[12]. All samples were cooled to room temperature under ultra-high purity N$_2$ (grade 5.5). Temperatures were monitored using a type K bimetallic-alloy thermocouple. Pressures and temperatures were accurate to within ±0.5 mbar and $\pm3^{o}C$, respectively. Temperatures were maintained to within $\pm1^{o}C$ throughout.

Figure 3.2 shows SEM micrographs (Zeiss Evo 50 operated at 15 kV / Philips XL30 sFEG operated at 15 kV) of individual aligned nanofibres (ITO/Ni) (Figure 3.2 (a)), nanotubes (Al/Fe) (Figure 3.2 (b)) and graphene flakes (Figure 3.2 (c)). Unpolarised 457 nm Raman
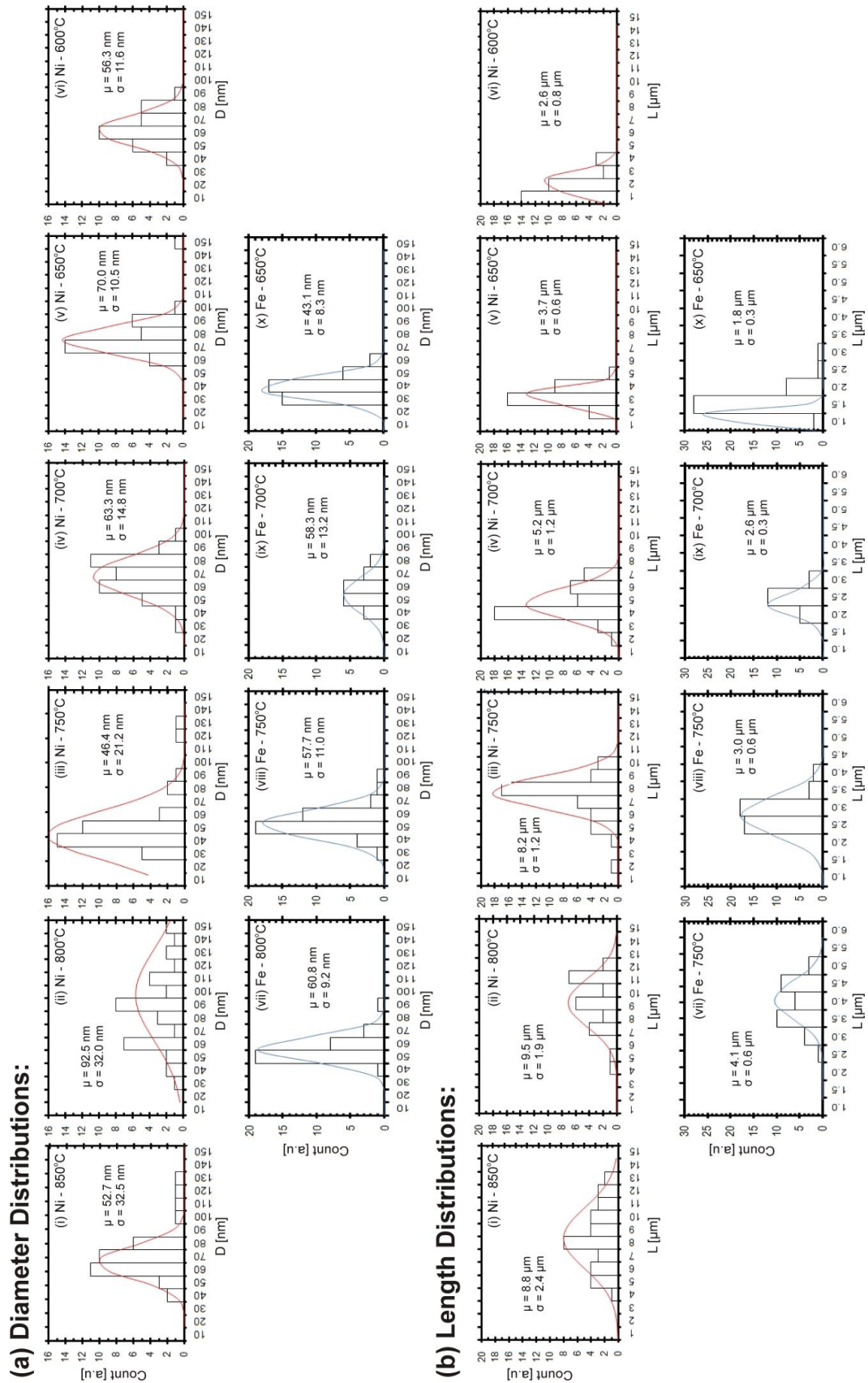
Figure 3.3 | Temperature dependence of nanofibre morphology (1). Length and diameter variations for ITO-Supported Fe and Ni nanofibres. **(a)** Diameter and **(b)** length as a function of growth temperature (600-860°C) taken from over 400 individual nanofibres. (μ = mean, σ = standard deviation)

spectra confirmed graphene monolayer nucleation. Raman spectra (633 nm) of the nanotubes confirmed their multi-walled nature, through the absence of any RBM signals and corroborating SEM diameter data. High resolution transmission electron microscopy (HR-TEM) studies were performed using a FEI Tecnai F20 operated at 80 kV, which independently verified the number of graphitic walls (Insert, Figure 3.2 (b)).

3.3 Nanofibres & Nanotubes: PE-CVD Vs. T-CVD

The growth rate for the nanofibres and nanotubes (graphene) samples are defined as the rate of change of length (diameter) with respect to time. Figure 3.3 shows the length and diameter histograms of the ITO-supported Ni and Fe-catalysed nanofibres. Increasing the reactor temperature monotonically increases the growth rate (Figure 3.4). Higher temperatures also appear to broaden the diameter range whereas, in this instance, the fibre mean diameter was largely independent of increases in temperature. Mass conservation can be applied to assess the validity of the nanofibre diameters. For an ideally annealed thin-film, a 10% catalyst packing density (neglecting interstitial nucleation) with an assumed regular FCC planar packing (in agreement with the bulk Ni and Fe crystal phases) the catalyst thin-film depth, δ, and nanofibre catalyst (ideally spherical) diameter, D, are related by $D \approx 12.5\delta$, assuming a perfectly hydrophobic support. This, admittedly simplistic model, indicates that a 5 nm annealed catalyst thin film will forms catalsyst islands ~ 62.5 nm in diameter thereby substantiating the experimental observations. The diameters of the Ni and Fe catalysed nanofibres were approximately equivalent and noticeably larger than those grown using alumina-supported Fe.

Figure 3.5(a) shows the typical variation in nanotube (Al_2O_x/Fe) and graphene growth rates as a function of time, measured by scanning electron microscopy. As is also true for nanofibres, the growth rates linearly decay and tend to saturate after 15-20 min. The catalytic activity plateaus due to *a*-C deposits poisoning the catalyst. This deactivation process is particularly effective as it prevents the hydrocarbon precursor from reaching the catalyst surface whilst also preventing carbon precipitation. Similarly, monolayer graphene growth saturates once the surface is fully covered with graphene because of the absence of a catalyst to pyrolyse the carbon feedstock. Interestingly, however, we observe subsequent (second) layer growth in the case of graphene. The exact nucleation sites for these layers is unclear at this stage, but may perhaps be associated with porous grain boundaries allowing the precursor
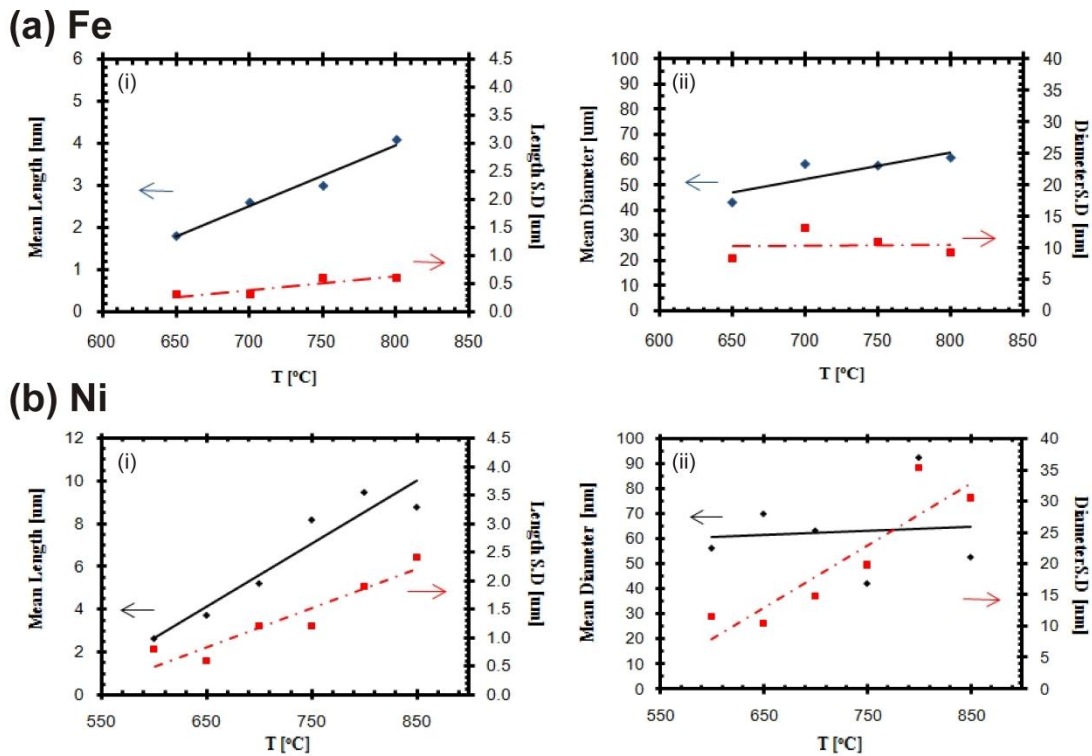
Figure 3.4 | **Temperature dependence of nanofibre morphology (2).** Nanofibre length mean **(i)** and standard deviation (S.D.) **(ii)** as a function of synthesis temperature (T) for ITO-supported **(a)** Fe and **(b)** Ni catalysts.

access to the underlying Cu catalyst. Alternatively, graphene self-catalysis cannot be ruled out, as activated charcoal has been shown to nucleate CNTs[13].

Nanofibre forests showed higher growth rates than individual patterned nanofibres, at equivalent growth temperatures. Catalyst patterning affected the growth rate. Nanotube forests have been shown by others[14, 15] to grow more rapidly at the edge of patterned catalysts. Gas flow conditions and thermal pre-treatment were considered viable candidate mechanisms to account for this. However, growth rate perturbation may be attributed to spatially compounded dissociative heating of the carbon precursor. Kanzow *et al.*[16], in agreement with the original suggestions of Baker *et al.*[17], conjectured that precursor decomposition occurring at the catalyst surface is sufficiently exothermic to increase the local temperature. Although local dissociative heating cannot be completely ruled out and is undoubtedly an important part of the complete growth mechanism (in the case of nanotubes and nanofibres, at least), Kricvoruchko *et al.*[18] and Klinke *et al.*[19] convincingly argued that the additional heating, for a single catalyst particle, is in fact negligible and cannot realistically contribute to a catalyst phase change or thermally stimulated variation between

bulk and surface diffusion coefficients, as initially proposed. Consider the exothermic hydrocarbon dissociation at the catalyst surface. A temperature gradient would exist across the bulk catalyst. Since the solubility of carbon in metals is strongly temperature dependent, increased dissolution occurs in the hotter zones (i.e. at the surfaces). However, over such small length scales a significant thermal gradient is physically intangible. Any surface localised exothermic reactions would be much more likely raise the temperature of the entire catalyst thereby equally modulating both the bulk and surface diffusion characteristics. As a result, for individual nanotubes and nanofibres, dissociative heating plays a largely minor role. Yet, when multiple catalyst particles are closely packed, as in the case of nanotube and fibre forests, the cumulative effect may very well increase the local temperature, albeit relatively marginally. This may account for the increased growth rates (increasing synthesis temperature has already been evidenced to proportionally increase the growth rate). The temperature difference associated with this amplified dissociative heating can be estimated by comparing the temperature dependent growth profiles of forest nanotubes and the individual nanotubes for equivalent catalysts and growth conditions. Localised heating suggests and temperature increase of ~ 50°C due to increased growth rates of some 15%. Due to the similarities in the processing conditions plasma effects were neglected.

The majority of the growth mechansims reported in the literature focus on surface and bulk diffusion-limited processes[8]. The widely accepted model by Baker *et al.*[20] proposed that carbon diffusion through the bulk catalsyt was the rate-limiting step based on the similarities in the activation energies of nanofibre growth and bulk carbon diffusion[7, 8, 21, 22]. However, the validity of this mechanism is under some scrutiny for nanofibres and the debate is ongoing as to whether this model strictly accomodates nanotubes and even graphene. Are these two seemingly similar carbon-latticed materials similarly rate-limited? Chowalla *et al.*[23], for C_2H_2:NH_3/Ni nanotubes grown by PE-CVD, suggested bulk-diffusion limited growth based on an activation energy of 1.4 eV. Vinten *et al.*[24], Puretzky *et al.*[25], and Zhu *et al.*[26] reported activation energies of 2.1-2.4 eV, whereas Lee *et al.*[27], Kim *et al.*[28] and Liu *et al.*[29] measured activation energies of 1.3-1.7 eV. Hofmann *et al.*[8], by PE-CVD, documented an extremely low activation energy of 0.25 eV, ascribing the reduction to plasma assisted precursor dissociation. Knudsen diffusion has also been considered[30], though the strong temperature dependence of the growth rates, consistent across multiple studies, casts some doubt on the validity of the proposed mechanism.
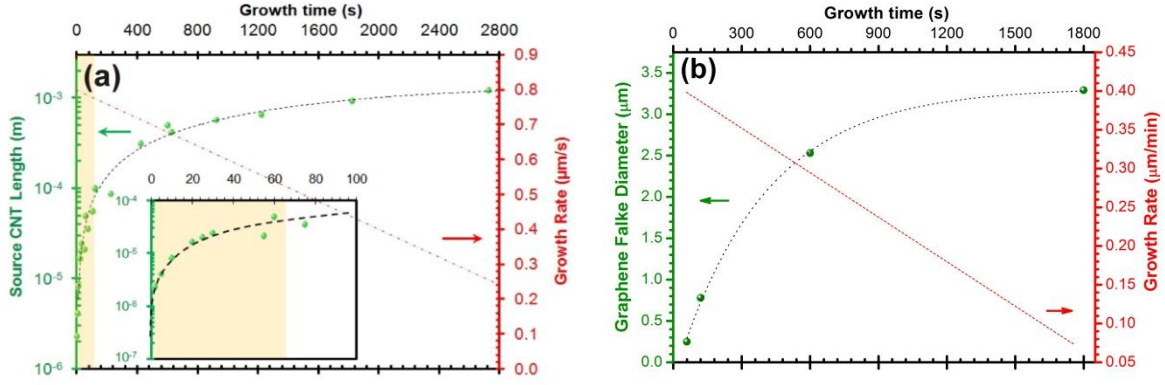
Figure 3.5 | Nanotube and graphene growth saturation. CVD growth rates of **(a)** MWCNTs (Al_2O_x/Fe : 10/1 nm) and **(b)** graphene.

Figure 3.6 shows the growth rate (R) as a function of reciprocal absolute temperature for various PE-CVD and T-CVD synthesised nanotubes, nanofibres and graphene[4, 7, 9]. Data has been linearly fitted according to the Arhenius relation;

$$R \propto D_o S_o \exp\left(\frac{-E_a}{k_B T}\right) \tag{3.1}$$

where T is the growth temperature, k_B is Boltzmann's constant and D_o and S_o denote the carbon diffusivity and solubility prefactors[7]. E_a is estimated by linear interpolation and gradient extrapolation[27]. For the ITO/Ni and ITO/Fe nanofibres (closed / open red squares) the activation energies are 0.51±0.15 eV and 0.44±0.17 eV, respectively. For the Al_2O_x/Fe and Al/Fe nanotubes (closed / open green squares) the activation energies are 1.33±0.10 eV and 1.94±0.96 eV. For Cu-catalysed graphene (orange squares) the activation energy was 2.33±0.10 eV.

Various early work determined the diffusion coefficients and solubility of carbon in Ni, Fe and Cu[31-33]. Here, the diffusion barriers can be extracted via linear interpolation of the diffusion coefficient against inverse absolute temperature. Majorica *et al.*[33] considered the barrier potentials to surface diffusion in polycrystalline Ni (0.27 eV) using surface sensitive Auger electron spectroscopy whilst Diamond *et al.*[34] focused on the bulk diffusion in Ni (1.52 eV). Berry *et al.*[35] summarised various work on Ni, spanning multiple techniques and provided a good estimate for the bulk diffusion activation energy (1.49±0.33 eV). Wert, Emsley, Massaro, Smithells, Homan and Lander[32, 36-40] all reported on the carbon solubility in Fe lattices α (BCC), γ (FCC) and polycrystalline phases using various techniques and cumulatively give a bulk Fe diffusion barrier of 0.81±0.09 eV for α- and polycrystalline
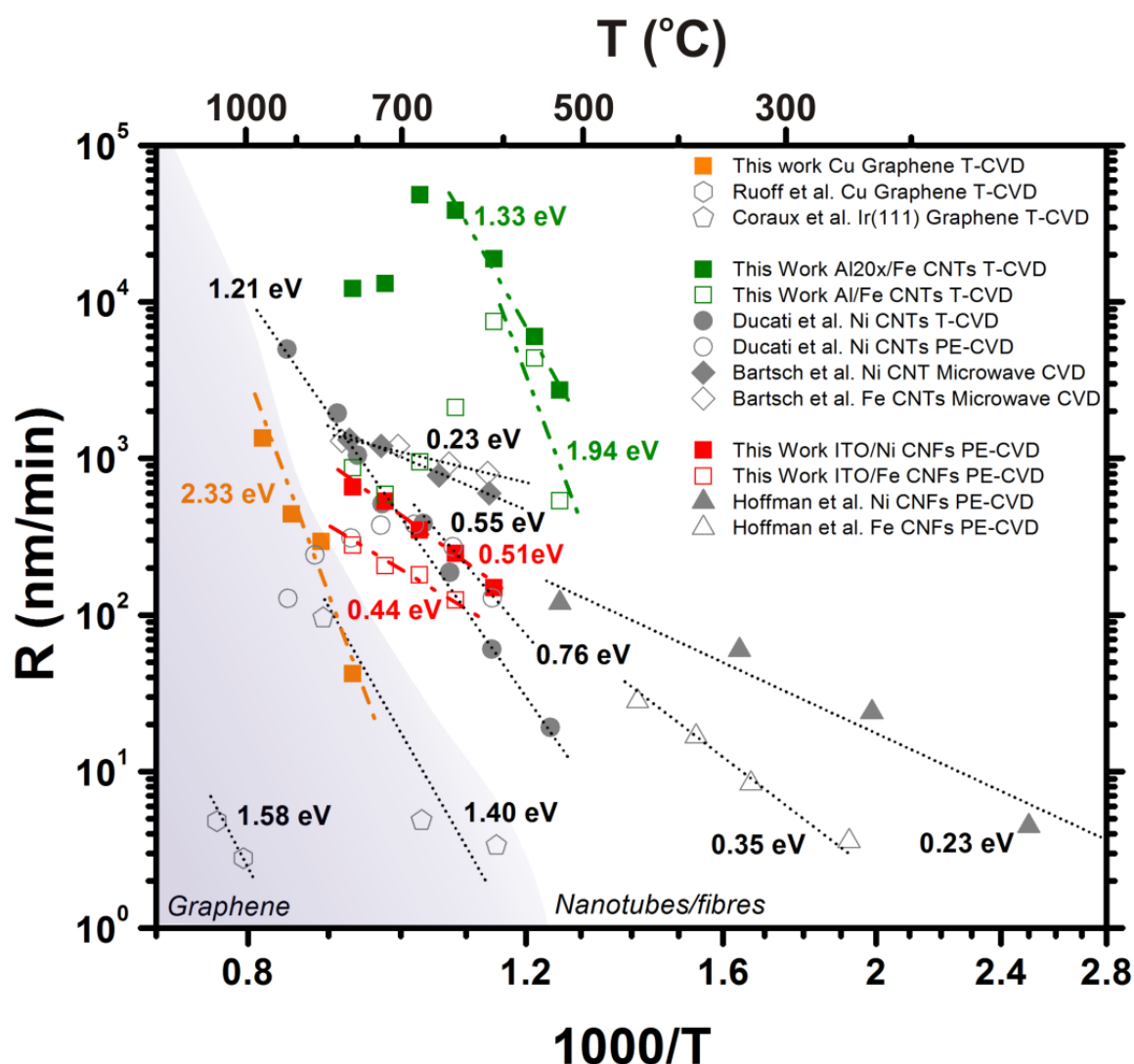
Figure 3.6 | **Nanofibre, nanotube and graphene CVD catalysis activation energies.** Arrhenius plot of the growth rates for > 400 samples. Least-squares fit. E_a estimated from gradient linear interpolation. ITO/Ni - 0.51 ($\pm$0.15) eV, ITO/Fe - 0.44 ($\pm$0.17) eV, Al/Fe - 1.94 ($\pm$0.96) eV, Al_2O_x/Fe - 1.33 ($\pm$0.10) eV. For Cu-catalysed Graphene E_a = 2.33 ($\pm$0.10) eV. Supporting data from Hofmann *et al.*[4, 5], Ducati *et al.*[7], Bartsch *et al.*[9], Coraux *et al.*[10] and Li *et al.*[11]. Experimental uncertainty $\pm$10 nm/min, unless otherwise stated.

phases and 1.25-1.68 eV[41] for the γ-phase. Although no empirical data on the surface diffusion of carbon on Fe is available in the literature the density functional theory calculations by Jiang and Carter[42] suggest a surface diffusion barrier of 0.64 eV. Evidently, nanofibre activation energies, in both the Ni (0.51 eV) and Fe (0.44 eV) cases, are significantly less than the values associated with bulk carbon diffusion (Ni~1.50 eV[43], Fe~1.00 eV[1]) and are comparable to the surface diffusion of carbon on (polycrystalline) Ni (0.3 eV[33]) and Fe (0.64 eV[42]) suggesting a dominant surface diffusion process, even at

---

[1] Approximate bulk value for α- and γ-phases
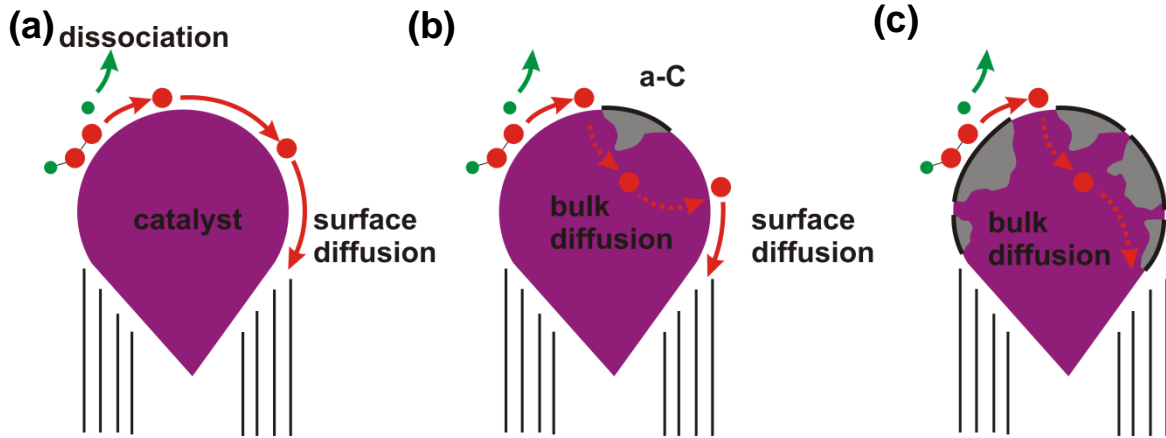
Figure 3.7 | PE-CVD (left) Vs. T-CVD (right). *a*-C induced surface-to-bulk diffusion transition. **(a)** A catalyst particle in the initial state with negligible *a*-C deposits permitting predominant surface diffusion. **(b)** *a-C* deposits increase during precursor exposure. Surface diffusion becomes less energetically favourable and the catalyst is forced to adopt bulk diffusion. The rate limiting step therefore deviates from surface to a bulk diffusion. Grey areas highlight local saturation. **(c)** PE-CVD efficiently etches *a-C* deposits and thusly retains a low activation energy. Whereas, *a*-C removal is far less efficient in T-CVD, hence the dominance of bulk diffusion, and the correspondingly increased activation energy.

elevated growth temperatures. Indeed, the surface diffusion simulations of Yazyev and Pasquarello[44] support this finding. The extrapolated activation energy also suggests that the Fe particle may very well be in its polycrystalline or α-phase, a puzzling result as the bulk γ-phase becomes increasingly favoured, due to its thermodynamic stability, at elevated temperatures (>750°C) and increased carbon content[45]. Nonetheless it is highly probable that multiple phases exist at particular times during the nanotube growth.

3.4   Support Implications on the Diffusion Regime in T-CVD & PE- CVD

To demonstrate the growth implications of varied support layers and the variations between PE-CVD and T-CVD, Al/Fe and Al_2O_x/Fe systems by T-CVD were considered. The growth rate initially increases monotonically as a function of substrate temperature before decreasing at sub-optimal high temperatures (Figure 3.6, green squares). This trend is similar to those reported by Cui *et al.*[46] and Ducati *et al.*[7] using microwave and hot-filament assisted PE-CVD, as well as Wirth *et al.*[21] for mid-pressure (>10 mbar) T-CVD using Al_2O_x/Fe. Here they noted that the sub-optimal decline in growth, as a function of increasing temperature, ceased at reduced partial pressures. Al/Fe and Al_2O_x/Fe offer increased growth rates,

compared to their ITO/Fe counterpart, whilst simultaneously reducing the optimal growth temperature. Evidently though the broadness of the growth regime suffers.

In the catalyst systems studied, the activation energies (Al/Fe - 1.94 eV, Al_2O_x/Fe - 1.33 eV) are significantly larger for T-CVD compared to PE-CVD are consistent with γ-phase bulk diffusion (1.68 eV). Though the process remains diffusion limited, the support appears to have augmented the diffusion regime. Many different factors may account for this. It is conceivable that the support layer adjusts the diffusion regime by alloying the catalyst with non-catalytic species[47]. It is also feasible that the support material plays an important role in the formation of metastable carbides that in turn affect the catalytic activity, which is perhaps more plausible given the strong temperature dependence of carbide formation[48]. Nonetheless, the large disparity between PE-CVD and T-CVD activations energies is evidently independent of the support material, as the increase is consistent across the Al and Al_2O_x supports. Perhaps the most viable explanation of the reduced barrier can be given by considering plasma effects. Ion bombardment could also heat the catalyst particle thereby favourably increasing carbon diffusivity and solubility. The temperature dependent plasma maintains catalytic activity by efficient etching of *a*-C deposits that inhibit hydrocarbon adsorption, dissociation and carbon precipitation[23]. Note that in a surface-diffusion limited case there is no requisite for catalyst saturation as in the case of bulk diffusion. Consider Figure 3.7. If a surface diffusion mechanism dominates then the catalyst interior has low carbon saturation. However, as *a-C* deposits increase, saturated volumes develop (grey, centre panel). If *a*-C deposits become significant, in the case of saturated thermal CVD (right panel), then growth must proceed via less-efficient bulk diffusion in attempts to access and precipitate through active catalyst sites. The surface diffusion activation energy increases with hydrocarbon exposure time to the point at which bulk diffusion becomes favourable.

3.5   Al Vs. Al_2O_x Support Layers & T-CVD

The question still remains - why are there such marked differences in the activation energies of Al_2O_x and natively oxidised Al supports? In general, the growth rate of CNTs depends on the catalytic activity of the surface Fe[49]. Catalytic activity is a function of barrier material and depth. To rule out thickness issues, nominal 10 nm Al and Al_2O_x supports were used throughout. The results of Lee *et al.*[50] revealed, using secondary ion mass spectroscopy, that Fe diffuses to a much greater depth in Al supports compared to Al_2O_3. Furthermore, they

surmised that the increased support oxidation enhanced catalytic activity giving higher growth rates. Thus, the variations in activation energies in the Al and Al$_2$O$_x$ cases are most likely a product of the variability in C solubility between Fe and the Al-Fe alloying, occurring as a result of increased Fe migration into the Al support, both of which have strong and differing temperature dependencies.

3.6 Cu-Catalysed Graphene & the Nanotube Analogue

The solubility of carbon in Cu (<0.001 At.% at 1000°C[31, 51]) is substantially lower than in either Ni or Fe (~1.3 At.% at 1000°C[52]). Since little C can dissolve into Cu one would speculate that carbon migration is achieved predominately through surface diffusion, as the nanotube analogue would certainly suggest[8]. Density functional theory calculations, presented by Yazyev *et al.*[53] determined surface and bulk diffusion barriers of 0.07 eV and 1.65 eV, respectively. In fact, estimates using the error function form of Fick's law applied to the data of McLellen *et al.*[51] and Lopez *et al.*[31] suggest diffusion barriers less than 0.1 eV. The discrepancy between the diffusion barriers and the estimated activation energy (2.33 eV) hints that Cu-catalysed graphene growth is in fact *not* bulk or even surface diffusion limited, but rather dissociation, precipitation or mass transfer limited. Note that is the catalysis is unlikely to be diffusion limited it is clear that it too is unlikely to be precipitation limited.

Dissociative heating was proposed to play a critical role for increased levels of surface diffusion compared to bulk diffusion. The exterior of the catalysts particle was thought to be hotter than the interior (bulk). The surface therefore offered greater C solubility compared to the bulk. In the case of Cu-catalysed graphene dissociative heating has negligible implications on carbon solubility. In metals, solubility positively correlates with increasing temperature. Nonetheless, Lopez *et al.*[31] showed that, for Cu/C systems, this dependence is extremely weak. Moreover, dissociative heating clearly has negligible effects as we have successfully employed CH$_4$, which undergoes endothermic dehydrogenation, to grow equally high quality graphene using similar process conditions (Figure 3.8(b)). Intermediary active hydrocarbons such as ethylene and acetylene, not sourced directly from the hydrocarbon precursor but rather from its intermediate reaction products, which exothermically decompose, have been suggested to account for this disparity in the case of nanotubes[54]. Indeed, the differentially pumped, electrostatic quadrupole plasma (EQP, Hiden Analytical) mass spectrum of the methane-based atmosphere, sampled during the growth, supports this
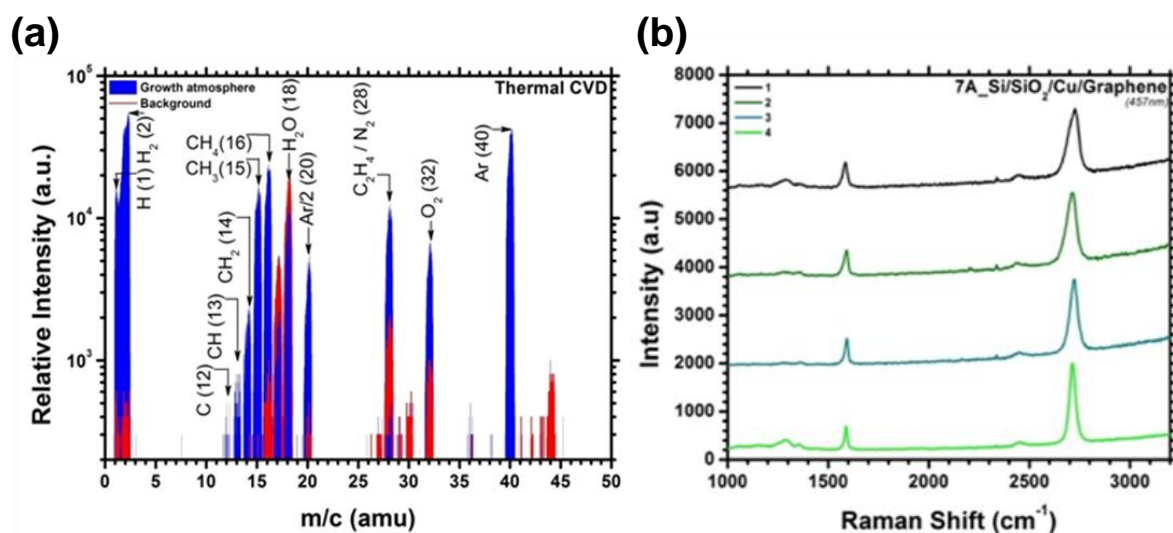
Figure 3.8 | **CH$_4$ Cu-catalysed graphene by T-CVD. (a)** EQP mass spectra of the sampled growth atmosphere during graphene thermal CVD probed downstream of the reactor (CH$_4$:H$_2$ / 35:175 sccm, 5 mbar, 10 min, 900°C). **(b)** Raman spectra (457 nm) of monolayer methane-based as-synthesised graphene on PVD deposited Cu/SiO$_2$/Si.

conjecture and directly evidences high ethylene (28 amu) content (Figure 3.8(a)). Nevertheless, it is important to realise that peak ambiguity exists within the data as residual atmospheric N$_2$ may similarly account for the apparent ethylene signal. In order to minimise this ambiguity the chamber was pre-evacuated to <10^{-5} mbar and repeatedly Ar purged prior to growth. As a result it is highly improbable that the large 28 amu signal is residual N$_2$. Nonetheless, such hypothesises remain largely speculative given the cracking nature of many mass spectrometers. Nevertheless, increased carbon solubility due to dissociative heating is certainly far less pronounced in C/Cu systems.

Thermal decomposition of ethylene, in the absence of a catalytic surface, has a barrier of 3.5-4.2 eV[55]. The kinetics studies of Pirard *et al.*[56], on MWCNT synthesis over Fe–Co/Al$_2$O$_3$, offered an ethylene decomposition activation energy of 1.35 eV. Different hydrocarbon feedstocks display different levels of, and barriers to, dissociation depending on the catalyst surface. Although the Fe-catalysed ethylene dissociation is less than the estimated activation energy in this present study, the estimate does lie within the tolerances of the catalysed and uncatalysed decomposition and as such cannot be ruled out completely. But is graphene growth truly precursor pyrolysis-limited? The barrier for carbon crystal growth is 2.30 eV[57], which shows a remarkable similarity to our estimate (2.33 eV) given experimental uncertainties.

It is unclear as to whether the pyrolysis or integration account for the rate-limiting step, especially given the relative uncertainty in the exact thermal decomposition barrier for Cu-catalysed ethylene. Indeed, the present data cannot discriminate between the two. Nevertheless, using low-energy electron microscopy, Loginove *et al.*[57], for carbon PVD on Ru(0001), determined an activation energy of 2.00±0.10 eV, suggesting that graphene growth is not adatom (surface) diffusion limited, but rather (lattice) integration limited. Even with their contrasting catalyst system the measured barriers show striking resemblance to the results presented here, and certainly lie within the experimental resolution. Likewise, Li *et al.*[58] concluded, using isotope labelling, that Ni-catalysed graphene is precipitation limited, whereas graphene on Cu grows by a surface adsorption process.

3.7   Summary

The activation energies of CVD grown nanofibres, nanotubes and graphene were considered in an attempt to draw suitable analogies between nano-carbon growth. Figure 3.6 summarises the key features of this work. Nanofibres and multi-walled nanotubes were shown to adhere well to the maturing posit of surface-diffusion limited growth for ITO-supported Ni and Fe catalysts by PE-CVD. Deviation to a bulk-diffusion limited regime occurred for T-CVD synthesised nanotubes. A possible surface-to-bulk diffusion transition was tentatively proposed. Growth variations due to the barrier material, namely Al and Al_2O_x, were considered and were ascribed to temperature dependent discrepancies between the carbon solubility in pure Fe and Fe-Al alloys. Cu-catalysed monolayer graphene was revealed to significantly deviate from the standard nanotube / nanofibre analogue and clearly evidenced carbon integration-limited growth with an activation energy of 2.33 eV.

References

1. Kukovitsky, E. F., L'Vov, S. G.& Sainov, N. A. (2000). VLS-growth of carbon nanotubes from the vapor, *Chem. Phys. Lett.*, **317**, pp. 65-70.
2. Jiang, K. L., Feng, C., Liu, K.& Fan, S. S. (2007). A vapor-liquid-solid model for chemical vapor deposition growth of carbon nanotubes, *J. Nanosci. Nanotechno.*, **7**, pp. 1494-1504.
3. Saito, Y. (1995). Nanoparticles and filled nanocapsules, *Carbon*, **33**, pp. 979-988.
4. Hofmann, S., Csanyi, G., Ferrari, A. C., Payne, M. C.& Robertson, J. (2005). Surface diffusion: The low activation energy path for nanotube growth, *Phys. Rev. Lett.*, **95**, pp. 0361011-0361014.
5. Graphene Brillouin Zone and Electronic Energy Dispersion - http://demonstrations.wolfram.com (/GrapheneBrillouinZoneAndElectronicEnergyDispersion/)
6. Kolasinski, K. W. (2006). Catalytic growth of nanowires: Vapor-liquid-solid, vapor-solid-solid, solution-liquid-solid and solid-liquid-solid growth, *Curr. Opin. Solid State Mat. Sci.*, **10**, pp. 182-191.

7.   Ducati, C., Alexandrou, I., Chhowalla, M., Amaratunga, G. A. J.& Robertson, J. (2002). Temperature selective growth of carbon nanotubes by chemical vapor deposition, *J. Appl. Phys.*, **92**, pp. 3299-3303.

8.   Hofmann, S., Ducati, C., Robertson, J.& Kleinsorge, B. (2003). Low-temperature growth of carbon nanotubes by plasma-enhanced chemical vapor deposition, *Appl. Phys. Lett.*, **83**, pp. 135-137.

9.   Bartsch, K., Biedermann, K., Gemming, T.& Leonhardt, A. (2005). On the diffusion-controlled growth of multiwalled carbon nanotubes, *J. Appl. Phys.*, **97**, pp. 1143011-1143017.

10.   Coraux, J., N'Diaye, A. T., Engler, M., Busse, C., Wall, D., Buckanie, N., Meyer Zu Heringdorf, F. J., Van Gastel, R., Poelsema, B.& Michely, T. (2009). Growth of graphene on Ir(111), *New J. Phys.*, **11**, pp. 1-22.

11.   Li, X., Magnuson, C. W., Venugopal, A., An, J., Suk, J. W., Han, B., Borysiak, M., Cai, W., Velamakanni, A., Zhu, Y., Fu, L., Vogel, E. M., Voelkl, E., Colombo, L.& Ruoff, R. S. (2010). Graphene films with large domain size by a two-step chemical vapor deposition process, *Nano Lett.*, **10**, pp. 4328-4334.

12.   Yu, Q., Jauregui, L. A., Wu, W., Colby, R., Tian, J., Su, Z., Cao, H., Liu, Z., Pandey, D., Wei, D., Chung, T. F., Peng, P., Guisinger, N. P., Stach, E. A., Bao, J., Pei, S. S.& Chen, Y. P. (2011). Control and characterization of individual grains and grain boundaries in graphene grown by chemical vapour deposition, *Nature Materials*, **10**, pp. 443-449.

13.   Chee, T. J., Buang, N. A., Aziz, M., Sanip, S. M.& Ismail, A. F. (2003). Heat treatment studies on activated carbon and charcoal for carbon nanotube synthesis, *Advances in Malaysian Fuel Cell Research and Development*, pp. 187-196.

14.   Futaba, D. N., Hata, K., Yamada, T., Hiraoka, T., Hayamizu, Y., Kakudate, Y., Tanaike, O., Hatori, H., Yumura, M.& Iijima, S. (2006). Shape-engineerable and highly densely packed single-walled carbon nanotubes and their application as super-capacitor electrodes, *Nature Materials*, **5**, pp. 987-994.

15.   Zhong, G., Iwasaki, T., Robertson, J.& Kawarada, H. (2007). Growth kinetics of 0.5 cm vertically aligned single-walled carbon nanotubes, *J. Phys. Chem. B*, **111**, pp. 1907-1910.

16.   Kanzow, H.& Ding, A. (1999). Formation mechanism of single-wall carbon nanotubes on liquid-metal particles, *Phys. Rev. B*, **60**, pp. 11180-11186.

17.   Baker, R. T. K. (1989). Catalytic growth of carbon filaments, *Carbon*, **27**, pp. 315-323.

18.   Krivoruchko, O. P.& Zaikovskii, V. I. (1993). **329**, p 744.

19.   Klinke, C., Bonard, J. M.& Kern, K. (2005). Thermodynamic calculations on the catalytic growth of multiwall carbon nanotubes, *Phys. Rev. B*, **71**, pp. 1-7.

20.   Baker, R. T. K., Harris, P. S., Thomas, R. B.& Waite, R. J. (1973). Formation of filamentous carbon from iron, cobalt and chromium catalyzed decomposition of acetylene *J. Catal.*, **30**, pp. 86-95.

21.   Wirth, C. T., Zhang, C., Zhong, G., Hofmann, S.& Robertson, J. (2009). Diffusion - and reaction - limited growth of carbon nanotube forests, *ACS Nano*, **3**, pp. 3560-3566.

22.   Baker, R. T. L.& Barber, M. A. (1978) *Chemistry & Physics of Carbon* **14**, eds. Walker, P. I.&Thrower, P. A., (Dekker, New York) pp. 83.

23.   Chhowalla, M., Teo, K. B. K., Ducati, C., Rupesinghe, N. L., Amaratunga, G. A. J., Ferrari, A. C., Roy, D., Robertson, J.& Milne, W. I. (2001). Growth process conditions of vertically aligned carbon nanotubes using plasma enhanced chemical vapor deposition, *J. Appl. Phys.*, **90**, pp. 5308-5317.

24.   Vinten, P., Lefebvre, J.& Finnie, P. (2009). Kinetic critical temperature and optimized chemical vapor deposition growth of carbon nanotubes, *Chem. Phys. Lett.*, **469**, pp. 293-297.

25.   Puretzky, A. A., Geohegan, D. B., Jesse, S., Ivanov, I. N.& Eres, G. (2005). In situ measurements and modeling of carbon nanotube array growth kinetics during chemical vapor deposition, *Appl. Phys. A*, **81**, pp. 223-240.

26.   Zhu, L., Xu, J., Xiao, F., Jiang, H., Hess, D. W.& Wong, C. P. (2007). The growth of carbon nanotube stacks in the kinetics-controlled regime, *Carbon*, **45**, pp. 344-348.

27.   Lee, Y. T., Park, J., Choi, Y. S., Ryu, H.& Lee, H. J. (2002). Temperature-dependent growth of vertically aligned carbon nanotubes in the range 800-1100°C, *J. Phys. Chem. B*, **106**, pp. 7614-7618.

28.   Kim, K. E., Kim, K. J., Jung, W. S., Bae, S. Y., Park, J., Choi, J.& Choo, J. (2005). Investigation on the temperature-dependent growth rate of carbon nanotubes using chemical vapor deposition of ferrocene and acetylene, *Chem. Phys. Lett.*, **401**, pp. 459-464.

29.   Liu, K., Jiang, K., Feng, C., Chen, Z.& Fan, S. (2005). A growth mark method for studying growth mechanism of carbon nanotube arrays, *Carbon*, **43**, pp. 2850-2856.

30.   Xiang, R., Yang, Z., Zhang, Q., Luo, G., Qian, W., Wei, F., Kadowaki, M., Einarsson, E.& Maruyama, S. (2008). Growth deceleration of vertically aligned carbon nanotube arrays: Catalyst deactivation or feedstock diffusion controlled?, *J. Phys. Chem. C*, **112**, pp. 4892-4896.

31.   López, G. A.& Mittemeijer, E. J. (2004). The solubility of C in solid Cu, *Scripta Materialia*, **51**, pp. 1-5.

32.   Wert, C. A. (1950). Diffusion coefficient of C in α-iron, *Phys. Rev.*, **79**, pp. 601-605.
33.   Mojica, J. F.& Levenson, L. L. (1976). Bulk-to-surface precipitation and surface-diffusion of carbon on polycrystalline nickel, *Surf. Sci.*, **59**, pp. 447-460.
34.   Diamond, S.& Wert, C. (1967). Diffusion of carbon in nickel above and below curie temperature, *T. Metallurg. Soc. Aime*, **239**, pp. 705-709.
35.   Berry, B. S. (1973). Diffusion of carbon in nickel, *J. Appl. Phys.*, **44**, pp. 3792-3793.
36.   Emsley, A. M.& Hill, M. P. (1983). Kinetics of monticular carbon growth on polycrystalline iron, *J. Chem. Soc. Faraday T. 1*, **79**, pp. 15-26.
37.   Massaro, T. A.& Petersen, E. E. (1971). Bulk diffusion of carbon-14 through polycrystalline nickel foil between 350°c and 700°c, *J. Appl. Phys.*, **42**, pp. 5534-5539.
38.   Smithells, C. J.& Ransley, C. E. (1936). The Diffusion of Gases through Metals. III. The Degassing of Nickel and the Diffusion of Carbon Monoxide through Nickel, *Proceedings of the Royal Society of London. Series A - Mathematical & Physical Sciences*, **155**, pp. 195-212.
39.   Lander, J. J., Kern, H. E.& Beach, A. L. (1952). Solubility and diffusion coefficient of carbon in nickel: reaction rates of nickel-carbon alloys with barium oxide, *Appl. Phys. Lett.*, **23**, pp. 1305-1309.
40.   Homan, C. G. (1964). Diffusion of carbon in alpha iron, *Acta Metallurgica*, **12**, pp. 1071-1079.
41.   Grigoriev, O. A. (1991) *Physical Properties, Energoatomizdat (Russian)* eds. Meilikhov, E. Z., (Moscow) pp. 385.
42.   Jiang, D. E.& Carter, E. A. (2005). Carbon atom adsorption on and diffusion into Fe(110) and Fe(100) from first principles, *Phys. Rev. B*, **71**, pp. 0454021-0454026.
43.   Siegel, D. J.& Hamilton, J. C. (2003). First-principles study of the solubility, diffusion, and clustering of C in Ni, *Phys. Rev. B*, **68**, pp. 0941051-0941057.
44.   Yazyev, O. V.& Pasquarello, A. (2008). Carbon diffusion in CVD growth of carbon nanotubes on metal nanoparticles, *Phys. Stat. Sol. B*, pp. 284-287.
45.   Raynor, G. V.& Rivlin, V. G. (1988) *Phase Equilibria in Iron Ternary Alloys* eds. (London).
46.   Cui, H., Zhou, O.& Stoner, B. R. (2000). Deposition of aligned bamboo-like carbon nanotubes via microwave plasma enhanced chemical vapor deposition, **88**, pp. 6072-6074.
47.   Nolan, P. E., Lynch, D. C.& Cutler, A. H. (1998). Carbon deposition and hydrocarbon formation on group VIII metal catalysts, *J. Phys. Chem. B*, **102**, pp. 4165-4175.
48.   de Bokx, P. K., Kock, A. J. H. M., Boellaard, E., Klop, W.& Geus, J. W. (1985). The formation of filamentous carbon on iron and nickel catalysts : I. Thermodynamics, *J. Catal.*, **96**, pp. 454-467.
49.   de los Arcos, T., Gunnar Garnier, M., Oelhafen, P., Mathys, D., Won Seo, J., Domingo, C., Vicente García-Ramos, J.& Sánchez-Cortés, S. (2004). Strong influence of buffer layer type on carbon nanotube characteristics, *Carbon*, **42**, pp. 187-190.
50.   Lee, H. C., Alegaonkar, P. S., Kim, D. Y., Lee, J. H.& Yoo, J. B. (2007). Growth of carbon nanotubes: Effect of Fe diffusion and oxidation, *Phil. Mag. Lett.*, **87**, pp. 767-780.
51.   McLellan, R. B. (1969). The solubility of carbon in solid gold, copper, and silver, *Scripta Metallurgica*, **3**, pp. 389-391.
52.   Cai, W., Piner, R. D., Zhu, Y., Li, X., Tan, Z., Floresca, H. C., Yang, C., Lu, L., Kim, M. J.& Ruoff, R. S. (2009). Synthesis of isotopically-labeled graphite films by cold-wall chemical vapor deposition and electronic properties of graphene obtained from such films, *Nano Research*, **2**, pp. 851-856.
53.   Yazyev, O. V.& Pasquarello, A. (2008). Effect of metal elements in catalytic growth of carbon nanotubes, *Phys. Rev. Lett.*, **100**, pp. 1561021-1561024.
54.   Harutyunyan, A. R., Kuznetsov, O. A., Brooks, C. J., Mora, E.& Chen, G. (2009). Thermodynamics behind carbon nanotube growth via endothermic catalytic decomposition reaction, *ACS Nano*, **3**, pp. 379-385.
55.   Tanzawa, T.& Gardiner Jr, W. C. (1980). Thermal decomposition of ethylene, *Combust. Flame*, **39**, pp. 241-253.
56.   Pirard, S. L., Douven, S., Bossuot, C., Heyen, G.& Pirard, J.-P. (2007). A kinetic study of multi-walled carbon nanotube synthesis by catalytic chemical vapor deposition using a Fe-Co/Al$_2$O$_3$ catalyst, *Carbon*, **45**, pp. 1167-1175.
57.   Loginova, E., Bartelt, N. C., Feibelman, P. J.& McCarty, K. F. (2008). Evidence for graphene growth by C cluster attachment *New J. Phys.*, **10**, pp. 1-16.
58.   Li, X., Cai, W., Colombo, L.& Ruoff, R. S. (2009). Evolution of graphene growth on Ni and Cu by carbon isotope labeling, *Nano Lett.*, **9**, pp. 4268-4272.

Chapter IV

Dry-Transferred MWCNTs
& Hot-Press Laminated Graphene
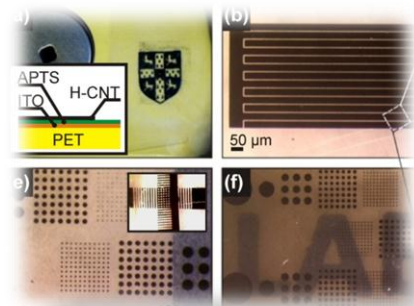
4.   Introduction

In order to usefully exploit the flexibility and transparency of the CVD synthesised nanocarbons discussed in the previous section, the supporting substrates must have similar transparency and flexibility performance. Thus, various transfer techniques must be developed. This chapter documents the development and opto-electronic / flexibility characterisation of MWCNT, and hot-press laminated graphene, thin films using dry-transfer processes to various flexible substrates. The Chapter concludes by comparing the macroscopic transport characteristics of these nominally metallic thin films by proposing a disorder dependent tunnelling model.

4.1   Dry-Transferred MWCNT Thin Films

Here the fabrication, optical, mechanical and conductive properties as well as practical application of well-aligned polymer-supported dry-transferred MWCNTs and graphene thin films is reported. MWCNT thin films were prepared by an inexpensive and facile mechanical dry-transfer process (Figure 4.2) that facilitates large-area roll-to-roll processing on polycarbonate, ITO coated polycarbonate and Al foil substrates. The opto-electronic and mechanical properties of the films have been studied in order to ascertain some understanding of the inter-MWCNT transport interactions and their relation to the films bulk conductivity.

CVD is limited to high-temperature stable, largely inflexible substrates and is therefore polymer incompatible. Low density short vertically aligned carbon nanofibres have been directly deposited on high temperature polymers[4] ($<200^{o}$C) but dense tall nanotubes have not. The presented dry-transfer process functions on the basis that the high surface area of the nanotubes induces significant Van de Waals forces between nanotubes and the nanotubes and the transfer substrate which results in substantial binding without the need of additional wet chemistry. Indeed, Pint *et al.*[5] demonstrated aligned dry contact transfer printing in 2010, at the same time as the work presented herein, though they required water-assisted CVD to etch the, most likely, root grown catalyst particles in order to mobilise their SWCNT forest. No such step is necessary in the technique presented below.
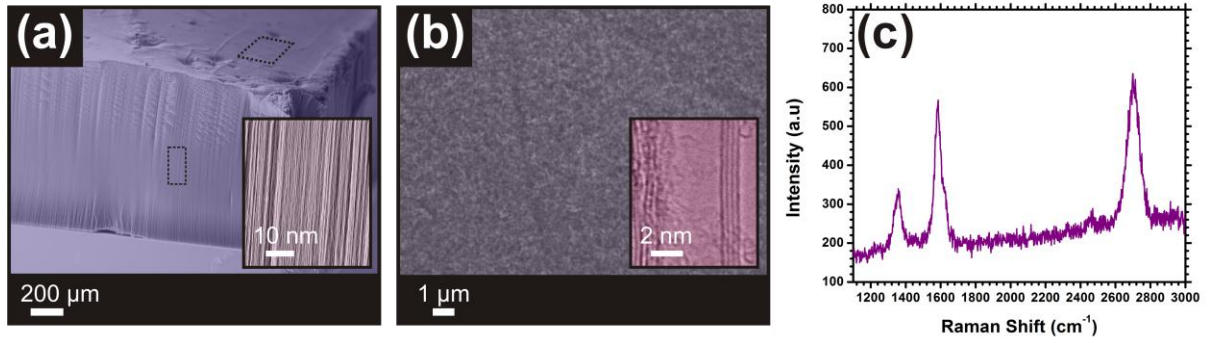
Figure 4.1 | Nanotube forest characterisation. (a) Side profile SEM micrograph of the source nanotubes. *Insert:* High-resolution (HR-) SEM micrograph profile of the side-walls showing extremely linear growth. **(b)** Areal SEM micrograph showing the spaghetti-like morphology of the forest surface. *Insert:* HR-TEM micrograph of an as-synthesised MWCNT clearly formed from four graphitic side walls. **(c)** Raman spectra (3 mW, 633 nm) of the as-grown MWCNTs.

The vertically aligned, source MWCNT forests were synthesised by Al_2O_x/Fe-catalysed T-CVD as previously described (Chapter II). 200-nm thermally oxidised Si wafers (SiO_2/Si) were magnetron sputtered with a 10 nm Al_2O_x (99.99%) and 1 nm evaporated (Lesker PVD75) Fe (99.95%) bilayer catalyst[6-8]. Catalyst samples were loaded into the growth reactor which was pressurised to a 27±1 mbar under a 4% ultra-high purity C_2H_2 atmosphere in a H_2 (192 sccm) diluent and were grown for up to 600 s (growth rate ~1 µm/s) at 700°c (5°c/s). Forests were controllably grown with lengths from <1 µm up to 500 µm (Figure 4.1(a)). The nanotubes had diameters ranging from 10 nm to 40 nm and were formed from 2-5 graphitic walls (Insert Figure 4.1(a)).

Figure 4.2 illustrates the scalable, room-temperature and facile dry-transfer process. The source MWCNT forests were not chemically treated in any way prior to transfer. Various polymer destination-substrates were angled toward the as-grown MWCNT forests and rolled (using a quartz rod 15 mm in diameter) whilst applying ~1 kg/cm^2 at a roll velocity of ~1 cm/s. The transferred untreated polymers considered in this study included polyethylene terephthalate (PET) and polypopylene carbonate, as well as aminopropyl-triethoxysilane (APTES) treated PET/ITO and Al foil. Dry-transferred films had a mean compression factor (original forest depth / rolled film depth) of 13.8, verified by stylus profilometry (Dektak 200-Si).

The morphology of the thin films and their constituent MWCNTs was characterised using a FEI Tecnai F20 FEG TEM operated at 80 kV, a Carl Zeiss SEM 50 operated at 10 kV and
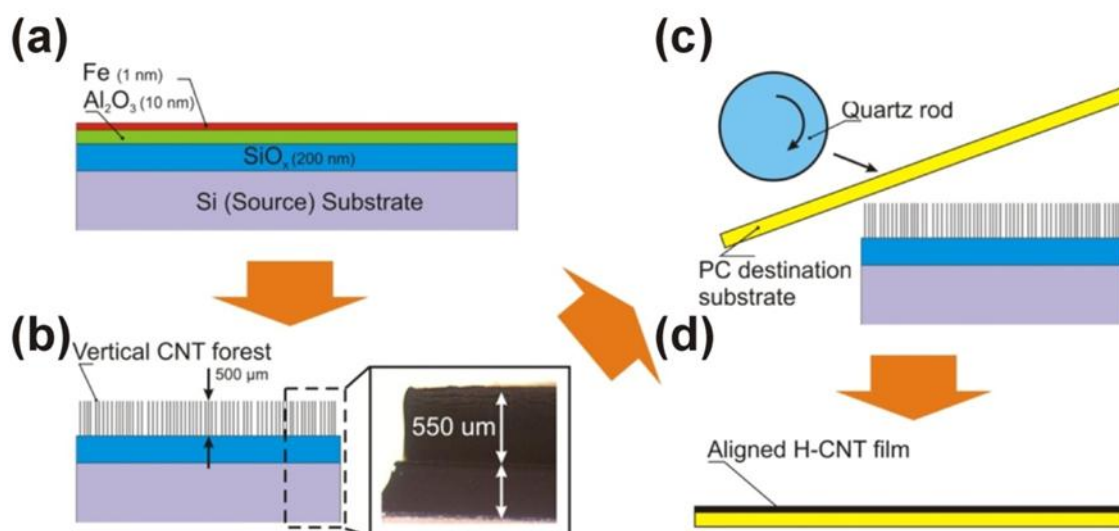
Figure 4.2 | Aligned MWCNT dry-transfer process. (a) Cross-sectional illustration of the Si/SiO$_2$ (200 nm) substrates magnetron sputtered with 10 nm Al$_2$O$_x$ / 1 nm Fe thermally evaporated (Lesker PVD). **(b)** MWCNT synthesis by thermal-CVD: 700°C, 26 mbar, 192 sccm H$_2$:8 sccm C$_2$H$_2$, 10 min. *Insert:* Optical micrograph of an as-grown 550 μm tall MWCNT forest. **(c)** PET destination substrate angled toward the sources nanotube forest. **(d)** PET and source nanotube substrate compressed by a rolled quartz cylinder, moving at a rate of ~1 cm/s.

EDX fitted Schottky FEG FEI-Philips XL30 SEM operated at 30kV and an Agilent atomic force microscope (AFM). Optical characterisation was performed using a Unicam UV-Vis-NIR spectrophotometer in transmission mode. Additional information on the graphitic structure of the MWCNTs was revealed spectroscopically using a Renishaw In-Via, He-Ne laser operated at 633 nm excitation with an incident power of 0.55 mW. Four-probe bond pads were patterned using Ag nanoparticle / Anisol dispersions deposited at room temperature using a vulcanised silicone soft-lithography imprint process. Four probe conductivity measurements were also performed using a Keithley 2100 Digital Meter. All measurements were performed at room temperature and pressure.

A typical Raman spectra of a dry-transferred film is shown in Figure 4.1(c). The D, G and 2D peaks are located at 1358.6 cm^{-1}, 1584.8 cm^{-1} and 2705.5 cm^{-1}. The I$_D$/I$_G$ ratio for the dry-transferred MWCNTs ~0.83. No RBMs were noted. The transfer process did not induce increased crystallographic disorder.

Figure 4.3 and Figure 4.2(b, insert) show SEM and optical micrographs (Nikon eclipse ME600L) of the as-grown vertical MWCNT forests and dry-transferred films on
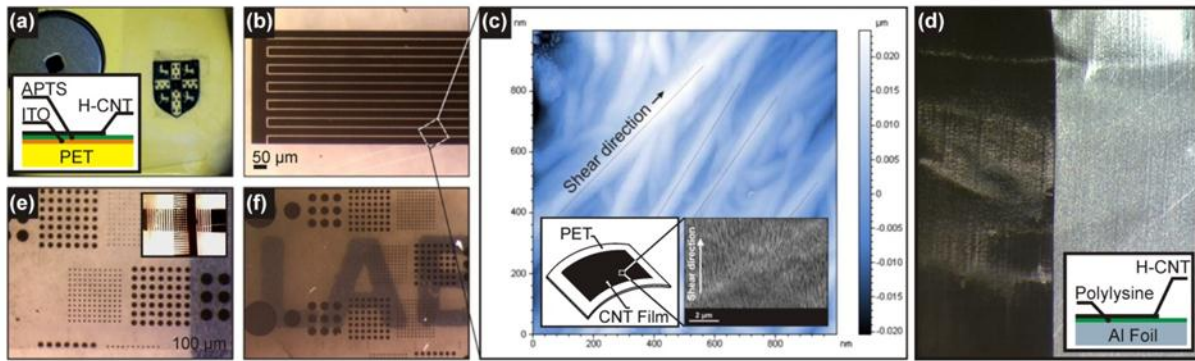
Figure 4.3 | Patterned dry-transferred MWCNT thin films. (a) Patterning by Mo catalyst passivation. The Al_2O_x/Fe bilayer catalyst was patterned using a laser-jet/paper transfer technique and Mo deposition. Patterned MWCNT films were then transferred to the destination PC. A self-assembled monolayer APTES was employed for PET/ITO substrates prior to transfer. **(b, e)** An aligned MWCNT film patterned into 5 μm interdigitated electrodes by standard photolithography and O_2 RIE (0.2 mbar, 100 W, 120 s). *Insert:* Optical micrograph of a Mo-passivated pre-patterned film transferred to a PET substrate and a second perpendicularly aligned pre-patterned forest transferred. **(c)** AFM micrograph (900 nm x 900 nm) of a dry-transferred MWCNT film on a PC substrate. *Insert*: SEM micrograph of a transferred film showing the high level of macroscopic alignment. **(d)** Optical micrograph of poly(lysine) treated Al foil with a dry-transferred MWCNT film. Prior to treatment MWCNTs did not adhere. *Insert*: Schematic of the substrate cross-section. **(f)** Transparency control by O_2 RIE with 5, 20, 50 μm dots photolithographically defined.

polypropylene carbonate (PPC) and polyethylene terephthalate (PET) substrates patterned by direct Mo catalyst passivation (Figure 4.3(a)) and O_2 reactive ion etching (RIE, Philips RIE) (Figure 4.3(b,e,f)). In the latter case, transparency control was achieved by controlling the duration of the RIE process, as depicted in Figure 4.3(e,f).

A second approach to transparency control was investigated by controlling the length of the source MWCNTs prior to the dry-transfer. Figure 4.4 shows optical micrographs of three pre-patterned transferred samples of differing patterned pitch and source MWCNT length. A wide range of a patterns and transparencies are accessible. The sheet resistance (R_s) and optical transmittance (%T) of the thin films were found to be strongly dependent on the length MWCNTs. Figure 4.5 shows the optical transmittance of thin films fabricated from MWCNTs that are <1 μm and up to 500 μm in length. The most opaque and highly conductive films had R_s~1.2 Ω/sq. with ~9 % transparency (550 nm). For equivalent samples, two- and four-probe conductivity measurements yielded R_s ~10.2 Ω/sq. and ~2.6 Ω/sq., respectively, evidencing a low contact resistance of 7.6 Ω/sq. The most transparent films (85 % for MWCNTs <1 μm) had sheet resistances as low as 550-1000 Ω/sq. Reducing the growth time substantially increased the optical transmission whilst only increasing the sheet resistance by

Figure 4.4 | Transparency control and alignment. (a-c) Optical micrographs of Mo-passivated patterned and dry-transferred MWCNT thin films on PET showing controllable transparency by adjusting the length of the source nanotubes.

approximately one order of magnitude (Figure 4.6). This observation can be explained due to the increased number of inter-nanotube junctions for films comprised of shorter nanotubes. The DC conductivity in such films is strongly dependent on tunnelling between individual nanotubes. Consequently the conductivity is critically dependent on the number of conduction pathways, junctions and the network morphology - all of which can are varied by adjusting the length and the degree of alignment of the networks.

The AC sheet resistance was also investigated at microwave frequencies using a technique described by Collier *et al.*[9]. The transmissive sheet resistances, in the 120-175 THz range, was 0.3 and 640 Ω/sq. for MWCNTs 500 μm and 1 μm long, and were broadly consistent with the DC measurements for films of similar optical characteristics, as discussed previously. The films demonstrated opto-electronic characteristics nearing the ITO benchmark and superior characteristics to organics such as enhanced PEDOT:PSS[1, 2]. Note also that the films showed very little colouration, observed quantitatively as a negligible variation in the rate of change of transmission with wavelength, across the entire visible spectrum, when compared to PEDOT:PSS and its undesirable characteristic blue hue, for example.

The degree of alignment of the MWCNTs within the films is considered in Figure 4.7. It was found that, depending on the way in which the forests were rolled, both well-aligned (Figure 4.7(a-d)) and isotropic (Figure 4.7(e,f)) networks could be formed. Extracted Str37 values were approximately 0.26 for the aligned transfers whilst 0.60 for the compressed / isotropic transfers. A possible benefit to such aligned films is in polarisation sensitive electrode materials. Figure 4.7(e) shows a fabricated bilayer of crossed and aligned MWCNT transfers on a PET substrate achieved by two successive transfers of pre-patterned forests.
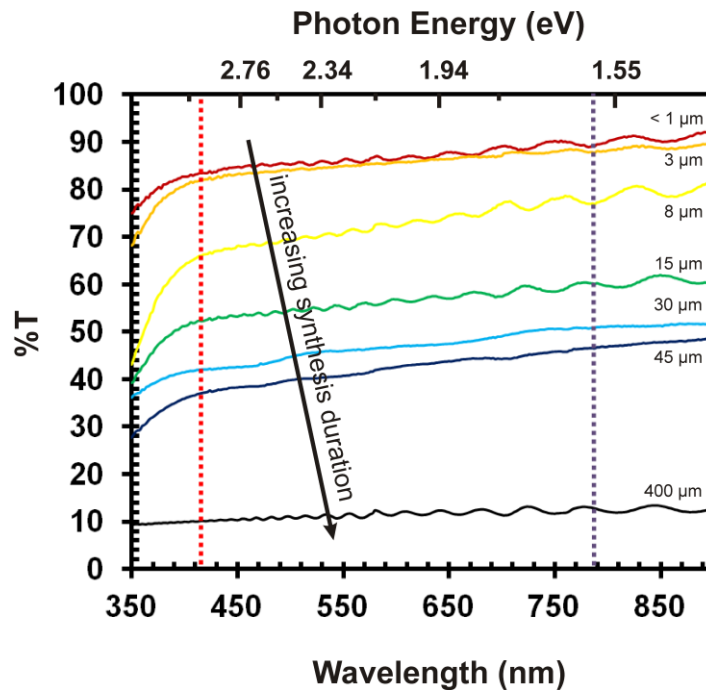
Figure 4.5 | **Optical transmission.** Variation in the UV-Vis-NIR optical transmission of films of dry-transferred MWCNTs of increasing length.

The use of MWCNT thin films as optical polarisation media is discussed in more detail in Chapter VI.

A major drawback to the dry-processing was that for MWCNTs <50 μm long, a self-assembled monolayer (SAM) adhesion promoter (APTES) was necessary to improve the uniformity of the transfer, especially when transferring to ITO, SiO_2 and other natively hydrophobic surfaces. Transfer was successfully demonstrated to natively oxidise (<5 nm) Al foil using a polylysine SAM (Figure 4.3(d)). Prior to SAM treatment MWCNTs did not adhere. Whereas after a dip-exposure (5 min) and N_2 drying, transfers were increased by up to nearly 100 % by area. The SAMs investigated were sufficiently narrow and / or porous to permit significant electrical conduction between the nanotube film and the underlying Al.

Applications of the dry-transferred MWCNTs thin films were then considered. Carbon-based electrodes offer extremely high surface areas which make them functionally desirable for high density energy storage. Because of the binder-less nature, strong surface and inter-tube adhesion without the use of bonding agents, combined with excellent conductivities and alignment make these MWCNT thin films ideal candidates for supercapacitor electrodes. To demonstrate this potential application two-electrode electric double-layer cells (EDLC) were
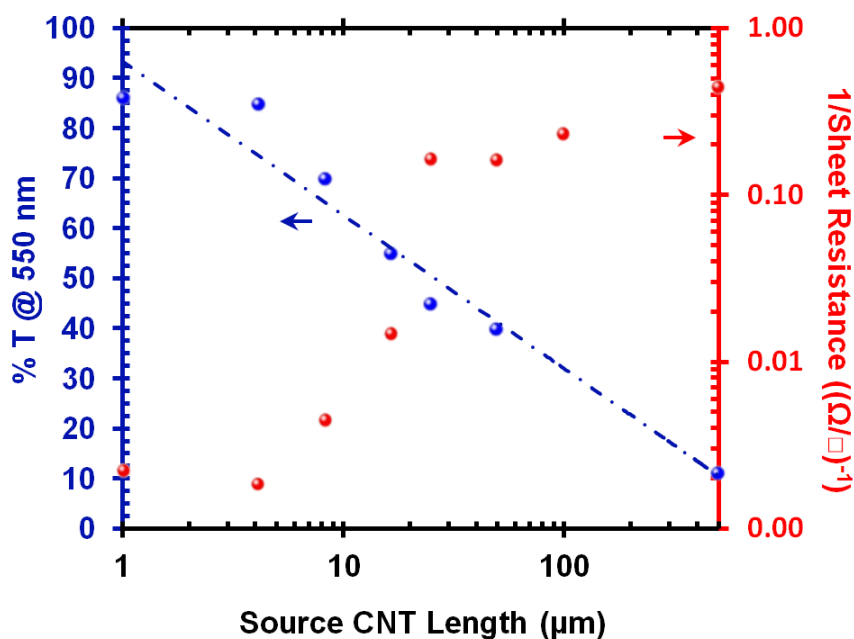
Figure 4.6 | **Sheet resistance and optical transparency as a function of MWCNT length.** Variation in 550 nm transmission and sheet conductance as a function of nanotube length.

constructed. The EDLCs electrodes were fabricated from the dry-transferred MWCNTs.

The EDLCs were constructed by transferring aligned MWCNTs of varying lengths onto PET substrates, as before. Given the film's high conductivity the MWCNTs functioned as both the active material and charge collector, reducing the overall material requirements and therefore increasing the weight fraction of active material in the device. The final devices were 10 mm x 10 mm (insert Figure 4.8). An insulating porous separator (Celgard 2500) soaked in electrolyte (1M Tetraethylammonium tetrafluoroborate (Et_4NBF_4) in propylene carbonate, Sigma-Aldrich) was then sandwiched between two MWCNT electrodes. Al tape was used to externally contact to the EDLC. Three different films comprised of different MWCNT lengths were tested; 1 min (MWCNT length 28.5 μm, active weight 0.6 mg/cm^2), 5 min (96 μm, 1.1 mg/cm^2) and 10 min (235 μm, 2.3 mg/cm^2). The electrochemical characteristics of the EDLCs where obtained by cyclic voltammetry (50 mV/s) and by galvanostatic charge/discharge (1 mA/cm^2), measured with an Autolab PGSTAT302N potentiostat.

As expected thicker films offered higher conductivities and longer nanotubes showed a higher capacitance per unit area as well as a lower equivalent series resistance (ESR), both of which are essential for high power delivery. The capacitance of the two-electrode nanotube

Figure 4.7 | MWCNT alignment. (a,c) SEM micrographs of the polarisation selective partially transparent electrodes. **(b,d)** Str37 analysis quantifying the alignment of the vertical (0.22) and horizontal (0.29) transfers, compared to **(e,f)** the unaligned compressed film (0.60). **(g)** SEM micrograph of crossed-transfers on a single untreated PET substrate. Arrows denote the transfer direction.

Figure 4.8 | Flexible dry-transferred MWCNT supercapacitor. Structure using a Celgard 2500 porous separator soaked in Et_4NBF_4. **(a)** Cyclic voltammetry for aligned MWCNT electrodes synthesised for *(1)* 10 min, *(2)* 5 min and *(3)* 1 min. The *insert* shows a fabricated device under flexing. **(b)** Schematic of the supercapacitor structure.

EDLCs was estimated to be between 6 and 17 F/g from the cyclic voltagrams (Figure 4.8) and the charge/discharge curves from cells charged to 1 V. This is roughly twice the capacitance reported for sprayed SWCNT devices under similar experimental conditions[10]. The ESR decreases with increasing film conductivity and ranges from 1000 Ω (1 min) to 44 Ω (10 min), values showing good agreement with the R_s estimates made previously. Although the overall ESR is still somewhat higher than expected, this is attributed to the resistive contact at the Al-CNT interface.

Electrodes of greater active weight increased the energy density allowing the active material to occupy high ratios of the volume and weight. However, such advantageous features are often offset by higher ion diffusion barriers in the inner regions of the electrode, resulting in higher internal resistance and consequently reduced high-power performance. This factor limits the practical thickness of any nanostructured electrode. Thus, ideally a thick electrode that possesses both high capacitance and that is operable at high power is desired. For the thicknesses studied, approximately constant power densities are observed (2.48 kW/kg), indicating that good permeability is maintained even for the thickest electrodes. The results demonstrated that the MWCNT electrodes are an excellent potential material for compact, high-power delivery and high-energy-density storage.

4.2 Opto-Electronic Performance of Dry-Transferred MWCNTs & Hot-Press Laminated Graphene

Although the MWCNTs considered above offered high conductivities they are of limited use in many applications because of their relatively low optical transparency. Graphene offers an extremely transparent alternative. It absorbs only 2.3 % (per layer) uniformly across the visible spectrum[11]. Consequently, an extremely wide range of conductivities and transparencies are accessible by the correct use of the CVD nanocarbons.

Carbon nanotubes and graphene are well suited for transparent flexible electronics for largely different regions. CNTs are not transparent and films formed from them are, in the limiting case at least, formed from a large number of overlapping rods which move freely and dynamically when mechanically strained. These percolative networks are very similar in morphology to Ag nanowire networks and even (in the most abstract sense) crossed electrode lines of PVD deposited metals, not unlike those one would normally find in any computer display. It is these voids that render CNT thin films transparent. ITO, PEDOT:PSS and graphene on the other hand are optically transparent materials and require no porosity to achieve this and are, in essence, solid. Evidently one would expect extremely different opto-electronic, transport and flexing performance from the nanotube and graphene. To investigate this, a dry-process was developed based on cold-wall CVD synthesised hot-press laminated graphene (HPLG) for comparison with the dry-transferred MWCNT films.
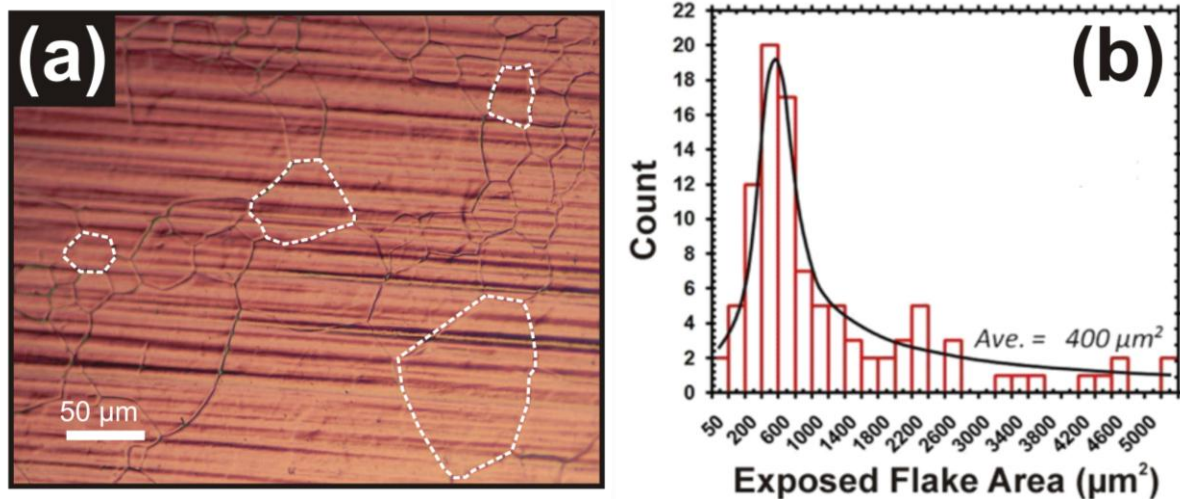
Figure 4.9 | Cu grain size post graphene growth. (a) Optical micrograph of the Cu-supported graphene with select grains highlighted (Scale bare: 50 μm). **(b)** Histogram of graphene flake size determined by considering the apparent flake size in optical microscopy after graphene growth at 1000°C using 1000 sccm H_2 / 35 sccm CH_4.

Graphene was grown by metal-catalysed thermal CVD using 25 μm Cu foil (99.999% Alfa Aesar). Foils were degreased in acetone and isopropanol baths and loaded into an adapted AIXTRON Black Magic CVD reactor. The chamber was evacuated to <10^{-3} mbar and pump-purged in triplicate under 1000 sccm N_2. Nitrogen was terminated and the chamber backed to <10^{-3} mbar. 1000-sccm-H_2 was introduced and stabilised at 10 mbar whilst the low-mass heater was ramped at 150°C/min to 1000°C to anneal the foils for 300 s. Hydrogen was reduced to 100 sccm during the thermal ramp and methane (35 sccm CH_4) was introduced to initiate growth. After 300 s, CH_4 was terminated whilst maintaining the H_2 (*a*-C etchant) flow allowing the stage to controllably cool at ~ 50°C/min until it was at a temperature <500°C. Hydrogen was terminated and the chamber flooded with 1000 sccm N_2 until a temperature <200°C at which point the samples were unloaded. Temperatures were measured using two independently mounted type-K thermocouples and a surface focused IR interferometer. Figure 4.9(a) shows a typical optical micrograph of the Cu grain distribution following CVD graphene growth. Cu grains are nominally between 10-100 μm in diameter and had a mean area of 400 $μm^2$ (Figure 4.9(b)).

Figure 4.10 illustrates the hot-press lamination process. Bae *et al.*[12] were the first to demonstrate a similar process. The as-grown conformally coated Cu/graphene is first passed through a hot-press laminator (~120°C) where two polymer sheets are bonded to the sample. One side of the polymer is mechanically removed, which in doing so partly removes the
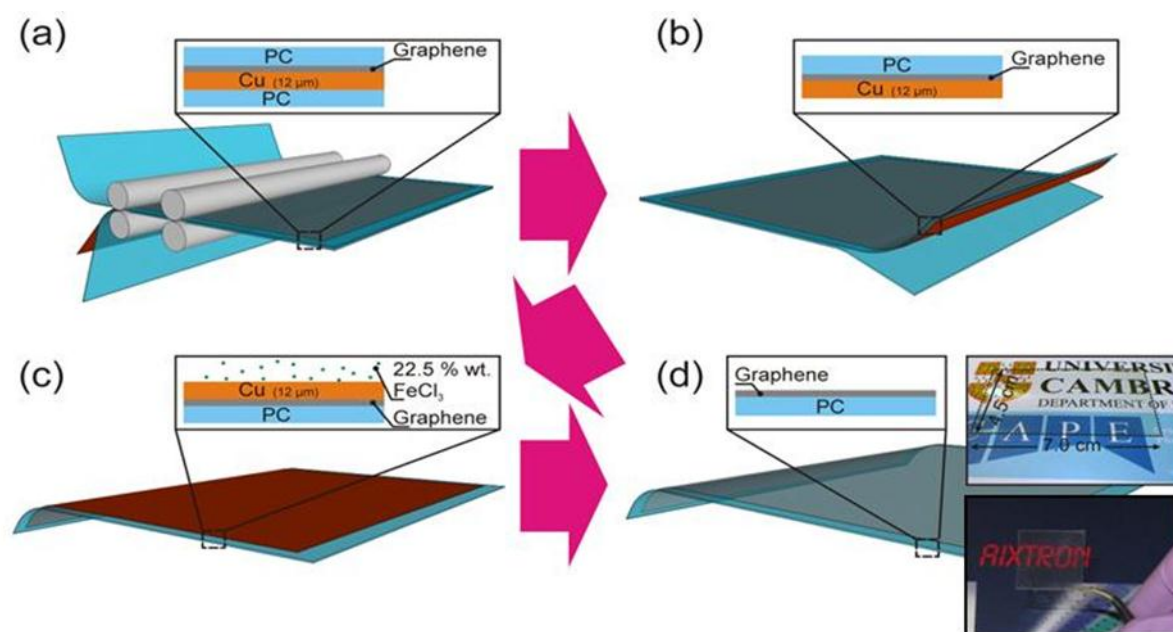
Figure 4.10 | Hot-press laminated graphene fabrication. (a) Graphene growth by Cu (foil)-catalysed CVD and hot-press lamination. **(b)** Removal of the backside polymer support. **(c)** Cu etching by 22.5 wt.% ferric chloride (FeCl₃). **(d)** The remaining TFCs. *Inserts:* Optical micrographs of typical HPLG samples.

underside graphene layer which exposes the Cu substrate. The Cu is then etched by bathing the samples in 22.5 wt.% ferric chloride ($FeCl_3$) for up to 5 h[13] whilst gently agitating the solution to prevent colloids settling. The presented transfer has been demonstrated on graphene grown on both Cu foils and PVD deposited Cu thin films on Si/SiO₂. The inserts of Figure 4.10(d) show optical micrographs of typical TFCs with areas up to 31 cm². The attainable area is limited by the size of the CVD reactor not the transfer process. Stylus profilometry (Dektak 200-Si) revealed typical surface roughness of the order of 1.8±0.4 µm, most of which is solely attributed to the substrate roughness.

Figure 4.11 shows Raman spectra (~5 mW, 457 nm) of the Cu-catalysed CVD graphene *in-situ* on the Cu growth substrate. Second-order polynomial fits have been subtracted to remove the high-wavenumber fluorescence associated with the substrate. The D, G and 2D peaks are at ~1382.5±6.9 (S.D) cm⁻¹, 1581.1±31.9 cm⁻¹ and 2762.9±10.7 cm⁻¹. The 2D-to-G intensity ratio can be used to infer the number of graphene layers[14-17] and was found to be 0.99±0.17 suggesting a bilayer material[18]. Indeed, the 2D-peak can be well fitted, given the noise floor of the spectrometer, with four Lorentzians, with a full-width half maximum of 50.5±7.1 (S.D) cm⁻¹, further supporting the presence of either bilayer or non-interacting few-layer graphene[19]. Raman data suggests flake sizes of 40-100 nm[20]. To validate the uniformity,
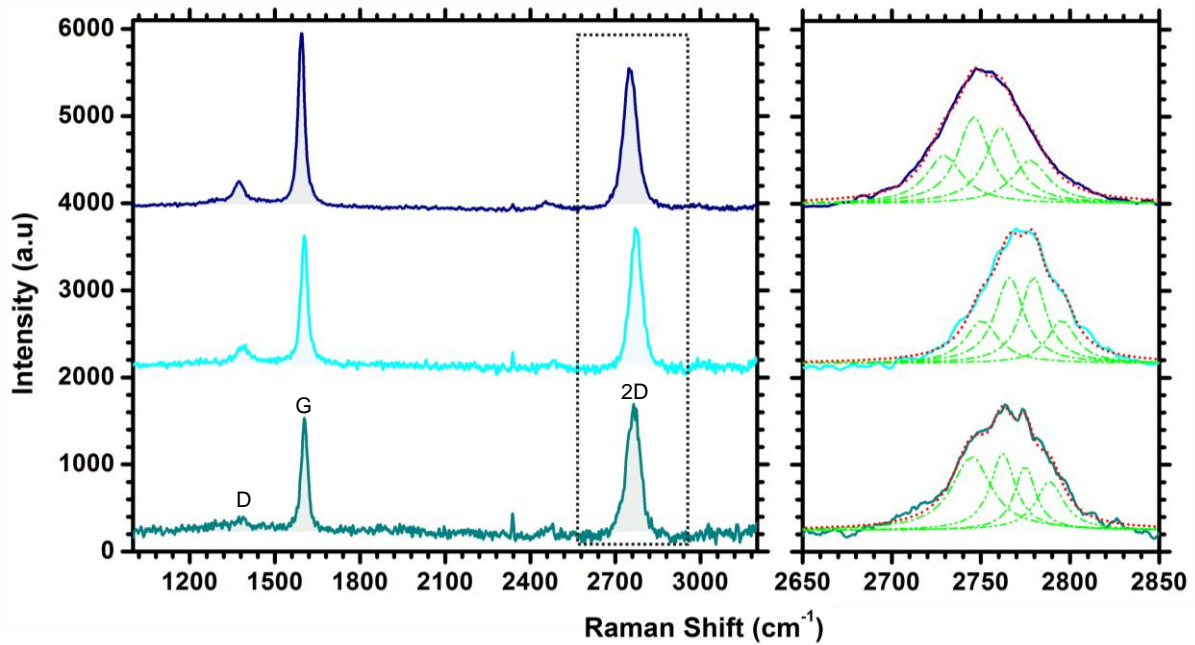
Figure 4.11 | Discrete Raman spectra. 457 nm Raman spectra of Cu foil catalysed graphene. Four-fold Lorentzian fitting to the 2D peak indicating bilayer *(right)*.

Raman mapping was employed. Cu-catalysed graphene was polymer-transferred[13] to Si/SiO_2 (300 nm) substrates and inspected using an In-Vie Renishaw Raman spectrometer fitted with a piezo-stage using 633 and 532 nm excitations with a spot size of ~1 μm. The I_D/I_G and I_{2D}/I_G Raman maps, of PMMA-transferred samples, are illustrated in Figure 4.12. Note that the D peak intensity is inversely proportional to excitation energy in graphitic materials[21-24], whereas the G and 2D peaks are largely independent of excitation energy[25, 26]. Thus 532 nm and 633 nm excitations were measured in order to give a clearer indication of the graphitic quality and layer number. The apparent reduction in quality, inferred from the D/G ratios (Figure 4.12(a,c)) is simply an artefact of the measurement procedure. *In-situ* (on the Cu) spectra (Figure 4.11) are more likely to give a realistic account of the actual graphitic quality and layer number as the as-grown graphene has not been altered in any way. It is quite possible that the etching and transfer processes have induced additional disorder. As illustrated in Figure 4.12(a,c), the D/G intensity ratios are consistently <0.4 across crystals with an approximate size of 125 μm^2. Indicated, Figure 4.12 suggests a mean I_D/I_G ratio of 0.41-1.3 (532-633 nm) and I_{2D}/I_G of 1.3-2.2 (633-532 nm) which shows modest agreement with the discrete *in-situ* measurements in Figure 4.11. The layer number is relatively uniform (Figure 4.12(d)) with ~78.9% (by area) having an I_{2D}/I_G ~1.5-2 (3-4 layer), ~14.2% with ~1 (bilayer) and ~6.9% with < 1 (monolayer).
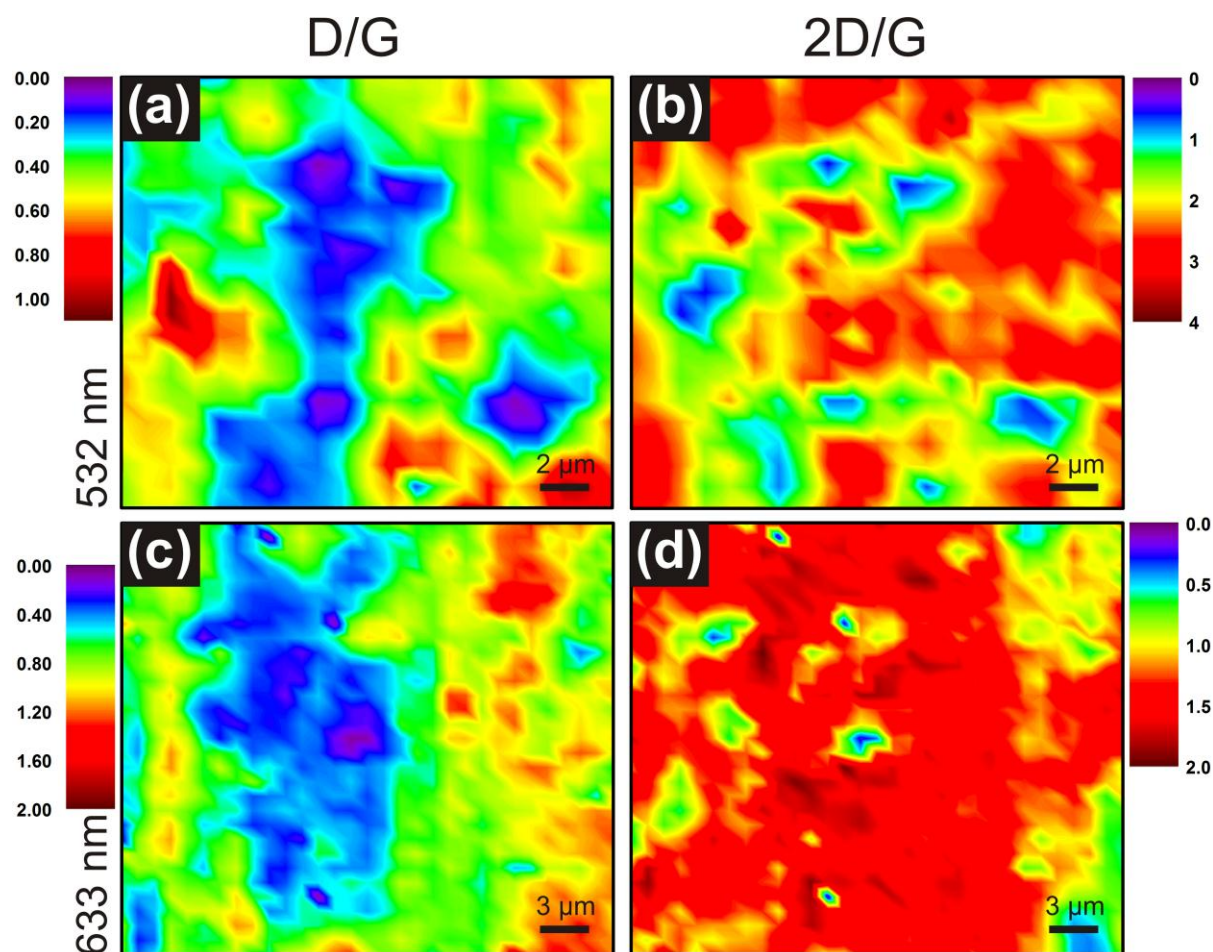
Figure 4.12 | Graphene uniformity. 532 nm and 633 nm Raman maps of the **(a,c)** I_D/I_G and **(b,d)** I_{2D}/I_G ratios for samples transferred to Si/SiO$_2$ (300 nm).

The UV-Vis-NIR spectrum of the as-received polymer substrate and the substrate with the transferred HPLG is given in Figure 4.13(a). The HPLG absorbs ~4.5% uniformly throughout the optical window supporting the bilayer conjecture. To independently verify the Raman and UV-Vis-NIR data, as-grown graphene was transferred to TEM grids and select area electron diffraction (SAED) patterns were recorded (Figure 4.13(b)) using a FEI Philips Tecnai operated at 200 keV where the SAEDs were assessed relative to a thallium chloride calibration standard. Weak patterns from the supporting grid and residual organics are present. Six-fold symmetry, characteristics of the graphites and graphenes, is clearly seen[27-29]. It is possible that the multiple, unassigned spots are associated with turbostratic alignment though possible film discontinuity makes verification of this difficult. Certainly the $\overline{1}010$ to $\overline{2}110$ intensity ratio ($I_{\overline{1}010}/I_{\overline{2}110}$), given in the insert of Figure 4.13(b), deviates somewhat from the more traditional A-A or A-B (Bernal) stacked intensity ratio and suggests this to the case[30-32].

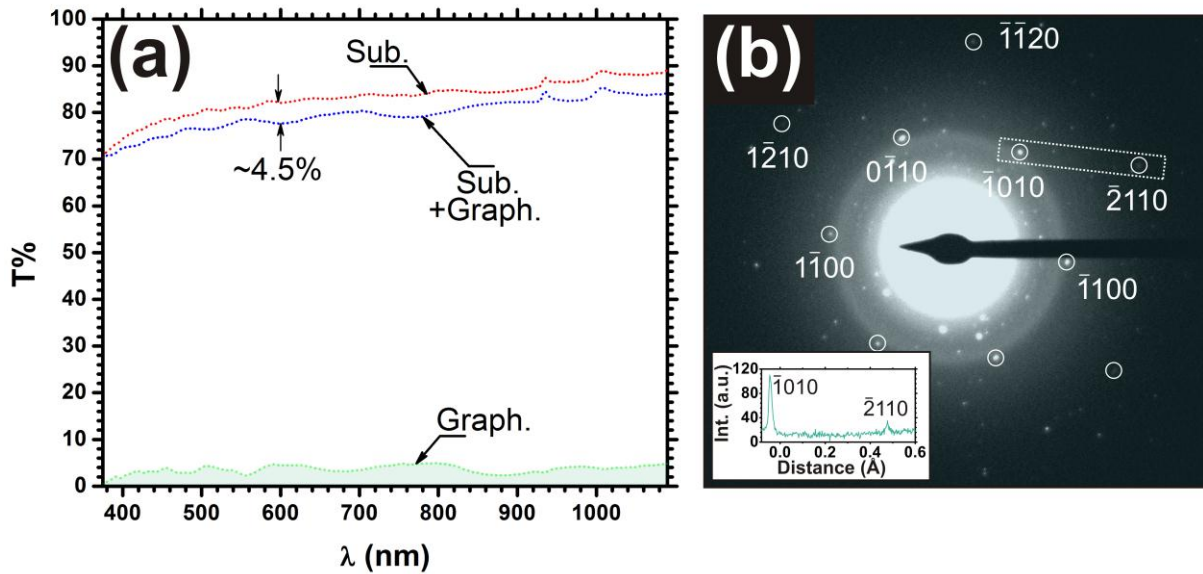**Figure 4.13 | HPLG crystallographic characterisation. (a)** UV-Vis-NIR optical transmission of the as-received polymer substrate (Sub.) and the graphene coated substrate (Sub.+ Graph.). The green "Graph." curve is the absorption for the as-received substrate transmittance subtracted from the substrate and graphene sample. **(b)** SAED pattern. *Insert:* Intensity (I) of the -1010 and -2110 peaks showing deviations from the typical intensity $I_{-1010} < I_{-2110}$ relation for A-A and A-B (Bernal) stacked bilayer graphene.

By way of comparison, solution-processed vacuum filtrated disordered MWCNT thin films were fabricated, as discussed in more detail in Chapter IV, using the same source MWCNTs as the dry-transferred thin films. For completeness, CVD graphene films were also transferred using heat-release tape[33, 34].

Figure 4.14(a) shows the optical transmission of the dry-transferred and vacuum filtrated MWCNTs, HPLG and heat release tape graphene, commercial ITO and commercial PEDOT:PSS. Substrate effects have not been subtracted. Figure 4.14(b) shows the corresponding optical transmission (at $\lambda=550$ nm) as a function of sheet resistance (R_s) for the previously stated thin films in addition to Ag NW networks[3]. The vacuum-filtrated networks, although comprised of equivalent MWCNTs as the dry-transferred films, showed a marked difference in their conductivity with elevated R_s for a given optical transmittance. Aggressive ultrasonication, the introduction of surfactants and disordered network morphology have all, most-likely contributed to a reduction in conductivity. Whether this reduction is simply attributed with the alignment or chemical processing is unclear. However, EDX and Raman analysis showed minimal variation in chemical content and negligible reduction in the degree
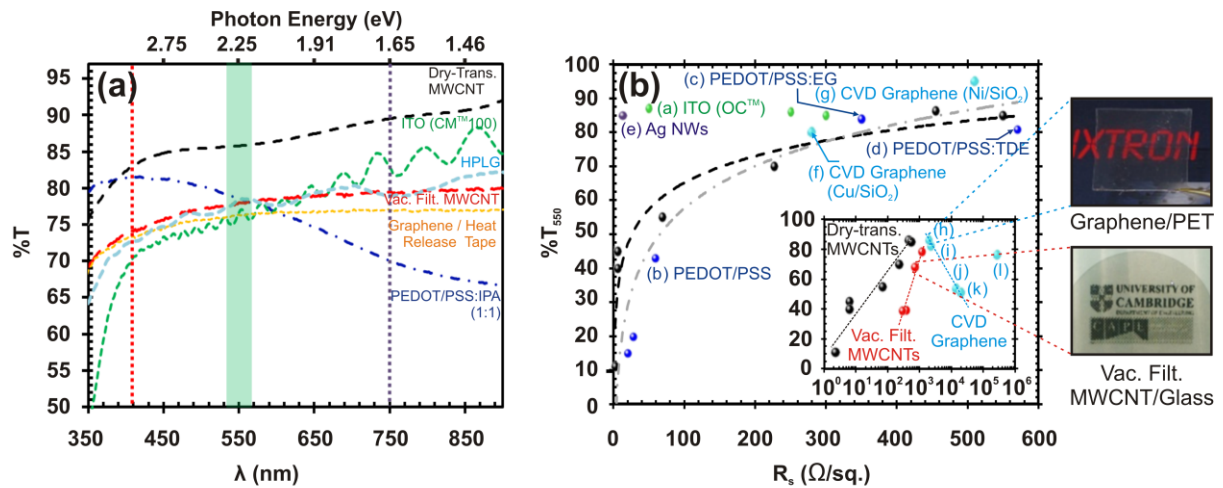
Figure 4.14 | **Opto-electronic comparison. (a)** Comparative UV-Vis spectra and **(b)** 550 nm optical transmission against sheet resistance of dry-transferred MWCNTs, ITO, vacuum filtrated (MCE) MWCNT film, HPLG and PEDOT/PSS:IPA. *Insert:* log-scale variation of dry-transferred MWCNT, MCE and graphene (HPLG and tape transfer) films. **(b)** Comparative sheet resistance (R_s) versus optical transmission at 550 nm (%T_{550}) of; **(a)** ITO (CPFilm OC^{TM}), **(b)** PEDOT:PSS[1] and **(c)-(d)** (poly)ethylglycol (PEG) and 2,2′-thiodiethanol (TDE) enhanced PEDOT:PSS[1, 2], **(e)** Ag NWs[3], **(f)-(g)** hot-press laminated graphene (this work), MCE networks (this work) and dry-trasnferred MWCNT films (this work). Eq. (3.1) fit (grey dot-dash) yields (σ_{opt}/σ_{dc})=1.7x10^{-1}. Graphene samples were transferred by hot-press lamination to PET from **(h)-(i)** 25 μm, **(j)** 100 μm, and **(k)** 127 μm source Cu foil. Graphene **(l)** was transferred from 900 nm electron beam evaporated Cu on SiO$_2$ by thermal release tape (Nitto Denko).

of graphitisation suggesting that it is most likely the network morphology that dominates. Increased interface densities increases the effective contributions from the junction resistance, which dominates the macroscopic transport behaviour in such low-dimensional nanostructured films.

The sheet resistance and optical transmission are related by[3, 35, 36];

$$T = \left[1 + \left(\frac{tZ_0}{2}\right)\sigma_{opt}\right]^{-2} = \left[1 + 188.5\frac{1}{R_s}\left(\frac{\sigma_{opt}}{\sigma_{dc}}\right)\right]^{-2} \qquad (3.1)$$

Where t is the film thickness, Z_0 is the impedance of free space (377 Ω), σ_{opt} is the optical conductivity, and σ_{dc} is the direct current electrical conductivity. A technologically viable transparent electrode must demonstrate low R_s and high T throughout the optical window, and for an ideal transparent conductor, (σ_{opt}/σ_{dc})→0. Fitting Eq. (3.1) gives (σ_{opt}/σ_{dc})=1.7x10^{-1} and 7x10^{-1} for the MWCNT thin films and HPLG. By comparison, (σ_{opt}/σ_{dc})=9.1x10^{-2} and 4.5x10^{-3} for graphite and current driven applications. The minimum industry standard for (inflexible) display TCOs requires 2.9x10^{-2} (>90% for <100 Ω/sq.)[35, 37]. Evidently the conductance ratio is someway off the TCO standard but is nevertheless close to the state-of-the-art for thin films
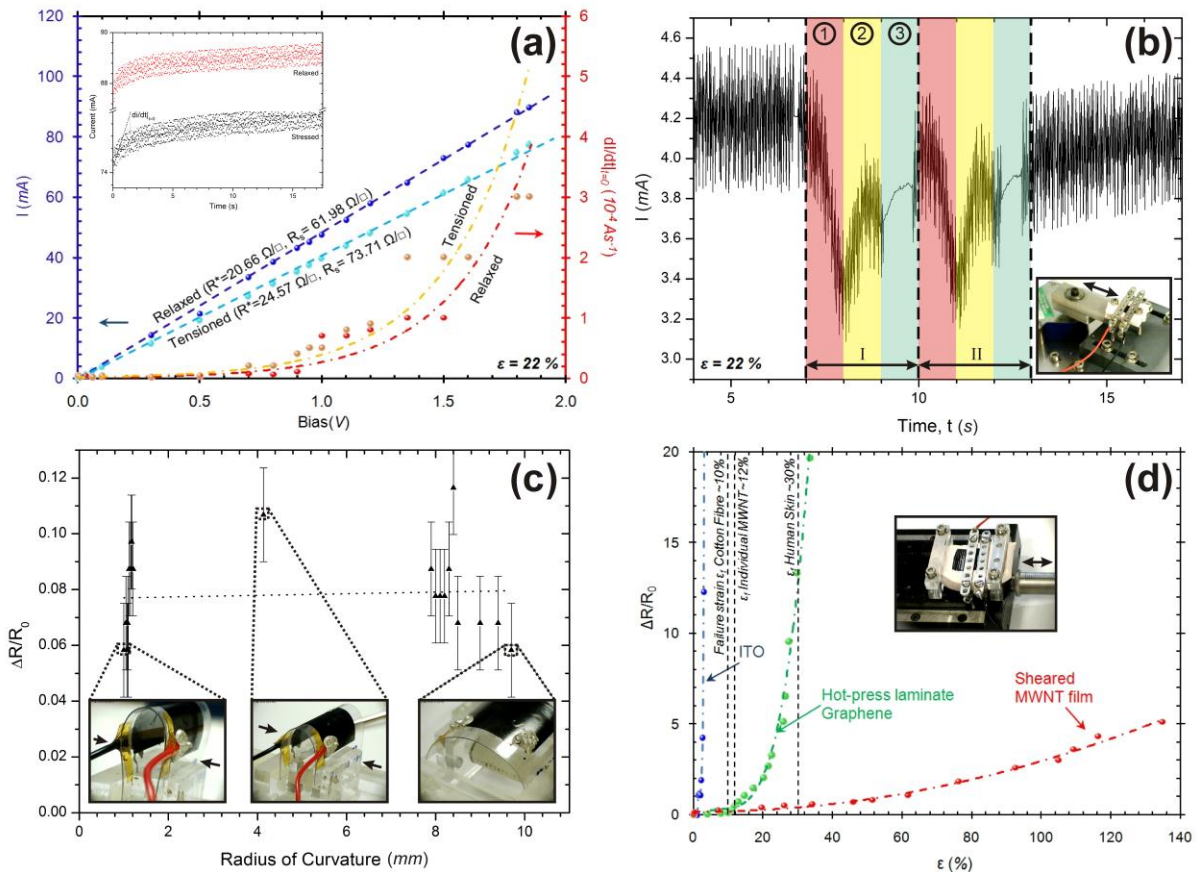
Figure 4.15 | **Flexing performance. (a)** *I-V* response of a dry-transferred MWNT film. *Insert:* typical relaxed and stressed response (1.8 V) highlighting significant heating (Initial gradients evaluated from logarithmic fit). **(b)** Detail of two stress-relaxation cycles; (1) indicates the tensioning process, (2) the relaxation phase and (3) a low-noise condition primarily attributed to film relaxation. *Insert:* Optical micrograph of the measurement system. **(c)** Variation in sample resistance as a function of the radius of curvature. *Insert:* Optical micrographs taken during a typical measurement. **(d)** Effects of uniaxial strain on nominally-relaxed normalised sample resistance ($\Delta R/R_o$) for ITO, HPLG and the dry-transferred MWNT films. Failure strains of human skin, cotton fibre and an individual MWNT are shown for comparison.

prepared from chemically modified graphene[35]. Nevertheless, for next-generation applications flexibility must be critically considered.

4.3   Flexing Performance & a TFC Figure of Merit

The uniaxial mechanical strain response of ITO/PET, HPLG and dry-transferred MWCNTs were measured using a custom-built motorised system attached to a Keithley source-measure unit and connected to a LABVIEW controlled computer interface. Experiments were performed at room temperature and pressure. Samples were contacted using mechanical clamps and conductive epoxy, as shown in the insert of Figure 4.15(b).

The maximum uniaxial tensile strain (ε) of commercially available ITO was found to be ~1.2%. HPLG samples failed at ~15% and showed excellent correspondence with the theoretical values for single flake failure[38, 39]. Interestingly, the dry-transferred MWCNT thin films withstood up to 140% strain (the limit of the apparatus) with only a modest reduction in conductivity ($\Delta R/R_o$~5, where R_o denotes the relaxed resistance). Indeed, Liangbing *et al.*[40] reported similar exceptional performance for SWCNT thin films. Graphene, although having excellent optical transparency, as discussed above, offers reduced flexibility compared to the MWCNT films. The graphene network failed via the formation of inter- or intra-flake discontinuities, whereas the MWCNT networks became increasingly aligned before the MWCNT themselves observe any significant strain. Consequently high failure strains are possible owing to the networks porosity and anisotropy.

To further investigate the intriguing high-failure strains of the dry-transferred MWCNT networks, dynamic studies were performed, the key features of which are summarised in Figure 4.15(b). Here the silicone-supported samples were strained to 22% repeatedly and the current monitored for a fixed bias at a flexing frequency of 0.4 Hz. Measurement noise is attributed to mechanical interactions between the film and the contacts. Interestingly, this noise was repeatedly passivated in region 3 of the strain cycle (Figure 4.15(b)). The exact reason for this in unclear, though it may pertain to the nominally relaxed state of the film. The insert of Figure 4.15(a) shows the current response for a relaxed and strained film and the corresponding I-V characteristics. Figure 4.15(a) also plots the rate of change of current with time (evaluated at t=0 s) after the bias was applied. This charging type artefact is attributed to the presence of substantial numbers of inter-tube junctions. When the sample is tensioned the rate of change of current with time at t=0 s increases for a given potential indicating an increase in the number, or length of inter-tube junctions. For a bias >1.5 V, the relaxed sample showed a $di/dt|_{t=0}$ ~10^{-4} A/s which increased to 1.7×10^{-4} A/s for 22% tensioned films. Figure 4.15(a) also shows evidences the minor increase in the total resistance (i.e. contact resistance + bulk resistance) from 62 Ω in the relaxed state to 74 Ω in the tensioned state.

To further consider the flexing behaviour of the dry-transferred MWCNTs the effect of the radius of curvature was investigated, as shown in Figure 4.15(c). Electrical contacts were made using Ag-loaded epoxy. The inserts of Figure 4.15(c) show optical micrographs during

a measurement. Measurements were acquired from the relaxed state to the strained state. Across a bend radius of 1-10 mm the measured films showed extremely low, and predominately uniform, $\Delta R/R_o$ of ~0.75.

Evidently the flexing performance of the dry-transferred MWCNTs and HPLG thin films outperform those of ITO. In multi-functional, flexible transparent and conducting materials a more suitable figure of merit (FoM) should take into account the materials macroscopic flexibility. Most studies have focused exclusively on the (σ_{opt}/σ_{dc}) FoM. However, although ITO performs extremely well in this sense, its flexibility performance is rather poor, as evidenced. Consider a flexible-transparent-conductor specific FoM, given by;

$$\gamma\mid_{\frac{\sigma_{opt}}{\sigma_{dc}}} = \left(\frac{\sigma_{opt}}{\sigma_{dc}}\right) . \left(\partial\left(\Delta R / R_o\right)\Big/\partial\varepsilon\Big|_{\varepsilon=0}\right) \tag{3.2}$$

($\Delta R/R_o$) is typically related to ε via an $A\exp(B.\varepsilon)$ type relationship, where A and B are constants. Thus ($\partial(\Delta R/R_o)/\partial\varepsilon|_{\varepsilon=0}$)=AB. For the ideal transparent conductor (σ_{opt}/σ_{dc})→0 and ideal flexible conductors $\partial(\Delta R/R_o)/\partial\varepsilon|_{\varepsilon=0}$→0. Thus for the ideal transparent flexible conductor equation (3.2) gives a FoM of $0|_0$, where the first term accounts for the entire three-dimensional metric and the second simply on the conductance ratio. For ITO, HPLG and dry-transferred MWCNTs $\gamma|_{\sigma_{opt}/\sigma_{dc}}$ were $0.004|_{0.03}$, $0.010|_{0.7}$ and $0.001|_{0.17}$, respectively. The combined FoM shows that although ITO has an extremely impressive conductivity ratio, the exceptional flexing performance and robust nature of the dry-transferred MWCNT thin films offer the highest performance. HPLG fails on both the conductivity ratio and flexing and will only be improved through doping and other routes to increase its conductivity.

4.4 Macroscopic Transport & the Implications of Disorder

In this section comparisons are drawn between the transport properties, and their relation with the degree of disorder, for the nominally metallic HPLG and dry-transferred MWCNT thin films developed above. Understanding the macroscopic electronic transport in discrete networks is perhaps more important than understanding the properties of the single nanotube and graphene flakes as most, if not all, engineering applications will ultimately employ macroscopic quantities rather than single nanoscopic entities.

50-nm thick aluminium contacts were deposited onto HPLG samples and sparsely aligned dry-transferred MWCNT thin films. In the case of the MWCNT samples probes were patterned either parallel or perpendicular to the nanotubes long-axes (Insert Figure 4.16(a,c)). Measurements were performed in a custom-built evacuated ($<10^{-5}$ mbar) cryostat using a Keithley 236 source-measure unit, controlled by a LABVIEW user interface via a BLP1.9 low-pass filter. Temperature control was achieved using a cryo-cooler (He working fluid) to control the temperature from 297 K to 15 K. Samples were heated using a resistively heated element and monitored using a locally-bonded thermometer in a specifically built copper enclosure. Low-temperature (4 K) random telegraph signal (RTS) events were measured using a sister system with devices directly immersed in liquid He and liquid N_2 baths. Figure 4.16 shows the resistance (R) of the measured samples as a function of temperature (T).

The presented data are typical of near-zero band gap, nominally metallic nanocarbons[41]. Note, sample resistance, rather than resistivity were considered due to conversion issues such as estimating sample cross-sectional area, etc. Multiple gradients in the resistance (R)-temperature (T) plot account for distinct activated transport mechanisms, and were similarly observed, though perhaps to a slightly lesser extent, in the studies of Matsubara *et al.*[42] for highly orientated pyrolytic graphite (HOPG). They developed models based on stacking-fault tunnelling and charge transfer by impurity-assisted hopping and thermal excitation across low-fault potential barriers. Nevertheless, the presented data deviate somewhat from these simple models. The most striking difference is the $\sim T^{-1/2}$ trend occurring between 200-300 K. A large numbers of electrons, or high mobility charge carriers, freeze out at T<200 K, leaving a localised population. This subsequent charge carrier population dominates the transport. This non-uniform density of states, as depicted in the insert of Figure 4.16, may possibly give
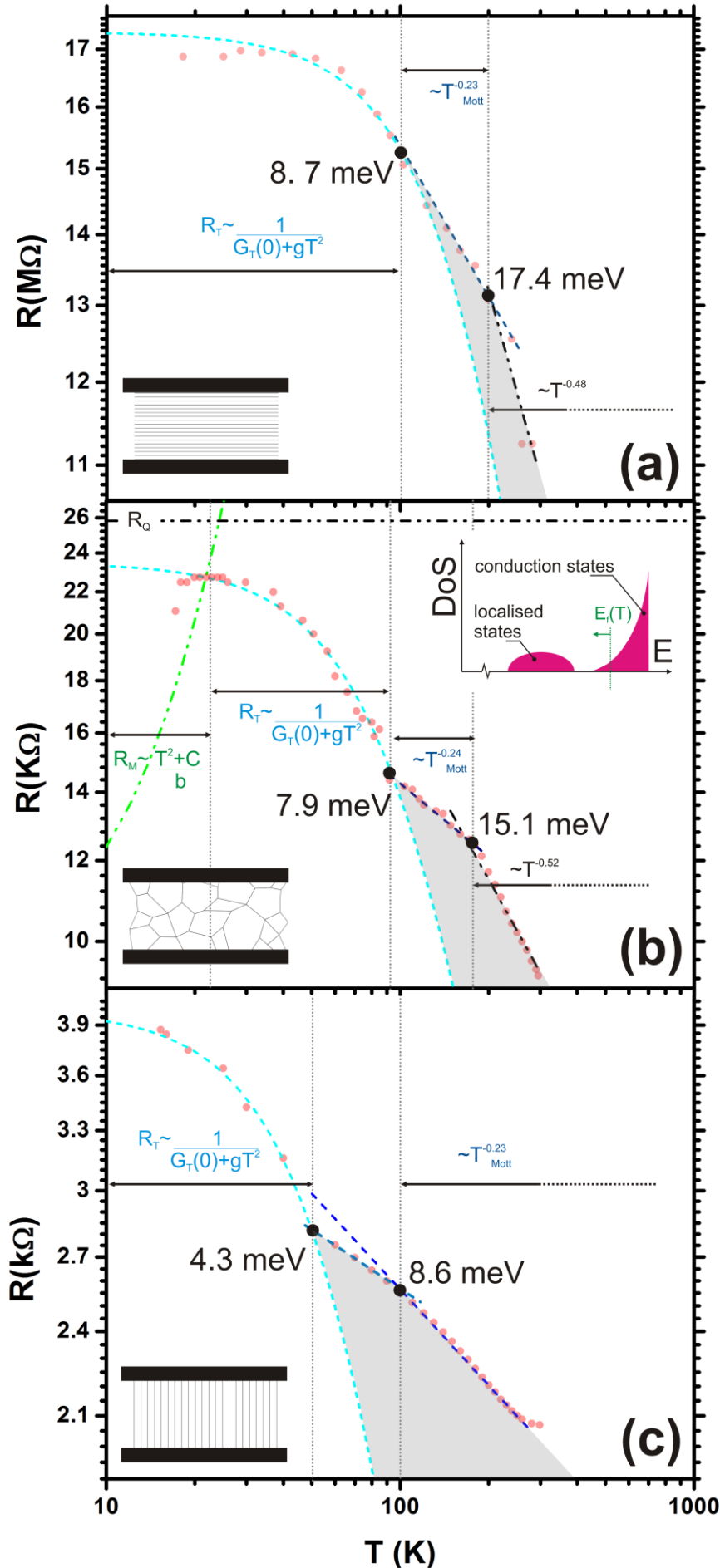
Figure 4.16 |
Macroscopic transport.
Temperature (T) dependence of the sample resistance (R). The *Inserts* illustrate the geometry of the electrodes in relation to the MWCNT and HPLG channels. R-T plots for **(a)** electrodes patterned parallel to the long axes of sparse dry-transferred MWCNTs. **(b)** Hot press laminate graphene channel. R_Q denotes the quantum resistance $\sim e^2/h \sim 28.5$ kΩ. *Insert:* Illustrative non-uniform density of states (DoS), as a function of energy (E), showing localised and conducting states that may account for the high-temperature $T^{-1/2}$ regime. **(c)** R-T for electrodes patterned perpendicular to the long axes of sparse dry-transferred MWCNTs. 3D-Mott variable range hopping ($\sim T_{Mott}^{-1/4}$), tunnelling and metallic contributions are shown in navy, blue and green, respectively.

rise to both localised and conducting states that are accessed across distinct temperature ranges.

The measured transports characteristics are non-trivial. Though multiple mechanisms clearly dominate the transport particular features are consistent between the samples. The considered thin films are formed from ensembles of discrete low-dimensional nominally metallic units, and as such significant tunnelling contributions are expected. Indeed, tunnelling conductance, of the form $R_T(T)=(G_T(0) + gT^2)^{-1}$, where $G_T(0)$ is the zero-temperature saturation conductance and g is a barrier, geometry dependent, constant[43], appears to fit well within particular temperature ranges. To account for the low-temperature (<15 K) reduction in resistance, specifically in the case of HPLG samples, a parallel metallic contribution is necessary (Figure 4.16(b)). For sub-100 K temperatures, a *c*-axis model is proposed based on tunnelling superimposed with a spatially limited semi-metallic conduction term, possibly due to a series of overlapping defects at grain boundaries and nanotube interfaces. Activation temperatures (energies) are intimately related to the network morphology. Thus, the metallic component may not be absent in the MWCNT networks, but rather it is accessed at a lower energy range (<15 K). It is reasonable to assume that this metallic (phonon-limited) contribution is similar to that in single-crystal graphite given the resemblance in the carrier and phonon densities[43] and that this mechanism, associated with the existence of extended states, can be quantified by $R_M(T)=(T^2+c)/b$ where b and c are temperature invariant fitting parameters. $R_T(T)$ and $R_M(T)$ are shown in Figure 4.16. The parallel, HPLG and perpendicular where fitted ($G_T(0)$ and g) in the tunnelling regime with 5.8×10^{-8}/ 4.3×10^{-5}/ 2.5×10^{-4} Ω^{-1} and 7.6×10^{-5}/ 3.0×10^{-9}/ 4.2×10^{-8} $K^{-2}\Omega^{-1}$, respectively, which when rescaled to their non-specific forms correspond to within an order of magnitude with the HOPG data of Uher *et al.*[43].

Although tunnelling appears to play a key role throughout, it does not account for the complete observations. Both the graphene and, to a greater extent, the MWCNT films are characterised by their large numbers of interfaces and their degree of disorder. Such interfaces, or crystal boundaries, can be described in terms of dislocations. Interfaces can be highly reflective and may impede *c*-axis charge carrier motion[44]. For sufficiently large barriers, charge carriers may become localised to a few dominant conduction pathways. If so, the behaviour would be characterised by phonon-assisted variable range hopping. Indeed, this

appears to be the case. Tunnelling evolves into 3D Mott variable range hopping transport with a characteristic $T^{-1/4}$ dependence. Efros-Shklovskii (ES) ($T^{-1.2}$) / Mott ($T^{-1/4}$) crossovers have been observed for discrete, nanoscale and nanotube systems elsewhere[45, 46]. Similar transitions are observed given that the ES-type behaviour is intrinsically accommodated by the proposed tunnelling model. For Mott, the conduction electrons tend to localise in individual elements, where the term elements, herein, pertains to individual nanotube, nanotube bundles or graphene flakes. In an ensemble of elements, conduction takes place by electrons hopping between elements. Tunnelling dominance increases with increasing network disorder. This dominance is characterised by an increase in the transition temperature (R_T to T_{Mott}), as denoted by the transition energies in Figure 4.16. Note also that the degree of disorder is intimately related to the junction number. Resistance rapidly increases as the number of inter-element junctions increases (with disorder).

RTS events were also observed, at 4 K, in all cases. RTS events are typically only visible for channels that contain small numbers of activated electrons, where this number itself is directly affected by discrete transitions in localised trap occupation associated with surface absorbates (as discussed in more detail in Chapter IV). At low-temperatures, thermally driven events occur increasingly infrequently such that individual charge contributions are observable in the measured channel current. A prerequisite here is the presence of a few, or a single dominant conduction pathway, perhaps in the form of a single graphene flake or MWCNT, or MWCNT bundle, consistent with the requisites of Mott conduction.

4.5 Summary

A rapid, facile and inexpensive MWCNT dry-transfer technique has been developed to fabricate MWCNT thin films on various flexible polymer and conductive substrates. Transparency control was demonstrated by adjusting the source MWCNT length prior to dry the transfer. The direct current sheet resistances were found to vary between 1.2-550 Ω/sq. with optical transparencies of 9% and 85%, respectively, with comparable THz sheet resistances. Conductivity was found to be stable under flexing for strains up to 140% (the limit of the testing equipment) with films substantially out performing both ITO and bi-layer CVD hot-press laminated graphene thin films. The technique described offers a viable means of depositing aligned nanotube thin films of controlled transparency without the need for material-degrading ultrasonication and chemical treatments.

The transport characteristics of dry-transferred and hot-press laminated graphene samples were considered and fitted well to a parallel combination of a tunnelling, 3D-varbiable range hopping Mott and high temperature $T^{-1/2}$ mechanism, the latter being associated with a second charge carrier population that dominate the sample conductivity due to the presence of both localised and conduction states. Increased interface density and sample disorder tended to evolve the transport characteristics toward a tunnelling dominated mechanism, whilst for less disorder systems Mott and $T^{-1/2}$ were increasingly prevalent and were not frozen out until much lower thermal energies.

References

1. Krebs, F. C.& Winther-Jensen, B. (2006). High-conductivity large-area semi-transparent electrodes for polymer photovoltaics by silk screen printing and vapour-phase deposition, *Sol. Energ. Mat. Sol. C.*, **90**, pp. 123-32.
2. Martin, B. D., Nikolov, N., Pollack, S. K., Saprigin, A., Shashidhar, R., Zhang, F.& Heiney, P. A. (2004). Hydroxylated secondary dopants for surface resistance enhancement in transparent poly(3,4-ethylenedioxythiophene)poly(styrenesulfonate) thin films, *Synth. Met.*, **142**, pp. 187-193.
3. De, S., Higgins, T. M., Lyons, P. E., Doherty, E. M., Nirmalraj, P. N., Blau, W. J., Boland, J. J.& Coleman, J. N. (2009). Silver nanowire networks as flexible, transparent, conducting films: Extremely high DC to optical conductivity ratios, *ACS Nano*, **3**, pp. 1767-1774.
4. Hofmann, S., Ducati, C., Robertson, J.& Kleinsorge, B. (2003). Low-temperature growth of carbon nanotubes by plasma-enhanced chemical vapor deposition, *Appl. Phys. Lett.*, **83**, pp. 135-137.
5. Pint, C. L., Xu, Y. Q., Moghazy, S., Cherukuri, T., Alvarez, N. T., Haroz, E. H., Mahzooni, S., Doorn, S. K., Kono, J., Pasquali, M.& Hauge, R. H. (2010). Dry contact transfer printing of aligned carbon nanotube patterns and characterization of their optical properties for diameter distribution and alignment, *ACS Nano*, **4**, pp. 1131-1145.
6. Mattevi, C., Wirth, C. T., Hofmann, S., Blume, R., Cantoro, M., Ducati, C., Cepek, C., Knop-Gericke, A., Milne, S., Castellarin-Cudia, C., Dolafi, S., Goldoni, A., Schloegl, R.& Robertson, J. (2008). In-situ X-ray photoelectron spectroscopy study of catalyst-support interactions and growth of carbon nanotube forests, *J. Phys. Chem. C*, **112**, pp. 12207-12213.
7. Delzeit, L., Chen, B., Cassell, A., Stevens, R., Nguyen, C.& Meyyappan, M. (2001). Multilayered metal catalysts for controlling the density of single-walled carbon nanotube growth, *Chem. Phys. Lett.*, **348**, pp. 368-374.
8. Zhong, G., Iwasaki, T., Robertson, J.& Kawarada, H. (2007). Growth kinetics of 0.5 cm vertically aligned single-walled carbon nanotubes, *J. Phys. Chem. B*, **111**, pp. 1907-1910.
9. Collier, R. J.& Hasko, D. G. (2002). Measurement of the sheet resistance of resistive films on thin substrates from 120 to 175 GHz using dielectric waveguides, *J. Appl. Phys.*, **91**, pp. 2547-2549.
10. Kaempgen, M., Chan, C. K., Ma, J., Cui, Y.& Gruner, G. (2009). Printable thin film supercapacitors using single-walled carbon nanotubes, *Nano Lett.*, **9**, pp. 1872-1876.
11. Mak, K. F., Sfeir, M. Y., Wu, Y., Lui, C. H., Misewich, J. A.& Heinz, T. F. (2008). Measurement of the optical conductivity of graphene, *Phys. Rev. Lett.*, **101**, pp. 1964051-1964054.
12. Bae, S., Kim, H., Lee, Y., Xu, X. F., Park, J. S., Zheng, Y., Balakrishnan, J., Lei, T., Kim, H. R., Song, Y. I., Kim, Y. J., Kim, K. S., Ozyilmaz, B., Ahn, J. H., Hong, B. H.& Iijima, S. (2010). Roll-to-roll production of 30-inch graphene films for transparent electrodes, *Nat. Nanotechnol.*, **5**, pp. 574-578.
13. Sun, J., Lindvall, N., Cole, M. T., Angel, K. T. T., Wang, T., Teo, K. B. K., Chua, D. H. C., Liu, J.& Yurgens, A. (2011). Low partial pressure chemical vapour deposition of graphene on copper, *IEEE. T. Nanotech.*, **1**, pp. 1-6.
14. Reina, A., Jia, X. T., Ho, J., Nezich, D., Son, H. B., Bulovic, V., Dresselhaus, M. S.& Kong, J. (2009). Large area, few-layer graphene films on arbitrary substrates by chemical vapor deposition, *Nano Lett.*, **9**, pp. 30-35.

15. Keun Soo, K., Yue, Z., Houk, J., Sang Yoon, L., Jong Min, K., Kim, K. S., Jong-Hyun, A., Kim, P., Jae-Young, C.& Byung Hee, H. (2009). Large-scale pattern growth of graphene films for stretchable transparent electrodes, *Nature*, **457**, pp. 706-710.
16. Gupta, A., Chen, G., Joshi, P., Tadigadapa, S.& Eklund, P. C. (2006). Raman scattering from high-frequency phonons in supported n-graphene layer films, *Nano Lett.*, **6**, pp. 2667-2673.
17. Graf, D., Molitor, F., Ensslin, K., Stampfer, C., Jungen, A., Hierold, C.& Wirtz, L. (2007). Spatially resolved raman spectroscopy of single- and few-layer graphene, *Nano Lett.*, **7**, pp. 238-242.
18. Wafer-scale graphene synthesized by chemical vapor deposition at ambient pressure - www.physics.purdue.edu (/quantum/files/CarbonNano/0910.4329.pdf)
19. Oznuluer, T., Pince, E., Polat, E. O., Balci, O., Salihoglu, O.& Kocabas, C. (2011). Synthesis of graphene on gold, *Appl. Phys. Lett.*, **98**, pp. 1831011-1831013.
20. Lucchese, M. M., Stavale, F., Ferreira, E. H. M., Vilani, C., Moutinho, M. V. O., Capaz, R. B., Achete, C. A.& Jorio, A. (2010). Quantifying ion-induced defects and Raman relaxation length in graphene, *Carbon*, **48**, pp. 1592-1597.
21. Wang, Y., Alsmeyer, D. C.& McCreery, R. L. (1990). Raman spectroscopy of carbon materials: Structural basis of observed spectra, *Chem. Mater.*, **2**, pp. 557-563.
22. Cançado, L. G., Jorio, A.& Pimenta, M. A. (2007). Measuring the absolute Raman cross section of nanographites as a function of laser energy and crystallite size, *Phys. Rev. B*, **76**, pp. 0643041-0643047.
23. Narula, R.& Reich, S. (2008). Double resonant Raman spectra in graphene and graphite: A two-dimensional explanation of the Raman amplitude, *Phys. Rev. B*, **78**, pp. 1654221-1654226.
24. Sato, K., Saito, R., Oyama, Y., Jiang, J., Cançado, L. G., Pimenta, M. A., Jorio, A., Samsonidze, G. G., Dresselhaus, G.& Dresselhaus, M. S. (2006). D-band Raman intensity of graphitic materials as a function of laser energy and crystallite size, *Chem. Phys. Lett.*, **427**, pp. 117-121.
25. Pócsik, I., Hundhausen, M., Koós, M.& Ley, L. (1998). Origin of the D peak in the Raman spectrum of microcrystalline graphite, *J. Non-Crystal. Sol.*, **227-230**, pp. 1083-1086.
26. Luo, Z., Yu, T., Ni, Z., Lim, S., Hu, H., Shang, J., Liu, L., Shen, Z.& Lin, J. (2011). Electronic structures and structural evolution of hydrogenated graphene probed by Raman spectroscopy, *J. Phys. Chem. C*, **115**, pp. 1422-1427.
27. Ferrari, A. C., Meyer, J. C., Scardaci, V., Casiraghi, C., Lazzeri, M., Mauri, F., Piscanec, S., Jiang, D., Novoselov, K. S., Roth, S.& Geim, A. K. (2006). Raman spectrum of graphene and graphene layers, *Phys. Rev. Lett.*, **97**, pp. 1874011-1874014.
28. Lee, S., Lee, K.& Zhong, Z. (2010). Wafer scale homogeneous bilayer graphene films by chemical vapor deposition, *Nano Lett.*, **10**, pp. 4702-4707.
29. Dato, A., Radmilovic, V., Lee, Z., Phillips, J.& Frenklach, M. (2008). Substrate-free gas-phase synthesis of graphene sheets, *Nano Lett.*, **8**, pp. 2012-2016.
30. Meyer, J. C., Geim, A. K., Katsnelson, M. I., Novoselov, K. S., Booth, T. J.& Roth, S. (2007). The structure of suspended graphene sheets, *Nature*, **446**, pp. 60-63.
31. Meyer, J. C., Geim, A. K., Katsnelson, M. I., Novoselov, K. S., Obergfell, D., Roth, S., Girit, C.& Zettl, A. (2007). On the roughness of single- and bi-layer graphene membranes, *Sol. State Comms.*, **143**, pp. 101-109.
32. Horiuchi, S., Gotou, T., Fujiwara, M., Sotoaka, R., Hirata, M., Kimoto, K., Asaka, T., Yokosawa, T., Matsui, Y., Watanabe, K.& Sekita, M. (2003). Carbon nanofilm with a new structure and property, *Jpn. J. Appl. Phys.*, **42**, pp. 1073-1076.
33. Lee, Y., Bae, S., Jang, H., Jang, S., Zhu, S. E., Sim, S. H., Song, Y. I., Hong, B. H.& Ahn, J. H. (2010). Wafer-scale synthesis and transfer of graphene films, *Nano Lett.*, **10**, pp. 490-493.
34. Caldwell, J. D., Anderson, T. J., Culbertson, J. C., Jernigan, G. G., Hobart, K. D., Kub, F. J., Tadjer, M. J., Tedesco, J. L., Hite, J. K., Mastro, M. A., Myers-Ward, R. L., Eddy Jr, C. R., Campbell, P. M.& Gaskill, D. K. (2010). Technique for the dry transfer of epitaxial graphene onto arbitrary substrates, *ACS Nano*, **4**, pp. 1108-1114.
35. De, S., King, P. J., Lotya, M., O'Neill, A., Doherty, E. M., Hernandez, Y., Duesberg, G. S.& Coleman, J. N. (2010). Flexible, transparent, conducting films of randomly stacked graphene from surfactant-stabilized, oxide-free graphene dispersions, *Small*, **6**, pp. 458-464.
36. Doherty, E. M., De, S., Lyons, P. E., Shmeliov, A., Nirmalraj, P. N., Scardaci, V., Joimel, J., Blau, W. J., Boland, J. J.& Coleman, J. N. (2009). The spatial uniformity and electromechanical stability of transparent, conductive films of single walled nanotubes, *Carbon*, **47**, pp. 2466-2473.
37. Gao, L. B., Ren, W. C., Zhao, J. P., Ma, L. P., Chen, Z. P.& Cheng, H. M. (2010). Efficient growth of high-quality graphene films on Cu foils by ambient pressure chemical vapor deposition, *Appl. Phys. Lett.*, **97**, pp. 1831091-1831093.

38.   Lee, C., Wei, X., Kysar, J. W.& Hone, J. (2008). Measurement of the elastic properties and intrinsic strength of monolayer graphene, *Science*, **321**, pp. 385-388.

39.   Pereira, V. M., Castro Neto, A. H.& Peres, N. M. R. (2009). Tight-binding approach to uniaxial strain in graphene, *Phys. Rev. B*, **80**, pp. 0454011-0454018.

40.   Liangbing, H., Wei, Y., Brochu, P., Gruner, G.& Qibing, P. (2009). Highly stretchable, conductive, and transparent nanotube thin films, *Appl. Phys. Lett.*, **94**, pp. 1611081-1611083.

41.   Wang, Y.& Santiago-Avilés, J. J. (2004). Low-temperature electronic properties of electrospun PAN-derived carbon nanofiber, *IEEE. T. Nanotech.*, **3**, pp. 221-224.

42.   Matsubara, K., Sugihara, K.& Tsuzuku, T. (1990). Electrical resistance in the c direction of graphite, *Phys. Rev. B*, **41**, pp. 969-974.

43.   Uher, C., Hockey, R. L.& Ben-Jacob, E. (1987). Pressure dependence of the c-axis resistivity of graphite, *Phys. Rev. B*, **35**, pp. 4483-4488.

44.   Ono, S. (1976). C-axis resistivity of graphite in connection with stacking faults, *J. Phys. Soc. Jap.*, **40**, pp. 498-504.

45.   Bose, E., Karmakar, S., Chaudhuri, B. K., Pal, S., Martin, C., Hébert, S.& Maignan, A. (2007). Correlation of structural, magnetic and transport properties with the tolerance factor in a low-doped $La_{0.875}Sr_{0.125-x}Ca_xMnO_3$, ($0 \leq x \leq 0.125$) system: Cross-over from Mott to Shklovskii-Efros variable range hopping conduction, *J. Phys. Cond. Mat.*, **19**, pp. 1-13.

46.   Laiho, R., Lisunov, K. G., Lähderanta, E., Stamov, V. N.& Zakhvalinskii, V. S. (2001). Variable-range hopping conductivity in $La_{1-x}Ca_xMnO_3$, *J. Phys. Cond. Mat.*, **13**, pp. 1233-1246.

Chapter V

Field Emission from MWCNT-based TFCs
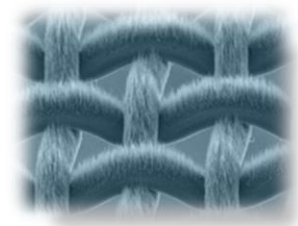
5.   Introduction

Unlike other conducting thin films, that simply offer large area conductivity, nanostructured thin films offer additional functionality that can be enhanced and augmented depending on the alignment of the constituent nanostructures. To achieve reliable and reproducible performance, engineering applications must exploit the bulk properties of the composite nanostructures and their alignment in applications that can tolerate the morphological and electrical variations between nanostructures. This is critical in attaining high yields. In this chapter the field emission performance of aligned MWCNT-based transparent flexible conductors is considered.

5.1   Field Emission

Electrons can be emitted from a solid in a number of ways. Of these the most notable are field emission, thermionic emission and photoemission. Thermionic and photoemission occur when electrons are thermally or optically excited which allows them to pass over the surface potential barrier. It is in this feature that field emission drastically differs. Field emission is strictly defined as the emission of electrons from the surface of a condensed phase, electron-rich surface into a separate electron deficient phase, usually a vacuum, under the influence of a large electric field[6]. Unexcited electrons quantum mechanically tunnel through the deformed barrier. Electrons emission occurs at room temperature, making plastic substrates accessible, and the emitters are consequently referred to as cold cathodes. The intense electric field profoundly modifies the interface barrier, narrowing it to just a few tens of atoms in thickness. Electrons tunnel through, rather than over, the barrier resulting in an exponential-type relationship characterised by an extremely fast on-off time.

In the case of thermionic emitters, found historically to pervade the display industry in the form of the cathode ray tube, the emission current, work function (ϕ=4-5 eV) and operational temperature are intimately related[6]. To stimulate appreciable emission currents temperatures in excess of 1500°C are required. Plastic substrates are consequently inaccessible. Thermionic sources are energetically demanding and the high operational temperatures induce severe emitter instabilities. Thermionic sources also have extremely poor transient behaviour with on-off times of the order of seconds. Photoemission on the other hand occurs when electrons are excited into higher energy states by incident radiation of the correct frequency, v. To
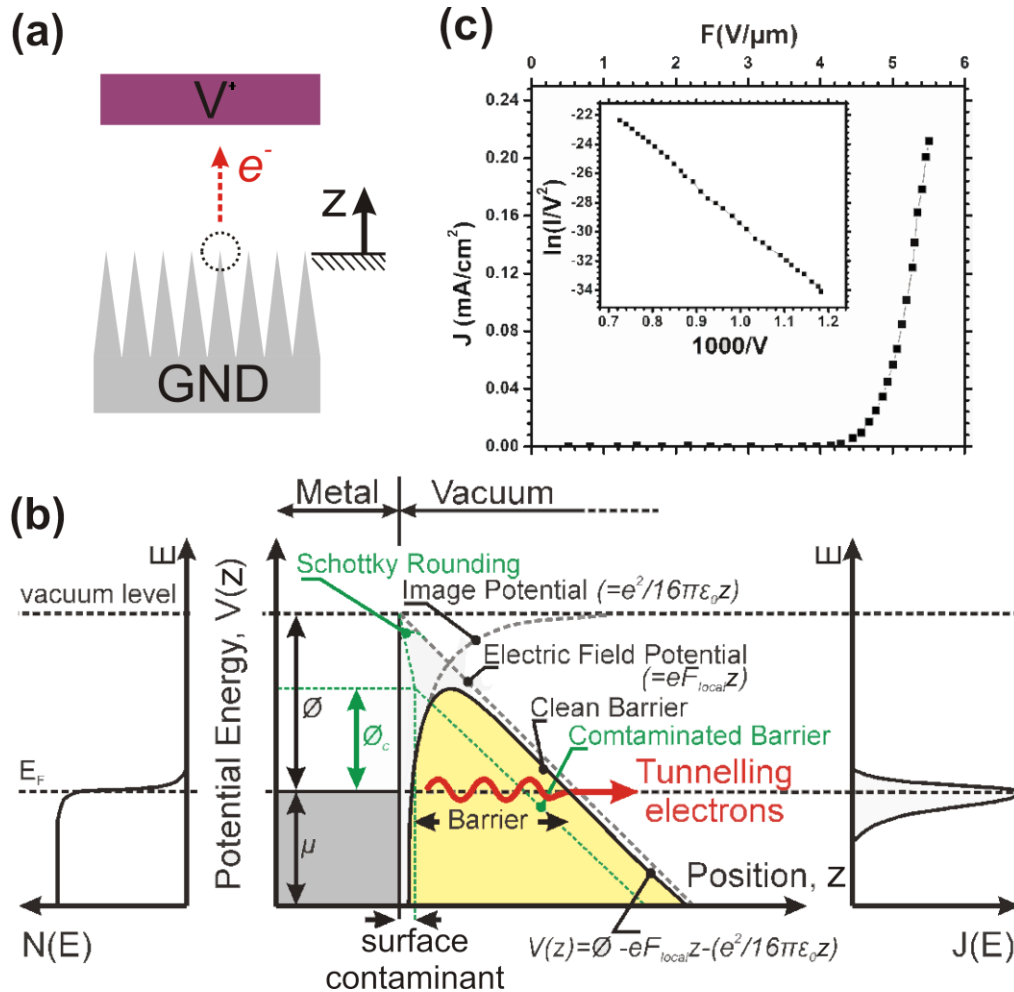
Figure 5.1 | The field emission process. (a) A large potential difference is applied between an emitter (grey) and a counter electrode (purple) which liberates electrons from the emitter. **(b)** Idealised potential energy profile at the metal-vacuum interface during the application of an external electric field. Non-idealities are depicted in green. N(E) and J(E) are the electron density and the emitted current density as a function of energy, respectively. **(c)** The emitted current density and corresponding Fowler-Nordheim plot for a traditional metallic W field emitter showing ideal FN characteristics[3].

achieve this the incident photons must have an energy $h.v \geq \phi$, where h is Planck's constant[6]. For most metallic surfaces the corresponding threshold wavelength is in the visible or ultraviolet region of the electromagnetic spectrum. The primary draw back with photoemission is that it is difficult to stimulate significant emission currents. Electrons are only liberated from the emitter's surface and the energy of the excited electrons is readily redistributed within the bulk due to interactions with the conduction electrons. Moreover, much of the incident irradiation is reflected. Photoemission is also largely inappropriate for optical displays as ambient light results in noisy emission due to the non-negligible variation in emitter conductivity when optically irradiated[7].

   Field emission sources have a number of extremely attractive features compared to photo and thermionic emitters. In addition to their room temperature operation, they respond instantaneously to field variations, have high tolerance to temperature fluctuations and incident radiation, are highly focusable, have good on/off ratios, possess highly nonlinear emission characteristics and are capable of providing high emission current densities[1].

5.2   Fowler-Nordheim Theory

Field emission is a wholly quantum mechanical phenomenon. It can be succinctly described in adequate detail using fairly simplistic descriptors based on the free-electron model. Figure 5.1(a) illustrates the process. A potential difference is applied between the electron-dense emitting surface and a counter electrode. Under sufficiently high electric fields electrons are extracted. To obtain stable performance vacuums of 10^{-9}-10^{-7} mbar are usually necessary to avoid tip damage by gas ionization and ion bombardment. The idealised potential profile is given in Figure 5.1(b). N(E) shows the variation in the electron density in the emitter. The majority of electrons are confined to the Fermi Sea. The combined effect of the applied electric field and the image potential produces a triangular barrier, as shown. Electrons tunnel through this barrier when it is less than a few nanometers across. Increasing the electric field increases the barriers gradient and therefore reduces the tunnel width. The narrower the barrier, at a given electric field, the higher the emission current. Surface contaminants and engineered coatings, such as Cs (1.9 eV), Ba (2.3 eV) and ZrO (2.3 eV), produce Schottky rounding and reduce the work function of the emitting surface[1] which in turn thins the barrier thereby reducing the turn-on potential. Figure 5.1(c) shows standard emission characteristics of a metallic W emitter[3].

   The emitted current density (as a function of the global electric field, F), J(F), is given by;

$$J(F) = \left(\frac{A}{\phi t^2(s)} \right) F^2 \exp\left(-Bv(s)\frac{\phi^{3/2}}{F} \right) \qquad (4.1)$$

where ϕ is the work function of the emitter, A= *(e³/8πh)* = 1.54x10^{-6} A.eV/V^2, and B = *(8π/3eh)(2m)$^{1/2}$* = 6.83x10^9 (eV)$^{-3/2}$ V/m. t(s) and v(s) are the purely mathematical slowly-varying dimensionless Nordheim elliptical functions[8, 9], and are approximated by;

---

[1] Surface impurities cannot be accommodated in the presented model using the Richardson's composite
   work function.

$$t(s) = (3.79x10^{-5})F^{1/2} / \phi \qquad (4.2)$$

$$v(s) = (0.956 - 1.062s^2) \qquad (4.3)$$

s is the slope correction factor. For simplicity v(s) is most often set to unity with minimal loss in accuracy.

A rather elegant, modification to equation (4.1) was proposed by Brodie *et al.*[10] to give a more tractable descriptor. By substituting the current density and emission area with the measured current (I) and the local electric field with the product of the applied bias (V) and a geometry dependent field factor, they determined that;

$$I = V^2 \beta^2 \left(\frac{A^* A}{\phi \delta^2} \right) \exp\left(\frac{-B\phi^{3/2}\delta}{\beta V} \right) \qquad (4.4)$$

where A* is the effective emission area, δ is the constant electrode separation and β, the field enhancement factor, is proportional to the aspect ratio of the emitting surface and is given by:

$$\beta = \frac{F_{local}}{F} \qquad (4.5)$$

Here F_{local} is the tip enhanced electric field. The sharper the emitter, the greater the enhancement factor and the steeper the gradient of the potential profile (Figure 5.1(b)), which narrows the corresponding tunnel barrier. The field enhancement factor is a standard performance metric that is empirically evaluated by measuring the I-V characteristics and plotting the so-called Fowler-Nordheim (FN) curve according to;

$$y = mx + c \implies \ln\left(\frac{I}{V^2} \right) = \left(\frac{-B\phi^{3/2}\delta}{\beta} \right)\frac{1}{V} + \ln\left(\frac{A^* A \beta^2}{\phi \delta^2} \right) \qquad (4.6)$$

Numerical estimates of β are extracted by linear interpolation of the gradient, where the B, ϕ and δ, in equation (4.7), are known constants.

$$m = \frac{dy}{dx} = \frac{d(I/V^2)}{d(1/V)} = \frac{-1}{\beta}\left(B\phi^{3/2}\delta \right) \qquad (4.7)$$

Similarly, the y-intercept specifies either the work function or the effective emission area. The field enhancement factor has extremely strong geometry dependence. This was succinctly illustrated through the theoretical work of Rohrbach *et al.*[11, 12]. Narrow, elongated emitters are preferential as they enhance the local field substantially compared to short and stubby geometries.

5.3   The History of Field Emission from Carbon

In 1972, graphite fibres were shown to offer enhanced emission stability in modest atmospheres compared to several common metallic emitters[13]. Wang *et al.*[14] and Geis *et al.*[15], in 1991, using diamond-based cathodes reported emission at surprisingly low threshold fields (<3 V/μm). Later that same year, Djuba *et al.*[16] supported their findings by measuring the emission from arrays of diamond-like carbon (DLC) cones at extraction potentials much lower than those of either Mo or Hf tips. At the time it was believed that carbon materials could be classified into two distinct groups based on their proposed emission mechanism. These were the structured graphites, which emitted as a result of field enhancement, and the diamond types where band bending effects[17, 18] were believed to be important[19-21]. In the latter, low and even negative electron affinities in wide band gap materials, such as diamond and its synthetic derivatives, were thought to account for the emission. Electrons that were injected into the conduction band encountered a reduced barrier and, as a result, were easily emitted into vacuum. It is now accepted that this is not the case. Band bending would apply homogenously over the entire surface resulting in spatially uniform emission, yet the observed emission was always confined within a few highly localized and randomly distributed sites. The widely accepted model and data were inconsistent. Spatial mapping of the emission characteristics hinted that there was something peculiar about the emission sites in relation to the rest of the (apparently) planar coating[22].

Simultaneous photo and field emission studies employing highly uniform CVD diamond films showed that the excited electrons were sourced from 5-6 eV below the vacuum level[22]. The electrons were emitted at unexpectedly low-fields due to field enhancement originating from the crystal grain boundaries[23, 24], a result that was largely supported by the superior emission characteristics of highly defective and interface-rich films. As a result, tetrahedral amorphous carbon (*ta*-C), a DLC derivative, was heavily studied. It appeared that the *ta*-C films only ever emitted after 'activation'. That is, when a vacuum arc discharge event occurs with sufficient vigour to perturb the surface topography to form a tip-like structure, typically at applied fields of 80-180 V/μm. Post-emission electron microscopy analysis of these *ta*-C coatings revealed sharp topographic features which had a propensity to function as suitable geometrically enhanced emission sites[25]. Prior to activation no surface perturbations existed and poor emission characteristics, due predominately to the grain boundaries, were recorded.

Further analysis surmised that what were originally believed to be smooth *ta*-C films were, in fact, covered in sub-micron-sized graphitic inclusions and particles[26] which functioned as emission sites with field enhancements of up to 250 - values far too high to be consistent with the films apparent planar nature.

A new trend emerged. The production of intentionally diverse composite carbon films, rich in a variety of graphitic nanostructures become commonplace. These films contained wide assortments of naturally occurring carbonaceous nanostructures, including, but certainly not limited to; particles, onions, clusters, fullerenes, nanotubes and nanofibres. These nanostructured carbon films performed significantly better than both the planar carbon and Spindt metallic emitters at the time and had turn-on fields as low as 1-5 V/μm.

More recently, field emission has been reported from DLC[27-29], CVD graphite[24] and various polymers[30]. Of those materials, those with the highest aspect ratios or particularly perturbed surfaces were found to outperform the more conformal and smooth coatings. Evidently sharp tips were still preferential. The first electron emission from a nanotube was demonstrated by de Heer *et al.*[31] who studied the emission properties of MWCNTs in the mid-1990s where they validated the general appropriateness of the Fowler-Nordheim equation.

5.4   Nanotube Thin Film Field Emitters

To-date most nanotube-based field emitters have been fabricated by depositing independently mass produced nanotube-containing pastes or powders. Regardless of the exact synthesis process the source CNTs are purified and mixed with an epoxy or binder and are either screen printed, cast or sprayed to form large-area films or selectively located using electron microscopy-monitored nanomanipulators[32]. Electrophoresis has also been exploited to position nanotubes at specific locations[33]. The emission characteristics of various nanotube types and geometries has been investigated, including individual SWCNTs[34] and MWCNTs[35], nanotube networks embedded in epoxy matrices[36] and vertically and horizontally aligned nanotube arrays[1, 37, 38]. Studies of pure, chemically untreated nanotubes transferred to more exotic substrates have been few and far between due to the difficulties in producing uniform cohesive nanotube films that are free of extraneous chemicals on
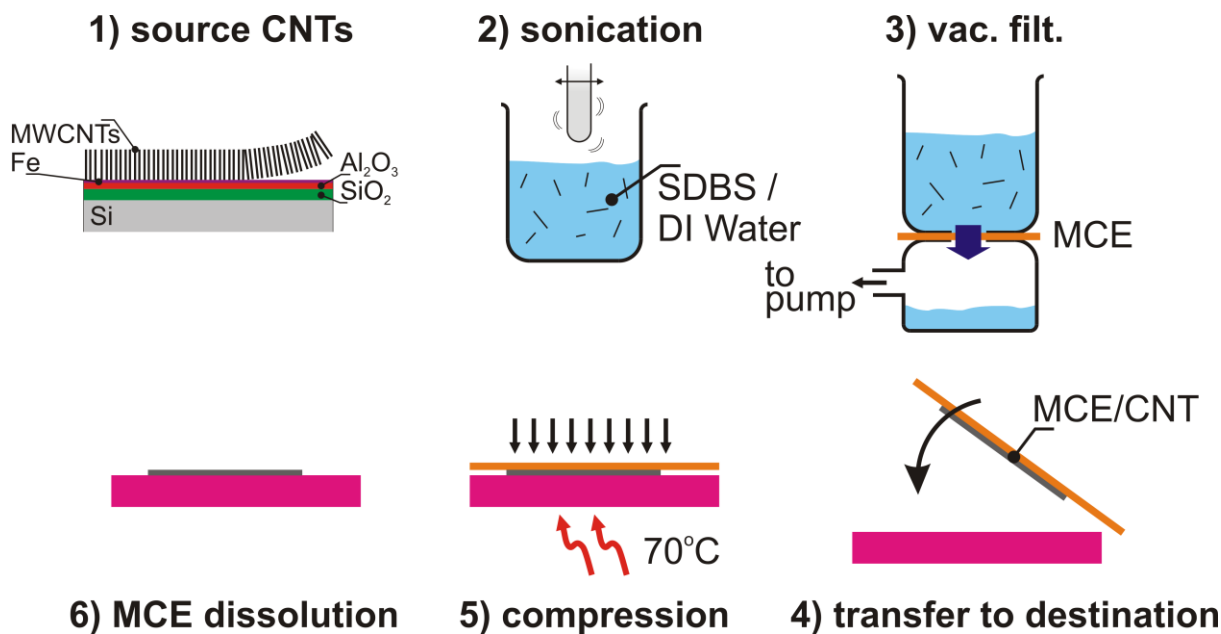
Figure 5.2 | MWCNT thin films by vacuum filtration. (1) Source nanotubes are cleaved from their growth substrate and **(2)** ultrasonicated in a surfactant solution of sodium dodecylbenzenesulfonate (SBDS) and DI water. **(3)** Nanotube solution vacuum filtered through a mixed cellular ester (MCE) membrane. **(4)** MCE/CNT placed in contact with the destination substrate (e.g. glass, quartz, plastics etc.). **(5)** The MCE/CNT/destination substrate and compressed and heated. **(6)** MCE dissolved in acetone / methanol or peeled away to leave the destination-supported nanotube network.

substrates other than the growth substrate. The dry-processing detailed in Chapter II offers a solution. In this section the field emission characteristics of these dry-processed films are critically compared with more standard vacuum filtered and screen printed nanotube films.

5.4.1   MWCNT Thin Film Emitters

For high throughput, low-end applications, such as environmental lighting and flexible field emission-based display backlighting, simple and low-cost processing are stringent requirements for successful commercialization. Functionality at comparatively high pressures (10^{-6} mbar) with currents of the order of 1-10 mA are necessary. An important feature of the work is that the emitters considered are low-temperature, plastic compatible. Quartz supported nanotube thin film electron sources, providing a current density of 100 mA/cm^2, are commercially available in portable X-ray systems. However, flexible field emission displays and environmental lighting are not. To appreciate why, some understanding of and the limitations associated with thin film deposition techniques were considered. The field emission properties of CNT films prepared from screen-printed CNT powders[39] and *in-situ*
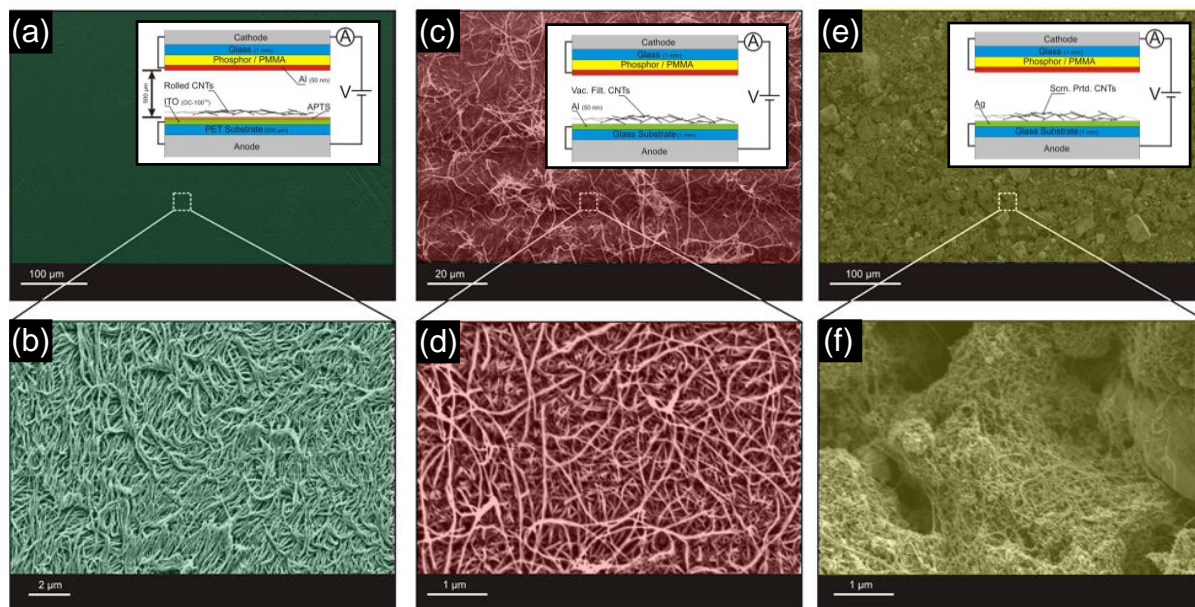
Figure 5.3 | MWCNT thin film field emitters. SEM micrographs of **(a, b)** Rolled **(c, d)** Vacuum filtered **(e, f)** Screen printed thin film field emitters. The *inserts* depict the measurement set-up in each case.

CVD grown arrays[40, 41] have been reported and have demonstrated impressive emission characteristics. Nonetheless, direct deposition by CVD is ultimately limited to high-temperature compatible substrates. For large-scale production of CNT film, screen printing is considered to be one of the most effective approaches and has the advantages of low-cost and easy preparation without size limitations. However, low current densities, low spot densities, poor emission uniformity and contaminated pastes restrict its application. Nevertheless, industrial research and development have focused primarily on this approach, though significant functional improvements are certainly possible.

The field emission performance of the dry-processed MWCNT films, detailed in Chapter II, is herein compared to vacuum filtered and commercially available screen printable nanotube paste, two of the most commonly used approaches to nanotube deposition (Figure 5.3). The same source material was used for the rolled and vacuum filtered films and was synthesized by thermal CVD on Si/SiO_2 (200 nm) substrates coated with a bilayer catalyst of magnetron sputtered Al_2O_x (10 nm) and thermally evaporated Fe (1 nm) grown in a 4% high purity, H_2 diluted, C_2H_2 atmosphere at a chamber pressure of 26 mbar at 700^oC for 10 minutes. These MWCNTs were rolled onto 150 μm ITO coated poly(ethylene terephthalate) (PET) substrates pre-treated with a self-assembled monolayer adhesion promoter aminopropyl triethoxysilane (APTES). Transferred MWCNT films were ~20 μm in depth (Figure 5.3(a,b)).
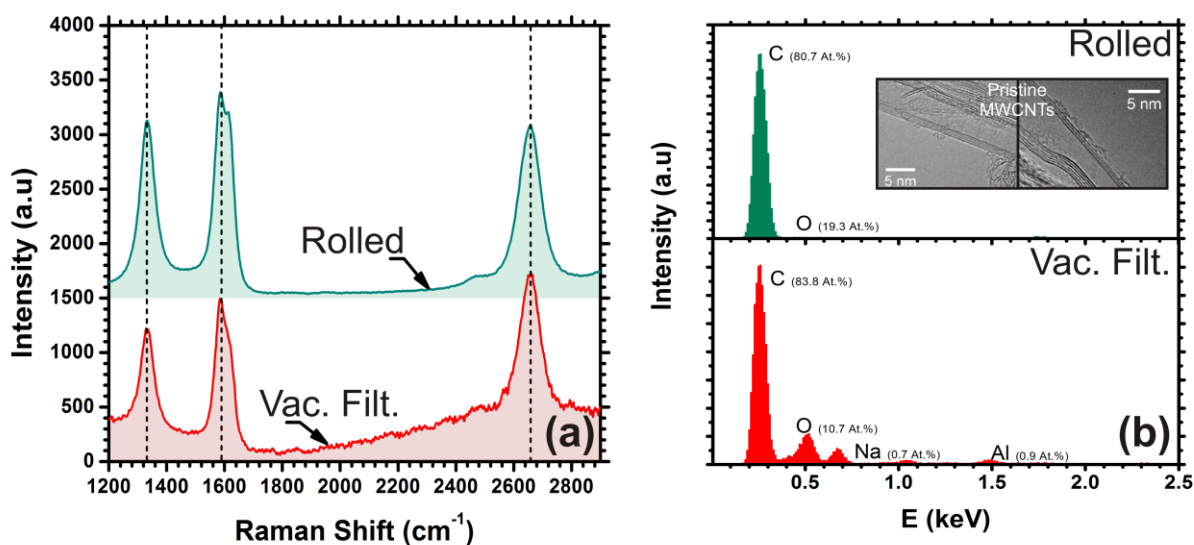
Figure 5.4 | The effect of solution-processing. Graphitic structure and elemental content characterisation. **(a)** Raman spectrum (633 nm, 0.55 mW) and **(b)** EDX Spectrum of the as-grown dry rolled MWCNTs (green) and solution processed vacuum filtered (Vac. Filt.) emitters (red). Residual surfactant (principally Na) is clearly seen on the vacuum filtered sample. *Insert:* HR-TEM micrographs of the as-grown MWCNTs used for both the vacuum filtered and dry-process thin films.

Figure 5.2 illustrates the vacuum filtration process, as described in more detail by Wu *et al.*[42]. 2-mg of the as-grown MWCNTs were cleaved from the growth substrate and dispersed into a solution of DI water and the surfactant sodium dodecylbenzenesulfonate (SDBS) (1 L:700 mg) using a high power tip ultrasonicator (250 W / 24 kHz) for 10 h. The dispersion was then filtered through a 50 μm pitch PET mesh to remove residual amalgamates. 5 mL of the solution was vacuum filtered through a mixed cellulose ester membrane (MCE, Millipore, 0.22 μm) and rinsed with DI water. The MCE supported MWCNT networks were then placed in contact with Al coated glass and heated to 70-80°C in ambient conditions under a compression of 35 g/cm^2 for 3 h. The MCE was dissolved in acetone, or gently peeled away to activate the film. The remaining emitters were rinsed in acetone, IPA, DI water and dried with N$_2$. For nominally equivalent filtrations the emitters had a 550 nm optical transparency of ~40% and a sheet resistance of 350 Ω/sq.

To give a suitable comparison to the current state-of-the-art nanotube-based field emitting materials, a third emitter was fabricated by screen printing a commercially available (Xintek / Xinano Materials, XPP08[43]) 20% CNT concentration (22 %wt. solid content) paste onto a screen-printed Ag paste electrode (sintered at ~560°C). These nanotubes were 2-15 nm in
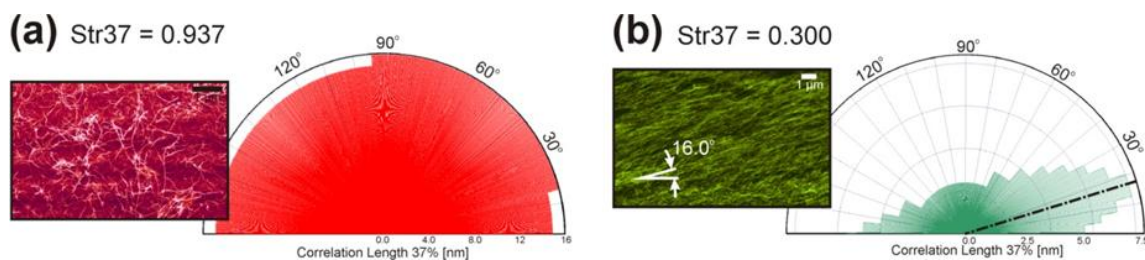
Figure 5.5 | **Morphology and alignment. (a)** Vacuum filtered samples show much greater macroscopic disordered (Str37=0.94) compared to the **(b)** dry-transferred rolled films (Str7=0.30).

diameter and <20 μm long. Samples were sintered at ~520°C in a N_2 atmosphere to increase the adhesion between the Ag paste electrode and MWCNT film and to remove remaining organic binders and impurities.

Figure 5.3 shows SEM micrographs of the prepared emitters and the experimental setup. Al/glass and ITO/PET controls were prepared by magnetron sputtering. The cathode was fabricated by spray coating a 1:20 (by wt.) polymethylmethacrylate (PMMA): phosphor mixture onto Corning glass. A 30 nm Al top contact was deposited by magnetron sputtering to form the partially transparent scintillator.

Equivalent source MWCNTs were used in the rolled and vacuum filtered emitters. Figure 5.4(a) shows the Raman spectra (633 nm) of the source MWCNTs in the rolled and the vacuum filtered films. There is little difference between the two. In fact, ultrasonication has appeared not to have affected the degree of disorder in the nanotubes at all. A rather unexpected result. Both the rolled and vacuum filtered samples have an I_D/I_G ~0.85. Sonication has been reported in the past to shorten nanotubes to <5 μm in length[44]. This snapping or shortening process increases the number of free edges and henceforth increases the intensity of the D peak. Dangling bonds are, in many ways, preferential as they form extremely high aspect ratio, though ultimately unstable, emission sites. Nonetheless, this is not the case in the solution processed films presented. The spatially averaged EDX spectrum (400 μm x 400 μm) of the vacuum filtered samples (dry dispersed onto a Cu TEM grid) revealed surfactant remnants after DI rinsing (Figure 5.4), principally Na.

Another major difference between the samples is the degree of nanotube alignment. Figure 5.5 shows the quantified alignment of the vacuum filtered (red) and dry-processed (green)
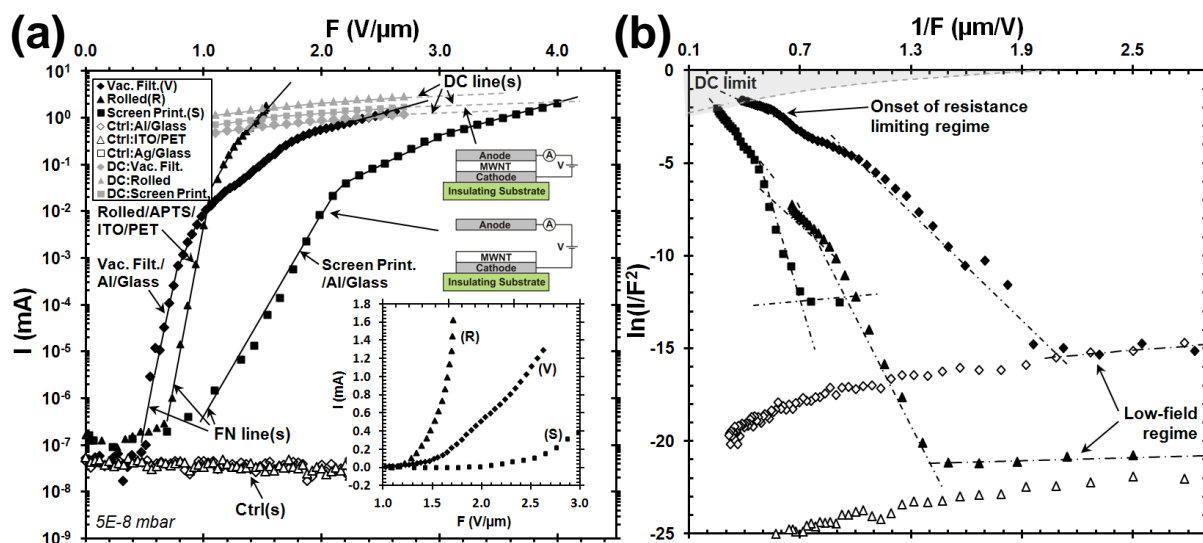
Figure 5.6 | Field emission from MWCNT-based thin films. (a) The electric field dependence of the emission current. *Lower right insert*: I-E data. *Upper right insert:* Measurement set-up to distinguish the FN regime and the resistive DC limit. **(b)** Corresponding FN plot. Dashed lines show linear fits to the FN relation and DC-limits.

films using the Str37 function in SPIP^{TM} image analysis software. Equivalent scale micrographs were used. The dry-transferred films show a much greater degree of macroscopic structural anisotropy (0.30) when compared to the vacuum filtered samples (0.94).

Field emission studies were performed in a home-built turbo-molecular-pumped vacuum chamber evacuated to <5x10^{-6} mbar at room temperature. Poor operational pressures were intentionally considered to study the robustness of the emitters. Ceramic spacers fixed the distance between the nanotube thin films and an ITO/glass counter-electrode to 500 μm. The bias was ramped (5 kV source) in <50 V increments and measured using a LABVIEW controlled HP 34401A meter recording in triplicate over 3 s intervals. The measured emission areas were approximately 1 cm^2.

The I-F and corresponding FN plot are illustrated in Figure 5.6(a) and (b). SEM analysis revealed that the MWCNTs are predominantly horizontally aligned. Electrons are transported along the tube length and are emitted from both the tips and side walls, although the latter less efficiently. The vacuum, rolled and screen printed emitters had turn-on fields of (defined as the field required to produce an emission current of 10 nA) 0.70, 0.85 and 1.40 V/μm, respectively. Interestingly the vacuum filtered samples turn on at lower field than the as-grown nanotubes. The EDX spectrum given in Figure 5.4(b) clearly identifies a relatively
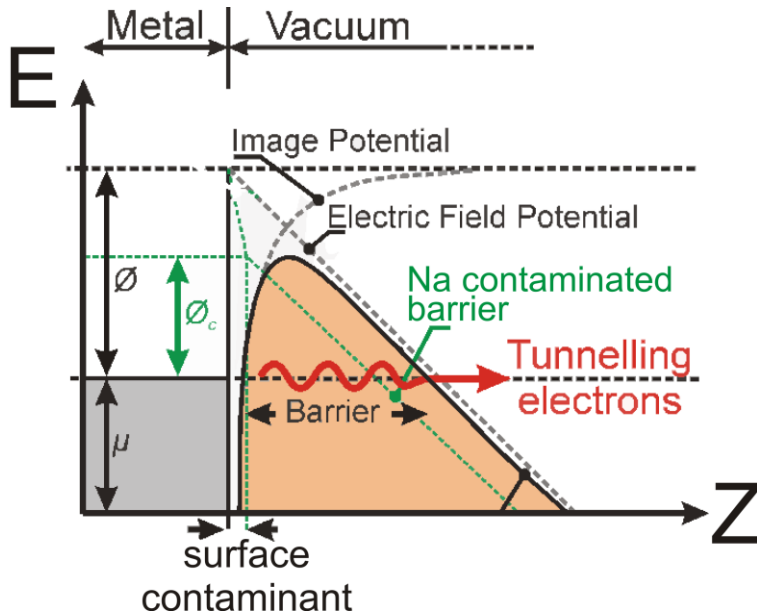
Figure 5.7 | Proposed emission model for surfactant treated MWCNT-based thin films. Electronic band diagram of showing the untreated (ϕ_{MWCNT}=5.0 eV) and a Na contaminated surface (ϕ_C=2.3 eV) (green). Note the narrowed tunnel barrier as a result of surface contamination from Na.

strong Na (0.7 At.%) signature for the vacuum filtered samples. The surfactant was not completely removed by DI rinsing. The work functions of MWCNTs and Na are 5.0 and 2.3 eV, respectively. The Na deposits may account for the reduced turn-on field for the vacuum filtered sample compared to the dry-processed sample, as illustrated in Figure 5.7. Cryogenic measurements on Na coated W emitters have previously shown that the work function of the emitting surface decreases rapidly with increasing sodium coverage[45]. Reducing the work function of the emitting surface reduces the height of the surface potential. This in turn narrows the emission tunnel barrier for a given electric field. Increasing numbers of electrons can therefore tunnel at lower fields which is expressed as a higher emission current. Nevertheless, Na is highly unstable under vacuum and readily migrates during field application[46].

The schematic inserts of Figure 5.6(a) depict the measurement set-up for the field emission and DC-limit studies. To validate the observed deviation from standard FN behaviour[47] DC measurements were employed. Standard FN emission does not take into account electron transport within the emitter. The critical field, denoted F_c for convenience, is the field at which FN emission departs to DC-limited behaviour. The FN equation is typically applied to metals and predicts no saturation due to high conductivities and high electron densities[6, 7]. However, in lower conductivity films, specifically percolating networks, the internal and contact resistance must be considered. Saturation currents of 2.6, 1.5, and 1.3 mA were observed at an applied field of 1.5, 2.5, 2.6 V/µm for the rolled, vacuum filtered and screen
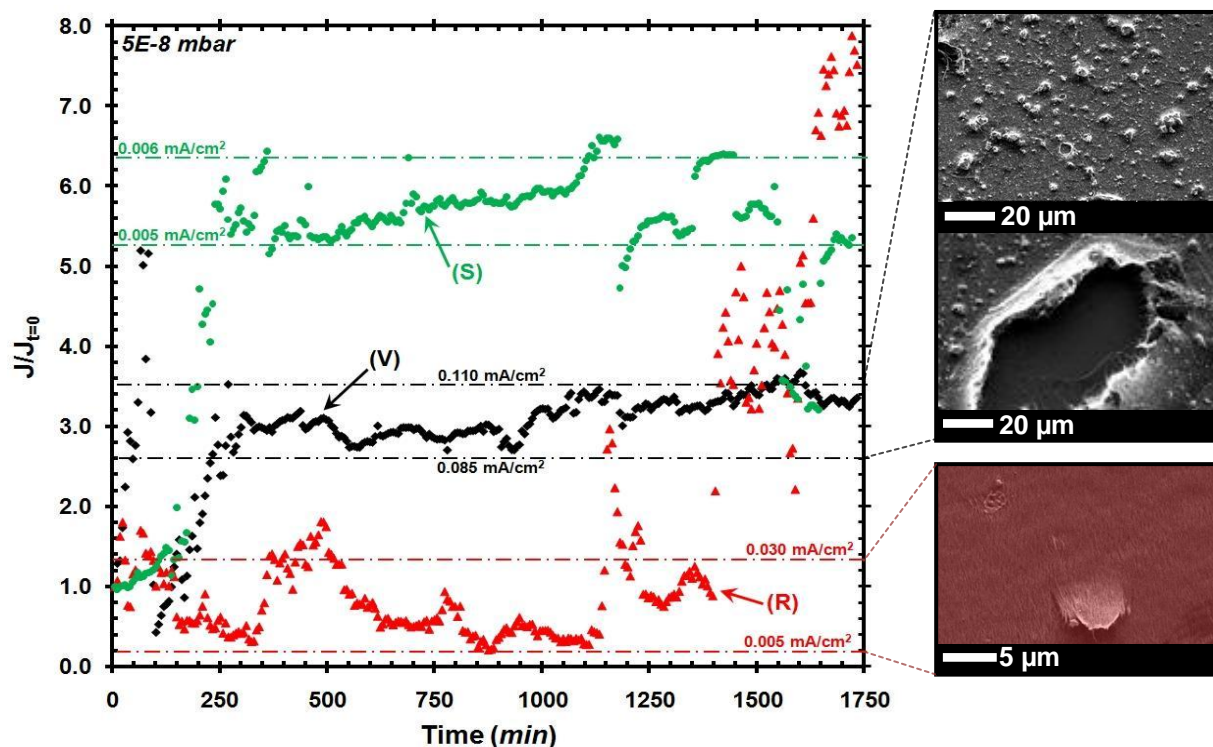
Figure 5.8 | Stability and failure. (a) Temporal stability of the (R) Rolled (red triangles), (V) vacuum filtered (black diamonds) and (S) screen printed (green circles). **(b)** SEM micrographs of the films post emission. The high fields have clearly up-lifted areas resulting in local over emission and tube burn out.

printed samples, respectively. In the low-field regime (<1.5 V/µm) conventional linear FN behaviour was observed. However, the emission characteristics deviated in the high-field region due to an emission saturation effect. All three cases showed a similar effect. Collins *et al.*[48] attributed this deviation to the electrostatic interaction between neighbouring nanotubes. For nanotube-based thin films these slopes are often attributed to the switchover from a predominately tip emission to side emission, caused by the differences in interface barriers and emission geometries. This effect is consistent with the data presented by De Jonge *et al.*[49] and accounts for the lack of a secondary *β*-regime in the case of short, axially conductive vertically aligned nanofibre arrays. In the presented instance, this saturation effect is more likely ascribed to the internal resistance of the MWCNT film (i.e. the inter-nanotube tunnel barrier / contact resistance), as discussed. Indeed, the earlier works by Cui *et al.*[47] showed that, by measuring the DC transport characteristics in a stacked nanotube structure, the low-field regime fitted well to pure FN emission whereas the high field regime showed resistance-limited emission associated with the transport behaviour within the emitter.

Interface dense films, such as nanotube networks, show an intensified saturation effect as a result, as evidenced above.

The variations between vertically aligned, well anchored nanofibre emitters and the thin film emitters above can be generalised if one considers the interaction between the MWCNT dipoles and the electric field. This interaction dynamically adjusts the nanoscopic structure of the film. This increases the mean inter-tube separation. In percolation networks conduction is largely dominated by variable range hopping between nanotubes[50]. Under increasing electric fields the inter-tube separation increases and the effective tunnel barriers, between nanotubes, similarly increase. As the inter-tube spacing increases the sheet resistance correspondingly increases which reduces the maximum emission current. The network dynamically adjusts which ballasts the emission, as shown in Figure 5.6. For strongly disordered, cohesive networks this effect is less prominent, whereas in aligned anisotropic networks this effect is amplified. However, this current-limiting mechanism is offset by an increase in local field enhancement due to topographic variations associated with the nanoscopic motion in the film. Individual tips move and start to dominate the emission. Poorly bound nanotube films, such as the rolled film, move more freely than highly bound and self-cohesive nanotube films, such as the screen printed emitters, causing saturation at lower fields. Interestingly, however, higher maximum emission currents are observed for the rolled films as the topographic alterations (which increases the number of emission sites) out-weigh the current reduction by enhanced inter-tube tunnelling.

Figure 5.8 shows the accelerated lifetime measurements of the emitters performed at $5x10^{-8}$ mbar. Both the screen printed and vacuum filtered samples clearly undergo an activation-type process. The emission current density linearly increases until a stable saturation is reached after ~250 min. In contrast, the rolled films show consistent emission from initiation until failure. Rolled films showed catastrophic failure showing no discernible activation. SEM analysis revealed torn regions of the rolled films (Figure 5.8) indicative of a failure site. Vacuum filtered samples too showed large pit-like structures. It is conceivable that the higher degree of nanotube connectivity in the vacuum filtered samples increases the effective self-adherence of the nanotubes thereby increasing the films resistance to the strong electric fields. The films deform less during field exposure. The rolled films have a much more anisotropic structure. The modest tube alignment increases the susceptibility of the film to rupture. In the

case of the screen printed sample the exact failure mechanism was less clear and electron microscopy provided little further insight.

5.4.2   *Zinc Oxide Nanowire Ballasted MWCNT Thin Films*

In order to attain the enhanced uniformities it is necessary to limit the emission current from the dominant tips. The spikes in the lifetime measurements of Figure 5.8 are due to the over-emission and consequent burn out of such tips. The integration of a ballast resistance structure, engineered using a material which itself is flexible and transparent, would achieve this. Zinc oxide nanowires (ZnO NWs), wide band gap compound semiconductors of modest axial resistance, have been previously shown to function as equivalent series resistances in periodic nanofibre arrays[51]. In addition to the large exciton binding energy, the thermal stability and high oxidation resistance, compared to nanotubes[52], make semiconducting oxide nanostructures particularly appealing in 'poor' vacuum field emission applications[53]. Nanotube/ZnO NW composite emitters offer the benefits of low turn-on fields, associated with the nanotubes, with an increased functional pressure range and emission uniformity. Herein data is presented on the development of large area ZnO NW ballasted MWCNT thin film field emitters.

The low-temperature processability of ZnO makes it a very attractive material. Recently, several groups have investigated the field emission characteristics of various zinc oxide (ZnO)-based morphologies, such as tetrapods[54, 55], nanodisks[56], and nanopins[57]. Jo *et al.*[53] reported field emission from ZnO NWs grown by a high-temperature vaporization-sublimation process on carbon cloth. They noted an extremely low turn-on field ascribed to the combined field enhancement. Wang *et al.*[58] extended these studies by considering the deposition of ZnO mulitpods, synthesized by high-temperature (750°C) vapour-solid self-catalyzing processing on screen-printed MWCNT films on Si substrates. They too found that combining MWCNTs and ZnO NWs drastically improved the field emission performance. So much so, in fact, that the composite demonstrated lower turn-on fields than either of the as-grown nanostructures on their own.

In an attempt to increase the field enhancement factor and achieve lower field operation than is generally accessible for pure ZnO-based emitters, dry-processed MWCNT films were
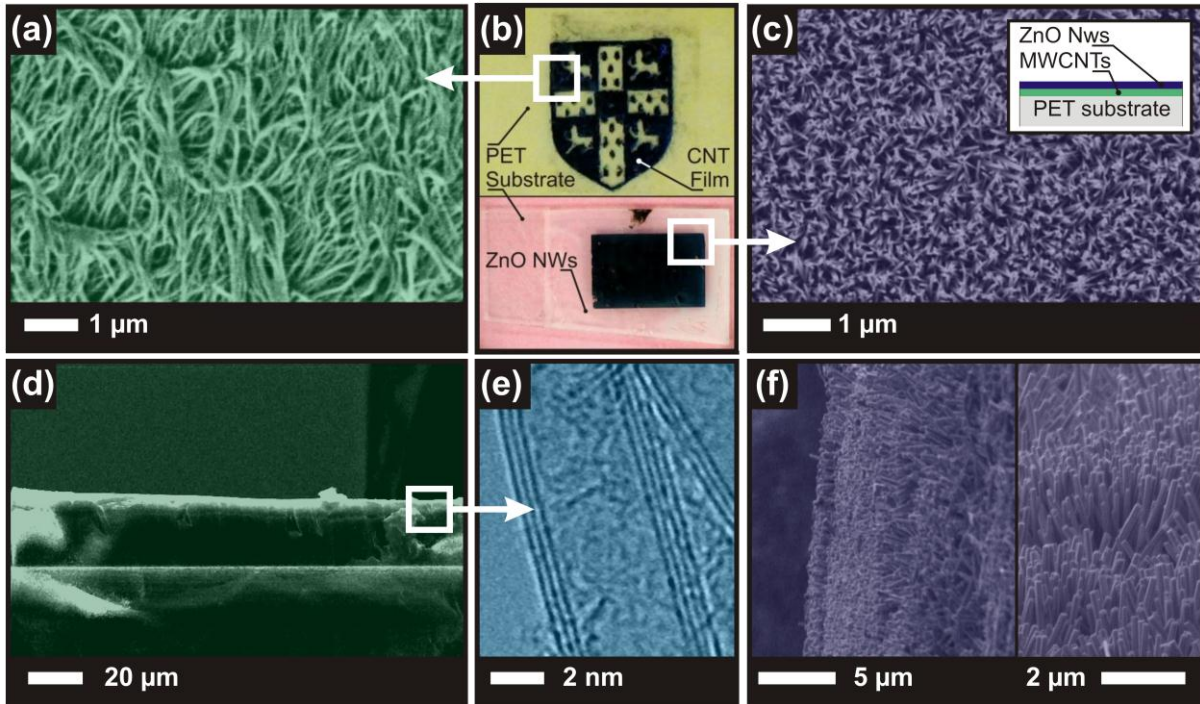
Figure 5.9 | ZnO NW ballasted MWCNT thin film field emitters. (a) (False coloured) SEM micrograph of a rolled MWCNT thin film. **(b)** Optical micrograph of a patterned rolled MWCNT thin film emitter (top) and ZnO NW coated emitter on APTES pre-treated PET (bottom). **(c)** SEM micrograph of a ZnO NW ballasted MWCNT field emitter. *Insert*: Schematic of the emitter cross-section. Cross-section SEM micrographs of a **(d)** MWCNT emitter and **(f)** a MWCNT/ZnO NW ballasted emitter. **(e)** HR-TEM micrograph of an as-grown MWCNT.

used as the substrate onto which ZnO nanowires (NWs) were grown via hydrothermal processing[59]. A 10 mM catalyst solution of zinc acetate dehydrate (98%, Aldrich) in 1-propanol (spectroscopic grade) was cast at 2000 rpm for 30 s onto the dry rolled PET-supported MWCNTs. Vertically aligned ZnO NWs were then grown by dipping the substrates into an equimolar solution of DI water, 25 mM zinc nitrate hexahydrate ($Zn(NO_3)_2 \cdot 6H_2O$, Sigma Aldrich) and hexamethylenetetramine (HMTA, Sigma Aldrich) heated to 80°C for up to 4 h.

Figure 5.9(b) shows a patterned MWCNT emitter. Patterning was achieved by combining standard low-cost laser jet printing with a nanotube catalyst passivation process prior to CVD growth. Areal and cross-sectional SEM micrographs of a rolled MWCNT film and ZnO NW coated film are given in Figure 5.9. The MWCNTs are ~4 nm in diameter and 500 μm long. When rolled they form a ~20 μm deep film (Figure 5.9(d)). HR-TEM analysis of the MWCNT film, shown in (Figure 5.9(e)), indicates the highly graphitic quality of the dry-processed MWCNTs that have between 2 and 5 graphitic sidewalls. Figure 5.9(b) shows an
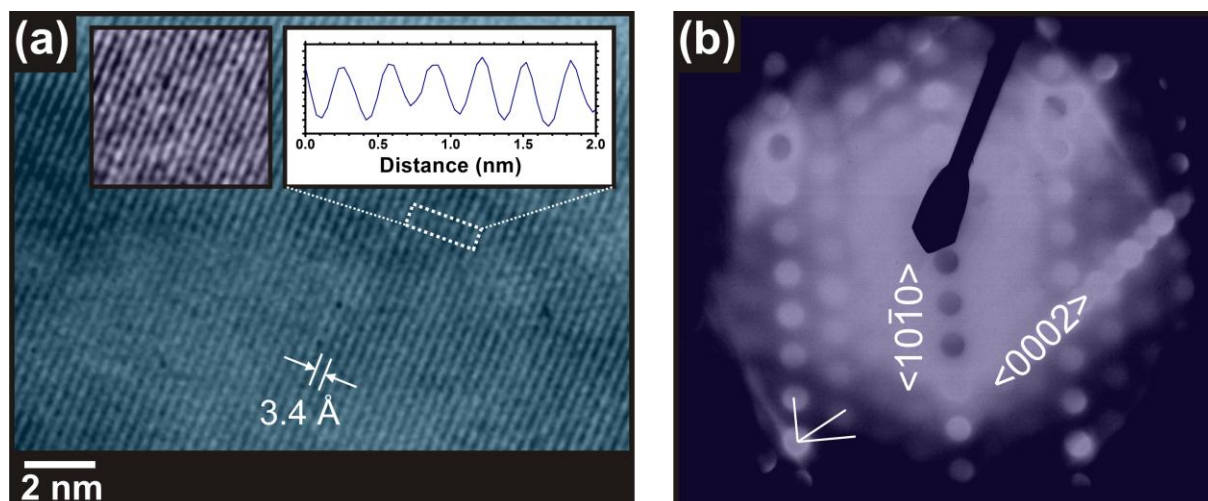
Figure 5.10 | ZnO NW TEM Analysis. (a) HR-TEM micrograph showing the periodic Wurtzite structure of the hydrothermal ZnO NW. The *insert* shows a Fourier-filtered image of the lattice and a lattice profile evidencing a fringe distance of 3.4 Å. **(b)** SAED pattern.

optical micrograph of a ZnO NW coated MWCNT thin film. The ZnO NWs (Figure 5.9(c,f)) are about 4 μm long, 63±11 nm in diameter and have an areal density of 5×10^5 cm^{-2}. The crystallinity of the hydrothermally grown ZnO NWs was studied by cleaving and drop casting IPA dispersed NWs onto a Si(100) substrate (Figure 5.11(a)) as well as by *in-situ* analysis (Insert, Figure 5.11(a)) using X-ray diffractometry (XRD, Bruker D8, Cu-Kα radiation, theta-theta geometry at 1.541 Å). The corresponding Miller indices are noted in the figure. The ZnO NWs are highly crystalline with unit cell lattice parameters of a = 3.25 Å and c = 5.21 Å. The NWs have a hexagonal (Wurtzite) structure similar to bulk ZnO. The strong 2θ=26° peak in the MWCNT-supported measurements (Insert, Figure 5.11(a)) originate from the graphitic planes of the MWCNTs. Representative HR-TEM and selected area electron diffraction (SAED) pattern (JEOL 2000FX TEM operated at 400 keV) of the hydrothermally grown ZnO NWs is given in Figure 5.10 and independently verifies the high crystallinity inferred from the XRD data.

EDX analysis (Figure 5.11(b)) clearly indicates the purity and stoichiometry of the ZnO NWs. The strong Si peak is associated with the supporting substrate. Assuming direct transitions[60], the estimated band gap of the ZnO NWs was determined from optical transmission spectrophotometry (Figure 5.11(c)). A Tauc gap of 3.37 eV, identical to that of bulk ZnO and consistent with the results of Anthony *et al.*[60], was estimated by linearly fitting to the $(\alpha h\upsilon)^2$ versus photon energy plot[61] (Insert, Figure 5.11(c)), where α is the absorption
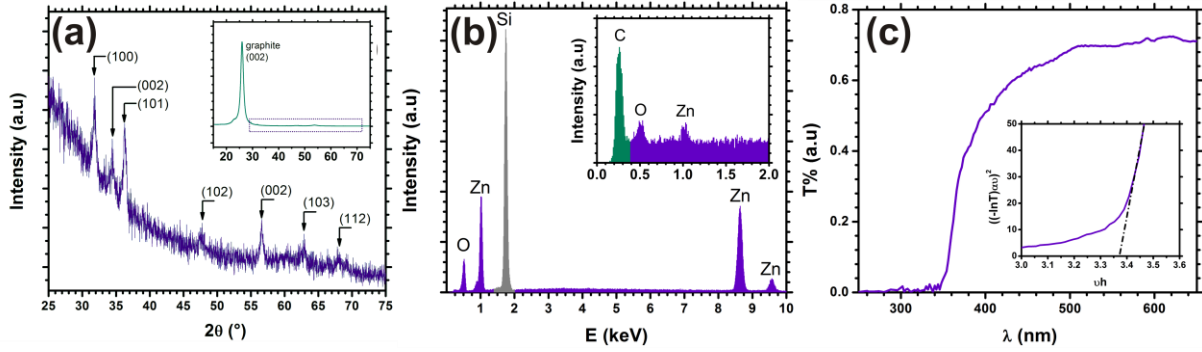
Figure 5.11 | ZnO NW crystallography. (a) X-ray diffraction pattern and **(b)** EDX spectrum of IPA-dispersed hydrothermally grown ZnO NWs dispersed on a Si substrate (grey). *Insert:* EDX spectrum of the ZnO NWs *in-situ* on the PET/CNT support clearly evidencing a strong graphitic signature (green) at $2\theta=26^o$ and the ZnO stoichiometry. **(c)** Optical transmission spectrum. *Insert:* $(\alpha h v)^2$ against photon energy (hv) giving a Tauc gap of 3.37 eV.

coefficient and is assumed to be proportional to -ln(T) for a direct transition. T is the measured optical transmittance[62].

The emission and FN characteristics of the bare MWCNT and the ZnO NW+MWCNT films are shown in Figure 5.12(a) and (b). Assuming work functions of 5.3 eV for the ZnO NWs and 5.0 eV for the MWCNTs, as reported elsewhere[58], the average field enhancement factors of bare MWCNTs and ZnO NW coated MWCNTs were 3457 and 3230, respectively. Field screening, associated with dense NW packing, has most likely prevented the enhancement factor from increasing. It is important to stress that for thin films the field enhancement factor is of little use when adequately describing the emission. The field enhancement factor relates to the geometry of the emitter[11]. Difficulties arise when one is posed the question: "What characteristic lengths is this field enhancement factor associated with?" In the case of vertically aligned nanofibres, the answer is simple – the emitter's aspect ratio (length/diameter). In the case of nanotube networks, such as those considered here, the ill-defined morphology of the network gives β a purely academic and comparative function. Consequently field enhancement factors can only be compared for nominally equivalent thin films, as was done above.

Large emission currents are important for realizing high brightness field emission displays and environmental lighting. As shown in Figure 5.12(a), the ZnO NWs reduce the maximum emission current by around one order of magnitude, under equivalent bias and vacuum conditions. The emission current has a positive exponential dependence on the applied field.
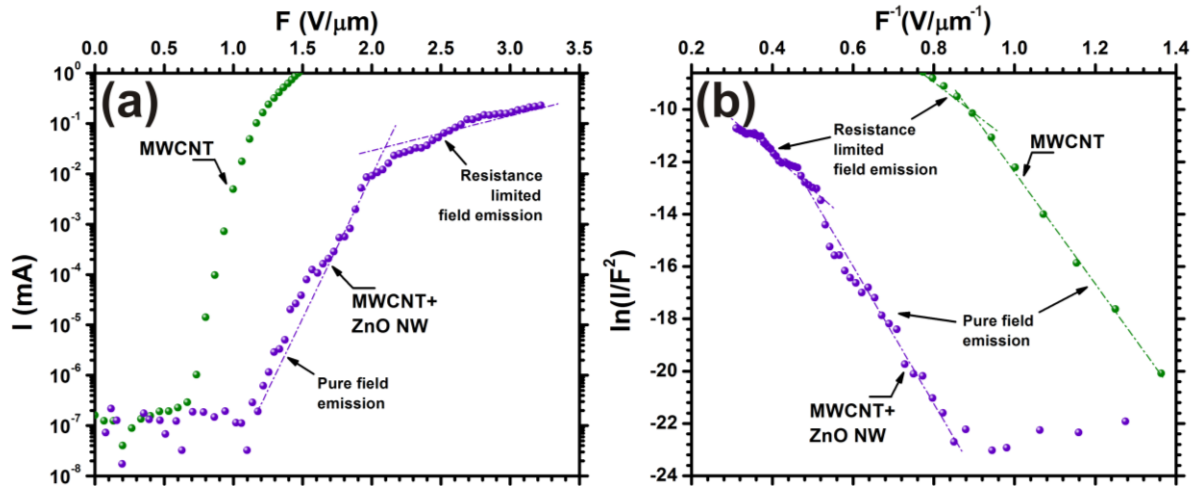
Figure 5.12 | MWCNT/ZnO NW field emission performance. (a) Accelerated I-F emission characteristics performed at 10^{-7} mbar and **(b)** the corresponding FN plot.

Surface protrusions, namely individual nanotubes and nanotube bundles with large enhancement factors emit at lower fields. As the field increases these 'dominating' nanotubes increasingly emit and eventually burn out before other emitters reach their threshold field. Thus, the current density is limited by the number of emitters switched on at any given time and bias. However, in the ZnO NW coated case, the axial resistivity of the nanowires limits the emission current from dominating emitters. Thus, these emitters do not burn out prior to the activation of other less-preferential emitters. The effect of the ballast resistance can be clearly seen in the FN plot shown in Figure 5.12(b). The maximum emission current is reduced by approximately one order of magnitude following ZnO NW deposition. Resistance limited field emission is amplified in the ZnO NW coated case. Indeed the bulk resistance of the nanotube network is combined, in series, with the axial resistance of the NWs which gives rise to the reduced saturation currents.

The turn-on fields of the bare MWCNTs and ZnO NW coated samples were 0.9 V/µm and 1.6 V/µm (for an emission current of 0.1 µA), respectively. The nanotube film does not purely function as the electrode. Lee *et al.*[63], Yang *et al.*[64] and Wei *et al.*[65] all reported that hydrothermally grown ZnO NWs typically emit at fields between 4 and 8 V/µm. Li *et al.*[51] too found, using equivalent hydrothermal ZnO NWs, negligible emission occurred for fields less than 10 V/µm. Thermally grown vapor-liquid-solid ZnO NWs typically turn-on at lower threshold fields[52, 53, 66, 67] though rarely less than 3 V/µm. Evidently, in the MWCNT+ZnO NW bi-layer structure detailed here the emission turn-on is dominated by the nanotubes but
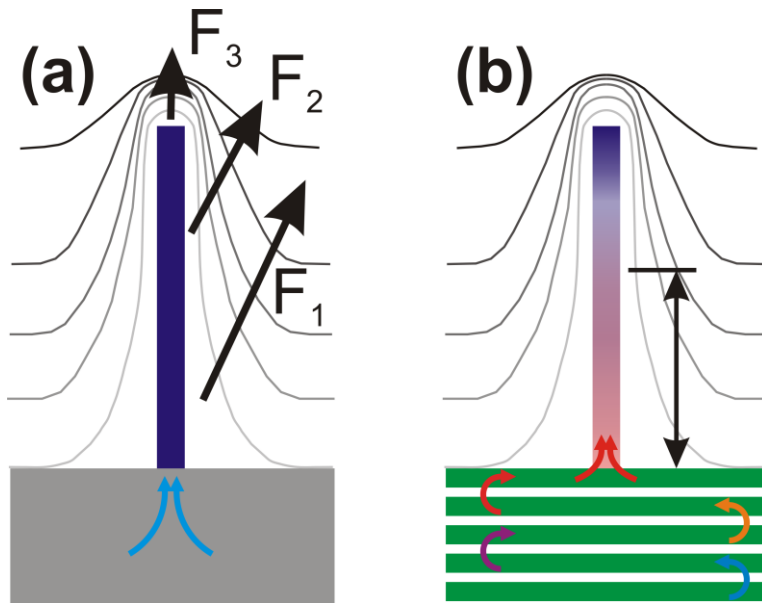
Figure 5.13 | Proposed hot-electron injection and emission. (a) ZnO NW emitter on a standard metallic support. (b) ZnO NW emitter on a MWCNTs. Hot electrons accumulate at the uppermost MWCNT. The injection depth is increased due to hot electron emission into the ZnO NWs. The greater the injection depth (arrow) the higher the observed extraction field ($F_1<F_2<F_3$). Lines of equipotential are shown in grey.

current-limited by the nanowires. Yu *et al.*[58] determined similar turn-on fields as those estimated in this study using Si-supported high temperature deposited ZnO nanomultipods on screen printed nanotubes. Li *et al.*[51] reported that conformally coating carbon nanofibres with ZnO NWs reduced the turn-on field by 4 V/µm. They offered no detailed explanation simply pointing out that the tip-on-tip geometry of their emitter increased the field enhancement factor which increased the local extraction fields, though Yu *et al.*[58] reasoned in favor of electron tunneling through the MWCNT/ZnO NW interfacial heterojunction. It was argued that, because ZnO has a smaller electron affinity (2.1 eV) than the nanotube support (4.8 eV), there was a lower-energy threshold for the electrons escaping from the conduction band into the vacuum. Hence the electrons were more readily emitted from the nanotube supported ZnO NWs than they would otherwise be in the bare metal-supported ZnO NW. Although the presented ZnO NW+MWCNT emitters do indeed turn-on at fields much less than pure ZnO NW emitters (Figure 5.12) the MWCNTs+ZnO NWs do not emit at fields less than the bare MWCNTs, as the studies of Li *et al.*[51] would suggest. One possible explanation for the reduced turn-on field of the MWCNT-supported ZnO NWs, compared to standard ZnO NW emitters on metallic supports, and the discrepancy between the results presented here and those of others can be derived by considering hot emission.

Figure 5.13(b) illustrates a possible hot electron model compared to a metal-supported ZnO NW (Figure 5.13(a)). The MWCNTs are highly graphitic and conduct with little scattering along their length. They have comparatively low electron densities, compared to a metal,
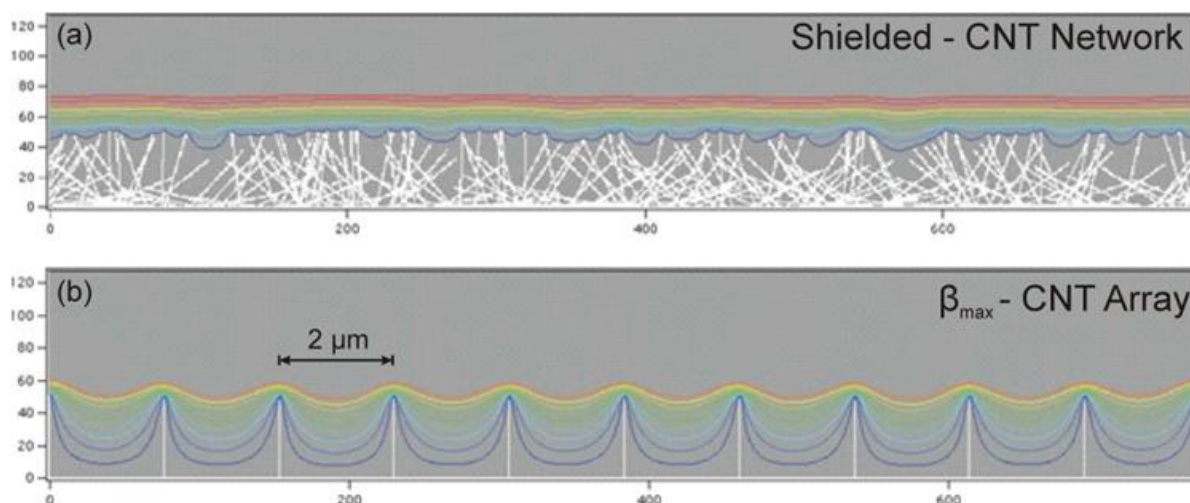
Figure 5.14 | Nearest neighbour electrostatic shielding. **(a)** A random network of high-aspect field emitters and **(b)** a period array of high aspect field emitters. The local electric fields are much higher in the periodic aligned array case as the emitters do not shield one another and give optimal field enhancement factors when the pitch is approximately twice the nanotube height. From Nilsson *et al.*[1, 2].

which substantially increases the thermalization time (50 fs for a metal[68] compared to 500 fs for a nanotube[69]). When excited electrons tunnel between nanotubes they have excess kinetic energy compared to the local population. These hot electrons accumulate at the uppermost MWCNT at the base of the ZnO NW emitter and are injected from the MWCNTs into the conduction band of the ZnO NWs through the Schottky barrier. The hotter the emission (i.e. the greater the kinetic energy of the electrons) the greater the injection depth into the NW. Combing the potential drop across the length of the NW and the field profile surrounding the NW (high field at tip, low field at base) then the greater the injection depth the higher the effective field the electrons see. The higher the observed field the more efficient the emission and the lower the turn-on field. The rapid thermalisation time and high electron densities in traditional metal electrodes prevents hot emission which manifests as a high turn-on field. Returning to the nanotube-supported case, if electrons are injected with high kinetic energy into a suitably long NW then turn-on fields less than those of the bare MWCNTs are certainly possible and this would account for the unusually low (less than carbon) turn-on fields reported by Li *et al.*[51]. The proposed model supports these findings.

Although high currents (mA) have been demonstrated using the nanotube-based thin film emitters developed here, extremely high current densities are still out of reach. To increase the emission current density further, which is important for applications such as X-ray and

microwave sources for example, significantly larger enhancement factors are necessary. For thin film technologies the high packing densities and nanotube misalignment results in significant electrostatic shielding which reduces the effective enhancement factor[70, 71]. Figure 5.14(a) illustrates this nearest neighbour electrostatic shielding process[1]. Lines of equipotential illustrate that although the composite nanotubes have high aspect ratios (and therefore potentially high field enhancement factors), it is not possible to access them. As a result, the current densities are substantially reduced. The inter-tube pitch must be approximately twice their height in order to minimize nearest-neighbor shielding for maximized emission current (Figure 5.14(b))[1]. Vertically aligned nanotube arrays solve this problem. Teo *et al.*[41] reported on the deposition of periodic arrays, grown by PE-CVD where the plasma sheath field aligns the nanotubes, giving current densities as high as 12 A/cm^2 (modulated)[72]. Accurate control over the nanotube alignment was also found to be critically important in optimizing the field emission properties. PE-CVD offers a viable means of accurately controlling not only the nanotube density (by careful consideration of the plasma pre-treatment) but also the alignment, length and even the crystallographic structure. However the PE-CVD of crystalline nanotubes and nanofibres of plastic substrates has yet to be demonstrated convincingly. Alternative substrates must therefore be considered.

5.4.3 In-situ Nanofibre Growth on Electrolysed Stainless Steel Mesh

A possible alternative to forming enhanced functionality TFCs out of nanomaterials is to employ more traditional porous TFC materials and combine them with nanostructures. Porous metal meshes, one such cheap and widely available TFC, are used in a variety of applications due to their mechanical flexibility, pitch-controlled transparency, and high thermal and electrical conductivities. In the past, composites have been developed where CNFs have been 'glued' to metallic substrates. Although such composites enhance the substrates field emission performance, weak adhesion and poor electron transparency at the CNF/substrate interface results in fibre de-anchoring and resistive losses during operation. Directly depositing CNFs onto metallic substrates, which has proven extremely difficult in the past due to catalyst diffusion and passivation, not only greatly increase the robustness of the surface adhesion, but simultaneously introduces arrays of high aspect-ratio tips which dramatically improves the field emission performance of the native surface[73, 74] and will ultimately facilitate the development of many novel field emission applications.
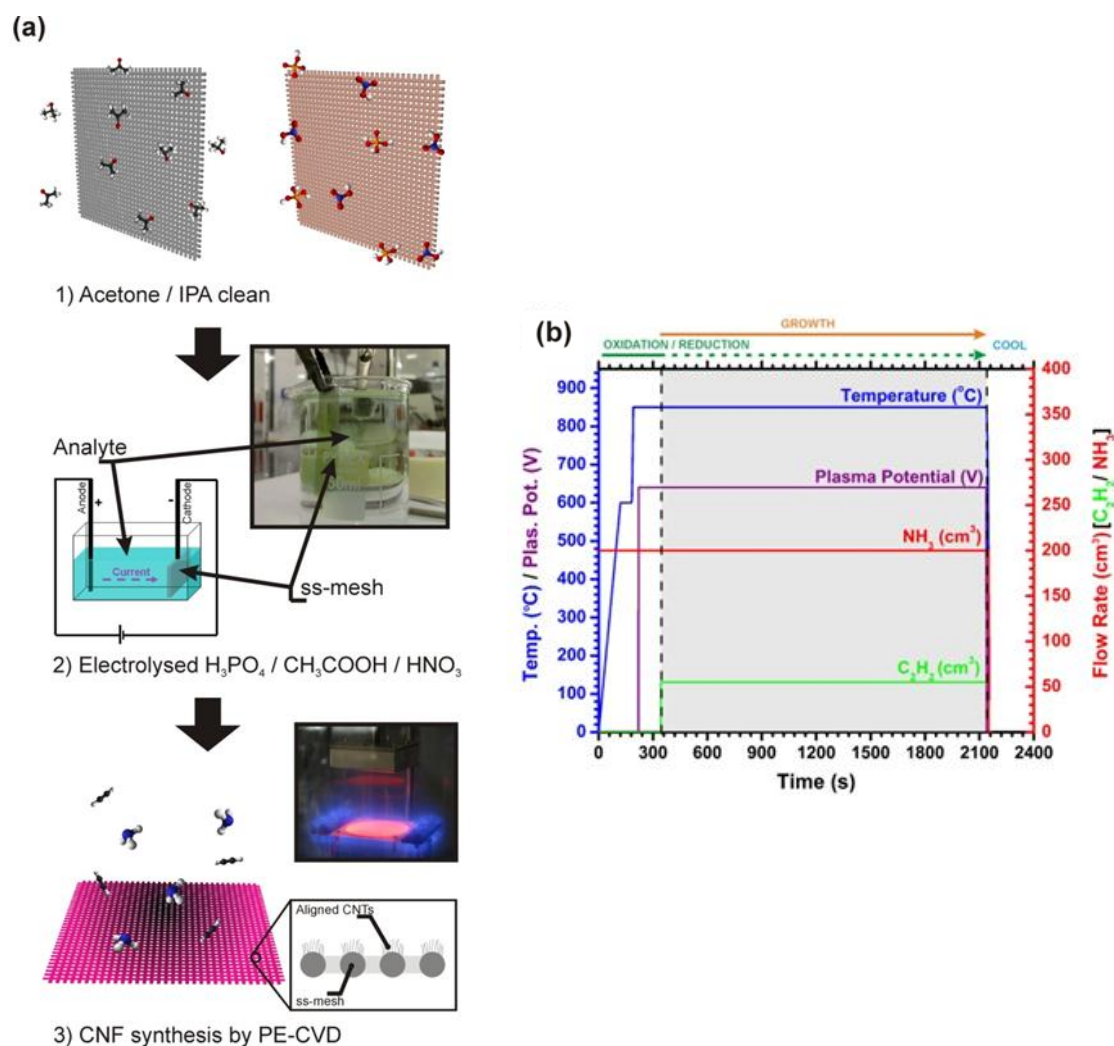
Figure 5.15 | Nanofibre PE-CVD on electrolysed stainless steel mesh. (a) Schematic of the vertical CNF synthesis on ss-mesh via electrolyzed etching. Typical applied bias = 10 V (250 V/m, ss-mesh cathode, Fe foil anode). Schematic and optical micrographs of the pre-treatment process and the PE-CVD system during CNF synthesis (200 sccm NH$_3$: 55 sccm C$_2$H$_2$. 5 mbar / 640 V, 45 W, 70 mA). **(b)** PE-CVD thermal, plasma potential and gas flow profiles during synthesis.

The main strategies for composite fabrication are *ex-situ* coating and *in-situ* deposition. In the *ex-situ* approach a variety of binding materials are employed to increase the level of adhesion between the substrate and pre-grown nanofibres[75, 76], as previously discussed. These nanofibres are homogenously dispersed into binders, such as Teflon and Nafion, via damaging acid treatments and ultrasonication, and then cast, sprayed, or dip deposited onto the desired substrates. A huge variety of substrates can be coated in this manner. However, nanofibre immobilization in the binder medium occludes much of the field emitting surface and introduces large interfacial resistances. Macroscopically uniform alignment of the

Fe	Cr	Ni	O	Mn	Si
64.40	18.86	8.30	4.04	2.40	2.00

Table 2 | Typical bulk composition of the as-received ss-mesh by weight per-cent (wt.%). Composition determined by EDX spectroscopy.

nanofibres is not possible. *In-situ* deposition negates many of these detrimental features. In this case, transition metal catalysts are deposited in powder[77], slurry[78] or vacuum processes[79]. Powder and slurry catalyst suspensions require considerable post-processing and, in practice, during their filtration and preparation experience significant losses in the available catalytically active species due to attrition[5]. Vacuum processes obviate many of these problems but are comparatively costly and particularly time consuming. Most studies on the *in-situ* growth of CNFs on metallic substrates detail the growth of highly disordered and unaligned nanofibre and nanotube networks and have focused on either catalyst deposition or surface preparation via physical abrasion and thermal oxidation[4, 5, 80]. Mesoporous silica supports based on sol-gel preparation[81], carbon cloth[74] and plastics[82] have also been considered though they all require direct catalyst deposition prior to growth. Various metallic alloys have also been considered. Metallic substrates including Kanthal, an Fe-Cr-Al alloy[83, 84], Inconel[85] and Nichrome / Chromel[86] have all showed some promise. Rather interestingly though the catalysts in these studies were typically solution or vapour-phase deposited, iron nitrate salts, rather than activating the intrinsic catalyst material available in the bulk native substrate[87]. Both Kanthal and Nichrome are over an order of magnitude more expensive per unit volume than stainless steel. Masarapu *et al.*[88] reported unaligned synthesis on stainless steel foil using strong acid exposures. However, as with the studies on Kanthal, Iconel and Nichrome, the resulting nanofibres were randomly aligned and spaghetti-like in morphology which degrades the composites field emission performance due to electric filed shielding, as discussed earlier. Furthermore, the relatively few studies that have managed to grow vertically aligned forests typically produced conformal and dense forests. Paradoxically, for optimal field emission, sparse arrays are preferential (Figure 5.14). In light of this it becomes apparent that there has been very limited success in producing the required geometrically defined CNF arrays through low-cost means on Fe and Ni containing alloys.

An industry compatible alternative for the direct-deposition of highly-aligned, well-spaced CNFs on metallic substrates is necessary in order to minimise nearest neighbour

electromagnetic shielding and produce high-performing field emitting composites. Catalysis activation of low-cost and widely available Fe, Ni or Co containing metallic supports through single-step electrochemical reactions offers one possible solution. The technique developed here produced high levels of CNF homogeneity, superior alignment and excellent inter-CNF spacing which have yet to be demonstrated elsewhere. In this section we investigate the field emission properties of these CNF/ss-mesh composites. The results presented establish a feasible, reliable, and scalable approach to the fabrication of low-end, flexible and porous field emitting conducting substrates.

Type 304 stainless steel (ss)-mesh (Alfa Aesar, 36% pitch, 50 μm fibre diameter) provided the combined support and catalyst material. The typical bulk composition is detailed in table 2. Preliminary SEM analysis on etchant exposed samples showed negligible surface alteration, which was not unexpected given the typically high corrosion resistance of stainless steel. Consequently an electrochemical approach was used to accelerate the surface preparation. 20x20-mm-samples were connected to the electrodes of a simplified potentiostat setup, as shown in Figure 5.15(a). Note that, unless otherwise stated, ss-mesh was used as both the cathode (CNF growth substrate) and the anode (driven electrode). All substrates were degreased in acetone and isopropanol prior to pre-treatment. No polymer passivation was applied to the driven electrode. The analyte was a commercially available metal etchant (Michrochem) nominally composed of phosphoric acid (H_3PO_4, 66.3-70.3 wt.%), acetic acid (CH_3COOH, 8.7-10.7 wt.%) and nitric acid   (HNO_3, 1.5-2.0 wt.%) diluted in a 1:1 ratio with de-ionised (DI) water. The analytes were agitated for 10 min prior to pre-treatment. Samples were carefully lowered into the solution for 10 s, under zero applied bias, to dynamically stabilise. A direct-current potential was then applied for a defined time to electrolyze the ss-mesh. Experiments were carried out at atmospheric pressure and ambient temperature. Figure 5.16(a,b) shows the surface before and after electrolysing pre-treatment.

Nanofibre synthesis was achieved by PE-CVD performed in a cold-walled, commercially available reactor (AIXTRON Nanoinstruments Ltd.). Pre-treated samples were placed on a resistively heated graphite stage which was thermally ramped to 600°C (5°C/s) and held constant for 30 s. The temperature was then further increased to 850°C (5°C/s), and growth was immediately initiated by the introduction of NH_3 (200 sccm) and C_2H_2 (55 sccm) under a controlled chamber pressure of 5 mbar. A low-power, direct-current glow-discharge plasma
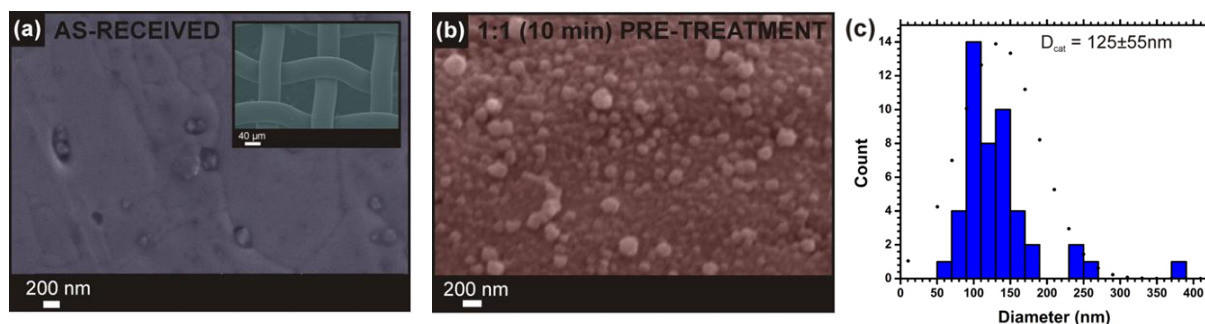
Figure 5.16 | Electrochemical surface modification. Comparative SEM micrographs of the ss-mesh; **(a)** as-received (*Insert:* low-magnification micrograph of the of the as-received ss-mesh); and **(b)** after pre-treatment. **(c)** Catalyst island diameter (D_{cat}) histogram after the pre-treatment process. Normal distributions were fitted to data to extract the mean (125 nm) and standard deviation (55 nm). Very few catalysts islands smaller than 50 nm were observed during high-magnification (<40 nm) inspection.

was then induced through the application of 640 V (45 W, 70 mA) between the stage and gas inlet to assist in CNF alignment. One major benefit of the direct growth of nanofibres on ss-mesh through a combined electrochemical process and PE-CVD is that any size and shape of substrate can be coated which imparts tremendous levels of design flexibility across a variety of application platforms. After 20 min CNF growth was terminated by evacuating the chamber to a base pressure of 2×10^{-2} mbar and cooling the stage to ambient under a flow of 200 sccm ultra-high purity N_2. The complete thermal profile, gas flows, plasma potentials, and chamber pressures are summarised in Figure 5.15(b). High resolution scanning and transmission electron microscopy (HR-SEM / TEM), selected area electron diffraction (SAED) and energy-dispersive X-ray (EDX) spectroscopy were performed using a Carl Zeiss 50 (operated at 10 kV), a JEOL JEM-4000EX (operated at 80 kV), and a Schottky field emitting FEI-Philips XL30 (operated at 30 kV), respectively, to examine the detailed structure and morphology of the synthesised CNFs and ss-mesh, in addition to analysing the elemental content of the analyte pre- and post-processing. Crystallographic information on the CNFs graphitic structure was extracted using a Philips CM300 field emission-TEM (operated at 300 kV) and an aberration corrected FEI Titan[3] 80-300 (operated at 80 kV) in scanning TEM mode with a bright-field detector and annular dark-field detector. Additional data on the graphitic structure was revealed spectroscopically using a Renishaw In-Via, He-Ne laser, Raman spectrophotometer operated at 633 nm with an incident power of 3 mW. EM micrographs were examined using SPIP[TM] image analysis software (v. 5.15) to ascertain the comparative quantified alignment of the CNFs synthesised in this work and to compare with
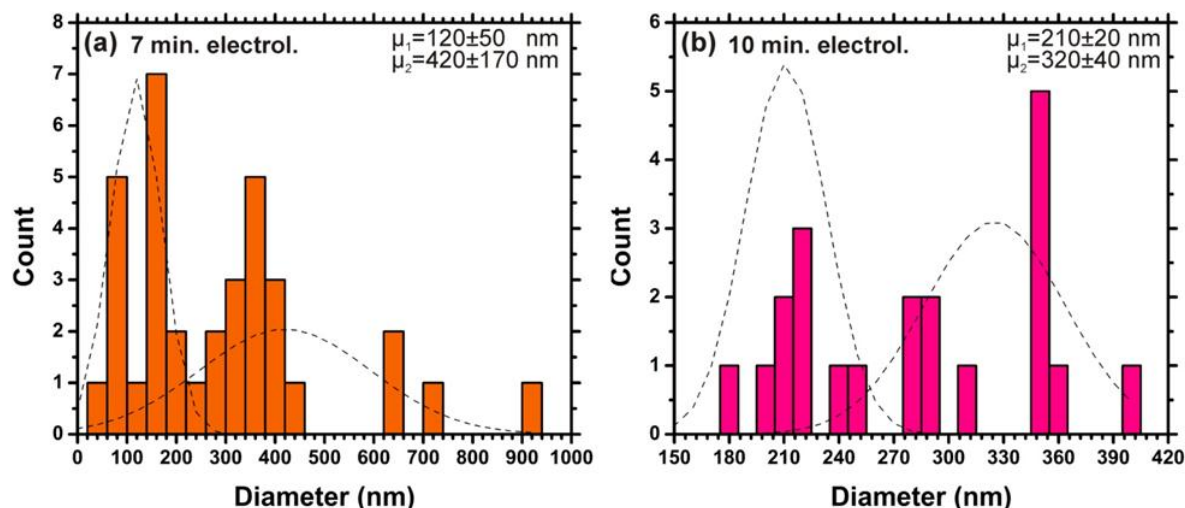
Figure 5.17 | Nanofibre diameter as a function of electrolysing time. CNF diameter distributions for samples electrolyzed for; **(a)** 7 min and **(b)** 10 min in a 1:1 solution at 250 V/m. Normal distribution fits shown indicating the CNF diameter means and standard deviations

other published data. Field emission measurements were performed using a LABVIEW controlled, home-built vacuum system evacuated using a turbo-molecular pump to $<2x10^{-7}$ mbar connected to a 5 kV power supply and a HP 34401A source-meter. CNF/ss-mesh samples formed the cathode and an indium tin oxide coated glass slide formed the anode. Potentials were swept several times and emission characteristics were recorded on both the positive and negative incremental sweeps.

Figure 5.16(a) and (b) show SEM micrographs of the as-received ss-mesh and the pre-treated ss-mesh (1 (DI):1 (etchant), 10 min). Spherical structures (catalyst islands) 125±55 nm in diameter, were found to cover the surface. High magnification SEM showed very few catalysts islands <40 nm in diameter. Figure 5.17(a) and (b) show the CNF diameter distributions for 7 and 10 min pre-treatments, respectively. Two dominant peaks occur in the normal distributions at 120±50 nm and 420±170 nm for the 7 min pre-treatment and 210±20 nm and 320±40 nm for the 10 min pre-treatment. These dominant peaks tend to a single diameter for increasing treatment times. Furthermore, the single peaks occur at increasingly large diameters indicating enhanced levels of surface uniformity over increasing electrolyzing durations. Accurate control over the pre-treatment time was vital for reproducible CNF growth. Varying the pre-treatment time coarsely controlled nominal catalyst island size, and the consequent CNF diameter. However, this approach to diameter control was limited by modest content variation in the as-received ss-mesh samples which affected the surface
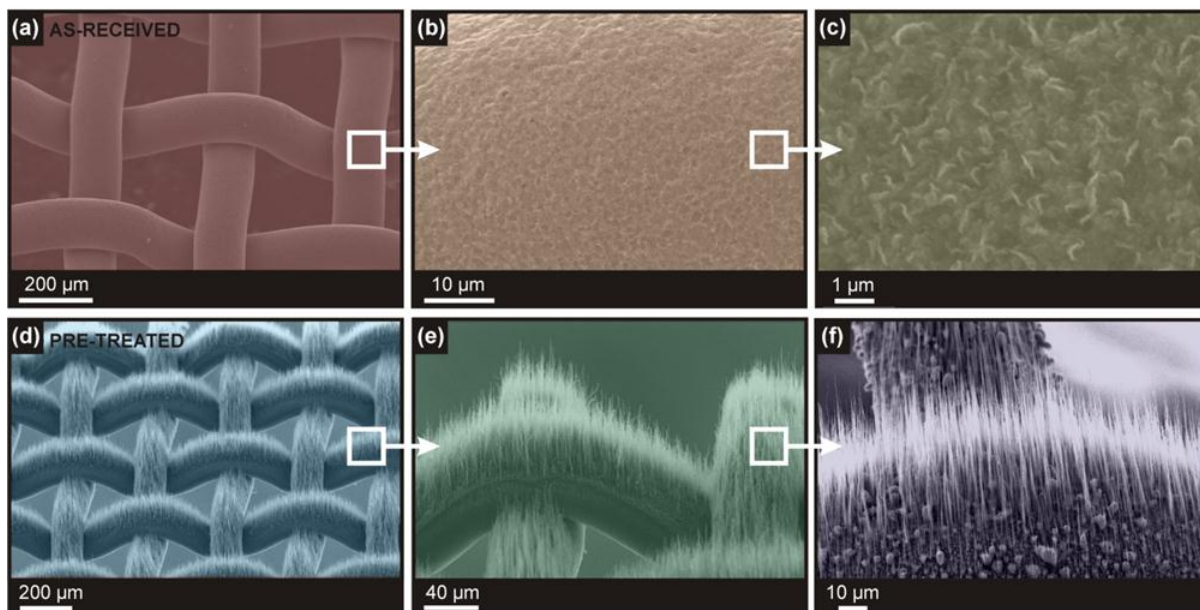
Figure 5.18 | Nanofibre growth with and without pre-treatment. SEM micrographs following exposure to PE-CVD growth conditions. **(a-c)** As-received ss-mesh. No CNF growth was observed. **(d-f)** Pre-treated mesh after PE-CVD. CNFs are clearly seen. The catalyst bed was prepared by the electrolyzed etchant technique.

modification rate. It was found that opting for a less aggressive electrolysing environment reduced the rapidity of the pre-treatment process and increased the degree of control. Using ss-mesh of higher uniformity may also permit greater diameter control.

Figure 5.18(a-c) and (d-f) show SEM micrographs (post-CNF synthesis) of the untreated as-received ss-mesh and the pre-treated ss-mesh, respectively. No CNFs were observed on the as-received ss-mesh, whilst vertically aligned CNFs grew on the pre-treated samples. The nominal length and diameter, which depend on the exact growth conditions, of the CNFs on the pre-treated ss-mesh were 10-50 μm (linear growth rate = 8-40 nm/s) and 70-310 nm, giving typical aspect-ratios in excess of 150. Figure 5.19(a) shows Raman spectra obtained under ambient conditions. Interestingly, little-to-no substrate electroluminescence related spectral features were observed. Lorentzian fitting to the measured spectra revealed nominal D and G peaks at ~1329 cm^{-1} and ~1595 cm^{-1}, respectively. An I_G/I_D ratio of 1.67-1.85, indicate that the CNFs are formed from relatively small carbon clusters and are most likely bamboo-structures, which is not wholly unexpected given the use of plasma during synthesis[89, 90]. Raman spectra were obtained at various positions and were consistent between the central and peripheral regions, demonstrating a high level of macroscopic uniformity in the electrolysing process and CNF growth. Figure 5.19(b) shows a typical HR-
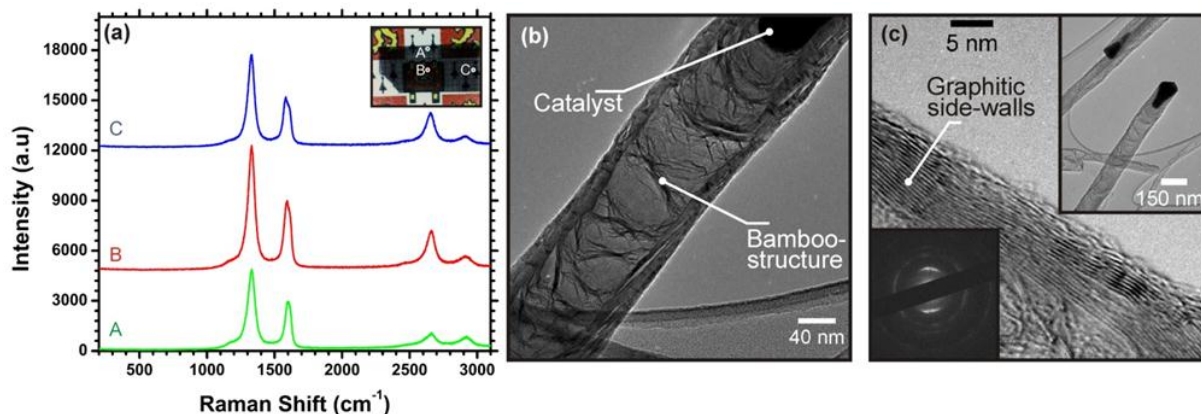
Figure 5.19 | Nanofibre characterisation. (a) Raman spectra collected at 3 mW incident power (633 nm excitation). The three spectra represent accumulations at locations A, B, C (detailed positions are shown on the insert). Intensity spectra, measured in arbitrary units (a.u), are vertically displaced for clarity. **(b)** A typical HR-TEM micrograph of a synthesised CNF highlighting the defective bamboo-structure. **(c)** High-resolution micrographs and the corresponding SAED pattern (Lower left insert) evidencing the multiple graphitic side-walls. Upper right insert: Low-resolution TEM micrograph showing an extruded catalyst particle at the CNFs tip.

TEM micrograph of a synthesised CNF. The crystalline nature of the side-walls is evidenced in Figure 5.19(c). The graphitic multi-walled CNFs are formed from 14-44 graphene planes with an inter-plane separation of ~0.39 nm. The characteristically nested circular features in the SAED pattern (lower insert, Figure 5.19(c)) support the relative crystallinity assessed from the Raman spectra, and the polycrystalline turbostratic nature associated with the multiple graphitic side-walls[91]. The HR-TEM analysis verified that the CNFs were formed from multiple defective bamboo-type sections spaced ~80 nm apart, and that the electrochemically derived catalyst particles tended to reside at the tips of the CNFs suggesting a predominately tip-growth mechanism (upper right insert, Figure 5.(c)). Cross-sectional EM analysis showed that approximately 42% of the total surface area was coated with vertically aligned CNFs. CNF packing densities and inter-CNF spacing were estimated to be 4×10^8 cm^{-2} and 0.5-5.0 μm, respectively.

Figure 5.20 shows the UV-Vis spectra of the as-received ss mesh and the nanofibre coated ss mesh. The ss-coated mesh has an optical transparency, at 550 nm, of ~25%. The CNFs reduced the transparency of the as-received ss-mesh by ~10%. Higher levels of transparency can be achieved using wider pitched mesh.
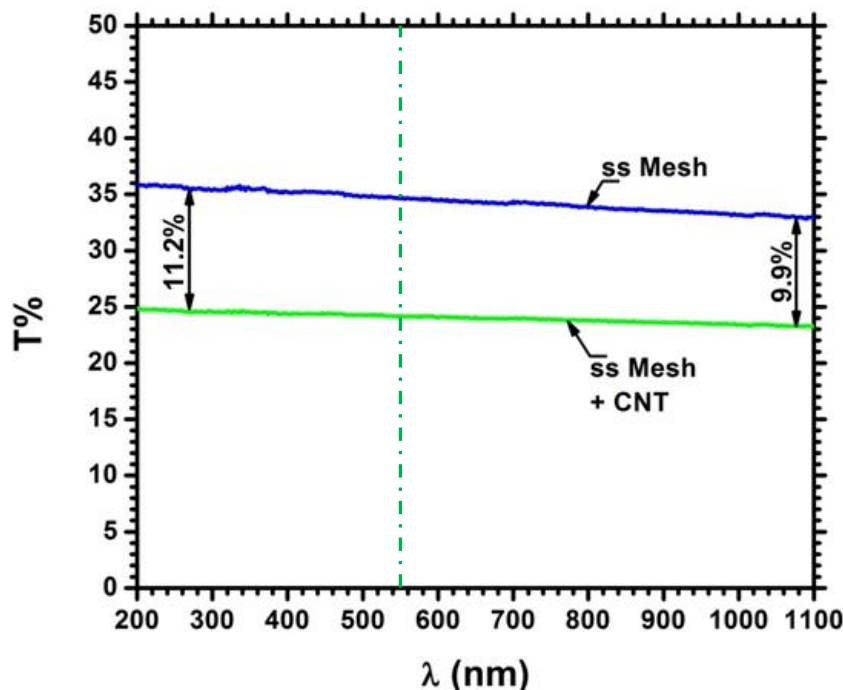
Figure 5.20 | Composite transparency. UV-Vis spectra of the as-received 50 μm pitch ss-mesh and the CNF coated ss-mesh. The nanofibres uniformly reduce the transmission by 10-11% across the entire optical window.

To investigate the mechanical robustness of our CNF-coated samples were flexed through approximately 10^2 cycles through an approximate bend radius of ~4 mm (sample dimensions 10 mm x 10 mm) to examine the extent of CNF de-binding. SEM analysis confirmed a negligible loss in CNFs post-flexing. However the ss-mesh did become increasingly brittle following the high-temperature CNF synthesis. One way to maintain mechanical stability of the ss-mesh is to reduce both the synthesis temperature and thermal ramp.

In order to demonstrate the commutability of the pre-treatment process, electrolysed mesh samples were exposure to various proven nanotube and nanofibre growth conditions (see chapter II). Exposure to alternative growth conditions formed nanofibres of varying types, as expected. For example, 4% C_2H_2 diluted in a H_2 atmosphere (25 mbar) at 700°C, resulted in a conformal coating of extremely dense vertically aligned forests of multi-walled nanotubes, 10.6±4.7 (S.D) nm in diameter. The suitability of both Fe and Ni foil anodes was also investigated (foil anode, ss-mesh cathode). Uniform CNFs were formed in both cases and negligible variation in CNF uniformity was observed by SEM microscopy for pre-treatment durations of 600 to 1200 s.
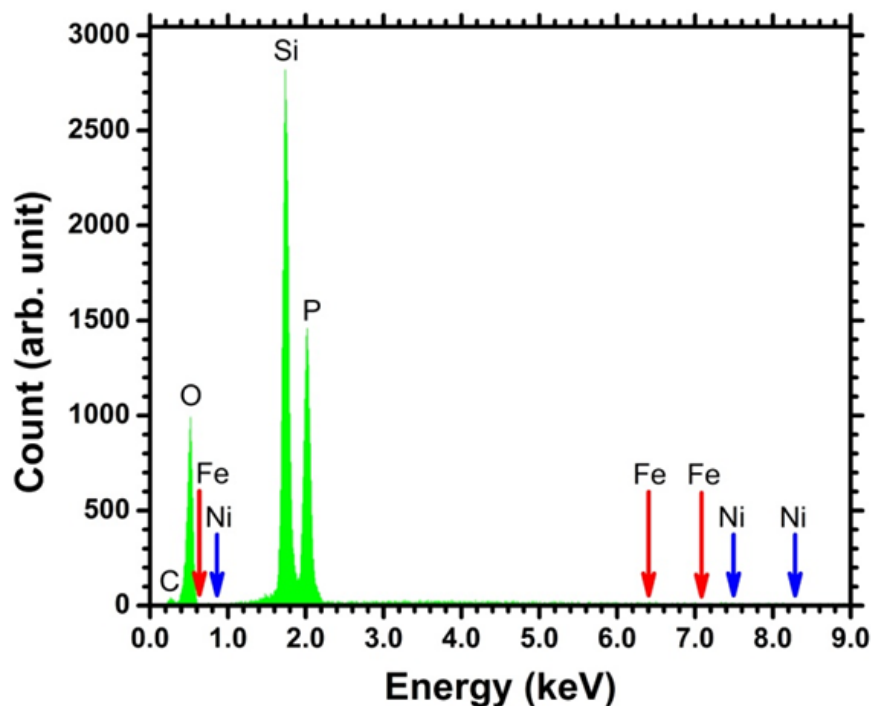
Figure 5.21 | Composition of the electrolyte post-treatment. EDX spectrum of the etchant solution post-processing. Rather unexpectedly, no Fe or Ni peaks were found across a wide range of process times and anodic potentials.

A large body of literature exists on the nitric and phosphoric acid corrosion resistance of stainless steel[92-94]. However, in most investigations standard potentiostats were used. Here the driven and measuring electrodes are polymer passivated relative to the material under study. Hence the available data, and speculations therein, only partly explain the surface evolution observed in this study. Nonetheless, two processes clearly dominate: dissolution and driven-precipitation. Driven-precipitation refers to the effect of the externally applied electric field. In an attempt to resolve the question: Is the solution etching (dissolution) or electroplating (driven-precipitation)? A variety of pre-treatment times, anodic potentials, polarities and electrode materials were investigated. A complex relationship exists between the dissolution and precipitation mechanisms occurring during the pre-treatment. In a weakly electroplating process the divalent Fe and Ni ions, the necessary CNF catalysts and primary constituents in the ss-mesh, liberated from either the counter electrode (Fe or Ni foil, Advent, 99.5%) and / or the ss-mesh itself, is deposited on the ss-mesh. However, to achieve this extent of surface roughness through dissolution alone, very high dissolution rates would be required. These would potentially exceed the liberation rate of the analyte, suggesting the presence of a concurrent surface evolution process. Nevertheless, the source of the catalyst material requires some clarification. If a dissolution-type process dominates then the acid pre-
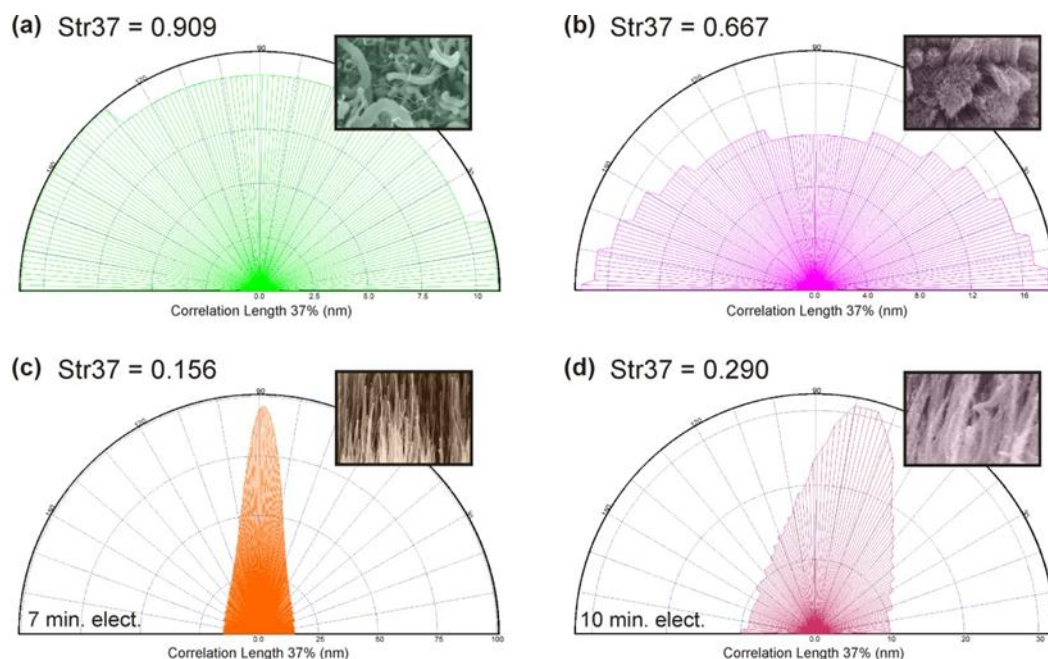
Figure 5.22 | Comparative alignment of various CNF deposition techniques. SEM micrographs reproduced from **(a)** Vander Wal *et al.*[4], **(b)** Martinez-Hansen *et al.*[5], **(c)** 7 min. (this work) and **(d)** 10 min. pre-treatments (this work).

treatment would simply increase the surface roughness of the ss-mesh whilst removing catalytically-poisonous material[95]. In this instance, catalyst island formation would be achieved through the removal of surface contaminants. To investigate this further, and potentially remove the possibility of driven-precipitation, electrolyzed pre-treatment was repeated using a graphite anode. Samples were then exposed to typical CNF synthesis conditions, as described above. Graphite was selected due to its excellent corrosion resistance to phosphoric and nitric acid[96] and negligible Fe, Ni or Co content (EDX data not shown). Analytes were electrolyzed for 10 min. Characteristic globular catalyst islands were formed, though much larger in size (560 ± 260 nm). In this instance no CNF growth was observed upon PE-CVD. This supports the conjecture that during the pre-treatment the analyte not only etches the ss-mesh but also, and perhaps more importantly, functions as a weakly electroplating (driven-precipitation) solution of the liberated metallic ions.

At this stage the role of the acetic acid is still unclear. Nevertheless, type 304 stainless steel has demonstrated extremely high resistance to acetic acid[97]. Plasma exposure during CNF synthesis is also believed to play an important role in catalyst reduction and surface evolution, rather than simply aligning the CNFs[98, 99]. Thermal CVD alone typically formed low-density,
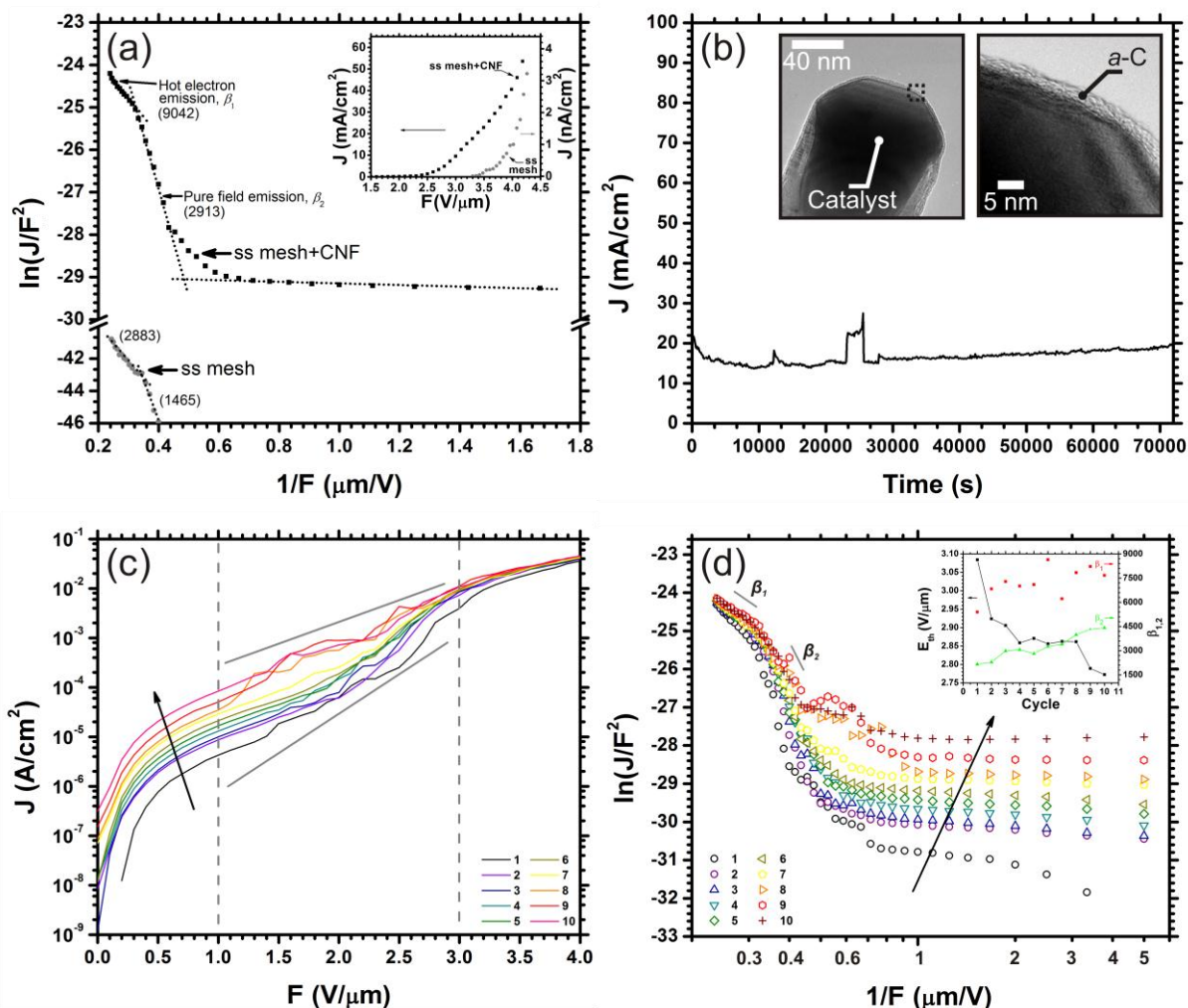
Figure 5.23 | Field emission performance. (a) Comparative FN plot of the as-received ss-mesh and the CNF/ss-mesh composite. Experimental data fitted to eq. (4.4). *Insert:* Electric-field dependence of the emission current density. **(b)** Temporal stability test conducted at 5×10^{-6} mbar. *Inserts:* HR-TEM micrographs of a narrow CNF tip. The metallic catalyst and *a*-C dominate the emission sites. **(c)** Successive cyclic stability test. **(d)** FN plot of the cyclic performance. *Insert:* Variation in threshold field (F_{th}) (for an emission current of 6.25 mA/cm^2), β_1 and β_2 as a function of the cycle number.

randomly orientated CNF mats, with poor reproducibility. This effect requires further investigation.

Nitric and phosphoric acids are known to be strong oxidising agents. At acid exposed surfaces, metallic elements within the alloy (and foil counter electrode) become oxidised and enter the analyte in their corresponding ionic form: Fe^{2+}, Ni^{2+} and Cr^{3+}. As reported elsewhere Fe, Cr and Ni oxides form at anodic potentials greater than the equilibrium potential[4]. The deposition of iron oxide on the ss-mesh takes place through a dissolution / driven-precipitation mechanism (i.e. a combined etching / electroplating-type reaction), as discussed

previously - where the presence of iron oxide is strongly evidenced by the orange discolouration of the ss-mesh upon air exposure. Conversely, Cr and Ni oxides tend to nucleate directly on the ss-mesh electrode[96]. At elevated temperatures during CNF synthesis, in a NH_3 atmosphere, these metal oxides reduce and revert to their catalytically active form[4, 100]. In contrast, however, phosphoric acid is known to convert iron(III) oxide, which is formed on the ss-mesh through the action of the nitric acid, to a catalytically inactive ferric phosphate layer; a reaction strongly suggested by the green hue of the etchant solution during pre-treatment processing. This passivation process renders portions of the stainless steels surface catalytically inactive and may therefore give rise to the observed inter-CNF spatial regulation.

To further investigate the underlying mechanism of catalyst island derivation by the electrochemical pre-treatment, the elemental content of the analyte was studied using EDX spectroscopy in the ss-mesh cathode and Fe foil anode case. After samples were electrolyzed residual solutions were drop cast onto 2x2 mm Si substrates, heated to 80°C and gently dried with N_2 to remove excess solution. Figure 5.21 shows the EDX spectrum of the post-electrolyzed solution. Across a variety of pre-treatment times (10-600 s) and applied potentials (0-750 V/m) EDX spectra showed consistently strong P (~19.4 wt.%), Si (~22.3 wt.%), C (~12.0 wt.%) and O (~46.3 wt.%) peaks. Most importantly, however, is that no catalyst (Fe, Ni or Co) signatures were observed. Thus, it is most likely that the majority of the liberated catalyst materials, from both the ss-mesh and anode, have short residence times in the analyte and are efficiently and rapidly deposited on the ss-mesh.

Although a conformal native oxide exists on the as-received ss-mesh, which in principal can be similarly reduced to form active catalyst sites, it is often substantially thinner and smoother than the electrochemically oxidised surface and the oxidation process of this native oxide proceeds through an inefficient tertiary oxidation-reduction-growth process during CNF synthesis. During reduction, the immobile native oxide does not readily reform into suitable catalyst sites. Thus, although suitable catalyst materials are accessible, suitable catalyst topographies are not. In general, catalyst restructuring and nucleation site formation in thin films occur through surface and interface free-energy minimization[101]. However, for bulk materials such island-formation is less energetically favourable. The electrochemical pre-

oxidation step enhances the surface roughness and removes the need for surface mobilisation during reduction and is, as a result, critical in the CNF nucleation.

Figure 5.22 depicts the comparative alignment of the CNFs (this work) and other published reports evaluated using the Str37 function of the SPIP[TM] Image analysis software, as employed in the previous section. Highly aligned fibres give enhanced field emission performance[11]. The Str37 values evaluated from Vander Wal *et al.*[4], Martinez-Hansen *et al.*[5] and this work (7 / 10 min pre-treatment) were found to be 0.91, 0.67 and 0.29 / 0.16, respectively, demonstrating the high-degree of alignment achieved through the single-step electrochemical pre-treatment. For field emission applications, employing vertically aligned CNFs, Nilsson *et al.*[2] and Groning *et al.*[102] (Figure 5.22) determined that to minimise inter-CNF electrostatic shielding, thereby optimising the attainable field enhancement factor without compromising the emitted current density, the optimum spacing between individual vertically aligned CNFs is approximately twice their height. Indeed, here we see that the inter-CNF spacing is regulated by the electrochemical pre-treatment and that for maximized field enhancement CNFs ~10 μm in length are desirable, which correlate well with our reported data.

To evaluate the current densities from the measured currents, the effective emission area was calculated by careful consideration of the sample area, the ss-mesh porosity, the CNF morphology and the CNF packing density. The field emission characteristics of the control (as-received) ss-mesh and the CNF/ss-mesh composite are shown in Figure 5.23. The emission characteristics are linear in the low-field regime and compare favourably with those of PE-CVD synthesised CNTs on less exotic substrates[51, 103]. The insert of Figure 5.23(a) shows the J-F plot. The corresponding FN plot has been fitted using the Fowler-Nordheim equation (4.6). Comparing the emission characteristics of the control and the CNF coated ss-mesh, performed under equivalent conditions, it is evident that substrate contributions are largely negligible. β factors were calculated from the gradient of the FN plot, assuming $\phi = 5.0$ eV for multi-walled CNFs[104]. Two dominant emission regimes exist. One is attributed to hot electron emission (β_1)[105] and the other to pure FN-type field emission (β_2). CNF inclusion increases the native β_2 (where this 'native' field enhancement is due to the cylindrical geometry of the ss-mesh fibres) by as much a factor of two, producing sufficiently large enhancement factors suitable for low-end field emission applications. Furthermore, CNF

coatings significantly reduce the turn-on fields from 4.5 V/μm (as-received ss-mesh) to approximately 2.5 V/μm (CNF/ss-mesh).

Figure 5.23(b) summarises an accelerated lifetime measurement performed at a pressure of 10^{-6} mbar, with an initial emission current density of 20 mA/cm^2. Stable performance is observed. Modest spikes in the emission current are attributed to thermal destruction of the CNFs caused by gas absorption. Gas absorption lowers the local work function which significantly increases the emitted current density and induces substantial heating in the perturbed CNF, resulting in tip burn-out. As shown in the inserts of Figure 5.23(b); *a*-C coats the CNF tips / emission sites. *a*-C has a greater absorptive capacity than graphitic carbon[106] suggesting that it is the tips which initiate burn-out. Removal or thermally stimulated graphitization of such *a*-C would improve the lifetime of the emitters and permit higher pressure functionality. Cyclic stability tests were also performed, as shown in Figure 5.23(c) and (d). Here, the extraction field was repeatedly cycled between 0 and 4 V/μm. We found that, upon successive cycles, the threshold field (F_{th}) for which *J* is 6.25 mA/cm^2, decays and tends toward a plateau after an approximate 10% reduction within 10 cycles (Insert, Figure 5.23(d)). No functional relationship in β_1 was apparent. The field enhancement factor in the pure FN regime (β_2) showed a strong positive correlation with cycle number. This is believed to be a result of increased levels of uniformity across the emission sites as dominant peaks are burnt off, thereby normalising the arrays and increasing the global enhancement factor. Moreover, CNF burn-out increases the inter-CNF spacing which reduces the level of electrostatic shielding[49], and simultaneously reduces F_{th} whilst increasing β_2.

5.5 Summary

The field emission performance of vacuum filtered, screen printed and dry-processed MWCNT thin films were considered. The thin films presented were shown to provide current densities of up to 5 mA/cm^2 under modest fields (1.7 V/µm) making them well suited for display and lighting applications. A reduction in the emitters surface work function in the case of surfactant treated MWCNTs was proposed to account for the lower turn-on fields in solution processed thin films than their untreated counterpart. It was also proposed that the degree of self-adhesion within the nanotubes films, inferred from the degree of alignment in the network, was the underlying mechanism as to why nominally equivalent films fail. Variations in emission characteristics were clearly demonstrated not to be associated with the

degree of graphitization. Performance enhancements were considered by including a surface bound layer of ZnO NWs. ZnO NWs ballasted the emission by reducing the peak emission current. A hot-electron model was proposed to account for the unexpectedly low turn-on fields.

Vertically aligned nanofibres were grown directly on electrolysed stainless steel mesh using a simple, low-cost route via catalyst activation of inexpensive and widely available stainless steel mesh. Nanofibres with aspect-ratios >150 were synthesised. The electrochemical pre-treatment was found to increase the surface roughness of the stainless steel which encouraged pre-oxidation and thermal reduction during nanofibre growth. A combined dissolution *and* driven-precipitation mechanism has been proposed to account for the evolution of the catalytically active surfaces. Field emission measurements showed substantial improvements in the field enhancement factors and turn-on fields of the as-received ss-mesh following nanofibre deposition. The pre-treatment technique discussed has the potential to be extended to a variety of Fe and Ni containing alloys and to realise the large-scale production of vertically aligned CNF arrays on conductive metal mesh electrodes that are well suited for field emission applications in environmental lighting and display back lighting.

References

1.   Milne, W. I., Teo, K. B. K., Amaratunga, G. A. J., Legagneux, P., Gangloff, L., Schnell, J. P., Semet, V., Binh, V. T.& Groening, O. (2004). Carbon nanotubes as field emission sources, *J. Mater. Chem.*, **14**, pp. 933-943.
2.   Nilsson, L., Groening, O., Emmenegger, C., Kuettel, O., Schaller, E., Schlapbach, L., Kind, H., Bonard, J. M.& Kern, K. (2000). Scanning field emission from patterned carbon nanotube films, *Appl. Phys. Lett.*, **76**, pp. 2071-2073.
3.   Lee, Y. H., Choi, C. H., Jang, Y. T., Kim, E. K., Ju, B. K., Min, N. K.& Ahn, J. H. (2002). Tungsten nanowires and their field electron emission properties, *Appl. Phys. Lett.*, **81**, pp. 745-747.
4.   Vander Wal, R. L.& Hall, L. J. (2003). Carbon nanotube synthesis upon stainless steel meshes, *Carbon*, **41**, pp. 659-672.
5.   Martinez-Hansen, V., Latorre, N., Royo, C., Romeo, E., Garcia-Bordeje, E.& Monzon, A. (2009). Development of aligned carbon nanotubes layers over stainless steel mesh monoliths, *Catal. Today*, **147**, pp. 71-75.
6.   Gomer, R. (1961). Field Emission and Field Ionization, *Harvard Monographs in Applied Sciences*, **9**, p 195.
7.   Jenkins, R. O.& Trodeen, W. G. (1965) *Electron & Ion Emission from Solids* In *Solid-State Physics* eds. Jacob, L., (Routledge and Kegan Paul Ltd., London).
8.   Forbes, R. G. (2006). Simple good approximations for the special elliptic functions in standard Fowler-Nordheim tunneling theory for a Schottky-Nordheim barrier, *Appl. Phys. Lett.*, **89**, pp. 1131221-1131223.
9.   Murphy, E. L.& Good, R. H. (1956). Thermionic emission, field emission, and the transition region, *Phys. Rev.*, **102**, pp. 1464-1473.
10.   Brodie, I.& Spindt, C. A. (1992). Vacuum Microelectronics, *Adv. Electron El. Phys.*, **83**, pp. 1-106.
11.   Rohrbach, F. (1971). **71-28**.

12. Wang, J. W.& Loew, G. A. (1997). Field emission and RF breakdown in high-gradient room-temperature Linac structures, *SLA-PUB-7684*, pp. 1-27.
13. Baker, F. S., Williams, J.& Osborn, A. R. (1972). Field-emission from carbon fibers - new electron source, *Nature*, **239**, pp. 96-97.
14. Wang, C., Garcia, A., Ingram, D. C., Lake, M.& Kordesch, M. E. (1991). Cold field-emission from CVD diamond films observed in emission electron-microscopy, *Electron. Lett.*, **27**, pp. 1459-1461.
15. Geis, M. W., Efremow, N. N., Woodhouse, J. D., McAleese, M. D., Marchywka, M., Socker, D. G.& Hochedez, J. F. (1991). Diamond cold-cathode, *IEEE Electron Device Lett.*, **12**, pp. 456-459.
16. Djubua, B. C.& Chubun, N. N. (1991). Emission properties of spindt-type cold cathodes with different emission cone material, *IEEE Trans. Electron Devices*, **38**, pp. 2314-2316.
17. Gerber, J., Robertson, J., Sattel, S.& Ehrhardt, H. (1996). Role of surface diffusion processes during bias-enhanced nucleation of diamond on Si, *Diam. Relat. Mat.*, **5**, pp. 261-265.
18. Gilkes, K. W. R., Sands, H. S., Batchelder, D. N., Milne, W. I.& Robertson, J. (1998). Direct observation of sp(3) bonding in tetrahedral amorphous carbon UV Raman spectroscopy, *J. Non-Cryst. Solids*, **227**, pp. 612-616.
19. Himpsel, F. J., Knapp, J. A., VanVechten, J. A.& Eastman, D. E. (1979). Quantum photoyield of diamond(111);A stable negative-affinity emitter, *Phys. Rev. B*, **20**, pp. 624-627.
20. van der Weide, J., Zhang, Z., Baumann, P. K., Wensell, M. G., Bernholc, J.& Nemanich, R. J. (1994). Negative-electron-affinity effects on the diamond(100) surface, *Phys. Rev. B*, **50**, pp. 5803-5806.
21. Bandis, C.& Pate, B. B. (1995). Photoelectric emission from negative-electron-affinity diamond(111) surfaces: Exciton breakup versus conduction-band emission, *Phys. Rev. B*, **52**, pp. 12056-12071.
22. Mann, M., Teo, K. B. K.& Milne, W. I. (2008). Carbon nanotubes as electron sources, *Transtech Publishers*.
23. Shim, J. Y., Baik, H. K.& Song, K. M. (2000). Effect of nondiamond carbon on electron transport path of field-emitted electrons from undoped polycrystalline diamond films, *J. Vac. Sci. Techol. A*, **18**, pp. 1977-1982.
24. Robertson, J. (1999). Mechanisms of electron field emission from diamond, diamond-like carbon, and nanostructured carbon, *J. Vac. Sci. Technol. B*, **17**, pp. 659-665.
25. Talin, A. A., Felter, T. E., Friedmann, T. A., Sullivan, J. P.& Siegal, M. P. (1996). Electron field emission from amorphous tetrahedrally bonded carbon films, *J. Vac. Sci. Technol. A*, **14**, pp. 1719-1722.
26. Teo, K. B. K., Rodil, S. E., Tsai, J. T. H., Ferrari, A. C., Robertson, J.& Milne, W. I. (2001). Effect of graphitic inclusions on the optical gap of tetrahedral amorphous carbon films, *J. Appl. Phys.*, **89**, pp. 3706-3710.
27. Zhu, W., Kochanski, G. P., Jin, S.& Seibles, L. (1995). Defect-enhanced electron field-emission from chemical-vapor-deposited diamond, *J. Appl. Phys.*, **78**, pp. 2707-2711.
28. Satyanarayana, B. S., Hart, A., Milne, W. I.& Robertson, J. (1997). Field emission from tetrahedral amorphous carbon, *Appl. Phys. Lett.*, **71**, pp. 1430-1432.
29. Amaratunga, G. A. J.& Silva, S. R. P. (1996). Nitrogen containing hydrogenated amorphous carbon for thin-film field emission cathodes, *Appl. Phys. Lett.*, **68**, pp. 2529-2531.
30. Musa, I., Munindrasdasa, D. A. I., Amaratunga, G. A. J.& Eccleston, W. (1998). Ultra-low-threshold field emission from conjugated polymers, *Nature*, **395**, pp. 362-365.
31. De Heer, W. A., Châtelain, A.& Ugarte, D. (1995). A carbon nanotube field-emission electron source, *Science*, **270**, pp. 1179-1180.
32. De Jonge, N., Allioux, M., Doytcheva, M., Kaiser, M., Teo, K. B. K., Lacerda, R. G.& Milne, W. I. (2004). Characterization of the field emission properties of individual thin carbon nanotubes, *Appl. Phys. Lett.*, **85**, pp. 1607-1609.
33. Choi, W. B., Jin, Y. W., Kim, H. Y., Lee, S. J., Yun, M. J., Kang, J. H., Choi, Y. S., Park, N. S., Lee, N. S.& Kim, J. M. (2001). Electrophoresis deposition of carbon nanotubes for triode-type field emission display, *Appl. Phys. Lett.*, **78**, pp. 1547-1549.
34. Dean, K. A.& Chalamala, B. R. (1999). The environmental stability of field emission from single-walled carbon nanotubes, *Appl. Phys. Lett.*, **75**, pp. 3017-3019.
35. Saito, Y., Hamaguchi, K., Uemura, S., Uchida, K., Tasaka, Y., Ikazaki, F., Yumura, M., Kasuya, A.& Nishina, Y. (1998). Field emission from multi-walled carbon nanotubes and its application to electron tubes, *Appl. Phys. A*, **67**, pp. 95-100.
36. Smith, R. C., Carey, J. D., Murphy, R. J., Blau, W. J., Coleman, J. N.& Silva, S. R. P. (2005). Charge transport effects in field emission from carbon nanotube-polymer composites, *Appl. Phys. Lett.*, **87**, pp. 1-3.
37. Jung, S. M., Hahn, J., Jung, H. Y.& Suh, J. S. (2006). Clean carbon nanotube field emitters aligned horizontally, *Nano Lett.*, **6**, pp. 1569-1573.

38. Milne, W. I., Teo, K. B. K., Mann, M., Bu, I. Y. Y., Amaratunga, G. A. J., De Jonge, N., Allioux, M., Oostveen, J. T., Legagneux, P., Minoux, E., Gangloff, L., Hudanski, L., Schnell, J. P., Dieumegard, L. D., Peauger, F., Wells, T.& El-Gomati, M. (2006). Carbon nanotubes as electron sources, *Phys. Status Solidi A-Appl. Mat.*, **203**, pp. 1058-1063.

39. Yukui, L., Changchun, Z.& Xinghui, L. (2002). Field emission display with carbon nanotubes cathode: prepared by a screen-printing process, *Diam. Relat. Mat.*, **11**, pp. 1845-1847.

40. Teo& B., K. (2001). Plasma Enhanced Chemical Vapor Deposited Carbon Nanotubes for Field Emission Applications, *Materials Research Society*.

41. Teo, K. B. K., Chhowalla, M., Amaratunga, G. A. J., Milne, W. I., Pirio, G., Legagneux, P., Wyczisk, F., Pribat, D.& Hasko, D. G. (2002). Field emission from dense, sparse, and patterned arrays of carbon nanofibers, *Appl. Phys. Lett.*, **80**, pp. 2011-2013.

42. Zhuangchun, W., Zhihong, C., Xu, D., Logan, J. M., Sippel, J., Nikolou, M., Kamaras, K., Reynolds, J. R., Tanner, D. B., Hebard, A. F.& Rinzler, A. G. (2004). Transparent, conductive carbon nanotube films, *Science*, **305**, pp. 1273-1276.

43. Carbon Nanotube Paste Catalogue - http://xinnanomaterials.com (/Pastes_EN.html)

44. Lucas, A., Zakri, C., Maugey, M., Pasquali, M., Van Der Schoot, P.& Poulin, P. (2009). Kinetics of nanotube and microfiber scission under sonication, *J. Phys. Chem. C*, **113**, pp. 20599-20605.

45. Klimenko, E. V.& Medvedev, V. K. (1989). *Sov. Phys. Solid State*, **10**.

46. Klimenko, E. V.& Naumovets, A. G. (1969). Electron state of sodium atoms adsorbed on tungsten and effect of electric field on adsorption energy, *Surf. Sci.*, **14**, pp. 141-155.

47. Cui, J. B., Teo, K. B. K., Tsai, J. T. H., Robertson, J.& Milne, W. I. (2000). The role of DC current limitations in Fowler-Nordheim electron emission from carbon films, *Appl. Phys. Lett.*, **77**, pp. 1831-1833.

48. Collins, P. G.& Zettl, A. (1997). Unique characteristics of cold cathode carbon-nanotube-matrix field emitters, *Phys. Rev. B*, **55**, pp. 9391-9399.

49. De Jonge, N.& Bonard, J. M. (2004). Carbon nanotube electron sources and applications, *Phil. T. Roy. Soc. A*, **362**, pp. 2239-2266.

50. Liu, B., Sundqvist, B., Andersson, O., Wågberg, T., Nyeanchi, E. B., Zhu, X. M.& Zou, G. (2001). Electric resistance of single-walled carbon nanotubes under hydrostatic pressure, *Sol. State Comms.*, **118**, pp. 31-36.

51. Li, C., Zhang, Y., Mann, M., Hiralal, P., Unalan, H. E., Lei, W., Wang, B. P., Chu, D. P., Pribat, D., Amaratunga, G. A. J.& Milne, W. I. (2010). Stable, self-ballasting field emission from zinc oxide nanowires grown on an array of vertically aligned carbon nanofibers, *Appl. Phys. Lett.*, **96**, pp. 143114-143117.

52. Wang, X., Zhou, J., Lao, C., Song, J., Xu, N.& Wang, Z. L. (2007). In-situ field emission of density-controlled ZnO nanowire arrays, *Adv. Mater.*, **19**, pp. 1627-1631.

53. Jo, S. H., Lao, J. Y., Ren, Z. F., Farrer, R. A., Baldacchini, T.& Fourkas, J. T. (2003). Field-emission studies on thin films of zinc oxide nanowires, *Appl. Phys. Lett.*, **83**, pp. 4821-4823.

54. Li, C., Hou, K., Lei, W., Zhang, X., Wang, B.& Sun, X. W. (2007). Efficient surface-conducted field emission from ZnO nanotetrapods, *Appl. Phys. Lett.*, **91**, pp. 163052-163505.

55. Wan, Q., Yu, K., Wang, T. H.& Lin, C. L. (2003). Low-field electron emission from tetrapod-like ZnO nanostructures synthesized by rapid evaporation, *Appl. Phys. Lett.*, **83**, pp. 2253-2255.

56. Xu, C. X., Sun, X. W., Dong, Z. L.& Yu, M. B. (2004). Zinc oxide nanodisk, *Appl. Phys. Lett.*, **85**, pp. 3878-3880.

57. Xu, C. X.& Sun, X. W. (2003). Field emission from zinc oxide nanopins, *Appl. Phys. Lett.*, **83**, pp. 3806-3808.

58. Yu, K., Zhang, Y. S., Xu, F., Li, Q., Zhu, Z. Q.& Wan, Q. (2006). Significant improvement of field emission by depositing zinc oxide nanostructures on screen-printed carbon nanotube films, *Appl. Phys. Lett.*, **88**, pp. 1531231-1531233.

59. Greene, L. E., Yuhas, B. D., Law, M., Zitoun, D.& Yang, P. (2006). Solution-grown zinc oxide nanowires, *Inorg. Chem.*, **45**, pp. 7535-7543.

60. Anthony, S. P., Lee, J. I.& Kim, J. K. (2007). Tuning optical band gap of vertically aligned ZnO nanowire arrays grown by homoepitaxial electrodeposition, *Appl. Phys. Lett.*, **90**, pp. 1031071-1031073.

61. Dalchiele, E. A., Giorgi, P., Marotti, R. E., Martín, F., Ramos-Barrado, J. R., Ayouci, R.& Leinen, D. (2001). Electrodeposition of ZnO thin films on n-Si(100), *Sol. Energ. Mat. Sol. C.*, **70**, pp. 245-254.

62. Unalan, H. E., Hiralal, P., Rupesinghe, N., Dalal, S., Milne, W. I.& Amaratunga, G. A. J. (2008). Rapid synthesis of aligned zinc oxide nanowires, *Nanotech.*, **19**, pp. 1-5.

63. Lee, C. J., Lee, T. J., Lyu, S. C., Zhang, Y., Ruh, H.& Lee, H. J. (2002). Field emission from well-aligned zinc oxide nanowires grown at low temperature, *Appl. Phys. Lett.*, **81**, pp. 3648-3650.

64. Yang, H. Y., Lau, S. P., Yu, S. F., Huang, L., Tanemura, M., Tanaka, J., Okita, T.& Hng, H. H. (2005). Field emission from zinc oxide nanoneedles on plastic substrates, *Nanotech.*, **16**, pp. 1300-1303.

65. Wei, A., Sun, X. W., Xu, C. X., Dong, Z. L., Yu, M. B.& Huang, W. (2006). Stable field emission from hydrothermally grown ZnO nanotubes, *Appl. Phys. Lett.*, **88**, pp. 2131021-2131023.

66. Wang, W., Zhang, G., Yu, L., Bai, X., Zhang, Z.& Zhao, X. (2007). Field emission properties of zinc oxide nanowires fabricated by thermal evaporation, *Physica E*, **36**, pp. 86-91.

67. Li, S. Y., Lin, P., Lee, C. Y.& Tseng, T. Y. (2004). Field emission and photofluorescent characteristics of zinc oxide nanowires synthesized by a metal catalyzed vapor-liquid-solid process, *J. Appl. Phys.*, **95**, pp. 3711-3716.

68. Romero, A. H., Garcia, M. E., Valencia, F., Terrones, H., Terrones, M.& Jeschke, H. O. (2005). Femtosecond laser nanosurgery of defects in carbon nanotubes, *Nano Lett.*, **5**, pp. 1361-1365.

69. Sun, C. K., Vallée, F., Acioli, L., Ippen, E. P.& Fujimoto, J. G. (1993). Femtosecond investigation of electron thermalization in gold, *Phys. Rev. B*, **48**, pp. 12365-12368.

70. Groning, O., Kuttel, O. M., Groning, P.& Schlapbach, L. (1999). Field emission properties of nanocrystalline chemically vapor deposited-diamond films, *J. Vac. Sci. Technol. B*, **17**, pp. 1970-1986.

71. Bonard, J. M., Stockli, T., Noury, O.& Chatelain, A. (2001). Field emission from cylindrical carbon nanotube cathodes: Possibilities for luminescent tubes, *Appl. Phys. Lett.*, **78**, pp. 2775-2777.

72. Minoux, E., Greening, O., Teo, K. B. K., Dalai, S. H., Gangloff, L., Schnell, J. P., Hudanski, L., Bu, I. Y. Y., Vincent, P., Legagneux, P., Amaratunga, G. A. J.& Milne, W. I. (2005). Achieving high-current carbon nanotube emitters, *Nano Lett.*, **5**, pp. 2135-2138.

73. Hiraoka, T., Yamada, T., Hata, K., Futaba, D. N., Kurachi, H., Uemura, S., Yumura, M.& Iijima, S. (2006). Synthesis of single- and double-walled carbon nanotube forests on conducting metal foils, *J. Appl. Chem.*, **128**, pp. 13338-13339.

74. Jo, S. H., Wang, D. Z., Huang, J. Y., Li, W. Z., Kempa, K.& Ren, Z. F. (2004). Field emission of carbon nanotubes grown on carbon cloth, *Appl. Phys. Lett.*, **85**, pp. 810-812.

75. Rubianes, M. D.& Rivas, G. A. (2003). Carbon nanotubes paste electrode, *Electrochem. Commun.*, **5**, pp. 689-694.

76. Wang, J., Musameh, M.& Lin, Y. H. (2003). Solubilization of carbon nanotubes by Nafion toward the preparation of amperometric biosensors, *J. Am. Chem. Soc.*, **125**, pp. 2408-2409.

77. Liu, Y., Qian, W. Z., Zhang, Q., Ning, G. Q., Wen, Q., Luo, G. H.& Wei, F. (2008). The confined growth of double-walled carbon nanotubes in porous catalysts by chemical vapor deposition, *Carbon*, **46**, pp. 1860-1868.

78. Tang, S. H., Sun, G. Q., Sun, S. G., Qi, J., Xin, Q.& Haarberg, G. M. (2010). Double-walled carbon nanotubes as catalyst support in direct methanol fuel cells, *J. Electrochem. Soc.*, **157**, pp. 1321-1325.

79. Zhang, C., Pisana, S., Wirth, C. T., Parvez, A., Ducati, C., Hofmann, S.& Robertson, J. (2008). Growth of aligned millimeter-long carbon nanotube by chemical vapor deposition, *Diam. Relat. Mat.*, **17**, pp. 1447-1451.

80. Gao, L. Z., Kiwi-Minsker, L.& Renken, A. (2008). Growth of carbon nanotubes and microfibers over stainless steel mesh by cracking of methane, *Surf. Coat. Technol.*, **202**, pp. 3029-3042.

81. Li, W. Z., Xie, S. S., Qian, L. X., Chang, B. H., Zou, B. S., Zhou, W. Y., Zhao, R. A.& Wang, G. (1996). Large-scale synthesis of aligned carbon nanotubes, *Science*, **274**, pp. 1701-1703.

82. Hofmann, S., Ducati, C., Kleinsorge, B.& Robertson, J. (2003). Direct growth of aligned carbon nanotube field emitter arrays onto plastic substrates, *Appl. Phys. Lett.*, **83**, pp. 4661-4663.

83. Rahaman, A., Patra, N.& Kar, K. K. (2008). Self catalyzing behavior of Kanthal wire for coating of carbon nanotubes, *Fuller. Nanotub. Car. N.*, **16**, pp. 78-87.

84. Sarangi, D., Hierold, C.& Karimi, A. (2005). Carbon nanotubes over metallic wires and its possible applications, *Fuller. Nanotub. Car. N.*, **13**, pp. 243-254.

85. Talapatra, S., Kar, S., Pal, S. K., Vajtai, R., Ci, L., Victor, P., Shaijumon, M. M., Kaur, S., Nalamasu, O.& Ajayan, P. M. (2006). Direct growth of aligned carbon nanotubes on bulk metals, *Nat. Nanotechnol.*, **1**, pp. 112-116.

86. Chen, T., Wang, L. L., Chen, Y. W., Que, W. X.& Sun, Z. (2007). Field emission properties of carbon nanotubes film grown on NiCr alloy films, *Appl. Surf. Sci.*, **253**, pp. 7046-7049.

87. Parthangal, P. M., Cavicchi, R. E.& Zachariah, M. R. (2007). A generic process of growing aligned carbon nanotube arrays on metals and metal alloys, *Nanotech.*, **18**, pp. 1-5.

88. Masarapu, C.& Wei, B. Q. (2007). Direct growth of aligned multiwalled carbon nanotubes on treated stainless steel substrates, *Langmuir*, **23**, pp. 9046-9049.

89. Melechko, A. V., Merkulov, V. I., McKnight, T. E., Guillorn, M. A., Klein, K. L., Lowndes, D. H.& Simpson, M. L. (2005). Vertically aligned carbon nanofibers and related structures: Controlled synthesis and directed assembly, *J. Appl. Phys.*, **97**, pp. 0413011-04130139.

90. Cui, H., Yang, X., Simpson, M. L., Lowndes, D. H.& Varela, M. (2004). Initial growth of vertically aligned carbon nanofibers, *Appl. Phys. Lett.*, **84**, pp. 4077-4079.

91. Jiong, Z.& Zuo, J. M. (2009). Structure and diameter-dependent bond lengths of a multi-walled carbon nanotube revealed by electron diffraction, *Carbon*, **47**, pp. 3515-3528.

92. Jeng, J. Y., Quayle, B. E., Modern, P. J., Steen, W. M.& Bastow, B. D. (1993). Laser-surface treatments to improve the intergranular corrosion-resistance of 18/13/NB and 304L in nitric acid, *Corros. Sci.*, **35**, pp. 1289-1296.

93. Otero, E., Pardo, A., Utrilla, M. V., Saenz, E.& Alvarez, J. F. (1998). Corrosion behaviour of aisi 304L and 316L stainless steels prepared by powder metallurgy in the presence of sulphuric and phosphoric acid, *Corros. Sci.*, **40**, pp. 1421-1434.

94. Kain, V., Shinde, S. S.& Gadiyar, H. S. (1994). Mechanism of improved corrosion-resistance of type 304L stainless-steel in nitric-acid environments, *J. Mater. Eng. Perform.*, **3**, pp. 699-705.

95. Meille, V. (2006). Review on methods to deposit catalysts on structured surfaces, *Appl. Catal. A-Gen.*, **315**, pp. 1-17.

96. Iken, H., Basseguy, R., Guenbour, A.& Bachir, A. (2007). Classic and local analysis of corrosion behaviour of graphite and stainless steels in polluted phosphoric acid, *Electrochimica Acta*, **52**, pp. 2580-2587.

97. Shih, H. C., Chen, Y. Y., Duval, T., Hung, U. D.& Yeh, J. W. (2005). Microstructure and electrochemical properties of high entropy alloys-A comparison with type-304 stainless steel, *Corros. Sci.*, **47**, pp. 2257-2279.

98. Esconjauregui, S., Fouquet, M., Bayer, B.& Robertson, J. (2010). Carbon nanotubes growth: From entanglement to vertical alignment, *Phys. Stat. Sol. B*, **247**, pp. 38-41.

99. Bayer, B. C., Hofmann, S., Castellarin-Cudia, C., Blume, R., Baehtz, C., Esconjauregui, S., Wirth, C. T., Oliver, R. A., Ducati, C., Knop-Gericke, A., Schlogl, R., Goldoni, A., Cepek, C.& Robertson, J. (2011). Support-catalyst-gas interactions during carbon nanotube growth on metallic Ta films, *J. Phys. Chem. C*, **115**, pp. 4359-4369.

100. Jarrah, N. A., Li, F. H., van Ommen, J. G.& Lefferts, L. (2005). Immobilization of a layer of carbon nanofibres (CNFs) on Ni foam: A new structured catalyst support, *J. Mater. Chem.*, **15**, pp. 1946-1953.

101. Hofmann, S., Sharma, R., Ducati, C., Du, G., Mattevi, C., Cepek, C., Cantoro, M., Pisana, S., Parvez, A., Cervantes-Sodi, F., Ferrari, A. C., Dunin-Borkowski, R., Lizzit, S., Petaccia, L., Goldoni, A.& Robertson, J. (2007). In-situ observations of catalyst dynamics during surface-bound carbon nanotube nucleation, *Nano Lett.*, **7**, pp. 602-608.

102. Groning, O., Kuttel, O. M., Emmenegger, C., Groning, P.& Schlapbach, L. (2000). Field emission properties of carbon nanotubes, *J. Vac. Sci. Technol. B*, **18**, pp. 665-678.

103. Fujii, S., Honda, S., Machida, H., Kawai, H., Ishida, K., Katayama, M., Furuta, H., Hirao, T.& Oura, K. (2007). Efficient field emission from an individual aligned carbon nanotube bundle enhanced by edge effect, *Appl. Phys. Lett.*, **90**, pp. 1531081-1531083.

104. Groning, O., Kuttel, O. M., Groning, P.& Schlapbach, L. (1999). Field emission spectroscopy from discharge activated chemical vapor deposition diamond, *J. Vac. Sci. Technol. B*, **17**, pp. 1064-1071.

105. Lee, M. J. G. (1973). Field-Emission of Hot-Electrons from Tungsten, *Phys. Rev. Lett.*, **30**, pp. 1193-1196.

106. Lowry, H. H.& Bozorth, R. M. (1928). The adsorptiok of gases by graphitic carbon: X-ray investigation of the adsorbents, *J. Phys. Chem.*, **32**, pp. 1524-1527.

Chapter VI

Enhanced Functionality
Through Horizontal Nanotube Alignment
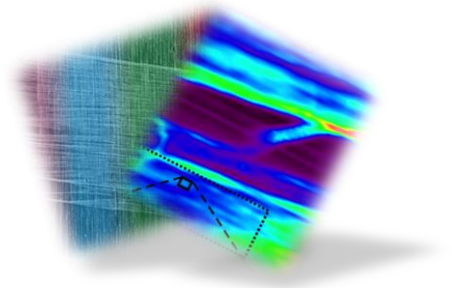
6.   Introduction

The benefits of vertical alignment, with regards to field emission, were alluded to in the previous chapter. The potential for directionally dependent functionality combined with conventional TFC operation is extremely valuable in many opto-electronic applications[3-6] and it was this that motivated the study of various nanotube horizontal alignment techniques.

In this chapter multiple horizontal alignment techniques developed throughout this work are presented, including; roll, scratch, density and electric field alignment. Specific emphasis is placed on the development of a global electric field alignment system. Although viable, the developed approaches all require optically opaque substrates and offer relatively short nanotubes. A freestanding, substrate-free alternative was deemed necessary for opto-electronic applications. A mechanical pulling technique was consequently developed. Optical sensors and broadband optical polarisers based on these free-standing nanotube membranes is also discussed.

6.1   Horizontal Alignment

Nanotubes can be aligned[10] by; (i) post-synthesis alignment, where external forces such as those derived from electric fields (i.e. dielectrophoresis)[11, 12] orientate the nanotubes once dispersed onto a substrate, often by means of a liquid medium; or (ii) aligned synthesis using magnetic fields[13], electric fields, gas flow, or graphoepitaxy[14] to align the nanotubes during synthesis.

A number of post-synthesis alignment techniques have been developed throughout the course of this work (Figure 6.1). Bulk alignment was deemed possible, though significant inter-tube interactions reduced the degree of alignment. Here, the nanotubes are compressed, rolled and sheared (Figure 6.3). Unfortunately, only approximate directionality could be achieved. Such techniques are largely inaccurate and suffer from poor reproducibility. Nanomanipulation has been reported, though the processing is serial and requires time-consuming electron microscopy monitoring[15]. Spin and drop casting of nanotube suspensions have shown moderate success[16, 17]. Nevertheless, despite the nanotubes in-plane alignment they have little or no linear directionality, which is to say that there is no controllable way to define the mean azimuth and that they are merely randomly orientated within the plane. Wei
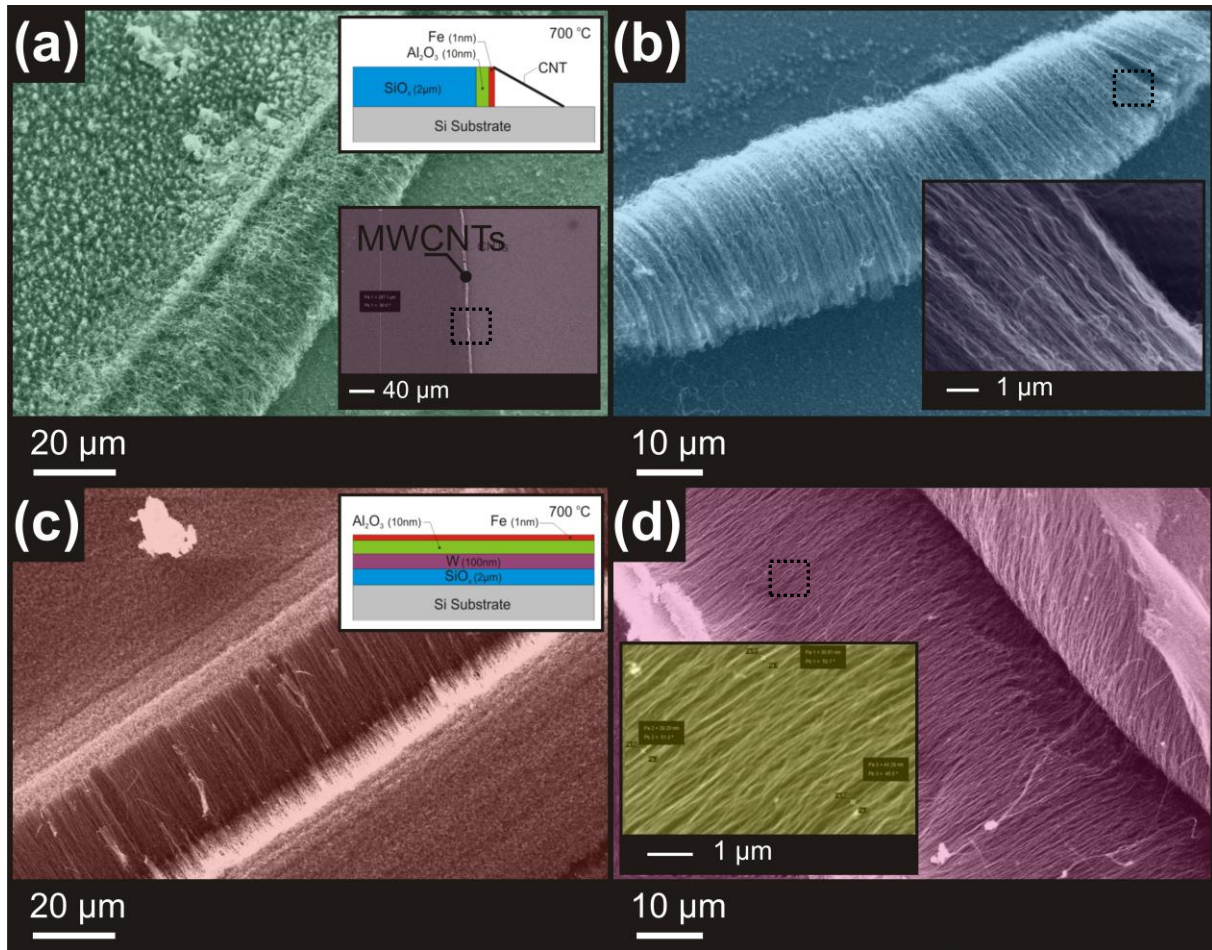
Figure 6.1 | Density and scratch alignment. SEM micrographs of; **(a, b)** Density aligned MWCNTs. Catalysts (Al$_2$O$_x$/Fe) were vertically deposited on the side of an exposed SiO$_2$ protrusion by angled sputtering. **(c, d)** Scratch alignment. Vertical MWCNT forests were carefully scratched with a sharpened diamond scribe. The *inserts* depict the stack cross-sections.

et al.[18] demonstrated the use of dielectrophoresis exploiting the weak nanotube dipole. An electric field, of the order of ~10 V/µm[9, 19-21], is required to align solution dispersed nanotubes, whereas only ~1 V/µm[8, 22, 23] is required to align the nanotubes during synthesis.

Initial efforts focussed on simple alignment techniques. Scratch, density and rolled alignment were all achieved successfully as illustrated in the SEM micrographs in Figure 6.1. To scratch align, nanotube forests were first grown (as in Chapter 2) and a diamond scribe was gently drawn across the forests surface to impart the alignment (Figure 6.1(a)). Roll alignment was discussed in some detail in the preceding chapters. Density alignment was achieved by depositing the catalyst material on the vertical face of a sputtered SiO$_2$ protrusion using angled PVD. During T-CVD the nanotubes grew perpendicular to the catalyst face (Figure 6.1(a,b)). Unfortunately, density alignment growths were prematurely passivated by
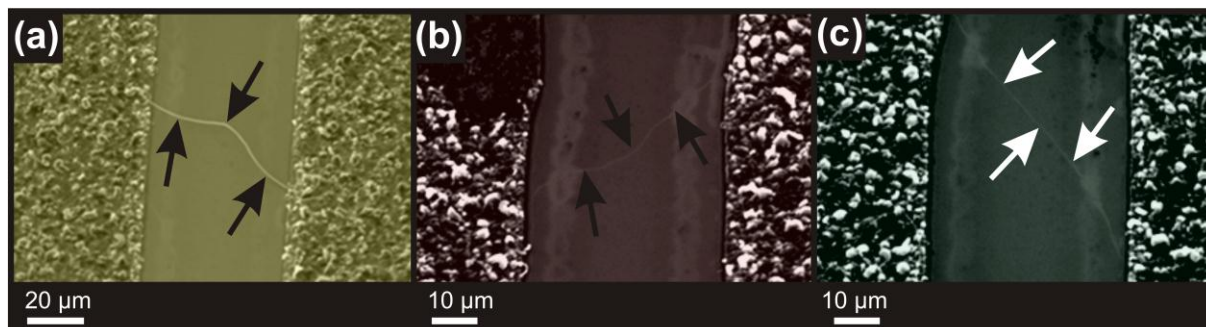
Figure 6.2 | **In-plane nanotubes by thermal randomisation.** SEM example micrographs of in-plane nanotubes synthesised by thermal randomisation; **(a-c)** W (25 nm)/ Fe (5 nm)-sputtered SiO$_2$(200 nm)/ Si substrates (CNT conditions: 30 V (S.C), C$_2$H$_2$:NH$_3$ = 200:50 sccm, 800°C, 1800 s). CNTs in **(b, c)** rest directly on the underlying SiO$_x$ oxide (hence the reduced contrast) whereas (a) is elevated off the surface. Arrows to guide the eye.

substrate interactions. In most case the nanotubes were 55±10 nm in diameter and less than 10 μm in length.

6.2 Aligned Synthesis

Low-density catalyst particles permit random alignment during growth. This produces the classic entangled spaghetti-like networks. In some instances it is possible to use such thermal randomisation to deposit in-plane nanotubes by careful consideration of the catalyst, diffusion barrier and growth conditions. In-plane alignment is possible, though in-plane directional control is not (Figure 6.2). Instead, the application of forces during growth can be used to align the nanotubes in plane.

Figure 6.3 shows SEM micrographs of various reported *in-situ* alignment techniques, including graphoepitaxy[24-26], gas flow[27-31] and electric field[20, 22, 23]. Nanotubes graphoepitaxially align to surface nanofacets during growth. The technique is surface critical which limits the broadness of the technique. Costly substrates are necessary, such as sapphire or quartz, though high degrees of alignment and uniformity have been evidenced through the production of highly linear, regular and periodic arrays[26, 32]. Despite this the process involves time-consuming substrate preparatory processes. Rational substrate design, using elevated Si pillars, offers another approach[33]. Here the nanotubes grow between elevated pillars. The micrometre pillars limit the practicality of the technique as well as restricting the maximum packing density. As a result, techniques based on electric field and gas flow alignment show perhaps the most promise. They are rapid, parallel processes that offer simplicity and
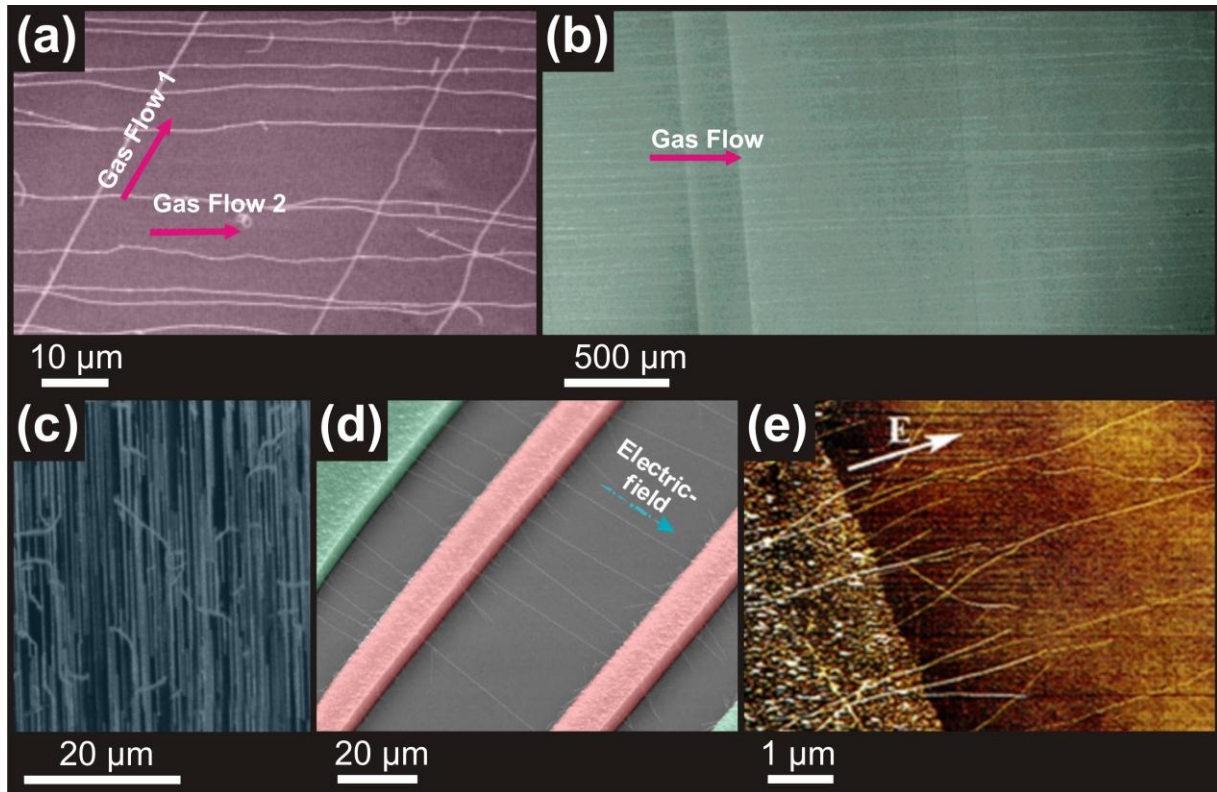
Figure 6.3 | **Nanotube alignment.** Examples of alignment by; **(a)-(b)** gas flow[1, 2], **(c)** graphoepitaxy[7] and **(d,e)** electric-fields[8, 9].

the ability to fabricate high density arrays.

In the case of gas flow alignment, the growth gases flow parallel to the catalyst substrate and this induces the alignment. Huang e*t al.*[30], Xin *et al.*[31] and Jin *et al.*[29] have demonstrated gas flow alignment with varying degrees of success. Law *et al.*[20] found, for electric field alignment, that plasma induced self-biasing and the resultant surface charging effects on metallic electrodes were sufficient to align the nanotubes. Zhang *et al.*[8] and Ural *et al.*[22] reported similar alignment effects ascribed to electric fields of the order of 0.5-4.0 V/μm. They argued that the nanotubes highly anisotropic polarisability induces large dipole moments when they interact with the local electric field. This interaction produces large aligning torques which govern the growth orientation. Blažek *et al.*[34] estimated the electric field aligning force to be of the order of 10^{-5} nN, a force approximately four orders of magnitude greater than the weight of the catalyst particle. Hertel *et al.*[35] estimated that a 10 nm wide nanotube experiences a Van der Waals surface binding force of the order of 35 nN, supporting the observed nanotube termination in the density alignment experiments. Few comprehensive attempts have been made in the literature to explain the orientation
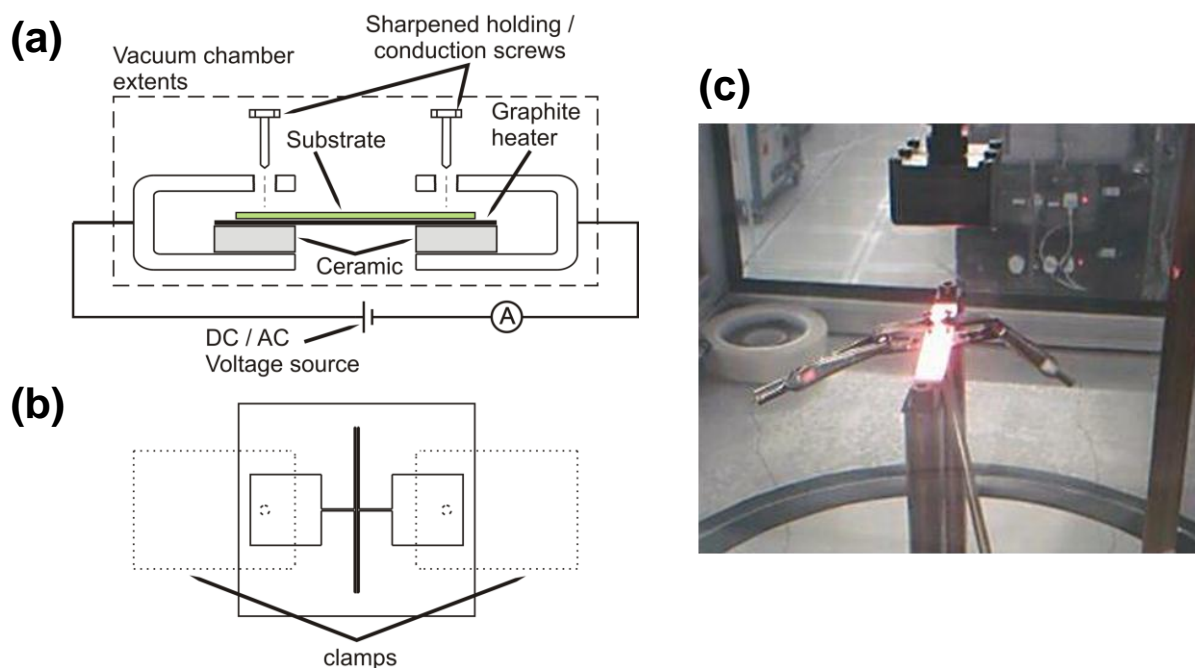
Figure 6.4 | Microelectrode / local electric field stage design. (a, b) Stage cross-section and plan schematic. **(c)** Image of the stage and substrate during typical synthesis.

mechanism involved. Chen *et al.*[36] proposed a so-called kite mechanism. Here the catalyst particle, located at the nanotube apex, is pulled in the direction of the prevailing electric field at an angle from the substrate. When growth terminates the nanotubes relax and fall to the substrate where they become strongly bound. Huang *et al.*[27] presented a similar mechanism, whereas Yu *et al.*[37] postulated that charged species form bonds along the electric field direction and that the nanotubes can only grow if they align to the electric field. Tanemura *et al.*[38] suggested that the alignment effect may be a result of an excess of electrostatically attracted positive charge ions at the nanotubes tip. They concluded that the plasma, composed of positive ions as opposed to radicals or excited molecules, plays a decisive role in the alignment by reducing the lateral mechanical stress exerted on the nanotubes.

6.2.1 Local Horizontal Electric-Field Alignment

Nanotubes were grown by T-CVD using 200:50 sccm (NH_3:C_2H_2) with W electrodes on Si/SiO_2 (200nm) substrates, separated by a 50 μm gap were photolithographically defined. A Ni catalyst strip or 80 nm catalyst dots (Al_2O_x/Fe - 10/1 nm) were patterned between the electrodes using poly(methylmethacrylate) (PMMA) mediated electron beam lithography. Figure 6.4 shows the (a, b) equipment setup and (c) an optical micrograph during growth. The

samples were electrically isolated from the heated graphite stage using ceramic spacers to prevent charging of the underlying Si.
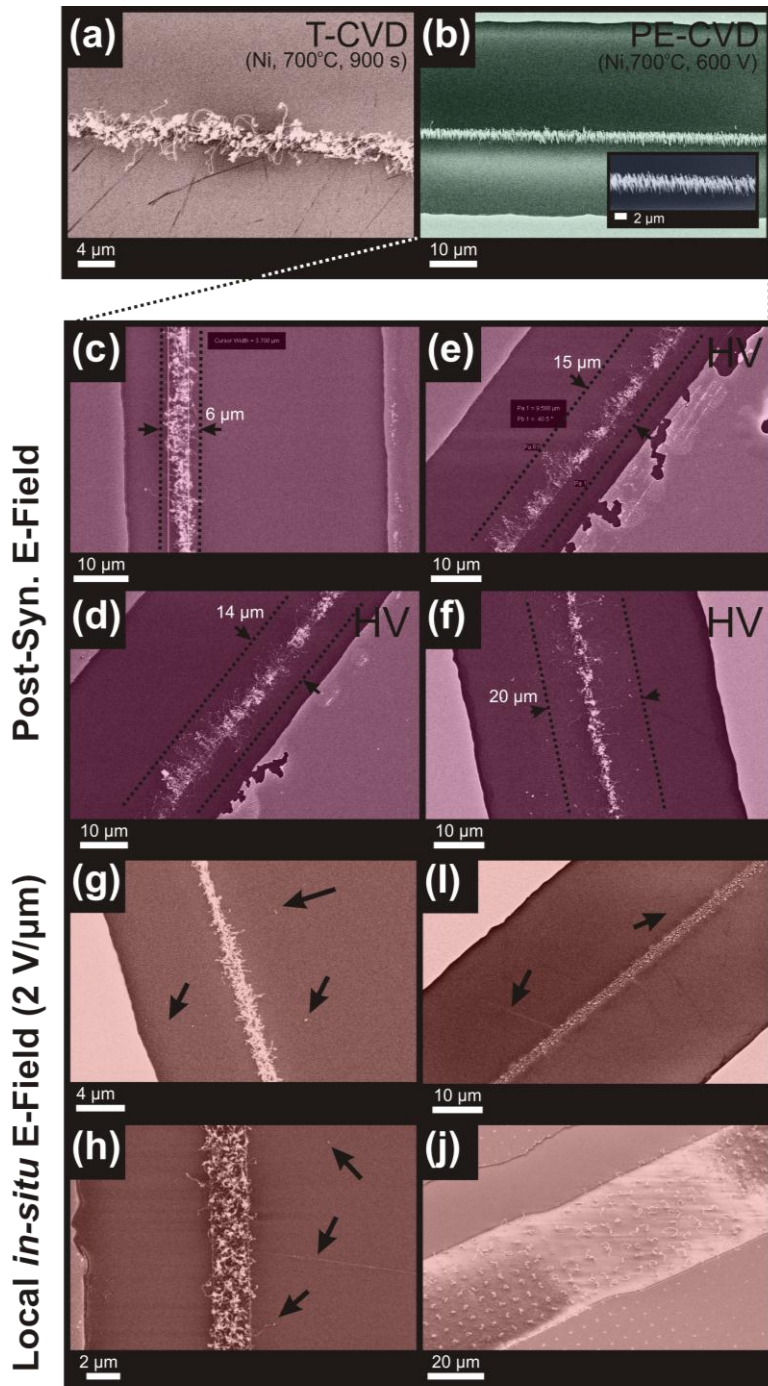

Figure 6.5 | **Local electric field alignment. (a)** T-CVD (no electric field), **(b)** Vertical PE-CVD. Applying an electric field after growth; **(c)** As-grown (T-CVD), **(d-f)** post-growth application of electric field (6 V/μm). HV denotes high voltage. **(g-j)** *In-situ* electric field (2 V/μm) during T-CVD.

Figure 6.5(a,b) show SEM micrographs of a catalyst sample grown by T-CVD (700°C, 900 s) and traditional vertical PE-CVD, respectively. No horizontal bias was applied in either case. The catalyst is clearly active and nanotubes grew to 3 μm in length and ~75 nm (PE-CVD) and ~77 nm (T-CVD) in diameter. To investigate the degree of interaction between the nanotubes and local electric field, DC fields were applied following T-CVD. Figure 6.5 shows an SEM micrograph before (c) and after (e-f) the application of a DC electric field of ~6 V/μm. The nanotubes strongly interact with the electric field and become increasingly laterally dispersed by up to 20 μm. The similarly wide distribution of catalyst particles would also suggest that the catalyst particles also interact strongly with the field and that tip growth is ultimately
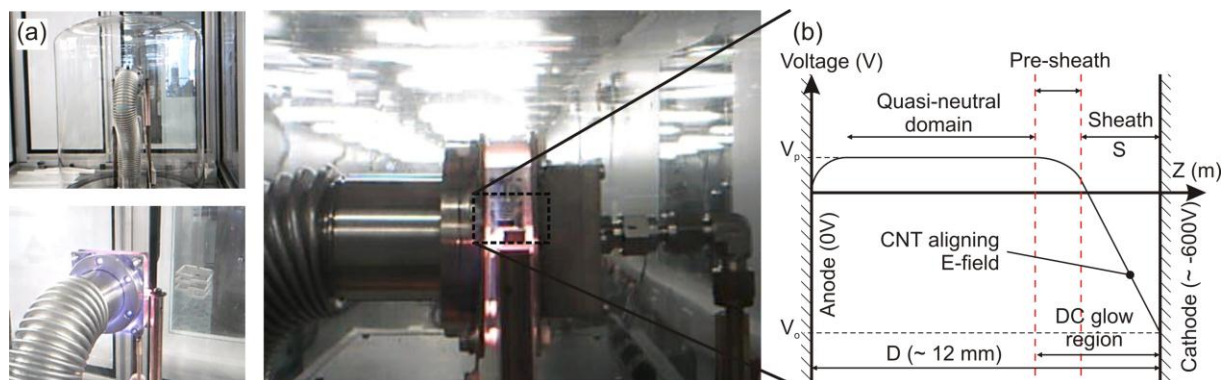
Figure 6.6 | **Global electric field reactor.** **(a)** Horizontal PE-CVD reactor. **(b)** Typical potential variation in a DC glow gas discharge plasma. (Typical process conditions: 50 W / 700 V, 700°C, 200:50 sccm, 3 mbar).

preferential supporting the posits of Chen *et al.*[36]. Figure 6.5(g-j) shows SEM micrographs of T-CVD synthesised nanotubes where a horizontal bias (~2 V/µm) was applied during growth. Catalyst dots (Figure 6.5(j)) showed little interaction with the field, perhaps due to a root growth which would support previous conjectures. Ni catalyst strips showed encouraging results with some tubes as long as 10 µm though linear densities were low (~100 mm^{-1}). Variations in alignment are a product of disparities in the electrode fabrication though alignment can certainly be attributed to the electric field given the extremely linear growth.

6.2.2 Horizontal PE-CVD Reactor

Other than the low-linear densities, a major limitation to local electric-field alignment is the requirement for microelectrodes patterned on the substrate. These structures interfere with post-growth processing and device fabrication. Substrate independent electrodes obviate the limitations of the patterned electrode. The electric field can then be applied across the *entire* sample. Such an approach has been widely demonstrated in a vertical context; however to the best of the author's knowledge, no one has hitherto demonstrated such alignment in a planar context. A new horizontal nanotube PE-CVD reactor was modelled, designed and fabricated. Figure 6.6 shows an optical micrograph of the reactor during a deposition. It consists of two 1.5 x 70 x 70 mm polished stainless steel electrodes. The cathode / gas inlet (right) is electrically grounded and the anode / gas outlet (left) is attached to a turbomolecular vacuum system that is electrically connected to a variable high-voltage DC supply (0-1000 V). The electrode separation can be altered by adjusting the ceramic spacers. The sample is ohmically
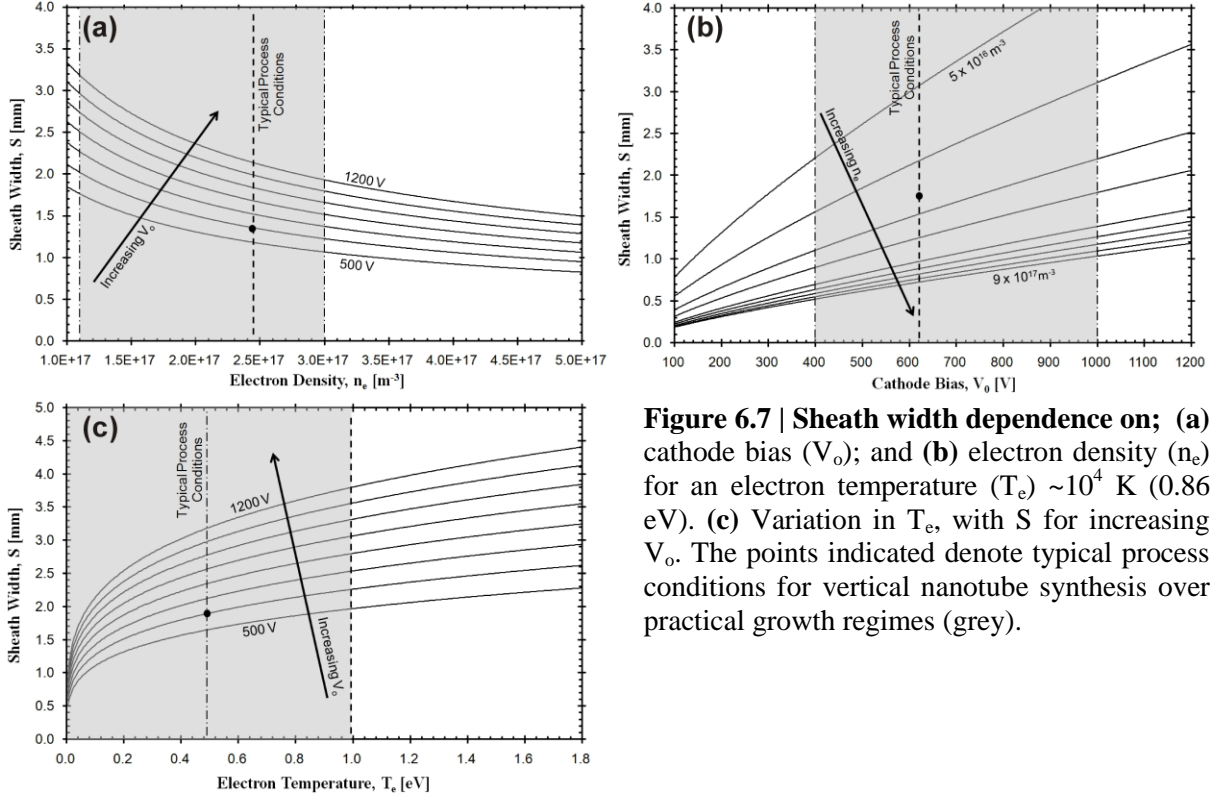
Figure 6.7 | Sheath width dependence on; (a) cathode bias (V_o); and **(b)** electron density (n_e) for an electron temperature (T_e) ~10^4 K (0.86 eV). **(c)** Variation in T_e, with S for increasing V_o. The points indicated denote typical process conditions for vertical nanotube synthesis over practical growth regimes (grey).

heated using a 0.13 x 10 x 100 mm graphite stage with a quartz, electrically isolating, cover-sheet. The entire reactor is enclosed in an evacuated quartz bell jar.

It has been widely postulated that, as for vertical nanotube growth, alignment is achieved by anisotropic torque induction within a narrow plasma sheath[39]. This sheath exists in the narrow glow region, ~3 mm wide, adjacent to the biased cathode. For a collisionless, quasi-neutral, Child's law ion sheath (Figure 6.6(b)) of electron temperature (T_e) and glow potential (V_P), the relation between the sheath width (S), charge carrier density (n) and cathode potential (V_0) is given by[40, 41]

$$S = \frac{\sqrt{2}}{3} \lambda_D \left(\frac{2e(V_0 + V_P)}{kT_e} \right)^{3/4} \tag{5.1}$$

where ε_o is the permittivity of free space, k is Boltzmann's constant and e is the electronic charge. The Debye length (λ_D) is given by;

$$\lambda_D = \sqrt{\frac{\varepsilon_0 kT_e}{n_e e^2}} \tag{5.2}$$

where n_e is the electron density. Combining (5.1) and (5.2), assuming quasi-neutrality (n~n_e), gives;
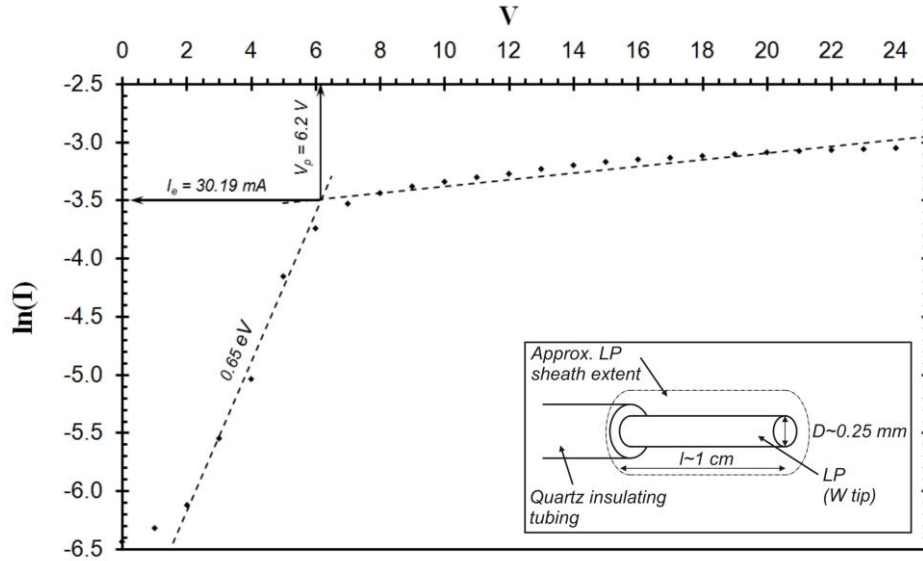
Figure 6.8 | Langmuir probe measurements. Typical Langmuir probe plot of the extracted probe current (I) at a given bias (V). *Insert:* Probe geometry.
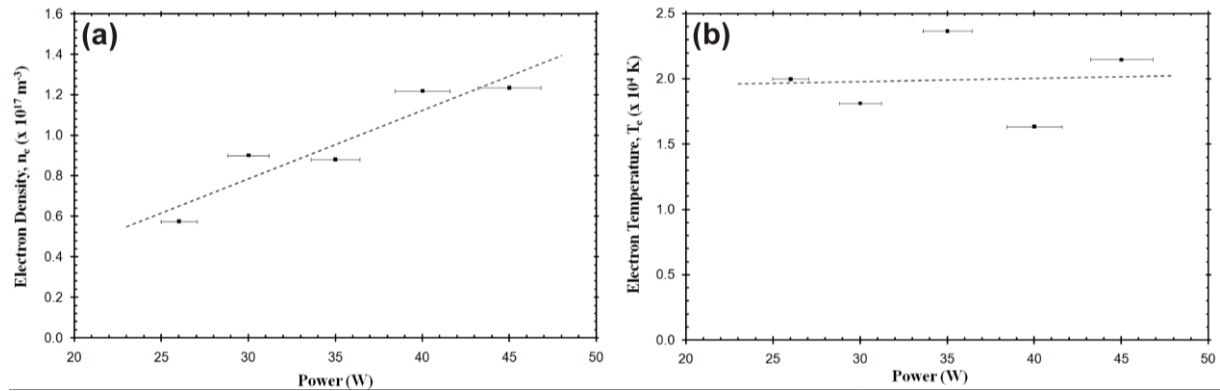

Figure 6.9 | Power dependence. Variation in **(a)** electron density and **(b)** electron temperature with power. (Typical plasma conditions: 700^0C, 3.2 mbar, 200:50 sccm). Error bars: 4 % power variation. Functional fits as indicated.

$$S = \kappa V_o^{3/4} T_e^{-1/4} n_e^{-1/2} = \kappa V_o^{3/4} F(T_e, n_e) \tag{5.3}$$

where $\kappa = (6.12 \times 10^4)\,\text{m}^{5/2}\text{V}^{-3/4}\text{K}^{1/4}$ and $F(T_e, n_e)$ denotes the (reactor) pressure and (plasma) power dependence of the electron temperature and the electron density. Note that the plasma potential $V_P \ll V_0$, where $V_P \approx 5\,\text{V}$ and $V_0 \geq 500\,\text{V}$. Typical data ($V_0 \approx 600$ V and $n \approx 10^{17}$ m^{-3}) gives a 1.6 mm sheath for $T_e \approx 1.5 \times 10^4\,K$ [40]. Equation (5.3) suggests that the sheath width is strongly dependent on the electron density and weakly dependent on the cathode bias. The derived dependencies are illustrated in Figure 6.7, where typical vertical nanotube synthesis bias ($V_0 \approx 600\,\text{V}$) and electron density ($n_e \approx 8.2 \times 10^{16}\,\text{m}^{-3}$) have been indicated (black dot) for
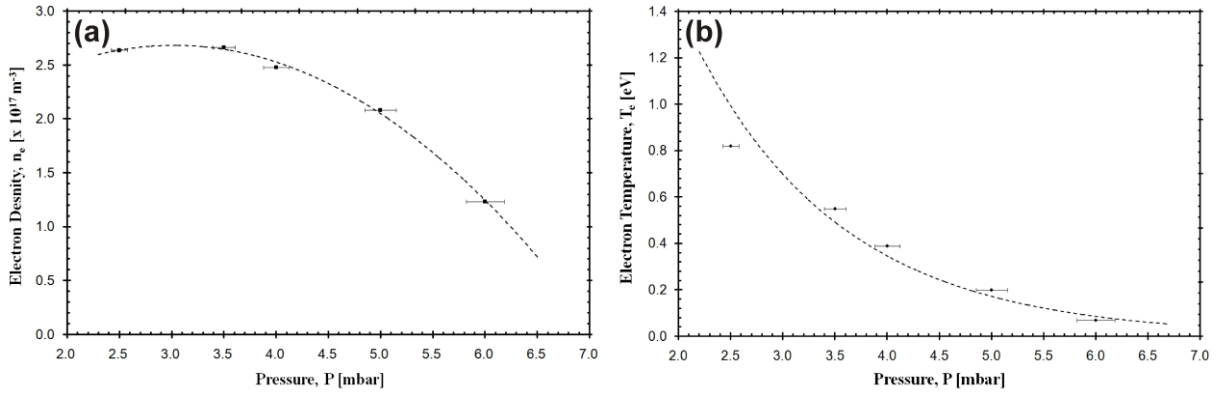
Figure 6.10 | Pressure dependence. Variation in (a) electron density and (b) electron temperature with reactor pressure. Functional fits as shown. (Typical plasma conditions: 45 W / 550 V, 700^{0}C, 4:1 gas ratio). Error bars: noted 3 % pressure variation. Functional fits as indicated.

clarity. Figure 6.7(b) suggests a plausible three-fold reduction in the electron density will result in a ten-fold increase in sheath width.

To investigate the variation in S with process conditions the pressure dependence of the electron density and electron temperature have been inferred from measurements made using a cylindrical Langmuir probe of length 10^{-2} m; radius, r = 0.25 x 10^{-3} m and exposed surface area, A$_{exp}$ ~10^{-5} m^2, as depicted in the insert of Figure 6.8. The probe was inserted into the plasma sheath under typical process conditions of 4:1 (C$_2$H$_2$:NH$_3$) at 700°C. The probes tip was 2-5 mm from the cathode centre in the glow discharge region. Following 300 s of plasma stabilisation the reactor pressure was reduced by either throttling the attached roughing pump or varying the input flow rates, followed by a second plasma stabilisation period of 300 s. The reactor pressure was varied from 2.5 to 6 mbar and the I-V characteristics were recorded using a Velleman DVM890. The probe bias was incrementally increased from 0 to 25 V using a Manson EP-613 source. The effect of the plasma power was also investigated. The power was incrementally increased for a fixed reactor pressure and the I-V characteristics recorded as before. Figure 6.8 shows a typical measured I-V characteristic.

Assuming equal electron and ion densities[42] ($n_e \approx n_+ = n$) the corresponding currents are;

$$I_{e,+} = \left(\frac{1}{4}\right) n A_{exp} e \bar{C}_{e,+} \tag{5.4}$$

where the subscripts 'e' and '+' refer to the electron and ion quantities respectively and $\bar{C}$ is the mean charge carrier velocity, given by;
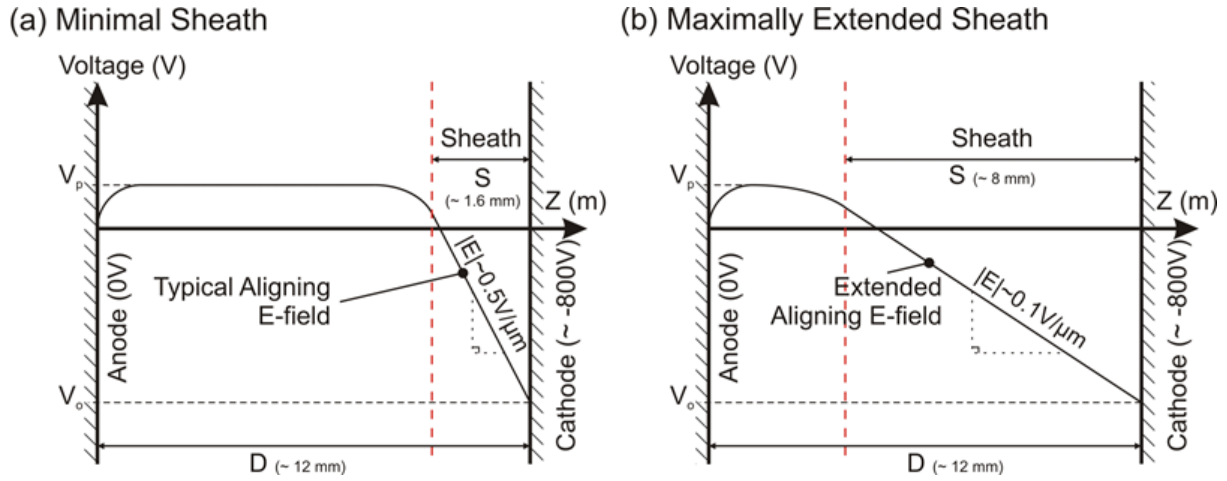
Figure 6.11 | Limiting cases. Illustrative examples of **(a)** typical and **(b)** optimal sheath width highlighting the magnitude of the associated lateral electric field.

$$\overline{C}_{e,+} = \sqrt{\frac{8kT_{e,+}}{\pi m_{e,+}}}$$

(5.5)

where the mass of the charge carriers (m_e, m_+) are known. The measured current is the sum of the electron and ion currents ($|I| = |I_e| + |I_+|$). However, $T_e \gg T_+$ ($\therefore \overline{C}_e \gg \overline{C}_+$) and hence $|I| \approx |I_e|$. The electrons exhibit a Maxwellian energy distribution which modulates the current accordingly to give[43];

$$I \approx I_e \exp\left(\frac{-e\Delta V}{kT_e}\right)$$

(5.6)

where $\Delta V (= V_p - V)$ is the potential difference between the plasma and probe. The electron density can now be found from equation (5.4). The parameters V_p, I_e and T_e are empirically accessible through the Langmuir probes I-V data (Figure 6.8). Therefore, for typical process conditions[1], $n_e = 2.5 \times 10^{17}$ m^{-3} and $T_e = 0.7$ eV; values which show excellent agreement with those reported by Blažek *et al.*[34].

The electron density linearly increases with plasma power (Figure 6.9(a)), a similar trend to that reported by Desai *et al.*[44], and quadratically decays with pressure (Figure 6.10(a)). The electron temperature is independent of plasma power (Figure 6.9(b)) and exponentially decays, with a transient of 0.7 mbar^{-1}, with increasing reactor pressure (Figure 6.10(b)).

---

[1] 3.2 mbar/ 50 W/ 550 V

Sheath elongation is therefore possible by decreasing the plasma power. The electron density
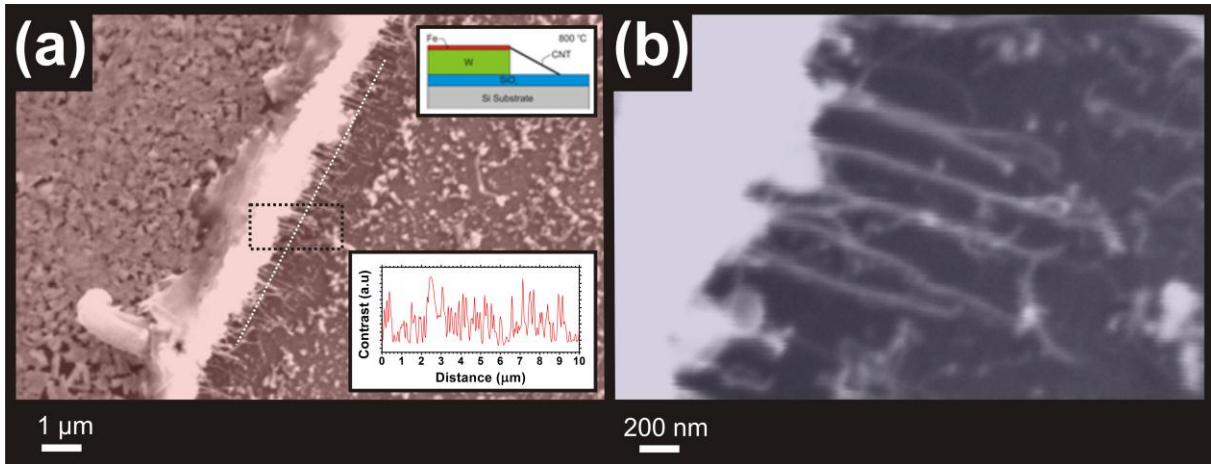

Figure 6.12 | Global electric field alignment. SEM micrographs of; **(a)** PE-CVD horizontally grown nanotubes on SiO_2 / 25 nm W /5 nm Fe thin-film. *Top insert:* Schematic stack cross-section. *Bottom insert:* Profile scan showing a liner density of $\sim 5 \times 10^4$ cm^{-1}. **(b)** high magnification image of the area highlighted in (a). (Typical growth conditions: C_2H_2:NH_3 = 200:50 sccm, 800°C, 1800 s). W/Fe deposited by DC magnetron sputtering employing a shadow mask technique. Poor alignment of the W/Fe layers resulted in the presence of Fe nanoparticles which may have contributed to growth deactivation.

and temperature decrease with increasing reactor pressure, consistent with the data of Shah *et al.*[45] and Desai *et al.*[44]. Thus, increasing the reactor pressure tends to increase the sheath width. The measured trends conflict. To increase the sheath width the pressure must be increased (to decrease n_e). However, the sheath width also increases at low pressures (to increase T_e). A more detailed functional dependence on n_e and T_e must therefore be evaluated. Equations (5.7) and (5.8) show the functional fits, where θ = plasma power, and where separation of variables has been assumed for $n_e(P,\theta)$.

$$T_e(P) = \left[\frac{e}{k \times 5.8 \exp(-0.7P)} \right] \tag{5.7}$$

$$n_e(P,\theta) = \kappa' n_e(P) n_e(\theta) = (1.74 \times 10^{17})(-0.16P^2 + 0.98P + 1.19)(0.034\theta - 0.23) \tag{5.8}$$

where κ' represents an averaging term which negates the scaling effects introduced by the assumed separation of variables. Equations (5.3), (5.7) and (5.8) can be combined to give a sheath width of the form $S = S(V_o, P, \theta)$. Hence,

$$\begin{aligned}
S(V_o, P, \theta) &= \kappa V_o^{3/4} F(T_e, n_e) \\
&= \kappa V_o^{3/4} T_e(P)^{-1/4} n_e(P,\theta)^{-1/2} \\
&= \kappa V_o^{3/4} T_e(P)^{-1/4} [\kappa' n_e(P) n_e(\theta)]^{-1/2}
\end{aligned} \tag{5.9}$$

Functional fits indicate that processing conditions of 7 mbar and 25 W (~1000 V) are necessary to achieve a sheath width comparable to the substrate dimensions (~7 mm).
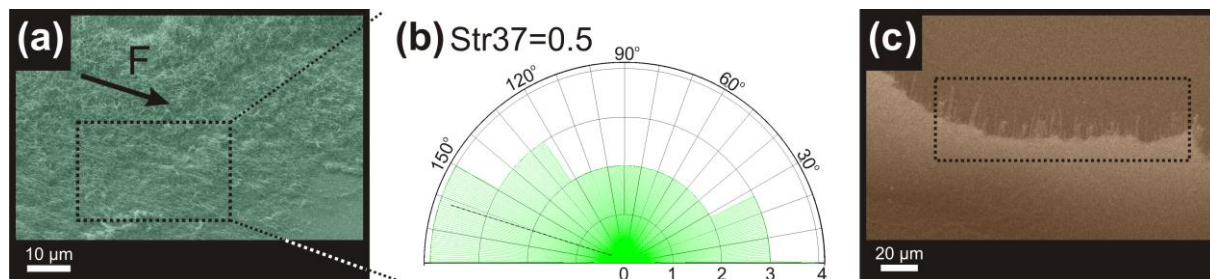

Figure 6.13 | Global electric field alignment. (a) SEM micrographs of an Al_2O_x/Fe sample grown in the horizontal PE-CVD reactor (435 V/ 15 W). F denotes the direction of the electric field. **(b)** Str37=0.5 using the global alignment rig. The reactor imparts horizontal alignment. **(c)** Accidental tearing of a MWCNT forest suggested alternative mechanical routes to alignment.

Estimates support the conjecture that sheath width extension can be facilitated by increasing the controllable plasma power and reactor pressure.

Note that the Debye length is ~22 μm, and is much smaller than the characteristic dimensions of the reactor (~1 mm), indicating a stable and largely collisionless plasma, thereby corroborating the validity of the proposed model.

The reactor was designed such that the catalyst samples were mounted with the gas flow parallel to the substrates surface. This gas flow may enhance or degrade the degree of alignment. If the flow is turbulent then electric field alignment may not be observed. The magnitude of the forces relating to the turbulent flow may very well dominate those associated with the electric field alignment, ~0.5 μN for nominally 45° misalignment[8]. The flow regime must therefore be considered. The Reynolds number associated with the chamber is given by $Re = UL/\upsilon$ where U is the free-stream flow velocity, $\upsilon = \mu/\rho$ is the kinematic viscosity (the ratio of the dynamic viscosity to density) and L is a characteristic dimension of the flow-perturbing feature. For an ideal gas a Reynolds number of ~100 is estimated, based on the data of Sun *et al.*[46] on the density and kinematic viscosity of what is a predominately an NH_3 flow at 3.5 mbar (250 sccm) / 700°C, which indicates a predominately laminar flow (turbulent flow → Re > 2300). Thus, in principle, limited alignment degradation should occur as a result of the feedstock/passivation gases.

The documented model has so far focused exclusively on the extension of the plasma sheath. Consider the two extreme cases of sheath extension illustrated in Figure 6.11. Evidently the electric fields lie somewhere between 0.1-0.5 V/μm. The combined findings of [8, 22, 47, 48] indicate that an electric field in the range of 0.1-2.0 V/μm is necessary, values that are consistent with these extremities. Note, also, that Jang *et al.*[23] reported negligible improvements in the alignment 'quality' for fields >2.0 V/μm, whilst Ural *et al.*[22] found an optimal field of 0.1 V/μm. The required alignment fields are evidently accessible with the proposed reactor.

W (25 nm)-supported Fe (5 nm) samples were prepared by photolithography and magnetron sputtering. Metallic supports were intentionally used to minimise the interaction between the growing nanotubes and the Si/SiO$_2$ substrate because, as determined in the previous studies, strong substrate interactions between the nanotubes and surface inhibits growth substantially. Catalyst samples were loaded into the reactor following an acetone and IPA degreasing step and nanotubes were grown at 800°C. Low gas flows were intentionally used (<300 sccm ~1.7 cm/s) to avoid turbulent interactions and to ensure the alignment was solely attributed to the electric field. Indeed, Xin *et al.*[31] showed, in a gas flow cell, free stream velocities of up to 9 cm/s were necessary for gas flow mediated alignment during T-CVD. Figure 6.12(a) shows an SEM micrograph of a typical alignment. As in the local electric field case the surface appears to passivate the growth. Nonetheless, samples showed a high mean linear packing density of 5×10^4 cm^{-1}. Al$_2$O$_x$/Fe planar catalyst samples were also considered (Figure 6.12(a)). The synthesised nanotubes demonstrated a Str37 of 0.5 (Figure 6.12(b)). The horizontal electric field aligned the nanotubes. Unfortunately, high catalyst density resulted in areas of misalignment due to strong randomising inter-nanotube interactions and therefore a reduction in catalyst density would be favourable. Nevertheless, to fully exploit aligned nanotubes in many applications, significantly longer nanotubes are necessary and various time-consuming techniques (most likely polymer-mediated) must also be developed to transfer the nanotubes from their optically opaque growth substrates to optically inactive substrates, such as quartz. During experimentation it was noticed that, when accidentally scraped, forests tore and the edge nanotubes became aligned, as illustrated in Figure 6.12(c). This spurred investigations into alternative routes toward alignment that promised a simple methodology and substrate-free alignment.

6.3   Large-Scale Alignment by Solid-State Peeling

Although the techniques developed above offer viable approaches to nanotube alignment, the demanding electrode and catalyst patterning processes limited scalability, both in terms of nanotube length and mass production. Practical devices require larger scales. The development of a simple, low-cost approach capable of spanning significant lengths (mm) was necessary. Therefore a mechanical peeling technique was investigated.

Degenerately phosphorus-doped, 200-nm-thermally-oxidised, *n*-type <100> Si substrates were degreased in an ultrasonicated acetone bath and rinsed with IPA, DI water and blown dry with ultra-high purity N_2. 10 ± 1 nm Al_2O_x (99.99%) was magnetron sputtered and exposed to atmosphere and a 1 ± 0.1 nm thin-film of Fe (99.95%) was thermally evaporated at a rate of 0.02 Å/s (Lesker PVD 75). Catalyst samples were then transferred to the T-CVD system evacuated to a base pressure of 3×10^{-3} mbar which was then pre-pressurised to 26 ± 1 mbar, prior to heating, in a diluted C_2H_2 (4% in H_2) atmosphere. The resistively heated graphite stage was then ramped at $5^oC/s$ to a growth temperature of 700^oC. Growth initiation was observed at $\sim510^oC$. Growth was terminated after 600 s by evacuating the chamber to $<10^{-2}$ mbar and cooling the stage to ambient temperature. No post-growth treatments were performed. For clarity, Figure 6.14(g) shows the mass spectrum of the neutral species under the stated growth conditions probed downstream of the CVD chamber[49]. Hydrocarbon species over 80 amu were negligible. For the given CVD synthesis conditions, the growth rate monotonically decreased with increasing feedstock exposure time. Initial growth rates were extremely high, ~800 nm/s. Nanotubes were ~300 μm in length, with diameters of 25.4 ± 13.3 nm consisting of 2-5 walls (Figure 6.15(a)) determined using SEM (Zeiss 50 and FEI Philips XL30 SFEG), HR-SEM (In-lens field emission Hitachi S5500), HR-TEM (FEI Tecnai F20) and AFM (Agilent 5400).

Nanotube membranes were fabricated using a similar technique to that first reported by Xiao *et al.*[50, 51] in 2008. Figure 6.14(a) illustrates the process. Kapton tape was carefully attached to the edge of the source MWCNT forest. The tape was retracted at an approximate

rate $\leq 10^{-2}$ m/s to form a highly aligned nanotube membrane (Figure 6.14(c)), which is structurally maintained by inter-nanotube Van der Waals forces. Figure 6.14(d-f) show a
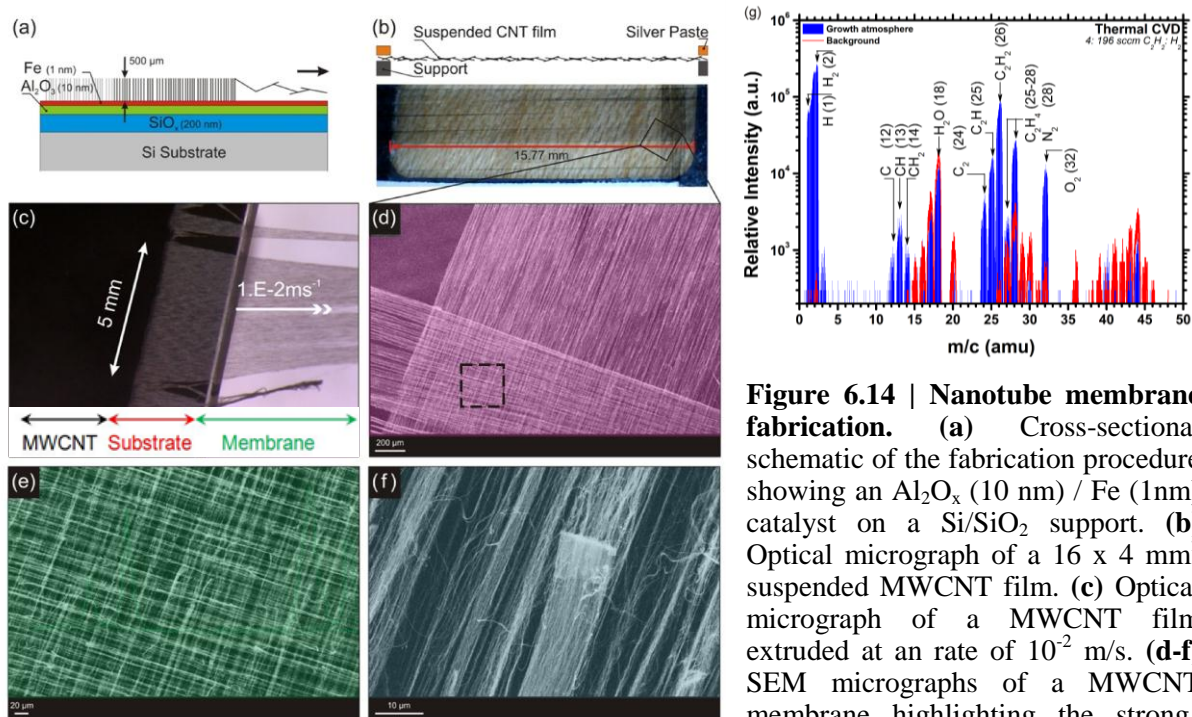

Figure 6.14 | Nanotube membrane fabrication. **(a)** Cross-sectional schematic of the fabrication procedure showing an Al_2O_x (10 nm) / Fe (1nm) catalyst on a Si/SiO_2 support. **(b)** Optical micrograph of a 16 x 4 mm^2 suspended MWCNT film. **(c)** Optical micrograph of a MWCNT film extruded at an rate of 10^{-2} m/s. **(d-f)** SEM micrographs of a MWCNT membrane highlighting the strong inter-MWCNT surface Van der Waals binding mechanism. **(g)** EQP mass spectrum of the background and growth atmosphere (neutral species) probed downstream of the thermal CVD chamber during carbon precursor exposure (C_2H_2 (4 sccm):H_2 (196 sccm), 25 mbar, 700°C).

typical membrane in more detail. The ability to easily fabricate crossed arrays, potential nanostructured metamaterials, is demonstrated in Figure 6.14(e).

Figure 6.15 shows the Raman spectra before and after the peeling process. Extruding did not increase the crystallographic disorder. The spectra at various central locations of an extruded membrane, have D, G and G' peaks at 1356.0 cm^{-1}, 1588.6 cm^{-1} and 2692.7 cm^{-1}, respectively, and an $I_D/I_G \sim 0.42$-0.85. Low D-G ratios, such as this, indicate relatively high defect densities, characteristic of low-temperature nanocrystallites. Raman spectroscopy is a spatially averaging technique (probe spot size ~ 1 μm^2). Hence, the lack of reproducible and often weak radial breathing mode supported the HR-TEM data and points towards a very low SWCNT content. This macroscopic uniformity was further supported as the measured Raman signatures which showed fairly modest spatial variation.

A major benefit of membrane fabrication is not only that the process is epoxy and binder-less and substrate-free, but also the incredibly efficient use of the source material. Films can

be extruded to span significant lengths. A 10 mm^2 sample, with a modest packing density of 7×10^{11} cm^{-2}[51], could be drawn into a ribbon approximately 335 m in length.
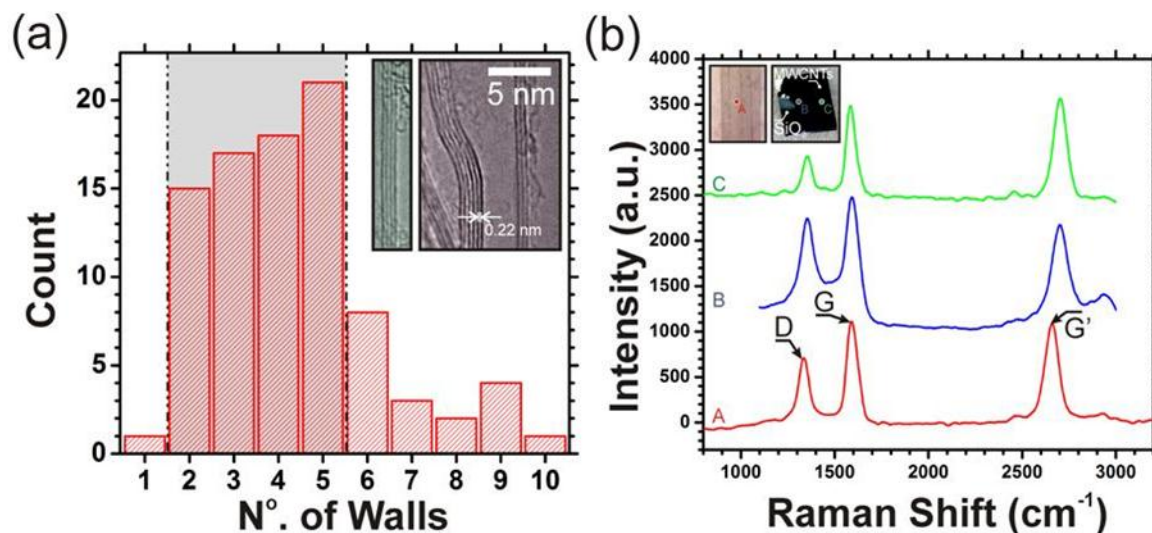
Figure 6.15 | **MWCNT crystallographic characterisation. (a)** Wall distribution. *Insert:* HR-TEM micrographs clearly showing the graphitic walls of the MWCNTs. Samples nominally had between 2 and 5 walls. **(b)** Raman spectra (633 nm, 3 mW) of a MWCNT forest synthesised under standard conditions and after peeling. *Insert:* Optical micrographs of the measured location. Spectra *A* (red) was measured on the extruded membrane, whilst *B* (blue) and *C* (green) pertain to the as-grown MWCNT forest.

6.3.1 The Unambiguous Photoresponse of MWCNTs

The wideband photoresponse of the as-synthesised suspended (substrate-free) anisotropic MWCNT membranes fabricated by the peeling technique is presented here. MWCNTs photoconduct though the exact mechanism by which they do so is unclear[52-55]. MWCNTs are of specific interest due to the large number of concentrically nested cylindrical walls which provide enhanced active surface areas, large photon absorption depths and multiple charge carrier pathways. The well-defined environmental thermal link, quantifiable and controllable inter-tube junctions and the potential for polarisation selective photo-responsivity are all advantageous features.

Due to the complex band structure of MWCNTs some debate still exists over the underlying mechanism(s) associated with the observed photoconductivity, warranting the development of modified experimental approaches. To-date most studies have employed ultrasonicated and chemically treated material on Si and SiO_2 substrates. This processing modifies the electronic structure whilst the use of various differing surfactants, as shown in Chapter III, invariably introduces inconsistencies across studies. Nevertheless, such studies did highlight a number of potentially important mechanisms including; (i) band gap and inter-
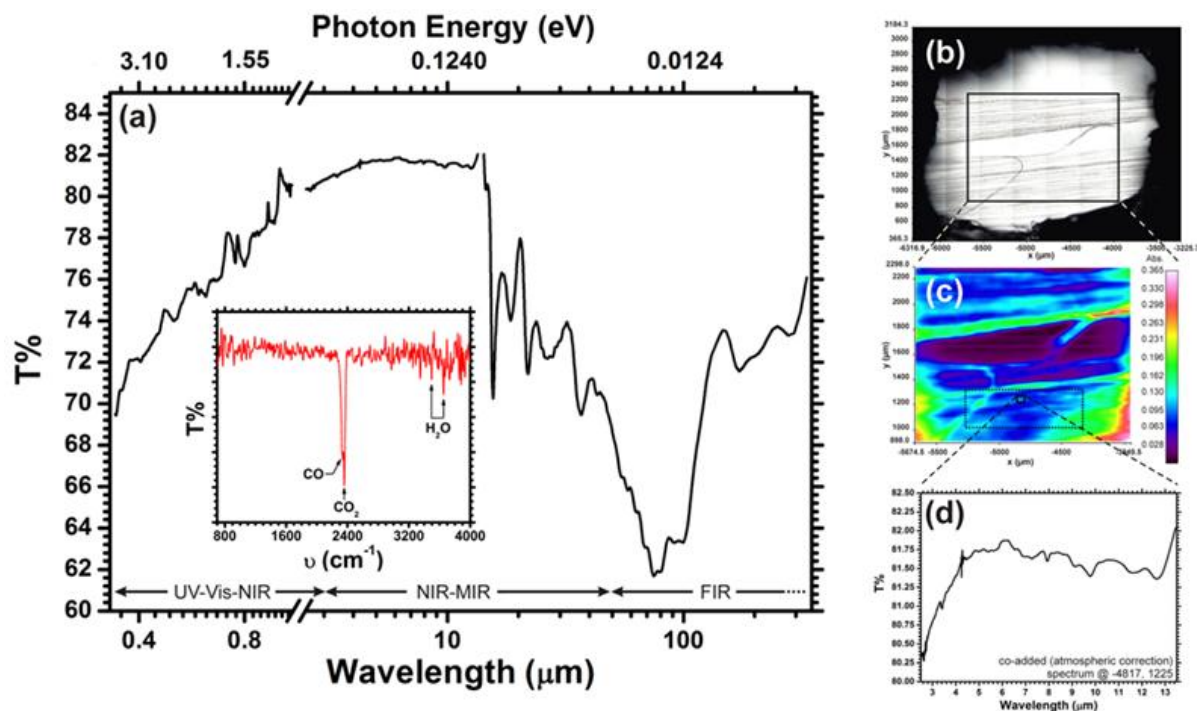
Figure 6.16 | Broad spectral absorption. (a) UV-Vis-FIR transmission (T%) spectrum under ambient conditions. NIR-MIR (2.5-13.5 μm) spectrum atmospherically compensated and averaged over the area highlighted in (c). *Insert:* Fourier Transform-Infrared (FT-IR) spectrum highlighting the CO, CO_2 and H_2O (O-H stretching mode) absorption peaks. **(b)** Optical micrograph of the inspected area. **(c)** Averaged full-range MIR absorbance map (υ=580-4000 cm^{-1}). **(d)** Typical co-added (and atmospherically corrected) MIR spectrum extracted from a single 5x5 μm pixel (-4817, 1225 μm) of the IR absorbance map in (c).

band transitions of free charge carriers[56, 57], (ii) low-energy exciton generation[58], (iii) direct thermal (bolometric) stimulation[52, 53], (iv) interface-barrier modulation (Schottky)[54, 59] and (v) photo-sorption of weakly bound surface species[60]. Stokes *et al.*[54] and Castrucci *et al.*[61] showed that interfacial effects, such as electrode-nanotube and Si/nanotube heterojunctions[62], also played a critical role and have been widely interpreted through a Schottky barrier model. Most studies have based their speculations on largely inappropriate experimental platforms and improved device structure and material purity are necessary before truly convincing data sets and arguments can be presented.

Bolometry, the direct heating of a material which adjusts its electrical resistance, is perhaps the most widely adopted model. Bolometry is challenging to validate due to the difficulties in measuring local temperatures accurately. It may also be immeasurably weak if the thermal link between the nanotubes and the environment is sufficiently high. Reducing this thermal link to the environment is necessary to enhance bolometric effects (if this mechanism were

indeed dominant). Evacuation is one way to achieve this. Another approach is to suspend the active material[53]. In this sense, the nanotube membranes show obvious advantages over solid-state materials, such as PbS[63] and PbSe[64]. Moreover, the naturally suspended inner shells of the MWCNT provide an ideal configuration. Nevertheless, it has, until recently, been difficult to suspend macroscopic films of chemically untreated MWCNTs, especially over the relatively large distances necessary to obviate electrode interface effects. In conventional thin film bolometers the volume of the absorbing material is typically 0.1 μm^3 and minimising this volume is critical to improve performance. Again, nanotube-based sensors offer appealing performance enhancements here. To irrefutably evidence and understand the underlying photoconductivity all extraneous interfaces must be removed; namely, the substrate and electrodes, whilst sample preparation must proceed without any post-growth chemical processing. The nanotube membranes developed in the preceding section offer such a platform. They are substrate-free, self-supporting and are devoid of non-nanotube interfacial charge traps and heterojunctions. Moreover, their comparatively large-scale means that samples can be optical stimulated without exposing the metallic contact interfaces. Colloidal Ag-anisol electrodes were deposited directly on the membranes with a longitudinal (parallel to the peel direction) and transverse (perpendicular to the peel direction) separation of 3 mm. Samples were mounted in header packages or polymer supports and were electrically connected using 30 μm Au wire.

Carbon nanotubes absorb over a wide spectral range[65-67]. Figure 6.16(a) shows the broad spectral transmittance (T%) from the ultraviolet (UV, 300 nm) to the far infra-red (FIR, 330 μm). Uniform absorption of 30±10% is noted throughout. To the best of the author's knowledge this is the first measurement over such a broad range for truly pure MWCNTs. Membranes offer an extremely useful platform to investigate the broad-range optical properties of the MWCNTs without limitations from the carrier substrate. Separate samples must typically be prepared to perform such broad range scans, but not in this instance. The broad spectral measurements were performed at room temperature using an ATI Unicam UV2, UV-vis-NIR (0.25-1.1 μm) spectrometer; Research Series Fourier Transform NIR-MIR (2.5-13.5 μm) spectrometer; and a co-added (atmospherically corrected) Perkin-Elmer spatially resolved Spectrum 400 Fourier Transform mid-IR (MIR) to FIR (50-330 μm) spectrometer under continuous N_2 purge. Figure 6.16(b-d) shows the mean MIR absorption map and an optical micrograph of the corresponding measurement area. The nanotubes absorb

uniformly over their entire surface. Areas of increased packing density show greater absorption.

Brennan *et al.*[56] showed that MWCNTs are efficient low-dimensional media for generating charge carriers due to the presence of van Hove singularities in the density of states. Few theoretical band structure models have been developed on these complex systems due to the largely immeasurable inter-tube interactions. As a result the intrinsic semiconductivity of MWCNTs is still unclear. A further point to note, more specific to nanotube networks, is that samples have unavoidable statistical variability in the number of metallic and semiconducting nanotubes. In low-density networks high proportions of semiconducting nanotubes may account for the photoresponse. Notwithstanding, Raman (Figure 6.15(b)) and TEM data clearly indicates negligible SWCNT content. However, consider a band gap related photoresponse. Assuming incommensurate, outer wall dominance the band gap, E_g, for the stated diameter range, is 21.3-68.1 meV, as calculated by[68]

$$E_g = \frac{2\gamma_0 a_{c-c}}{d}$$

(5.10)

where γ_0 is the C–C tight-binding overlap energy (2.9 eV), a_{c-c} is the nearest neighbour C–C distance (0.142 nm) and d is the nanotubes diameter. For MWCNTs with d >32.9 nm, ambient thermal excitations are suppressed. By way of a comparison, the typical band gaps of (ideal, semi-metal) graphite, bi-layer graphene and semiconducting-SWCNTs are 40 meV[69], 0.2 eV[70] and 0.7 eV[71]. The adjacent graphene layers comprising the MWCNTs are most likely turbostratic in their stacking arrangement which greatly reduces the interlayer carbon-carbon interaction relative to AA or AB graphite, and it is the strength of this interlayer interaction that is responsible for the wider band overlap in graphite[72]. Xu *et al.*[57] estimated a band gap of 0.14 eV for their highly ordered vertical MWCNT arrays. The estimate presented here is approximately equivalent to the band gap of graphite. However, for a band gap model to be truly valid one would expect a sharp absorption edge at a particular wavelength in the transmission spectrum, given by;

$$\lambda^* = \frac{hc}{E_g}$$

(5.11)

For the estimates above, this would indicate $\lambda^* \sim 39$ μm. No such cut-off was noted. Figure 6.16(a) evidences a rapid increase in transmittance (i.e. reduced photon absorption) for $\lambda > 100$
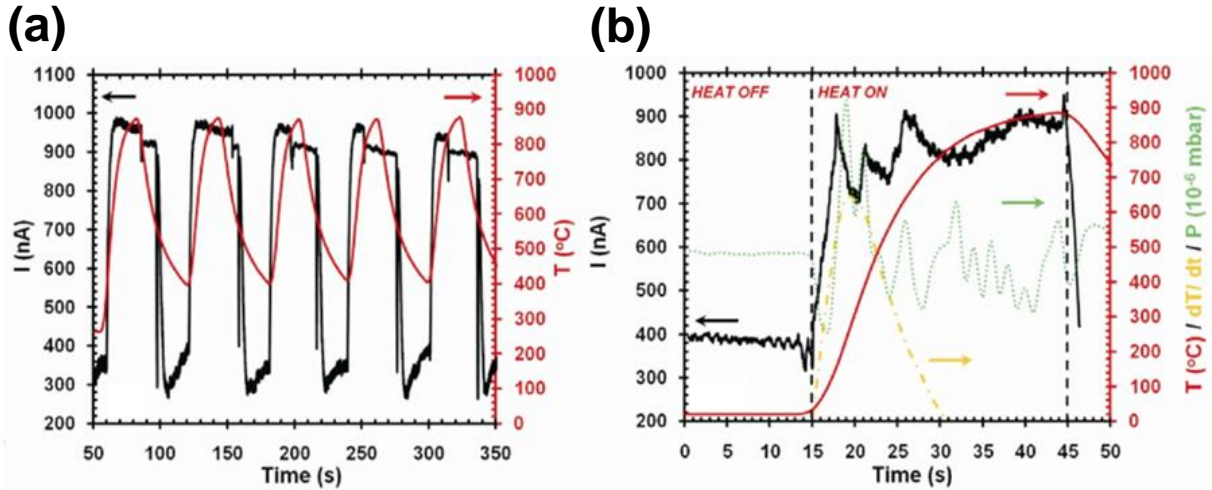
Figure 6.17 | Broadband IR response. (a) Current response (100 µV bias) at a thermal ramp rate of 50°C/s. 30 mm heater-sample separation. **(b)** Detailed step response showing a current variation of ~20% under direct IR exposure attributed to fluctuations in chamber pressure with temperature.

µm (E_g~10 meV). Although inconsistent with the band gap estimates, this cut-off edge is in fact consistent with the activation energies estimated from the transport data given in Figure 6.25, which will be discussed in more detail later. However, for λ>100 µm, %T is greater than 38% which is substantial and hints at a concurrent or, more likely, alternative photoconductive mechanism. Note though that these band gap estimates implicitly assumes a sample composed of only one MWCNT diameter. This is not the case and in reality a wide diameter range would certainly smear the sharp cut-off wavelength. The membrane shows a uniform response across an incredibly wide spectral window, much wider than most state-of-the-art detectors, offering potential functionality as a truly ubiquitous photodetector for optical, IR and sub-mm detection. Indeed, the wideband absorption of the membrane is favourable compared to optical detectors based on PbS (E_g = 0.42 eV at 295 K), which has λ*= 2.9 µm and PbSe (E_g = 0.23 eV at 195 K) with λ*= 5.4 µm.

The membrane response to simultaneous thermal and optical stimulation is reported in Figure 6.17. Measurements were performed by exposing the membranes to a heated black-body source. The response was measured using a LABVIEW controlled and logged Keithley 6430 source-meter. The variation in the stimulated current correlates well with thermal pulsing, as shown in Figure 6.17(a). Figure 6.17(b) shows in some detail a single thermal ramp (red), the chamber pressure (green) and the thermal gradient (orange). Noise is a result of the thermally stimulated fluctuations in the pressure. Pressure was manually controlled by
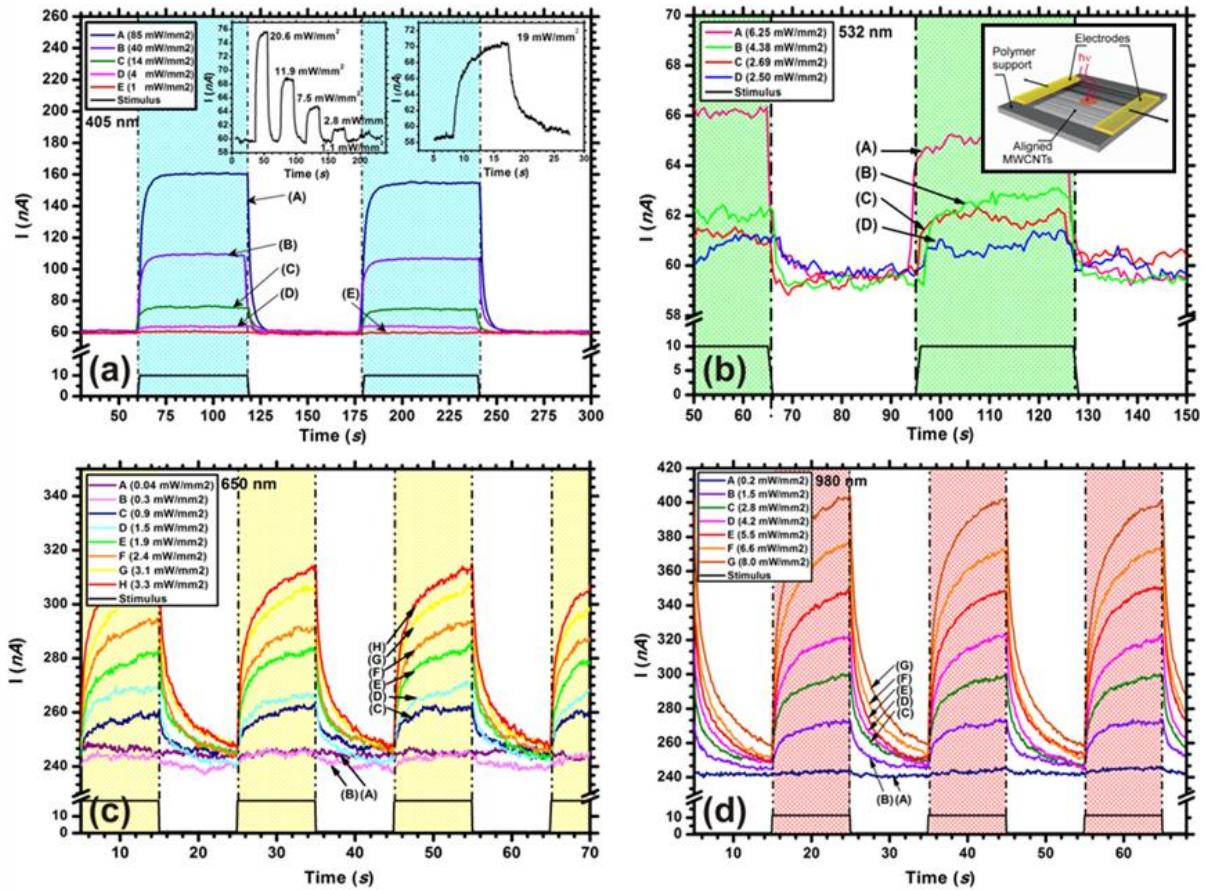
Figure 6.18 | Broad spectral photoresponse. Transient photoresponse during monochromatic lasing at varied power densities in ambient atmosphere (1-5x10^{-2} Hz). **(a)** 405 nm (violet, 1.0-85.0 mW/mm^2), *Insert 1*: Variation in photoresponse with power densities (20.6-1.1 mW/mm^2). *Insert 2*: Detailed 405 nm transient (19 mW/mm^2). **(b)** 532 nm (green, 2.50-6.25 mW/mm^2), *Insert:* Experimental set-up, **(c)** 650 (red, 0.04-3.3 mW/mm^2) and **(d)** 980 nm (NIR, 0.2-8.0 mW/mm^2). (Black) Heaviside step-functions represents the on-period of the modulated laser source. The sample is exposed in the shaded regions.

throttling. Samples were supported on an alumina frame and were placed 30 mm from the heated stage. W wires connected the sample to the ambient feedthroughs. The chamber was evacuated from atmospheric pressure to 10^{-3} mbar. The stage was thermally ramped at ~50°C/s from room temperature to 900°C and was manually modulated. A W wire control was prepared which exhibited a significantly lower sensitivity indicating that the observed response was a product of the MWCNT membrane rather than the contacts or lead wires. Measurements were inconclusive with regards to the response mechanism(s). Nonetheless, bolometry, band effects (optical) and absorption effects (pressure) were all implicated to varying degrees. Despite uncertainty in the mechanism, currents of up to 400 nA and decay time constants of the order of 5 s were observed which encouraged further studies.
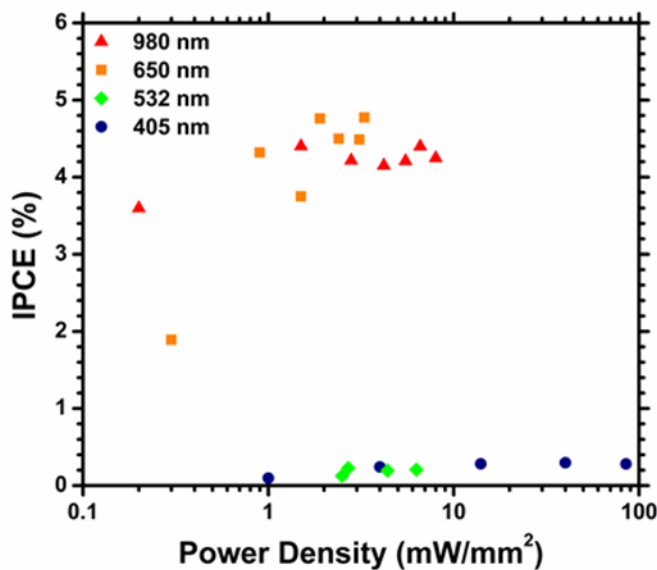
Figure 6.19 | Incident photon-to-electron-conversion efficiency. IPCE (%) as a function of wavelength and power density.

Time-dependent photoresponse measurements during monochromatic lasing were performed using an HP 33120A function generator (0.1 mHz - 15 MHz) modulating a Thorlabs semiconductor laser diode (λ = 405, 532, 650, 980 nm) with a spot size, A_{spot} = 1.3×10^{-7} m^2. Optical filters were placed in the beam path to ensure narrow band exposure (Insert, Figure 6.20(a)). Incident intensities were monitored using a calibrated Si photodiode (Thorlabs). A source-to-sample separation of 60 cm was used throughout. All experiments were carried out under constant voltage mode operation (100 µV, unless otherwise stated) to minimise electro-absorption artefacts[73]. The incident beam was passed through a chopper and lock-in amplifiers were employed. Photocurrents were sampled using a HP Semiconductor Parameter Analyser with sub-pA resolution. For all experiments the optical stimulus was focused at the centre of the membranes. All optical measurements were performed in air at room temperature. Membrane temperature was immeasurable given the experimental set-up.

Figure 6.18 shows the transient photoresponse during λ = 405, 532, 650 and 980 nm irradiation at various power densities, p(λ) from 1-85 mW/mm^2. The measured photocurrents are irrefutable evidence that the MWCNTs themselves are photoconductive over a wide spectral range, rather than any residual surfactants. Similarly, the measured photoconductivity is independent of substrate and electrode interface effects – which, although they may enhance or augment the observed photoconductivity, certainly do not account for it. Local heating effects where minimised by modulating the exposures. Note also that the driven currents (<500 nA) were insufficient to induce significant self-heating, validated by the zero steady-state drift in the photoresponse. Room temperature photoresponses of up to 154 % were noted. Relatively high dark currents were noted (60-100 nA). High dark currents reduce sensitivity to low-level exposure and permit signal screening by ambient thermal excitation.

The incident photon-to-current efficiency (IPCE) is a widely employed performance metric and is defined as the fraction of incident photons that contribute to the measured photocurrent. The IPCE takes the general form[61];

$$IPCE\,(\%) = \left(\frac{100hcI(\lambda)}{e\lambda p(\lambda)A_{spot}} \right) \tag{5.12}$$

where h is Planck's constant and c is the speed of light. The IPCEs (Figure 6.19) under red (650 nm) and near-IR (NIR, 980 nm) irradiation are ~4.5% and are more than one order of magnitude larger than the 405 nm (blue) and 532 nm (green) stimulation (~0.4%). The presented NIR IPCE is more than ten times larger than the values reported by Khakani and co-workers[55]. Studies on solution processed SWCNTs on quartz substrates realised quantum efficiencies of around 1.5 %[74].

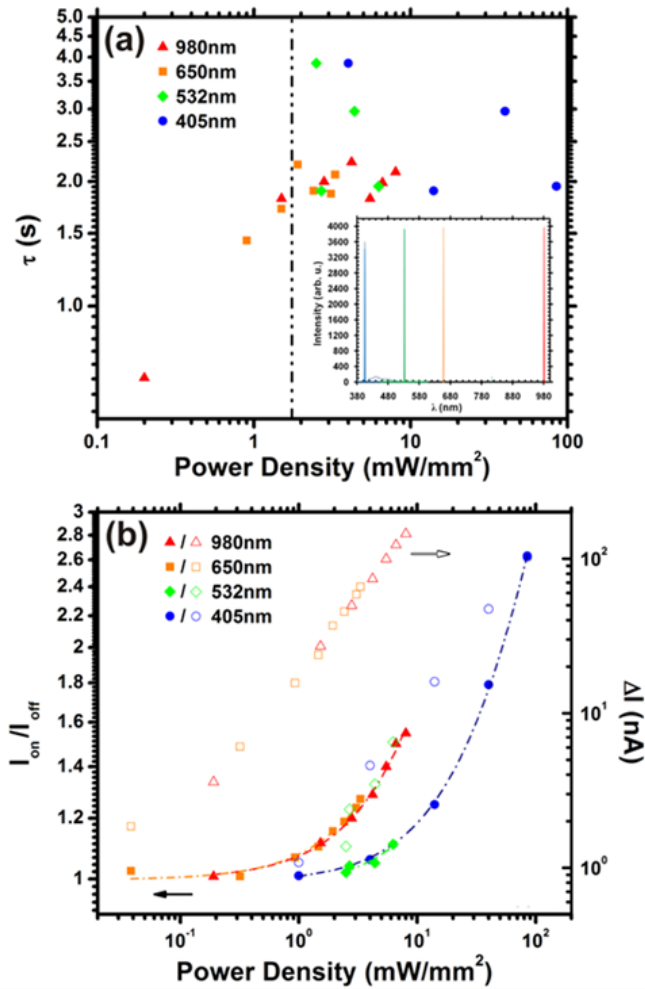The dynamic response data (Figure 6.18) was fitted using $I(\lambda) = I_o + I^* \cdot \exp((t_o - t)/\tau)$, where $I(\lambda)$ is the wavelength (λ) dependent photocurrent, t is the time and τ is the decay constant. Figure 6.20(a) shows the decay constant as a function of the power density, $p(\lambda)$. Decay constants were largely independent of λ and $p(\lambda)$ and were consistently of the order of 2 s. The time constants extrapolated from the transient photoresponse measurements agree well

Figure 6.20 | Photoresponse performance. (a) Decay time constants (τ) for varied $p(\lambda)$ and λ. *Insert:* Optical spectra showing narrow-band illumination. **(b)** Variation in the on-off ratio (I_{on}/I_{off}) and ΔI (=I_{on}-I_{off}) for incident λ at varied $p(\lambda)$. [Exponential fit, $I(\lambda) = I_o + I^*\exp((t_o-t)/\tau)$].
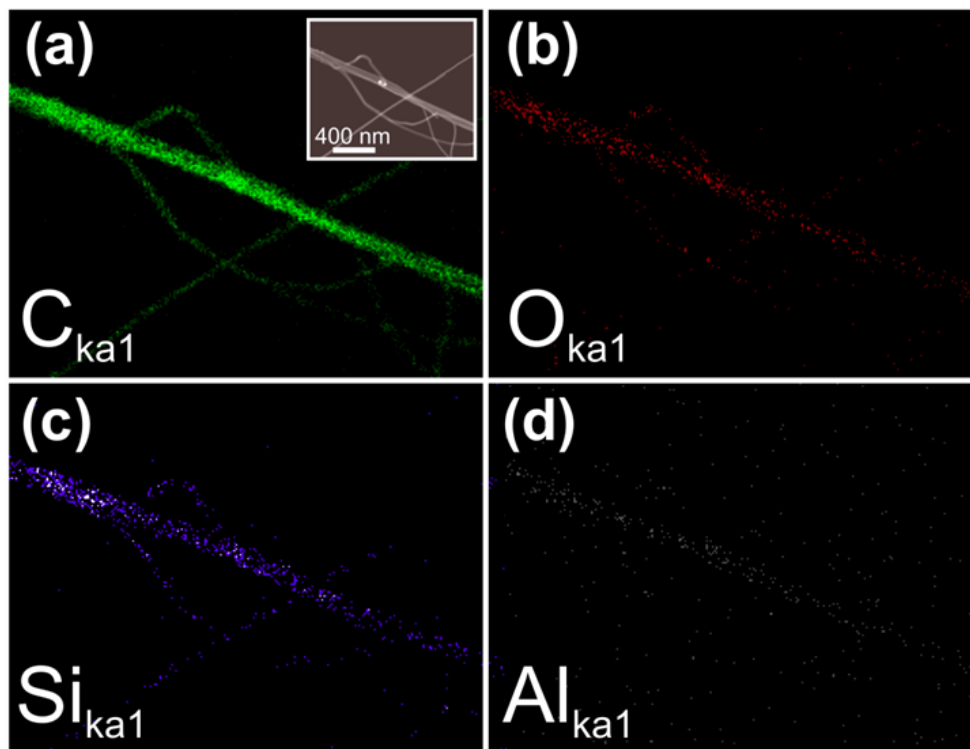
Figure 6.21 | Elemental content and distribution. Energy dispersive X-ray for the kα transitions of **(a)** carbon (C), **(b)** oxygen (O), **(c)** silicon (Si) and **(d)** aluminium (Al). Uniform distributions are noted for each. *Insert:* SEM micrograph of the measured MWCNTs.

with the decay constants estimated from the simultaneous photo and thermal excitation (Figure 6.17), suggesting the activation of the same underlying mechanism. The transient photoresponse measurements also crudely suggest a bolometric response which is known to demonstrate decay constants of 1-100 ms[52]. The decay constants also imply that the response is unlikely to be band gap related as exciton recombination in semiconducting SWCNTs occur on a time scale of <100 ps, at room temperature[75]. Band gap effects are further dismissed due to the similarities in modulation depths at different wavelengths. Nonetheless, slow decays have been explained via exciton formation and charge carrier diffusion due to the low mobility of the interconnected networks for semiconducting nanowires[76, 77]. Ham *et al.*[78] reported decay constants and modulation depths, similar to those above, for SWCNT samples on quartz supports. They argued the dominance of optically activated electro-absorption. However, fixed potentials were ensured throughout experimentation and such effects require high semiconducting populations, which (as previously stated), given the transport and Raman characteristics, is not the case.

Figure 6.20(b) summarises the variation in on-off ratio, (I_{on}/I_{off}) and ΔI (=I_{on}-I_{off}), for incident λ for varied p(λ). The change in current is directly proportional to the incident power density, consistent with Stoletov's law for the photoelectric effect in irradiated metals, which strongly argues against inter-band transition models[56].

The measured photoconductivity is either a surface or bulk related phenomenon. Bulk phenomenon relate to band gap or bolometric effects, whereas surface effects are primarily governed by the addition or removal of specific surface species / absorbates. Oxygen is one such commonly implicated species. In ZnO NWs, oxygen produces shallow traps. UV generated holes neutralise surface-bound oxygen ions and liberate an electron. This increases the conductivity[76]. Given that an appropriate band gap is unlikely to exist the general mechanism almost certainly differs. Nonetheless, surface and band structure modification through oxygen absorption warrant some investigation.

Various experimental studies have demonstrated that the electronic properties of semiconducting SWCNTs are extremely sensitive to various gas
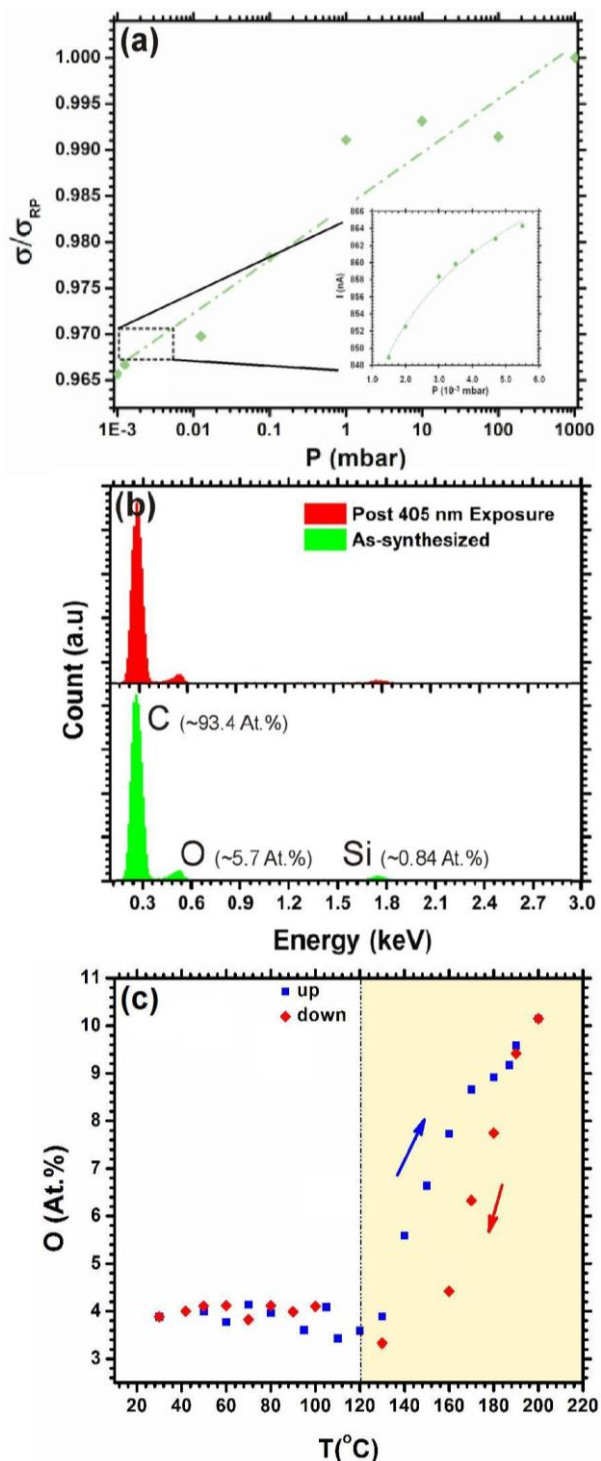
Figure 6.22 | Oxygen sorption. (a) Variation in membrane current as a function of pressure. High and low oxygen contents are denoted for clarity. *Insert:* Detailed variation in conductivity over a one order of magnitude change in pressure. A weak dependence on ambient pressure (compared to thermal excitation) is noted. **(b)** EDX spectra (8 kV acceleration) before and after 405 nm (5 mW) irradiation under 5×10^{-5} mbar chamber pressure. **(c)** Oxygen content as a function of sample temperature. The heat (up) and cooling (down) sweeps are illustrated.

molecules[79, 80]. The insert of Figure 6.16(a) shows the Fourier Transform infra-red (FT-IR) spectrum of a MWCNT membrane. Spectra were base-lined against atmosphere. The main transmissions occur in the NIR regime. The C-O (CO, CO_2) and H_2O (O-H stretching vibration) groups have signatures at 2400 cm^{-1} and 3338 cm^{-1}[81-85] indicating the presence of water and/or oxygen or even trapped gases[86]. C=O (1726 cm^{-1}), C-OH (1226 cm^{-1}) and C-O (1103 cm^{-1}) peaks were weak and for the most part indistinguishable[87]. Oxygen content was independently verified by spatially averaged EDX spectroscopy (Philips XL30 SFEG operated at 20 kV) and EDX mapping (Hitachi S5500 operated at 30 kV), given in Figure 6.21. EDX mapping indicated that the membranes were 88.4 At.% C, 10.4 At.% O, 0.4 At.% Si and 0.2 At.% Al.

To investigate the effect of the gaseous atmosphere and the molecules therein, membranes were loaded into a vacuum chamber and the conductivity monitored, using a Keithley 6430 source-meter, during evacuation. No optical stimulation, other than ambient, was present. Figure 6.22(a) shows the variation in the room-pressure-normalised conductance as a function of pressure. The membrane conductivity decreased by 3.5% over a range of pressures exceeding six orders of magnitude. The trend supports the oxygen doping model, in that oxygen enhances conductivity. Evidently, the removal or addition of surface-bound molecules may very well account for the observed variation in conductivity, even in the absence of direct stimulation. The insert shows a detail of a logarithmic fit to the data across the 1-6x10^{-3} mbar range.

To dissuade bolometry-based arguments in favour of oxygen adsorption, the oxygen content was monitored by EDX in an evacuated chamber (5x10^{-5} mbar) before and after *in-situ* 405 nm laser irradiation. Prior to exposure membranes contained 5.24 At.%, whilst following exposure the oxygen content increased by ~0.5% (Figure 6.22(b)). Oxygen was sourced from the chamber ambient. Trace elements did not vary. Lasing tends to increase the oxygen content, which, by implication increases the conductivity. Thus would suggest that lasing stimulates oxygen absorption. To corroborate this and to determine whether binding occurs as a result of heating, EDX spectra monitored the oxygen content during thermal stimulation (300-500 K). Figure 6.22(c) shows the variation in oxygen as the temperature is ramped (<4°C/min) (blue) and cooled (red). Chamber pressure was constant throughout. The oxygen content increased with temperature. Above a critical temperature (~120°C), oxygen
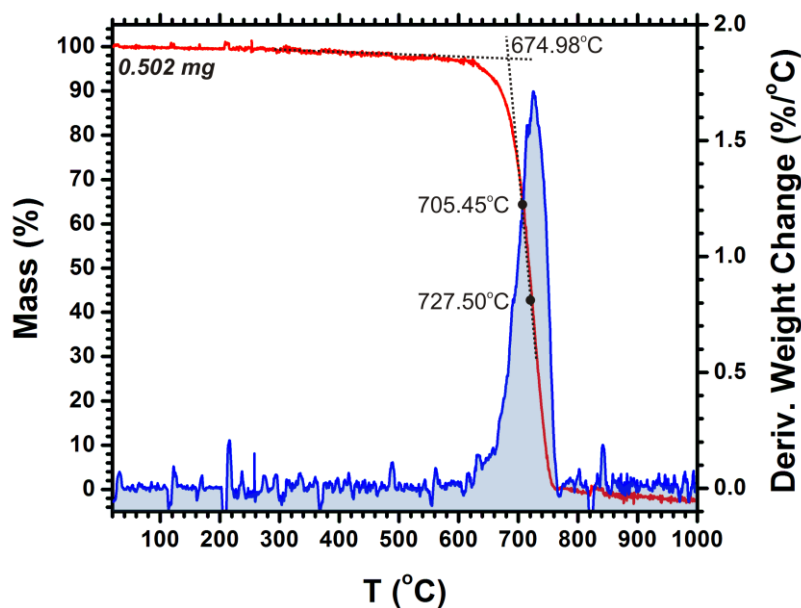
Figure 6.23 | MWCNT burning. Thermogravimetric analysis (TGA) of nanotube sample heated from room temperature to $1000^{o}C$ in an air standard atmosphere.

content increased rapidly. Interestingly, Figure 6.22(c) suggests that heat must be maintained to maintain elevated oxygen content. The data strongly suggests that binding is reversible and transient. The data is consistent with the hypothesis that laser exposure heats the membrane, although to a relatively minor degree ($<50^{o}C$. Figure 6.22(b, c)). Thus, it would seem that surface modification by the adsorption of oxygen accounts for the varied conductivity, as when thermally excited, either by direct heating or by lasing, oxygen binds to the nanotubes which increases the conductivity[88]. Collins *et al.* [80] showed that under atmospheric oxygen carbon nanotubes are 15% more conductive than when under vacuum ($\leq 10^{-6}$ mbar) compared to the 3.5% variation noted previously. They however did not estimate the degree of oxygen saturation. All three data sets in Figure 6.22 support these findings.

Figure 6.21 shows an EDX map of the MWCNTs. Oxygen is uniformly distributed across the nanotube, though whether this distribution is throughout the bulk or surface cannot be determined. Nonetheless, the uniform distribution may account for the large photoresponse given the large active area. Trace Al and Si are residues from the growth substrate. As-synthesised MWCNTs are most likely oxygen-saturated (mass spectrum, Figure 6.14(g)) which tends to reduce the bulk resistivity via charge doping owing to contact potential variations and surface polarisation[59]. Data presented thus far suggests that oxygen binding is triggered by optical excitation and heating therein. Indeed, Levitsky *et al.*[89] proposed that electron-plasmon excitation facilitates charge transfer to physisorbed molecules, leading to stimulation and relaxation transients of the order of 5 s, which is comparable to the relaxation times estimated in Figure 6.17 and Figure 6.20(a).
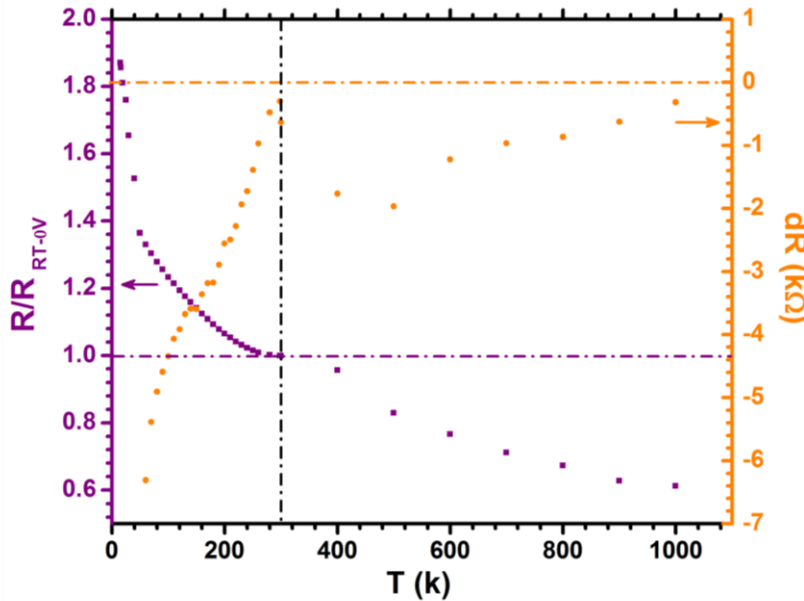
Figure 6.24 | High - temperature transport characteristics. Change in normalised membrane zero-bias resistance with temperature from 15-1000 K. Room temperature, zero-bias resistance R_{RT-0V} = 2.1 kΩ.

Consider the photoresponse and transport characteristics in Figure 6.18 and Figure 6.25. Itkis *et al.*[52] argued that the change in conductivity was purely bolometric (i.e. heating). However, data presented here indicates otherwise. To increase the conductivity by a factor of two, as indicated by the photoresponse data, requires an increase of temperature of ~500°C. Such heating would unquestionably degrade or even thermal decompose the MWCNTs in oxygen rich atmospheres (i.e. air). Thermogravimetric analysis (TGA), for an air standard atmosphere, revealed that the MWCNTs thermally decompose at ~675°C (extrapolated onset temperature). Measurements were inconclusive regarding increased oxygen binding. Any possible increase in weight, attributed to thermally stimulated oxygen binding, as a function of temperature was below the detectable limit of the apparatus. Nevertheless, data suggests that that it is indeed viable to heat to 500°C without subliming the MWCNTs and goes someway to validate the inferred extreme heating during lasing. Indeed, the lack of thermal decomposition is also evidenced in the transient photoresponse data. If the MWCNTs did thermally decompose a decay in the measured photocurrent (as the conducting pathways resistance increased) with exposure time, would have been apparent, which it was not. The peak currents were consistent between pulses (Figure 6.18). Nevertheless, it is physically implausible that the carbon lattice would heat by such an extent within the transient exposures (<5 s). However, the extremely high specific heat of the electrons (compared to the lattice), their long residency time and the low electron-phonon-dominated lattice interactions would suggest that the electrons most likely do. Weak thermal coupling between the electrons and lattice produce a hot electron population. This hot electron model goes some way towards

explaining a bolometric response. The electrons have high-energy and as a result observe less potential features, such as scatter sites, resulting in an increase in membrane conductivity. However, the presence of a hot electron population is largely speculative due to measurement difficulties. Furthermore, the extrapolated time constants argue to the contrary. The decay associated with such processes would differ for the positive and negative going slopes. The leading edge would express a time constant of approximately milliseconds[90] due to the high specific heat of the electrons, whereas the negative-going slope would be much slower as it would be dominated by lattice cooling. In addition, to derive a hot electron population, metallic bolometers often require cryogenic temperatures[91]. Nevertheless, given the nanotubes wide ranging dissimilarities to standard metals, a hot electron population could potentially account for the promotion or breaking of chemical bonds between the lattice and surface absorbates.

Surface molecular oxygen (O_2) can be chemisorbed (bound by the formation of a chemical bond)[85, 92-94] or physisorbed (bound by the transient dispersive van der Waals electrostatic forces)[92, 94-96]. These bonding types are extremely different in regards to their binding energy and implications on the nanotubes electronic structure. In an attempt to identify which bonding dominates, DC transport and transfer measurements were carried out in an evacuated (10^{-5} mbar) home-built cryostat (15-297 K) using a LABVIEW controlled, BLP1.9 low-pass filter connected, Keithley 6430 sub-FA source-meters in standard two and four terminal geometries. Sheet resistances were independently verified using a Jandel four-probe 100 μm contact stylus connected to a Keithley 2100 Digital Multimeter at room temperature. Measurements were also carried out on samples immersed in a liquid He bath (4 K). High-temperature measurements (297-1000 K) were implemented in an evacuated ohmically heated chamber. Figure 6.25(a, b) shows the variation in conductivity as a function of temperature (T). Two and four probe measurements were found to be nominally equivalent at room temperature, 77 K and 4 K due to the large channel and electrodes. Two terminal measurements afforded greater thermal stability in the cryostat and allowed for lower base temperatures (reduced thermal mass / heat load). Conductivity variations between samples were a product of variations in membrane density and size.

Figure 6.25(b) points towards thermal activation as the main mechanism for carrier transport at room temperature. Different gradients in the transport characteristics imply
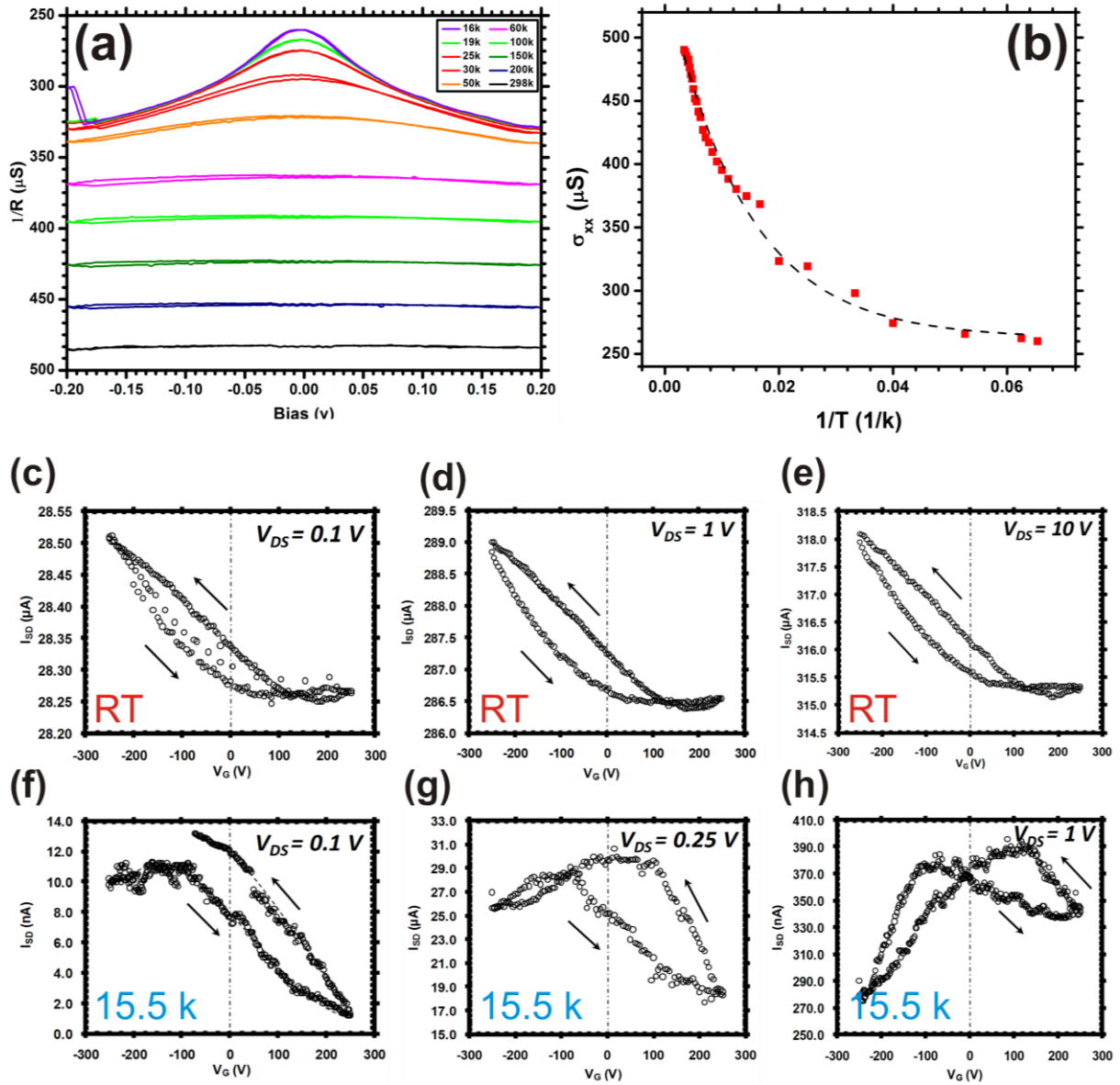
Figure 6.25 | Membrane electronic characteristics. (a) Conductance as a function temperature and a two-terminal bias. The zero-bias differential conductance becomes non-linear at low-temperatures, indicative of a quasi-metallic behaviour. **(b)** Typical differential membrane conductance as a function of temperature indicating an activation energy of 6.2 meV. **(c-e)** Transfer characteristics for V_G=0.1, 1 and 10 V at room temperature (RT) and **(f-h)** V_G=0.1, 0.25 and 1 V at 15.5 K.

distinct transport mechanisms. Fitting an Arrhenius-type relationship indicates an approximate room temperature activation energy of 2-8 meV, consistent with the findings of Charlier *et al.*[72]. This value is broadly consistent with the previously estimated band gap assuming incommensurate walls and outer-wall dominance[68]. Nevertheless, at room temperature such small band gaps would almost certainly be thermally masked, though Dai *et al.*[97] did empirically determine band gaps of the order of 10 meV in their transport measurements. The activation energies extrapolated from the transport data are, however,
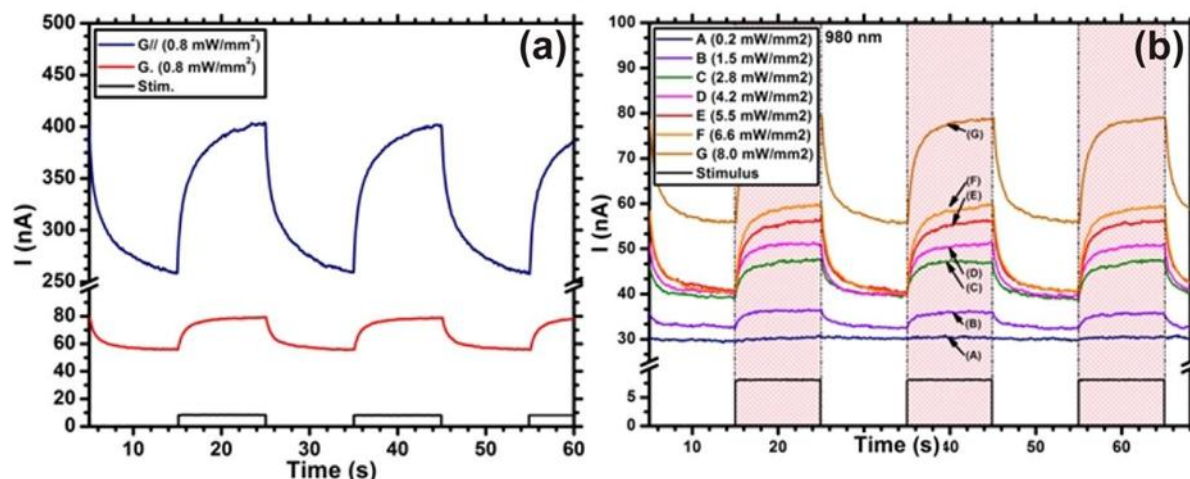
Figure 6.26 | Photoresponse anisotropy. . **(a)** Parallel (//) and perpendicular (⊥) photoresponse (0.8 mW/mm², 200 µV, 980 nm)). **(b)** Perpendicular photocurrent variation (0.05 Hz s) at various power densities (0.2-8.0 mW/mm²). The shaded regions denote the lasing on periods.

comparable to the lattice binding energy of molecular oxygen (13-190 meV[95, 98, 99]). Indeed, Jhi *et al.*[93] reported on the bonding of molecular oxygen, in its triplet ground state, via physisorbtion to the outer face of SWCNTs. On the basis of their calculated density of states, it was suggested that the adsorbed oxygen dopes the nanotubes such that their conducting states are present near the band gap. A similar argument would account for the similarities in the band gap estimates and activation energies indicated in the presented data. Sorescu *et al.*[92] also theoretically considered the chemisorbtion and physisorbtion on graphite and SWCNTs by density function theory. They found that molecular oxygen physisorbs on nanotubes and graphite with binding energies of the order of 30 meV, whereas outer wall chemisorbtion on nanotubes had a much larger binding energy of 440 meV. Comparison with the activation energies extrapolated from the transport characteristics (above) strongly suggests a physisorbtion process. This is not unexpected. Porous nanostructured networks are junction / tunnel barrier dominated. Thus, in such dynamic networks, oxygen migration would almost certainly affect the measured conductivity by interacting with these tunnel junctions to a greater extent than the immobile chemisorbed species. In contrast, Gianozzi *et al.*[94] surmised that oxygen physisorbtion gives rise to negligible charge transfer compared to chemisorbed oxygen suggesting that conductivity variations associated with physisorbed oxygen are much less than those for chemisorbed oxygen[92]. Sorescu *et* al.[92] found that both physisorbed and chemisorbed bonds are highly unstable. This metastability implies that both are viable candidates given the photoresponse transients, as each has a characteristic lifetime.

Lifetime estimates are unfortunately unavailable for chemisorbed and physisorbed species making bond assignment difficult. Given the comparable size of the estimated band gap and the oxygen binding energies, one cannot draw a suitably clear distinction between the two using the transport and photoresponse data alone. To further investigate the potential effect of resident oxygen (albeit chemisorbed or physisorbed) the transfer characteristics of the MWCNTs were considered. Degenerately doped Si/SiO$_2$ back gated FET structure were fabricated with nanotube membrane channels. At room temperature, a weak, but nevertheless *p*-type behaviour was noted, consistent with reports attributing the effect to oxygen doping[100, 101]. The channel characteristics (at equivalent pressure, 10^{-5} mbar) deviate to a more undefined state at 15.5 K suggesting the presence of significant numbers of charge traps. Both these artefacts can be attributed to surface bound oxygen augmenting the local band structure. Figure 6.24 shows the normalised variation in resistance from 15-1000 K. The high rate of

Figure 6.27 | Frequency dependent photoresponse. (a) Anisotropic photoresponse as a function of stimulus frequency under 980 nm irradiation. **(b)** HR-SEM micrograph of suspended film highlighting the film anisotropy. *Insert:* SEM micrograph of a bundle-like formation. **(c)** Per unit-area ($\delta A = \delta x . \delta y$) distributed RC model showing the inter-tube junction resistance (R_{int}), inter-tube capacitance (C_{int}) and nanotube resistance (R_{MWCNT}).

change in resistance with respect to temperature, between 300 K and 500 K, suggests increased absorption rates. Nevertheless, the corresponding estimated activation energy is still <30 meV across this extended range, which consistently supports a physisorbtion model.
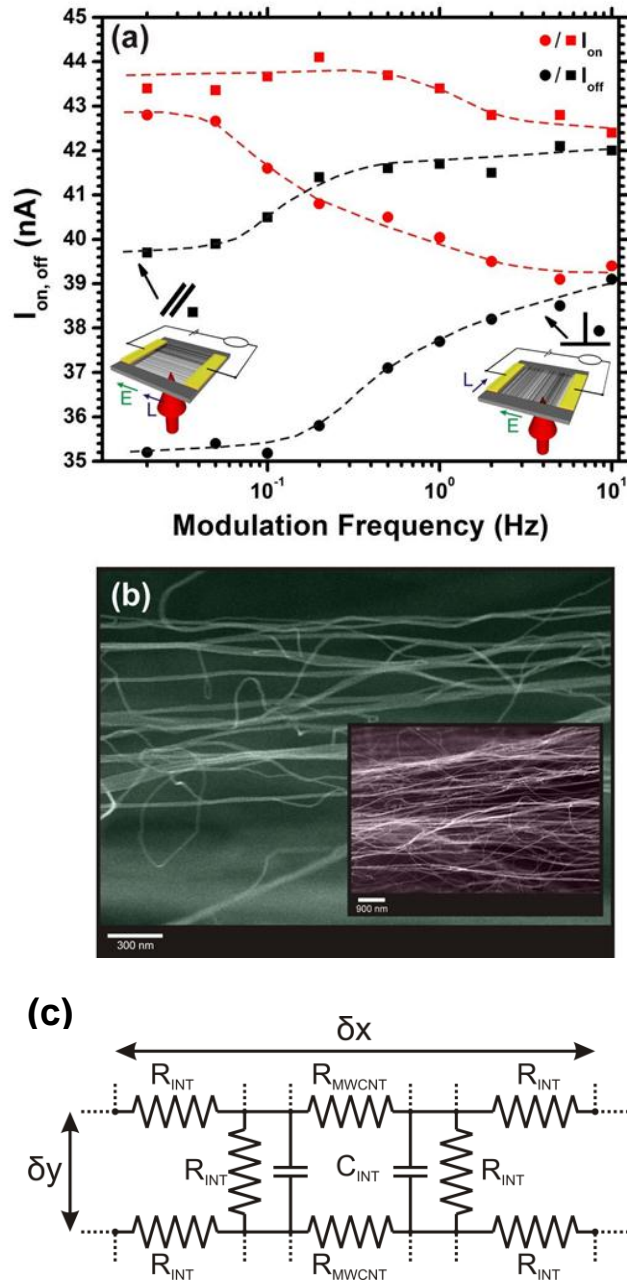
Notwithstanding, the physisorbed bond density should decay with increasing temperature. In a sense, physisorbtion is thermally degraded due to the low bond energy. In contrast, chemisorbed bond density should increase with temperature (up to a critical temperature) due to thermal stimulation. Lasing heats the membrane as indicated by Figure 6.22(c). Evidently for a physisorbed model, oxygen content should decay and the conductivity should reduce when heated. The opposite occurs. Physisorbed species may be thermally promoted to chemisorbed species, which increase in density with temperature. Promotion may perhaps be mediated by the hot electron population as discussed previously.

The morphological, optical and electronic asymmetry of the network has been considered and is illustrated in Figure 6.26. Notable off currents are observed with increasing incident power in the perpendicular ($\perp$) case (Figure 6.26(b)). An increased number of inter-tube junctions and charge traps, as well as trapping duration, may account for this. The lower perpendicular photoresponse occurs because the nanotubes absorb differently in each direction, an important effect that is exploited later to form wideband nanotube membrane optical polarisers. Just like the constituent nanotubes, the membrane has an anisotropic absorption tensor. It selectively absorbs polarised, or partially polarised light[66] where the polarisation state is in line with the nanotubes' long axes. Liu *et al*.[102] and Xiao *at al*.[103] also documented enhanced photoconductivity and polarisation selective absorption at the same time as the work presented. This accounts for the modest variation in the photocurrent that was observed when the incident beam moves in-plane. Samples were large (~5 mm^2) and the irradiated areas significantly smaller (approx. 0.1 mm^2) ensuring that the measured response was not a result of Schottky barrier (nanotube-electrode) modulation. This is most likely the case in the work published by R. Lu *et al*.[53] due to the small separation between the interdigitated electrodes. In the nanotube membranes, nanotube alignment varies by approximately $\pm 5^{\circ}$ throughout the membrane and the associated absorption also varies as a result.

Membranes had a typical parallel sheet resistance of 1.3 kΩ/sq. Sheet resistance anisotropy ($R_{s//}/R_{s}\perp$) was ~2.8 and showed good agreement with the 550 nm optical transmission anisotropy (~2.7). Figure 6.27 illustrates the frequency-dependent variation in current during 980 nm irradiation at various strobe rates. Figure 6.27(a) shows the clear frequency dependency of the on (exposed) and off (ambient) currents. Figure 6.27(b) goes some way to
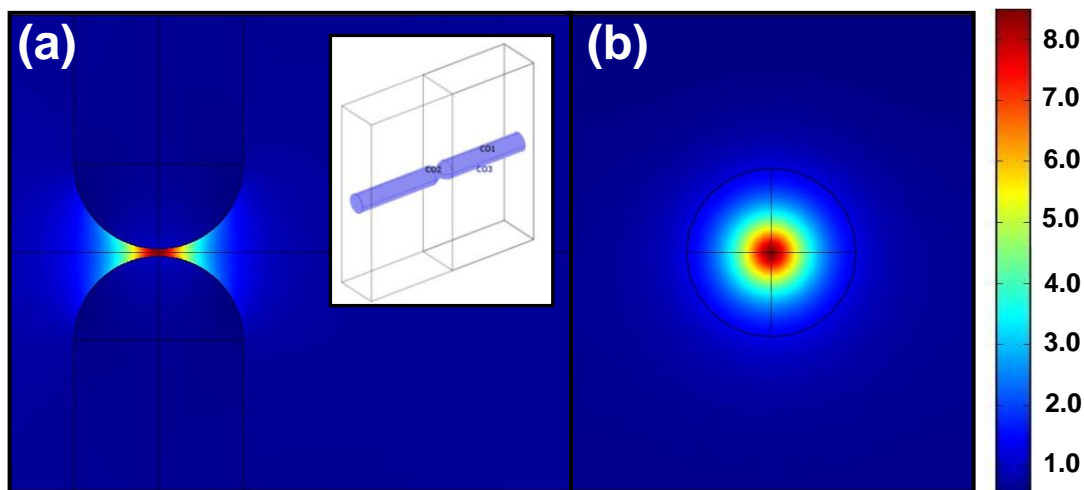
Figure 6.28 | Oxygen migration by electric field enhancement. Simulated electric field enhancement (V/m) at an ideal nanotube tip-tip junction. **(a)** Areal view of the tip enhanced fields. *Insert:* tip-tip geometry. **(b)** Tip field cross section. (Scale bar in V/m)

elucidate this. The network morphology is non-trivial. Although macroscopically aligned, nanoscopically the networks demonstrate relatively high disorder. Not only are the MWCNTs capacitively (C) coupled, but cross-MWCNTs exist within the films which introduce an associated cross-resistance (R), as illustrated in Figure 6.27(c). The inter-tube junction resistance also contributes toward the measured R. The RC system's response tails off at around 10 Hz and 5 Hz in the perpendicular and parallel cases, respectively, which was not unexpected given the decay constants (~2 s) detailed in earlier studies. The RC time constant in the principle axes differ. This is attributed to the number of nanotube junctions (and therefore resistance) in each case. Nonetheless, the decay constants of the parallel and perpendicular response are similar in magnitude indicating the underlying photoresponse mechanism is the same in both directions and is an effect that is largely independent of the junction density. Thus absorbates are not preferentially located in the inter-tube space, but rather conformally coat the entire nanotube, as verified by EDX mapping (Figure 6.21). Activation energies (4-300 K) for the // and ⊥ directions were considered though data was inconclusive.

Thus far, data has gone some way toward implicating increased oxygen physisorbtion for the increase in conductivity during lasing. Oxygen absorption appears to be thermally stimulated even under relatively modest temperatures (<50°C for a 0.5% increase in oxygen). Physisorbed oxygen is inevitably surface mobile. Nanostructures enhance incident electric
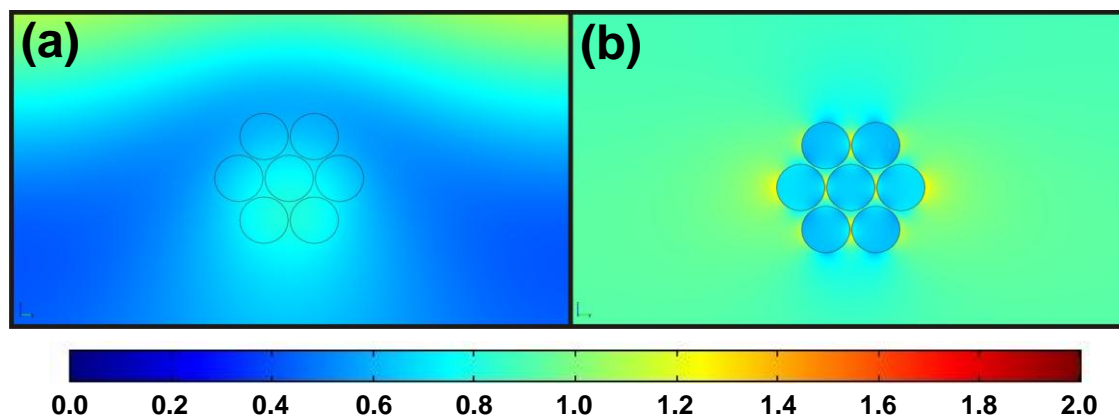
Figure 6.29 | Electric-field enhancement in MWCNT bundles. Simulated electric field enhancement for **(a)** parallel and **(b)** perpendicularly polarised incident irradiation. (Scale bar in V/m)

fields through their detailed structure due to localised surface plasmon (collectively excited electron oscillations) resonances associated with the high aspect ratio of conductive substrates[104, 105]. The free electrons respond collectively by oscillating in resonance with the incident light[106]. Indeed, surface plasmons have been identified in MWCNT systems previously[107, 108] though the higher conductance offered by metals increases the effect somewhat and as a result is more widely reported. It is highly plausible then that it is not the nanotubes themselves coupling to the incident irradiation but rather the uniformly distributed ~10 nm metallic Al clusters throughout the nanotubes (Figure 6.21). Such metallic nanostructures facilitate efficient light-to-heat conversion through the excitation of surface plasmons[109] and may contribute toward the efficient heating of the local electron population.

The conductivity in nanostructured networks is variable range hopping constrained[110, 111] and tunnel barriers at inter-tube junctions dominate the transport characteristics. It is possible that the enhanced electric fields interact with the nanotube dipoles, perturbing the membrane morphology and narrowing the inter-tube separation. The narrower the inter-tube tunnel barrier, the higher measurable membrane conductivity. The incident and coupled fields are dynamic. Consequently the size of the tunnel barriers oscillate about a narrower mean compared to the unexcited state. The interfacial tunnel barriers are non-equilibrated. Moreover, such enhanced fields may interact with dipolar absorbates. The arguments presented thus far have pertained exclusively to surface oxygen; however it is perfectly plausible that the inferred oxygen signals in the FT-IR and EDX data are in fact a product of surface hydration. Molecular water has an electric dipole[112] and has been shown to propagate

at rates of up to tens of cm/s as a result of applied electric fields[113]. Thus, rather than simply encouraging increased tunnelling currents, the enhanced electric fields may instigate absorbate migration which in turn contributes to the modulated membrane conductivity.

In collaboration with the Queens University, Belfast, the electric field enhancement was modelled for the proposed system, the core results of which are presented in Figure 6.29 and Figure 6.28. Here the nanotube tip-tip junctions and seven-member nanotube bundles have been considered. The details of the simulations will not be reported here. Gunji *et al.*[113] showed that electric fields of the order of 10^6 V/m are necessary to instigate motion in very large (nL-µL) drops whereas Fuchs *et al.*[114] demonstrated their floating water bridge by applying 15 kV across tens of millimetre gaps (~10^7 V/m). The electric fields suggested by the model, which were consistently <10 V/m, are insufficient to encourage water migration, though may still account for tunnel barrier reduction given the unconstrained nature of the MWCNTs within the membrane. The model assumes solid carbon cylindrical conductors free of metallic impurities. This only partly captures the true system. The nanotubes are hollow, contain metallic nanoclusters and are formed from graphitic planes which increase the degree of capacitive coupling to the incident irradiation. Increasingly conductive MWCNTs would similarly increase the field enhancement. These combined effects may very well enhance the local electric fields to the extent where absorbate migration away from high field inter-tube regions is stimulated.

6.4 Wideband Multi-Walled Carbon Nanotube Optical Polarisers

According to the theory of electromagnetic scattering and absorption, anisotropic nanomaterials, which are small compared to the wavelength of incident light, absorb light differently in particular directions[115]. Optical polarisation should, as a result, be attainable using the nanotube membranes presented previously. Indeed data for the anisotropic photoresponse (Figure 6.26) certainly suggest this. This section reports on the development of MWCNT-based UV-NIR polarisers that show functionality across a spectral range exceeding that of commercial polarising materials.
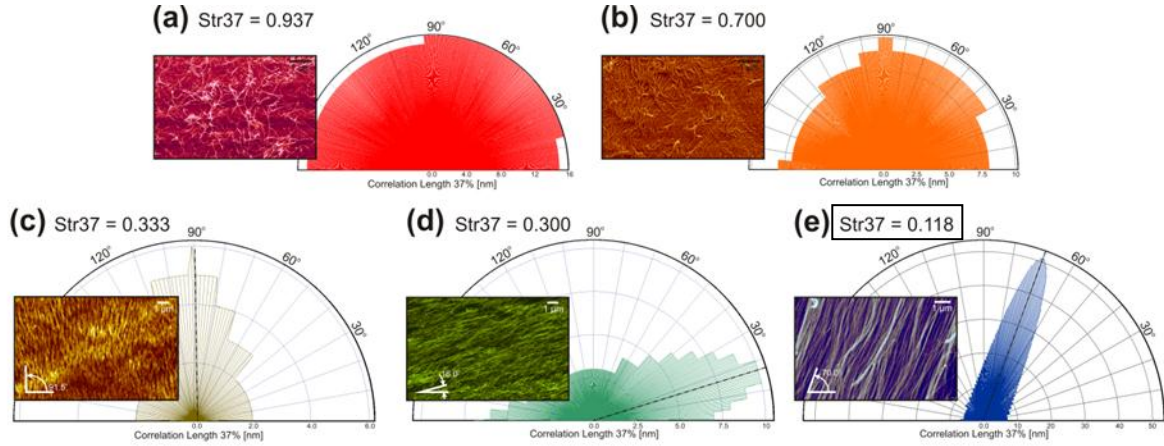
Figure 6.30 | **Comparative alignment.** **(a)** Comparative alignment analysis (Str 37) of the various planar nanotube fabrication techniques employing the same source nanotube forests: **(a)** mixed cellulose ester membrane vacuum filtrated (Chapter IV) (0.94), **(b)** compressed (500 g/cm^2) (0.70), **(c)** mechanically sheared (Chapter II, IV) (0.33), **(d)** rolled (0.30) and **(e)** an extruded nanotube membrane (0.12).

The electric field of light propagating in a homogenous media consists of two mutually orthogonal plane polarised components, both orthogonal to the direction of propagation. For elliptically polarised light these field vectors vary in time and position and are out of phase with one another. The two extremes of elliptical polarisation are circular and linear, the selection of which depends on the phase shift between the orthogonal components. When the components are equal in magnitude and $\pi/2$ out of phase the light is circularly polarised, whereas when they are in-phase it is said to be linearly polarised. The propagation of light in a material is described by the materials refractive and absorption indices. The complete refractive index, N, is a complex matrix quantity of the form;

$$N = n + jk = \begin{pmatrix} n_{xx} & n_{xy} & n_{xz} \\ n_{yx} & n_{yy} & n_{yz} \\ n_{zx} & n_{zy} & n_{zz} \end{pmatrix} + j \begin{pmatrix} k_{xx} & k_{xy} & k_{xz} \\ k_{yx} & k_{yy} & k_{yz} \\ k_{zx} & k_{zy} & k_{zz} \end{pmatrix} \tag{5.13}$$

where n is the (real) refractive index and k pertains to the materials absorption index. Each element of the nine-element tensor describes the refractive and absorption characteristics for a given principle axis. In isotropic media the n and k components take the same values in all three dimensions and the off-axis values are typically nulled. Consequently the polarisation state does not change during propagation. In an anisotropic media the scalars in the tensor are inequivalent and in complex geometries the off-axis components are non-negligible. The light becomes polarised as it propagates through the medium.
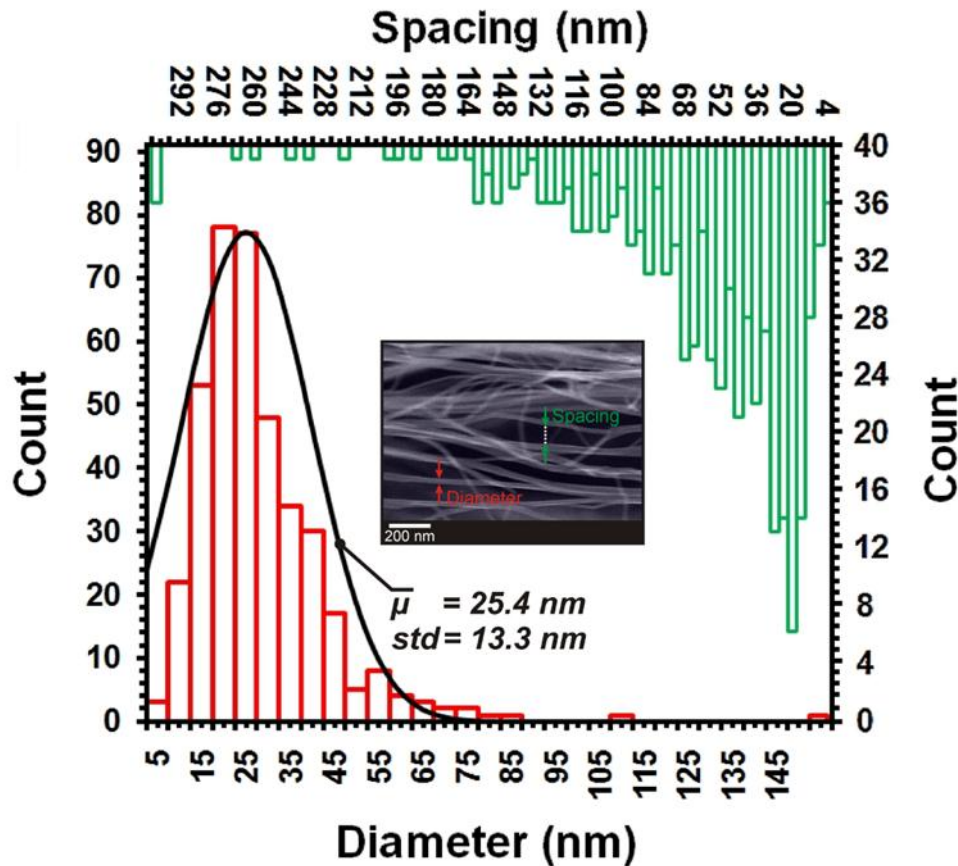
Figure 6.31 | Membrane topography. The diameter and inter-tube pitch of over 200 nanotubes. *Insert:* SEM micrograph of a typical membrane showing the variation in spacing / pitch and nanotube diameter.

Birefringent polarisers change the polarisation state by double refraction. Monochromatic light incident at a non-zero angle to optical axis (assuming uniaxial anisotropy) is split into two orthogonally polarised components which travel at different speeds through the material due to differing absorption characteristics in each direction, giving rise to linear dichroism. One polarisation state is selectively absorbed in preference to its orthogonal counterpart. Dichroism is a particular type of birefringence. Dichroic polarisers are fabricated from polymer-embedded uniformly orientated birefringent crystals or polymers, the molecules of which have been uniaxially aligned by mechanical stretching. Dye molecules are selectively attached to the aligned polymer chains. The absorption is very high in one direction and weak in the other. The transmitted beam is linearly polarised. It is in this structure that the nanotube membrane (absorptive) polarisers are similar.

The major drawback to dichroic films is their limited range. The high-energy limit, typically ~400 nm, is defined by the strong absorption of the polymer backbone or substrate.
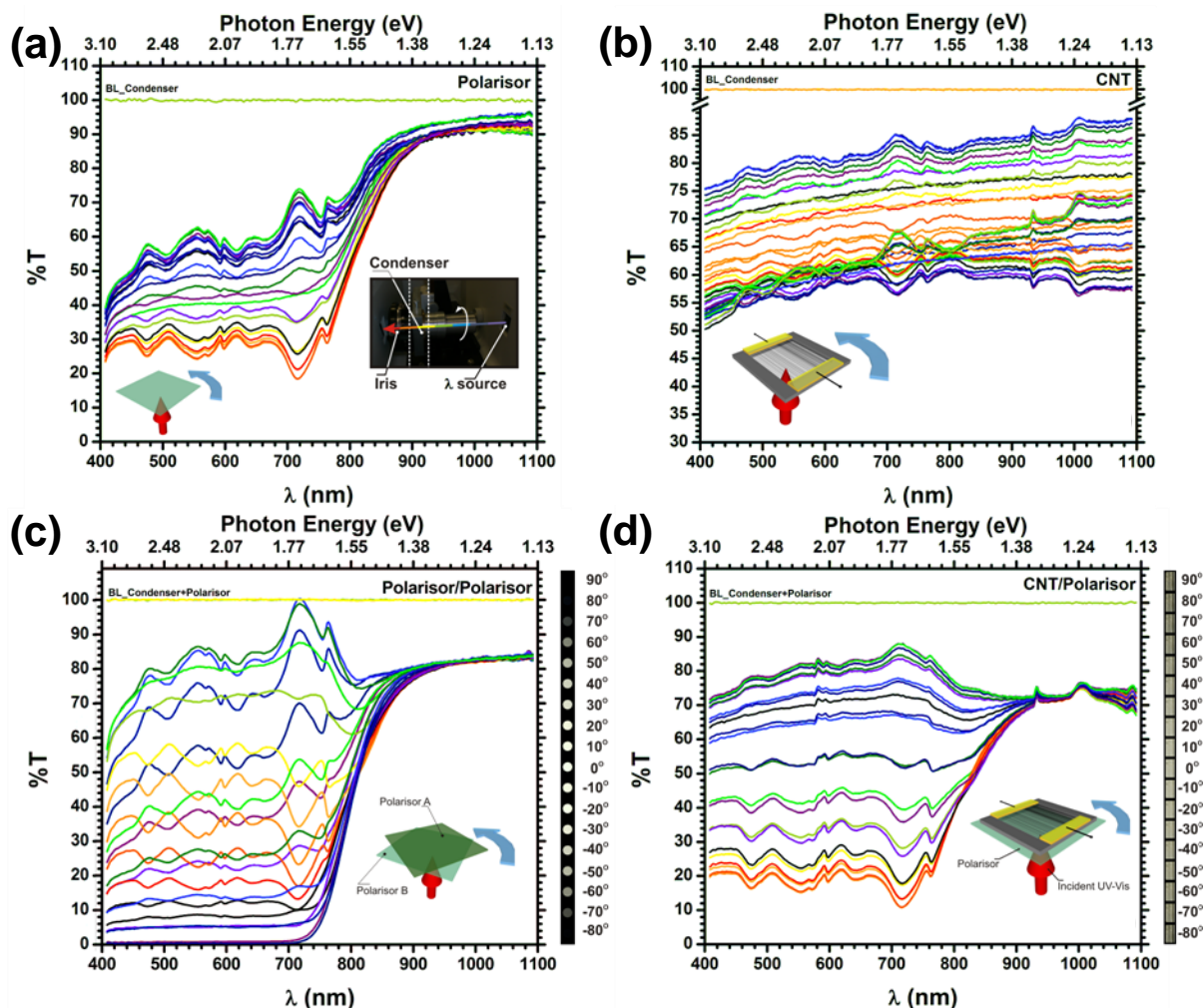
Figure 6.32 | **Optical polarisation.** Wavelength and rotation dependent optical transmittance of; **(a)** a single polymer-based dichroic polariser. *Insert:* Measurement set-up. **(b)** Single nanotube membrane. **(c)** Polymer-based polariser pair. **(d)** Nanotube membrane-polymer polariser pair. Note that the spectral peaks are associated with dichroic films intrinsic absorbance. Rotation dependent peak inversion is a product of the condensing lens in the measurement setup. *Inserts:* Optical micrographs showing the variation in unpolarised white light transmission as a function of rotation angle for polymer polariser pair (c) and a nanotube pair (d).

The minor transmittance limits the blocking capacity in the NIR region inducing severe leakage at λ>850 nm (Figure 6.32(a,c)). Above ~1200 nm leakage dominates and typical dichroic polarisers no longer polarise. IR polarisers are commercially available and include; calcium fluoride (CaF$_2$, 126 nm-9.8 um)[116], Calcite (2.5-16 um)[117] and KRS-5 (560 nm-22 um)[118] though most are inflexible and costly**.** Notwithstanding, it is ultimately the optical properties of the substrate which determines, and limits, the functional wavelength range. The substrate-free nature consequently makes the presented nanotube-membrane polarisers extremely attractive for broadband applications. Simple parallel processing and easy to control pitch increases their attractiveness.
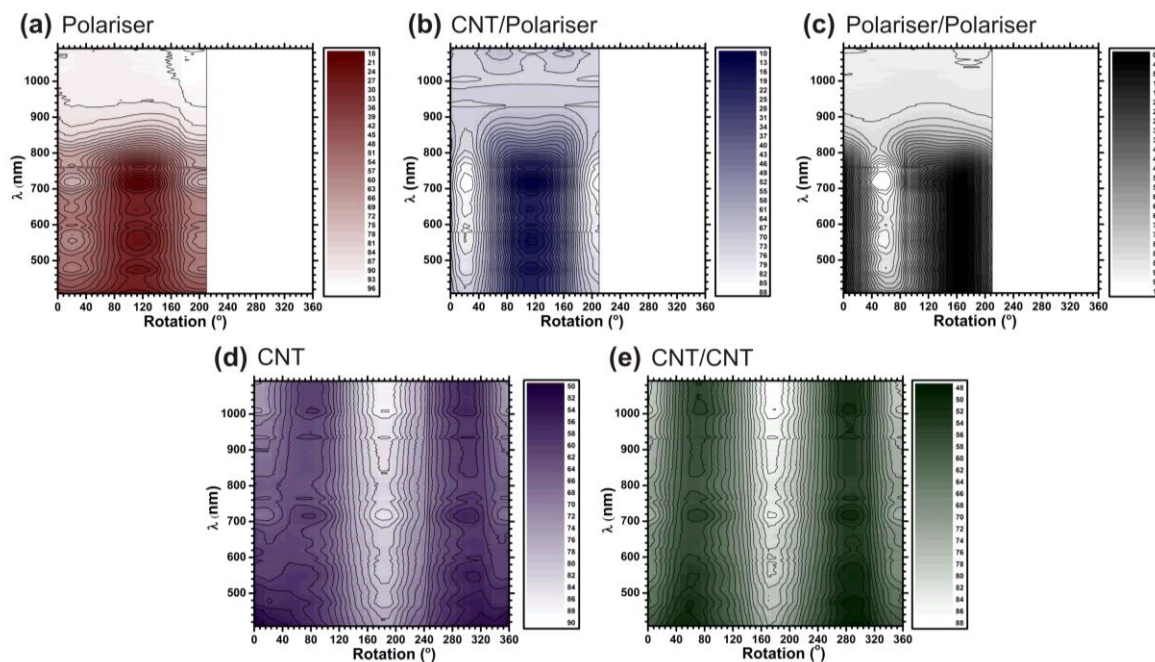
Figure 6.33 | **Polarisation maps. (a)** Single polariser, **(b)** CNT/polariser, **(c)** polariser/polariser, **(d)** single nanotube, **(c)** nanotube/nanotube polariser. Note that the incident beam is partially polarised from to the multiple reflecting stages in the spectrophotometer.

The polarisation efficiency depends on the spacing, periodicity and 'wire' conductivity. NIR-MIR polarisers are fabricated from ruled or holographic wire grids on expensive IR transmitting windows. Ruled grids are made by diamond-scribe-patterning of fine parallel lines ($\sim$1-2 μm^{-1}) on hard, inflexible surfaces, such as ZnSe, that is PVD coated with a metallic layer. In the case of holography, two coherent lasers pattern a layer of photoresist. The lines between the exposed regions are removed and PVD coated with a metal, as before. Although softer substrates can be used in holography the processes are ultimately serial and are therefore rather time consuming.

Figure 6.30 illustrates the high degree of alignment attainable compared to other nanotube aligning processes considered during this work. High resolution-SEM indicated that the membranes consist of MWCNTs with an approximate inter-nanotube pitch and diameter of 25 nm (Figure 6.31) giving an approximate linear density of 20 μm^{-1}. Note that the range in diameter and pitch permit multiple regions of the electromagnetic spectrum to be accessed.

Polarisation studies were performed in an ATI Unicam UV-Vis-NIR spectrophotometer with a deuterium/tungsten source capable of 2 nm spectral resolution. Sample rotation was
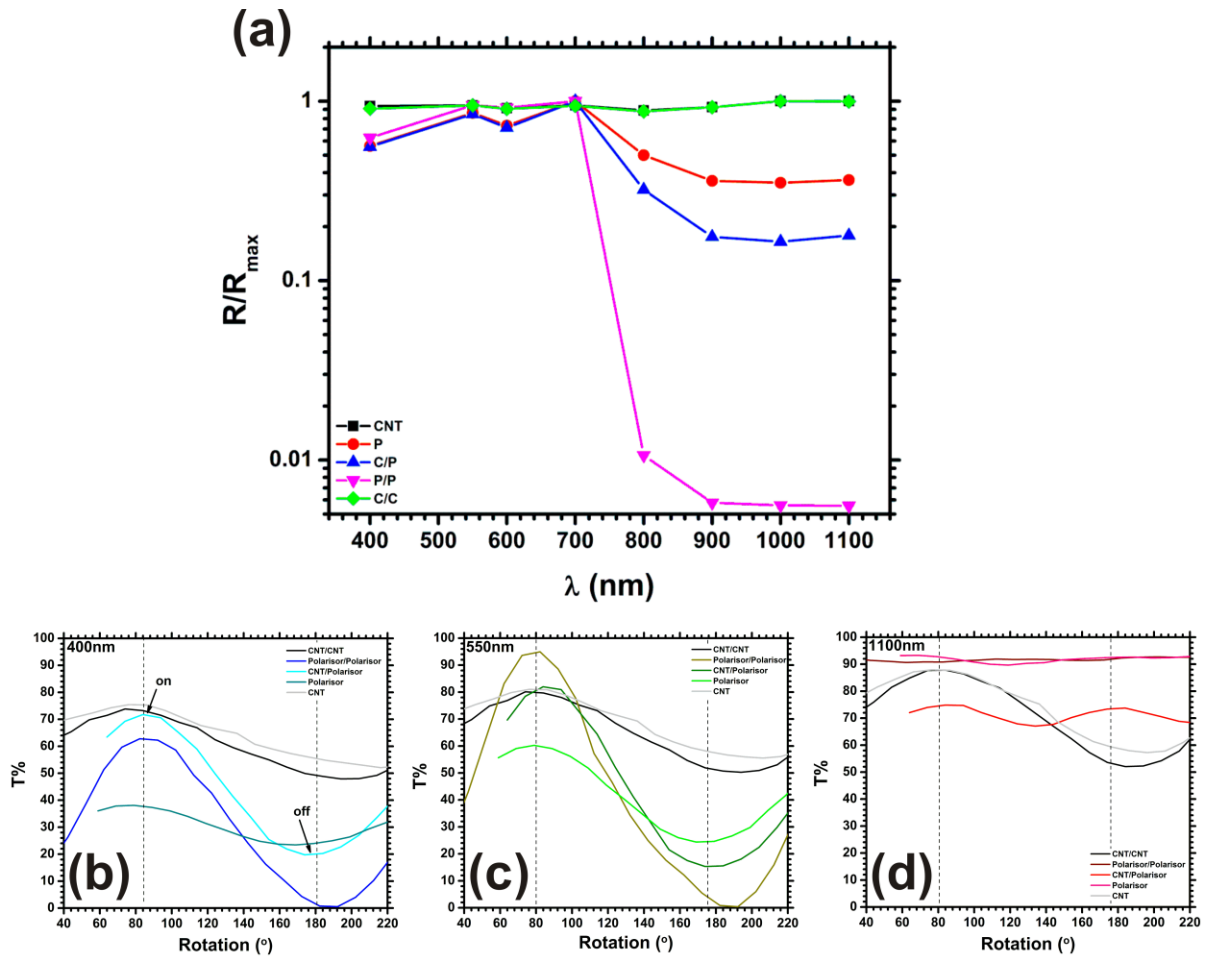
Figure 6.34 | Extinction Ratio. (a) R/R_{max} ratio as a function of incident wavelength (λ). The nanotube membranes polarises well into the NIR, whilst the efficiency of the traditional dichroic films tails off from ~700 nm. Squared-sinusoidal angular dependence of the optical transmission for **(b)** 400 nm (blue), **(c)** 500 nm (green), **(d)** 1100 nm (NIR). Nanotube membranes show continued functionality into the NIR.

monitored using a manually indexed optical mount. A condensing lens and aperture were used to focus the beam region. The inserts of Figure 6.32(a-d) depict the experimental set-up. Incident radiation was partially polarised due to the multiple reflective stages within the spectrophotometer. Commercially dichroic films (Vis) were considered for comparative means. Figure 6.32 shows the optical transmittance (%T) as a function of wavelength (λ) and polariser angle (δ). Note that Murakami *et al.*[66] observed similar peak evolution as a function of rotation in their polarisation studies on vertically aligned, Si-supported samples. The corresponding polarisation maps are illustrated in Figure 6.33. Here the intensity denotes the degree of transparency (dark=opaque, white=transparent). The membranes clearly offer wideband polarisation from 400 nm to 1.1 μm. whereas the leakage of the dichroic films becomes substantial above 850 nm. The angular dependence of the nanotube-nanotube polariser pair is given in Figure 6.35(b-d) and can be fitted with a $\cos^2\delta$ function (Malus' law)
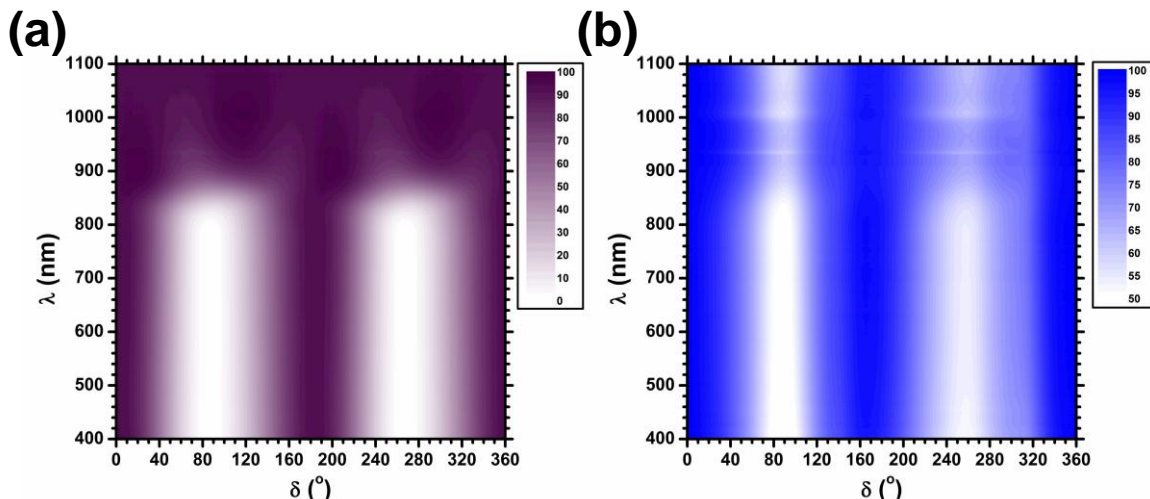
Figure 6.35 | **High-resolution polarisation maps**. Optical transparency, as a function of rotation angle (δ) and incident wavelength (λ) for a pair of standard linear glass-based polarisers (Thor labs) compared to a **(b)** polariser/nanotube polariser pair. Spectra acquired every $2(\pm0.5)^o$ measured using an indexed rotation mount. Note: Condensing lens removed.

throughout the spectral range considered. Translations along the abscissa are a product of difficulties in zero referencing the nanotube membranes and polarisers with respect to one another. The inserts of Figure 6.32(c,d) show optical micrographs of the optical transmission through a polariser pair and MWCNT membrane pair for a 'white' unpolarised light source as a function of rotation.

Experimental repeats, with glass-based polarisers and the condensing lens removed, showed negligible peak evolution or inversion. The corresponding polarisation maps, measured every 2 ± 0.5^o, are given in Figure 6.35 for polariser/polariser and nanotube/nanotube systems. As for the earlier polymer dichroic polarisers, the nanotube/nanotube system continues to polarise well into the NIR, whereas the commercial polariser leaks substantially after 850 nm, as illustrated in Figure 6.34(a). Both show leading edge functionality from ~400 nm.

The data presented in Figure 6.34 and Figure 6.35 were consistent with *ab initio* calculations on the optical characteristics of the nanotube membranes performed in collaboration with the Queens University Belfast. Here the electromagnetic response of the aligned MWCNT membranes was modelled using an effective medium approach and a full numerical simulation to confirm the validity of the original model. In a planar wire array, where the dimensions of the structures are much less than the wavelength of the incident
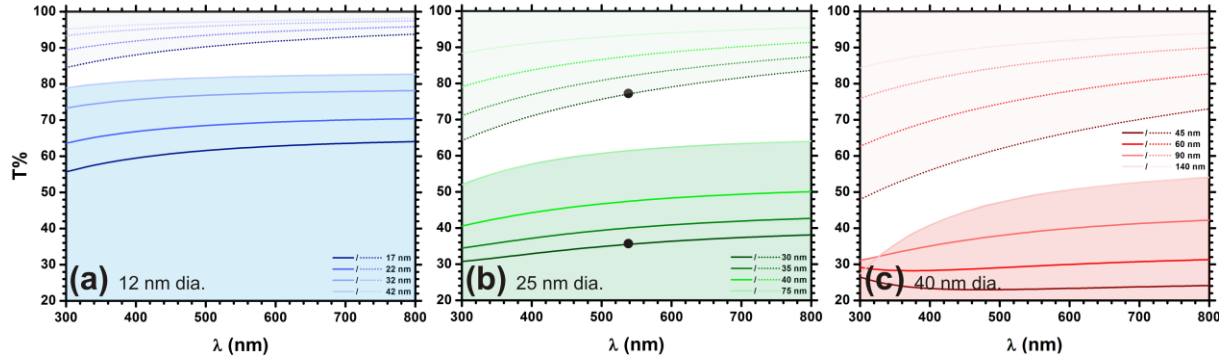
Figure 6.36 | Simulated transmission. Optical transmission (300-800 nm) of linearly polarised light through parallel and perpendicularly aligned MWCNT membranes formed from nanotubes of diameters; **(a)** 12 nm, **(b)** 25 nm and **(c)** 40 nm OF various pitch (see legends). The spot in (b) denotes a standard fabricated membrane with a pitch of 30 nm and diameter of 25 nm.

radiation, the composite structure behaves as an homogeneous, uniaxially anisotropic thin film. The effective refractive indices of an array of cylindrical wires of complex refractive index $\tilde{n}_{CNT}$ embedded in a medium of index $\tilde{n}_a$ are given by:

$$\tilde{n}_{//}^2 = f\tilde{n}_{CNT}^2 + (1-f)\tilde{n}_a^2 \tag{5.14}$$

$$\tilde{n}_{\perp}^2 = \tilde{n}_a^2 + \frac{f(\tilde{n}_{CNT}^2 + \tilde{n}_a^2)}{1 + \left[\dfrac{(1-f)(\tilde{n}_{CNT}^2 + \tilde{n}_a^2)}{\tilde{n}_a^2}\right]} \tag{5.15}$$

where f is a fill factor[119-121]. The subscripts '//' and '⊥' refer to the polarisation direction of the incident radiation parallel and perpendicular to the MWCNTs long axis, respectively. The transmission was calculated for a thin film of this effective index[122]. Due to the inherent cylindrical shape of the nanotubes, they present an effective refractive index and the measured dielectric properties are not directly available or empirically assessable. Previous studies have instead used the optical constants of graphite and graphene[123], due to the lattice similarities. Reported values of the refractive index and the absorption index for graphite vary; in the present study n_{cnt}=3.00 and k_{cnt}=(γ/n)λ along the nanotube long axis, where γ= 5.446 μm^{-1}[124] and n_{cnt}=1.36 and k_{cnt}= 0.05 perpendicular to the axis[123]. The host medium is air ($\tilde{n}_a$ =1).

The validity of the effective medium approach was confirmed using a full-wave numerical simulation. Periodic boundary conditions were assumed using a commercial finite element package with an adaptive meshing routine (COMSOL 3.5a). The surface was approximated by an infinite periodic array of cylindrical nanotubes embedded in a dielectric (air). The

transmission through the array, given in Figure 6.36, was calculated for plane-wave polarised radiation at normal incidence for wavelengths between 300 and 800 nm.

The model and data show excellent agreement. The modelled extinction ratio $(T_{//}/T_{\perp})$ for a membrane with incident linearly polarised light at 550 nm, for a 25 nm diameter and 30 nm pitch, was 0.46 compared to the measured (polariser/CNT, Figure 6.35(b)) value of 0.48. Discrepancies arise due to the inaccuracies in the estimates and variability in the nanotube separation. The membrane is not completely periodic or regular at the nanoscale. Some nanotube bundles exist and this causes deviations. Nonetheless, such variations most likely impart the membrane with its wide spectral response which can be potentially beneficial to engineer wideband polarisers.

6.5   Summary

The ability to align nanotubes by scratch, density and electric fields has been demonstrated. The viability of local and global electric fields was investigated and was shown to offer relatively high linear packing densities of 3.3×10^5 cm^{-1}. The development and use of a horizontal PE-CVD growth reactor was also presented by considering the measured and modelled dimensions of the aligning sheath. A physical peeling technique was also developed to produce highly-aligned free-standing nanotube membranes over large areas.

The photoresponse of mechanically extruded MWCNT membranes was considered due to the ideal nature of the platform. Membranes were operated in constant voltage mode (100 µV) and exposed to 405, 532, 650 and 980 nm laser stimuli at various power densities showed time decay constants of the order of 2 s and room temperature photoresponses of up to 154%. Decay constants supported an oxygen physisorbtion model. Conductivity measurements showed a weak dependence on pressure (~3.5 %) from atmospheric pressure to 10^{-3} mbar. Surface modification via physisorbed molecular oxygen content was implicated through a number of techniques including mass spectroscopy, FT-IR, EDX during *in*-situ lasing and heating, as well as EDX mapping and low-temperature transport and transfer studies. The discrepancy between transport and photoresponse data has been interpreted in terms of a hot electron population. A picture based on the activation energies of molecular oxygen absorption was discussed. Models were presented on the potential for local electric field

enhancement and suggestions were presented on the possible interaction of mobile surface oxygen with these enhanced electric fields which may adjust the inter-tube tunnel barriers thereby increasing the corresponding membrane conductance. Models were largely inconclusive though increased oxygen was found be critical in the photoresponse of the nanotube membranes. The studies here have, for the first time, unambiguously and definitively evidenced the photoresponse of MWCNTs by removing the effects of electrode-MWCNT and substrate-MWNCT interfaces and surfactants.

UV-NIR polarisers have been developed using the extruded nanotube membranes. High-resolution polarisation maps were presented and showed excellent correspondence with modelled systems indicating that polarisation is achieved by polarisation selective absorption. The wide spectra polarisability of the membranes was attributed to the wide variation in nanotube diameter and pitch.

References

1. Huang, S. M., Maynor, B., Cai, X. Y.& Liu, J. (2003). Ultralong, well-aligned single-walled carbon nanotube architectures on surfaces, *Adv. Mater.*, **15**, pp. 1651-1655.
2. Jin, Z., Chu, H. B., Wang, J. Y., Hong, J. X., Tan, W. C.& Li, Y. (2007). Ultralow feeding gas flow guiding growth of large-scale horizontally aligned single-walled carbon nanotube arrays, *Nano Lett.*, **7**, pp. 2073-2079.
3. Della Valle, G., Osellame, R., Galzerano, G., Chiodo, N., Cerullo, G., Laporta, P., Svelto, O., Morgner, U., Rozhin, A. G., Scardaci, V.& Ferrari, A. C. (2006). Passive mode locking by carbon nanotubes in a femtosecond laser written waveguide laser, *Appl. Phys. Lett.*, **89**, pp. 2311151-2311153.
4. Wang, F., Rozhin, A. G., Scardaci, V., Sun, Z., Hennrich, F., White, I. H., Milne, W. I.& Ferrari, A. C. (2008). Wideband-tuneable, nanotube mode-locked, fibre laser, *Nature Nanotechnol.*, **3**, pp. 738-742.
5. Shoji, S., Suzuki, H., Zaccaria, R. P., Sekkat, Z.& Kawata, S. (2008). Optical polarizer made of uniaxially aligned short single-wall carbon nanotubes embedded in a polymer film, *Phys. Rev. B*, **77**, pp. 1534071-1534074.
6. Kang, B. G., Lim, Y. J., Jeong, K.-U., Lee, K., Lee, Y. H.& Lee, S. H. (2010). A tunable carbon nanotube polarizer, *Nanotech.*, **21**, pp. 1-5.
7. Kocabas, C., Hur, S. H., Gaur, A., Meitl, M. A., Shim, M.& Rogers, J. A. (2005). Guided growth of large-scale, horizontally aligned arrays of single-walled carbon nanotubes and their use in thin-film transistors, *Small*, **1**, pp. 1110-1116.
8. Yuegang, Z., Aileen, C., Jien, C., Qian, W., Woong, K., Yiming, L., Morris, N., Yenilmez, E., Jing, K.& Hongjie, D. (2001). Electric-field-directed growth of aligned single-walled carbon nanotubes, *Appl. Phys. Lett.*, **79**, pp. 3155-7.
9. Joselevich, E.& Lieber, C. M. (2002). Vectorial growth of metallic and semiconducting single-wall carbon nanotubes, *Nano Lett.*, **2**, pp. 1137-1141.
10. Cao, Q.& Rogers, J. A. (2009). Ultrathin films of single-walled carbon nanotubes for electronics and sensors: A review of fundamental and applied aspects, *Adv. Mater.*, **21**, pp. 29-53.
11. Smith, P. A., Nordquist, C. D., Jackson, T. N., Mayer, T. S., Martin, B. R., Mbindyo, J.& Mallouk, T. E. (2000). Electric-field assisted assembly and alignment of metallic nanowires, *Appl. Phys. Lett.*, **77**, pp. 1399-1401.
12. Yamamoto, K., Akita, S.& Nakayama, Y. (1998). Orientation and purification of carbon nanotubes using ac electrophoresis, *J. Phys. D*, **31**, pp. 34-36.

13. Hone, J., Llaguno, M. C., Nemes, N. M., Johnson, A. T., Fischer, J. E., Walters, D. A., Casavant, M. J., Schmidt, J.& Smalley, R. E. (2000). Electrical and thermal transport properties of magnetically aligned single walt carbon nanotube films, *Appl. Phys. Lett.*, **77**, pp. 666-668.

14. Kang, S. J., Kocabas, C., Kim, H. S., Cao, Q., Meitl, M. A., Khang, D. Y.& Rogers, J. A. (2007). Printed multilayer superstructures of aligned single-walled carbon nanotubes for electronic applications, *Nano Lett.*, **7**, pp. 3343-3348.

15. De Jonge, N., Allioux, M., Doytcheva, M., Kaiser, M., Teo, K. B. K., Lacerda, R. G.& Milne, W. I. (2004). Characterization of the field emission properties of individual thin carbon nanotubes, *Appl. Phys. Lett.*, **85**, pp. 1607-1609.

16. Hecht, D. S.& Gruner, G. (2009) *Solution Cast Films of Carbon Nanotubes for Transparent Conductors and Thin Film Transistors* In *Flexible Electronics: Materials & Applications* eds. Wong, W. S.&Salleo, A., (Springer), pp. 297-328.

17. Ago, H., Petritsch, K., Shaffer, M. S. P., Windle, A. H.& Friend, R. H. (1999). Composites of carbon nanotubes and conjugated polymers for photovoltaic devices, *Adv. Mater.*, **11**, pp. 1281-1285.

18. Wei, Y., Xie, C., Dean, K. A.& Coll, B. F. (2001). Stability of carbon nanotubes under electric field studied by scanning electron microscopy, *Appl. Phys. Lett.*, **79**, pp. 4527-4529.

19. Kim, P.& Lieber, C. M. (1999). Nanotube nanotweezers, *Science*, **286**, pp. 2148-2150.

20. Law, J. B. K., Koo, C. K.& Thong, J. T. L. (2007). Horizontally directed growth of carbon nanotubes utilizing self-generated electric field from plasma induced surface charging, *Appl. Phys. Lett.*, **91**, pp. 2431081-2431083.

21. Maeda, M., Hyon, C. K., Kamimura, T., Kojima, A., Sakamoto, K.& Matsumoto, K. (2005). Growth control of carbon nanotube using various applied electric fields for electronic device applications, *Jpn. J. Appl. Phys. 1*, **44**, pp. 1585-1587.

22. Ural, A., Li, Y. M.& Dai, H. J. (2002). Electric-field-aligned growth of single-walled carbon nanotubes on surfaces, *Appl. Phys. Lett.*, **81**, pp. 3464-3466.

23. Jang, Y. T., Ahn, J. H., Ju, B. K.& Lee, Y. H. (2003). Lateral growth of aligned mutilwalled carbon nanotubes under electric field, *Sol. State Comms.*, **126**, pp. 305-308.

24. Ishigami, N., Ago, H., Nishi, T., Ikeda, K. I., Tsuji, M., Ikuta, T.& Takahashi, K. (2008). Unidirectional Growth of Single-Walled Carbon Nanotubes, *J. Am. Chem. Soc.*, **130**, pp. 17264-17265.

25. Ding, L., Yuan, D. N.& Liu, J. (2008). Growth of high-density parallel arrays of long single-walled carbon nanotubes on quartz substrates, *J. Am. Chem. Soc.*, **130**, pp. 5428-5429.

26. Ismach, A., Kantorovich, D.& Joselevich, E. (2005). Carbon nanotube graphoepitaxy: Highly oriented growth by faceted nanosteps, *J. Am. Chem. Soc.*, **127**, pp. 11554-11555.

27. Huang, L. M., Cui, X. D., White, B.& O'Brien, S. P. (2004). Long and oriented single-walled carbon nanotubes grown by ethanol chemical vapor deposition, *J. Phys. Chem. B*, **108**, pp. 16451-16456.

28. Huijun, X.& Woolley, A. T. (2004). Directional orientation of carbon nanotubes on surfaces using a gas flow cell, *Nano Lett.*, **4**, pp. 1481-1484.

29. Jin, Z., Chu, H., Wang, J., Hong, J., Tan, W.& Li, Y. (2007). Ultralow feeding gas flow guiding growth of large-scale horizontally aligned single-walled carbon nanotube arrays, *Nano Lett.*, **7**, pp. 2073-2079.

30. Huang, S., Cai, X.& Liu, J. (2003). Growth of millimeter-long and horizontally aligned single-walled carbon nanotubes on flat substrates, *J. Am. Chem. Soc.*, **125**, pp. 5636-5637.

31. Xin, H.& Woolley, A. T. (2004). Directional orientation of carbon nanotubes on surfaces using a gas flow cell, *Nano Lett.*, **4**, pp. 1481-1484.

32. Ismach, A.& Joselevich, E. (2006). Orthogonal self-assembly of carbon nanotube crossbar architectures by simultaneous graphoepitaxy and field-directed growth, *Nano Lett.*, **6**, pp. 1706-1710.

33. Cassell, A. M., Franklin, N. R., Tombler, T. W., Chan, E. M., Han, J.& Dai, H. J. (1999). Directed growth of free-standing single-walled carbon nanotubes, *J. Am. Chem. Soc.*, **121**, pp. 7975-7976.

34. Blaek, J., Spatenka, P., Pacal, F., Taschner, C.& Leonhardt, A. (2005). Computations of local electric field and electric forces acting on carbon nanotubes in a direct current plasma sheath, *Thin Solid Films*, **489**, pp. 291-5.

35. Hertel, T., Walkup, R. E.& Avouris, P. (1998). Deformation of carbon nanotubes by surface van der Waals forces, *Phys. Rev. B*, **58**, pp. 13870-13873.

36. Chen, Y., Guo, L., Patel, S.& Shaw, D. T. (2000). Aligned conical carbon nanotubes, *J. Mat. Sci.*, **35**, pp. 5517-5521.

37. Yu, J., Bai, X. D., Ahn, J., Yoon, S. F.& Wang, E. G. (2000). Highly oriented rich boron B-C-N nanotubes by bias-assisted hot filament chemical vapor deposition, *Chem. Phys. Lett.*, **323**, pp. 529-533.

38. Tanemura, M., Iwata, K., Takahashi, K., Fujimoto, Y., Okuyama, F., Sugie, H.& Filip, V. (2001). Growth of aligned carbon nanotubes by plasma-enhanced chemical vapor deposition: Optimization of growth parameters, *J. Appl. Phys.*, **90**, pp. 1529-1533.

39. Chhowalla, M., Teo, K. B. K., Ducati, C., Rupesinghe, N. L., Amaratunga, G. A. J., Ferrari, A. C., Roy, D., Robertson, J.& Milne, W. I. (2001). Growth process conditions of vertically aligned carbon nanotubes using plasma enhanced chemical vapor deposition, *J. Appl. Phys.*, **90**, pp. 5308-5317.

40. Bell, M. S., Teo, K. B. K., Lacerda, R. G., Milne, W. I., Hash, D. B.& Meyyappan, M. (2006). Carbon nanotubes by plasma-enhanced chemical vapor deposition, *Pure Appl. Chem.*, **78**, pp. 1117-1125.

41. Lieberman& A., M. (1999) *Principles of Plasma Discharges and Materials Processing* eds. (John Wiley, New York) pp. 164-166.

42. Teo, K. B. K. (2002). Aligned Carbon Nanotube Technology for Field Emission Application, *Department of Engineering*, **PhD**, p 34.

43. Chapman& N., B. (1980) *Glow Discharge Processes* eds. (John Wiley, New York) pp. 49-82.

44. Desai, T. M., Gogawale, S. V., Shukla, A. B., Joshi, N. K., Salgaonkar, U. S.& Bhale, G. L. (1995). Electron-temperature measurements in UHV systems by spectroscopic and langmuir probe techniques, *Vacuum*, **46**, pp. 223-226.

45. Shah, M. S., Salem, M., Ahmad, R., Zakaullah, M., Qayyum, A.& Murtaza, G. (2008). Langmuir probe characterization of nitrogen plasma for surface nitriding of AISI-4140 steel, *J. Mater. Process. Tech.*, **199**, pp. 363-368.

46. Sun, S. B. K.& Storvick, T. S. (1979). Viscosity of ammonia at high temperature and pressure, *J. Chem. Eng. Data*, **24**, pp. 88-91.

47. Bower, C., Zhu, W., Jin, S. H.& Zhou, O. (2000). Plasma-induced alignment of carbon nanotubes, *Appl. Phys. Lett.*, **77**, pp. 830-832.

48. Matsuda, T., Mesko, M., Ishikawa, T., Sato, J., Ogino, A., Tamura, R.& Nagatsu, M. (2008). Role of negative electric field biasing on growth of vertically aligned carbon nanotubes using chemical vapor deposition, *Jpn. J. Appl. Phys.*, **47**, pp. 7436-7439.

49. Zhong, G., Hofmann, S., Yan, F., Telg, H., Warner, J. H., Eder, D., Thomsen, C., Milne, W. I.& Robertson, J. (2009). Acetylene: A key growth precursor for single-walled carbon nanotube forests, *J. Phys. Chem. C*, **113**, pp. 17321-17325.

50. Xiao, L., Chen, Z., Feng, C., Liu, L., Bai, Z. Q., Wang, Y., Qian, L., Zhang, Y. Y., Li, Q. Q., Jiang, K. L.& Fan, S. S. (2008). Flexible, Stretchable, Transparent Carbon Nanotube Thin Film Loudspeakers, *Nano Lett.*, **8**, pp. 4539-4545.

51. Kai, L., Yinghui, S., Lei, C., Chen, F., Xiaofeng, F., Kaili, J., Yonggang, Z.& Shoushan, F. (2008). Controlled growth of super-aligned carbon nanotube arrays for spinning continuous unidirectional sheets with tunable physical properties, *Nano Lett.*, **8**, pp. 700-705.

52. Itkis, M. E., Borondics, F., Yu, A.& Haddon, R. C. (2006). Bolometric infrared photoresponse of suspended single-walled carbon nanotube films, *Science*, **312**, pp. 413-416.

53. Rongtao, L., Shi, J. J., Baca, F. J.& Wu, J. Z. (2010). High performance multiwall carbon nanotube bolometers, *J. Appl. Phys.*, **108**, pp. 0843051-0843056.

54. Stokes, P., Liu, L., Zou, J., Zhai, L., Huo, Q.& Khondaker, S. I. (2009). Photoresponse in large area multiwalled carbon nanotube/polymer nanocomposite films, *Appl. Phys. Lett.*, **94**, pp. 0421101-0421103.

55. El Khakani, M. A., Le Borgne, V., Aissa, B., Rosei, F., Scilletta, C., Speiser, E., Scarselli, M., Castrucci, P.& De Crescenzi, M. (2009). Photocurrent generation in random networks of multiwall-carbon-nanotubes grown by an "all-laser" process, *Appl. Phys. Lett.*, **95**, pp. 0831141-0831143.

56. Brennan, M. E., Coleman, J. N., Drury, A., Lahr, B., Kobayashi, T.& Blau, W. J. (2003). Nonlinear photoluminescence from van Hove singularities in multiwalled carbon nanotubes, *Opt. Lett.*, **28**, pp. 266-268.

57. Xu, J. M. (2001). Highly ordered carbon nanotube arrays and IR detection, *Infrared Phys. Techn.*, **42**, pp. 485-491.

58. Avouris, P., Freitag, M.& Perebeinos, V. (2008). Carbon-nanotube optoelectronics, *Carbon Nanotubes: Advanced Topics in the Synthesis, Structure, Properties and Applications*, **111**, pp. 423-454.

59. Lien, D. H., Hsu, W. K., Zan, H. W., Tai, N. H.& Tsai, C. H. (2006). Photocurrent amplification at carbon nanotube-metal contacts, *Advanced Materials*, **18**, pp. 98-103.

60. Chen, R. J., Franklin, N. R., Kong, J., Cao, J., Tombler, T. W., Zhang, Y.& Dai, H. (2001). Molecular photodesorption from single-walled carbon nanotubes, *Appl. Phys. Lett.*, **79**, pp. 2258-2260.

61. Castrucci, P., Scilletta, C., Del Gobbo, S., Scarselli, M., Camilli, L., Simeoni, M., Delley, B., Continenza, A.& De Crescenzi, M. (2011). Light Harvesting with Multiwall Carbon Nanotube/silicon Heterojunctions, *Nanotech.*, **22**, pp. 115701-115709.

62. Li, Z., Kunets, V. P., Saini, V., Xu, Y., Dervishi, E., Salamo, G. J., Biris, A. R.& Biris, A. S. (2009). Light-harvesting using high density p-type single wall carbon nanotube/n-type silicon heterojunctions, *ACS Nano*, **3**, pp. 1407-1414.

63. Bakueva, L., Musikhin, S., Hines, M. A., Chang, T. W. F., Tzolov, M., Scholes, G. D.& Sargent, E. H. (2003). Size-tunable infrared (1000-1600 nm) electroluminescence from PbS quantum-dot nanocrystals in a semiconducting polymer, *Appl. Phys. Lett.*, **82**, pp. 2895-2897.

64. Auble, D. L.& Meyers, T. P. (1992). An open path, fast response infrared-absorption gas analyzer for H_2O and CO_2, *Bound.-Lay. Meteorol.*, **59**, pp. 243-256.

65. Kouklin, N., Tzolov, M., Straus, D., Yin, A.& Xu, J. M. (2004). Infrared absorption properties of carbon nanotubes synthesized by chemical vapor deposition, *Appl. Phys. Lett.*, **85**, pp. 4463-4465.

66. Murakami, Y., Einarsson, E., Edamura, T.& Maruyama, S. (2005). Polarization dependent optical absorption properties of single-walled carbon nanotubes and methodology for the evaluation of their morphology, *Carbon*, **43**, pp. 2664-2676.

67. Wei, J., Sun, J.-L., Zhu, J.-L., Wang, K., Wang, Z., Luo, J., Wu, D.& Cao, A. (2006). Carbon nanotube macrobundles for light sensing, *Small*, **2**, pp. 988-993.

68. Odom, T. W., Huang, J. L., Kim, P.& Lieber, C. M. (1998). Atomic structure and electronic properties of single-walled carbon nanotubes, *Nature*, **391**, pp. 62-64.

69. Dresselhaus, M. S., Dresselhaus, G.& Endo, M. (2001). Topics in Applied Physics - Carbon Nanotube: Synthesis, Structure, Properties & Applications, **80**.

70. Schwierz, F. (2010). Graphene transistors, *Nature Nanotechnol.*, **5**, pp. 487-496.

71. Song, W., Jeon, C., Kim, Y. S., Kwon, Y. T., Jung, D. S., Jang, S. W., Choi, W. C., Park, J. S., Saito, R.& Park, C.-Y. (2010). Synthesis of Bandgap-Controlled Semiconducting Single-Walled Carbon Nanotubes, *ACS Nano*, **4**, pp. 1012-1018.

72. Charlier, J. C.& Issi, J. P. (1996). Electrical conductivity of novel forms of carbon, *J. Phys. Chem. Sol.*, **57**, pp. 957-965.

73. Zhao, H.& Mazumdar, S. (2007). Elucidation of the electronic structure of semiconducting single-walled carbon nanotubes by electroabsorption spectroscopy, *Phys. Rev. Lett.*, **98**, pp. 1668051-1668054.

74. Lu, S.& Panchapakesan, B. (2006). Photoconductivity in single wall carbon nanotube sheets, *Nanotech.*, **17**, pp. 1843-1850.

75. Berger, S., Voisin, C., Cassabois, G., Delalande, C., Roussignol, P.& Marie, X. (2007). Temperature dependence of exciton recombination in semiconducting single-wall carbon nanotubes, *Nano Lett.*, **7**, pp. 398-402.

76. Kumar, S., Kim, G. H., Sreenivas, K.& Tandon, R. P. (2007). Mechanism of ultraviolet photoconductivity in zinc oxide nanoneedles, *J. Phys. Cond. Mat.*, **19**, pp. 1-10.

77. Merchant, C. A.& Marković, N. (2008). Effects of diffusion on photocurrent generation in single-walled carbon nanotube films, *Appl. Phys. Lett.*, **92**, pp. 2435101-2435103.

78. Ham, M. H., Kong, B. S., Kim, W. J., Jung, H. T.& Strano, M. S. (2009). Unusually large Franz-Keldysh oscillations at ultraviolet wavelengths in single-walled carbon nanotubes, *Phys. Rev. Lett.*, **102**, pp. 0474021-0474024.

79. Kong, J., Franklin, N. R., Zhou, C. W., Chapline, M. G., Peng, S., Cho, K. J.& Dai, H. J. (2000). Nanotube molecular wires as chemical sensors, *Science*, **287**, pp. 622-625.

80. Zettl, A. (2000). Extreme oxygen sensitivity of electronic properties of carbon nanotubes, *Science*, **287**, pp. 1801-1804.

81. Luo, H., Shi, Z., Li, N., Gu, Z.& Zhuang, Q. (2001). Investigation of the electrochemical and electrocatalytic behavior of single-wall carbon nanotube film on a glassy carbon electrode, *Anal. Chem.*, **73**, pp. 915-920.

82. Xu, Y., Bai, H., Lu, G., Li, C.& Shi, G. (2008). Flexible graphene films via the filtration of water-soluble noncovalent functionalized graphene sheets, *J. Am. Chem. Soc.*, **130**, pp. 5856-5857.

83. Bourlinos, A. B., Gournis, D., Petridis, D., Szabó, T., Szeri, A.& Dékány, I. (2003). Graphite oxide: Chemical reduction to graphite and surface modification with primary aliphatic amines and amino acids, *Langmuir*, **19**, pp. 6050-6055.

84. Stankovich, S., Piner, R. D., Nguyen, S. T.& Ruoff, R. S. (2006). Synthesis and exfoliation of isocyanate-treated graphene oxide nanoplatelets, *Carbon*, **44**, pp. 3342-3347.

85. Ellison, M. D., Good, A. P., Kinnaman, C. S.& Padgett, N. E. (2005). Interaction of water with single-walled carbon nanotubes: Reaction and adsorption, *J. Phys. Chem. B*, **109**, pp. 10640-10646.

86. Matranga, C., Chen, L., Smith, M., Bittner, E., Johnson, J. K.& Bockrath, B. (2003). Trapped CO_2 in Carbon Nanotube Bundles, *J. Phys. Chem. B*, **107**, pp. 12930-12941.

87. Parades, J. I., Villar-Rodil, S., Martínez-Alonso, A.& Tascón, J. M. D. (2008). Graphene oxide dispersions in organic solvents, *Langmuir*, **24**, pp. 10560-10564.

88. Watts, P. C. P., Mureau, N., Tang, Z., Miyajima, Y., Carey, J. D.& Silva, S. R. P. (2007). The importance of oxygen-containing defects on carbon nanotubes for the detection of polar and non-polar vapours through hydrogen bond formation, *Nanotech.*, **18**, pp. 1-6.

89. Levitsky, I. A.& Euler, W. B. (2003). Photoconductivity of single-wall carbon nanotubes under continuous-wave near-infrared illumination, *Appl. Phys. Lett.*, **83**, pp. 1857-1859.

90. Boyle, W. S.& Rodgers JR., K. F. (1959). Performance Characteristics of a New Low-Temperature Bolometer, *J. Opt. Soc. Am.*, **49**, pp. 66-69.

91. Wellstood, F. C., Urbina, C.& Clarke, J. (1994). Hot-electron effects in metals, *Phys. Rev. B*, **49**, pp. 5942-5955.

92. Sorescu, D. C., Jordan, K. D.& Avouris, P. (2001). Theoretical study of oxygen adsorption on graphite and the (8,0) single-walled carbon nanotube, *J. Phys. Chem. B*, **105**, pp. 11227-11232.

93. Seung-Hoon, J., Louie, S. G.& Cohen, M. L. (2000). Electronic properties of oxidized carbon nanotubes, *Phys. Rev. Lett.*, **85**, pp. 1710-1713.

94. Giannozzi, P., Car, R.& Scoles, G. (2003). Oxygen adsorption on graphite and nanotubes, *J. Chem. Phys.*, **118**, pp. 1003-1006.

95. Ulbricht, H., Moos, G.& Hertel, T. (2002). Physisorption of molecular oxygen on single-wall carbon nanotube bundles and graphite, *Phys. Rev. B*, **66**, pp. 0754041-0754047.

96. Dag, S., Gülseren, O., Yildirim, T.& Ciraci, S. (2003). Oxygenation of carbon nanotubes: Atomic structure, energetics, and electronic structure, *Phys. Rev. B*, **67**, pp. 1654241-16542410.

97. Zhou, C. W., Kong, J.& Dai, H. J. (2000). Intrinsic electrical properties of individual single-walled carbon nanotubes with small band gaps, *Phys. Rev. Lett.*, **84**, pp. 5604-5607.

98. Kang, D., Park, N., Hyun, J., Bae, E., Ko, J., Kim, J.& Park, W. (2005). Adsorption-induced conversion of the carbon nanotube field effect transistor from ambipolar to unipolar behavior, *Appl. Phys. Lett.*, **86**, pp. 1-3.

99. Vidali, G., Ihm, G., Kim, H. Y.& Cole, M. W. (1991). Potentials of Physical Adsorption, *Surf. Sci. Rep.*, **12**, pp. 133-181.

100. Kang, D., Park, N., Ko, J. H., Bae, E.& Park, W. (2005). Oxygen-induced p-type doping of a long individual single-walled carbon nanotube, *Nanotech.*, **16**, pp. 1048-1052.

101. Javey, A., Shim, M.& Dai, H. (2002). Electrical properties and devices of large-diameter single-walled carbon nanotubes, *Appl. Phys. Lett.*, **80**, pp. 1064-1066.

102. Liu, Y., Lu, S.& Panchapakesan, B. (2009). Alignment enhanced photoconductivity in single wall carbon nanotube films, *Nanotech.*, **20**, pp. 1-7.

103. Xiao, L., Zhang, Y., Wang, Y., Liu, K., Wang, Z., Li, T., Jiang, Z., Shi, J., Liu, L., Li, Q. Q., Zhao, Y., Feng, Z., Fan, S.& Jiang, K. (2011). A polarized infrared thermal detector made from super-aligned multiwalled carbon nanotube films, *Nanotech.*, **22**, pp. 1-7.

104. Dawson, P., Duenas, J. A., Boyle, M. G., Doherty, M. D., Bell, S. E. J., Kern, A. M., Martin, O. J. F., Teh, A. S., Teo, K. B. K.& Milne, W. I. (2011). Combined antenna and localized plasmon resonance in raman scattering from random arrays of silver-coated, vertically aligned multiwalled carbon nanotubes, *Nano Lett.*, **11**, pp. 365-371.

105. Echtermeyer, T. J., Britnell, L., Jasnos, P. K., Lombardo, A., Gorbachev, R. V., Grigorenko, A. N., Geim, A. K., Ferrari, A. C.& Novoselov, K. S. (2011). Strong plasmonic enhancement of photovoltage in graphene, *Nature Comms.*, **2**, pp. 1-5.

106. Barnes, W. L., Dereux, A.& Ebbesen, T. W. (2003). Surface plasmon subwavelength optics, *Nature*, **424**, pp. 824-830.

107. Bursill, L. A., Stadelmann, P. A., Peng, J. L.& Prawer, S. (1994). Surface plasmon observed for carbon nanotubes, *Phys. Rev. B*, **49**, pp. 2882-2887.

108. Bondarev, I. V., Woods, L. M.& Tatur, K. (2010). Electrostatic field control of exciton-surface-plasmon coupling in individual carbon nanotubes, *Quant. Electr. & Las. Sci.*

109. Cao, L., Barsic, D. N., Guichard, A. R.& Brongersma, M. L. (2007). Plasmon-assisted local temperature control to pattern individual semiconductor nanowires and carbon nanotubes, *Nano Lett.*, **7**, pp. 3523-3527.

110. Yosida, Y.& Oguro, I. (1999). Variable range hopping conduction in bulk samples composed of single-walled carbon nanotubes, *J. Appl. Phys.*, **86**, pp. 999-1003.

111. Yosida, Y.& Oguro, I. (1998). Variable range hopping conduction in multiwalled carbon nanotubes, *J. Appl. Phys.*, **83**, pp. 4985-4987.

112. Silvestrelli, P. L.& Parrinello, M. (1999). Water molecule dipole in the gas and in the liquid phase, *Phys. Rev. Lett.*, **82**, pp. 3308-3311.

113. Gunji, M.& Washizu, M. (2005). Self-propulsion of a water droplet in an electric field, *J. Phys. D*, **38**, pp. 2417-2423.

114. Fuchs, E. C., Woisetschläger, J., Gatterer, K., Maier, E., Pecnik, R., Holler, G.& Eisenkölbl, H. (2007). The floating water bridge, *J. Phys. D*, **40**, pp. 6112-6114.

115. Wang, D., Guo, S., Ren, H.& Yin, S. (2002). Optical characteristics of silver-doped polarizing glass, *Opt. Lett.*, **27**, pp. 992-994.

116. Burnett, J. H., Levine, Z. H.& Shirley, E. L. (2001). Intrinsic birefringence in calcium fluoride and barium fluoride, *Phys. Rev. B*, **64**, pp. 2411021-2411024.
117. Bridges, T. J.& Kluver, J. W. (1965). Dichroic Calcite Polarizers for the Infrared, *Appl. Optics*, **4**, pp. 1121-1125.
118. Polavarapu, P. L., Deng, Z.& Weibel, S. (1996). Polarization-division beamsplitters with KBr and KRS-5 substrates for fourier transform infrared spectroscopy, *Appl. Spectrosc.*, **50**, pp. 98-101.
119. Maxwell, J. C. (1873) *A Treatise on electricity & Magnetism* eds. (Cambridge).
120. Rayleigh, L. (1982). *Philos. Mag.*, **34**.
121. Yeh, P. (1981). *SPIE*, **307**.
122. Bohren, C. F.& Huffman, D. R. (2004) *Absorption & Scattering of Light by Small Particles* eds. (Wiley-VCH, Weinheim).
123. De Los Arcos, T., Oelhafen, P.& Mathys, D. (2007). Optical characterization of alignment and effective refractive index in carbon nanotube films, *Nanotech.*, **18**, pp. 1-5.
124. Bruna, M.& Borini, S. (2009). Optical constants of graphene layers in the visible range, *Appl. Phys. Lett.*, **94**, pp. 0319011-0319013.

Chapter VII

Conclusions & Outlook
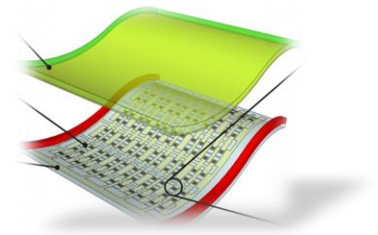
7.0 From Materials & Processes to Devices

This thesis charted the authors work on the development of graphene and MWCT-based flexible transparent electrodes offering enhanced functionality, through alignment, in applications such as field emitters, polarization sensitive optical sensors and optical polarisers.

The chemical vapour deposition of graphene and MWCNTs was studied and revealed that graphene CVD catalysis is profoundly different from its carbon nanotube and nanofibre counterparts. An activation energy of 2.4 eV was found, for the first time, suggesting that the growth is rate-limited by carbon integration into the existing graphene lattice rather than diffusion (surface or bulk) or precursor dehydrogenation due to the extremely low C solubility in Cu and the ill-defined barrier associated with Cu-catalysed ethylene surface dehydrogenation. In contrast both the nanotubes and nanofibres were found to be surface-diffusion limited, with Fe (and Ni) activation energies of the order of 0.5 eV and 1.5 eV for ITO and Al-derivative diffusion barriers, given the similarities in the activation energy extracted from earlier works on the temperature dependent solubility of C in Ni, Fe and Cu.

The development of a dry-transfer technique was demonstrated offering large-area, room temperature processing of controlled transparency and polarisation selective electrode materials. MWCNTs were transferred, without any chemical treatments, to various standard polycarbonate supports. The developed process was found to offer high performance for supercapacitor applications though remained someway off the commercial ITO optoelectronic benchmark. The optoelectronic properties of hot-press laminated (bilayer) graphene was also considered. Graphene was synthesised by methane-based CVD and was investigated by Raman spectroscopy (both *in-situ* and transferred), UV-Vis spectroscopy, select area TEM diffraction patterns and spatial Raman mapping. Although offering high

transparencies, which was limited by the transferred substrate rather than the graphene itself, HPLG samples offered little in the way of highly conductive or flexible electrode materials. HPLG samples failed under ~15% maximum strain whereas dry-transferred MWCNTs showed only a modest reduction in conductivity up to strains of 150%. Low-temperature transport measurements revealed that macroscopically both the HPLG and MWCNTs behaved similarly to *c*-axis dominated turbostratic graphite with the onset of tunnel dominance at lower, sub-cryogenic, temperatures.

The field emission performance of MWCNT-based thin films was considered and it was suggested that surfactant treated solution processed thin films offer lower turn-on potentials compared to the as-grown dry-transferred material due to the lowered surface work function of the MWCNTs which narrowed the triangular tunnel barrier and permitted emission at lower electric fields. Sodium is nevertheless highly unstable under vacuum and as such alternative surfactants should therefore be investigated in a similar vain. Low-temperature, hydrothermally synthesised ZnO NWs were found to ballast the emission characteristics of polymer-supported dry-transferred MWCNT thin film emitters by limiting the maximum emission current and preventing tip burn-out. A hot electron model has been proposed to consolidate the lower-than-expected turn-on electric fields from such hybrid emitters. To increase the current density sparse vertically aligned arrays of carbon nanofibres were grown directly on electrochemically treated stainless steel mesh. The technique developed showed excellent alignment compared to previous reports and highly stable emission currents.

Various horizontal alignment techniques were consider which included density, scratch and roll alignment. Local electric fields, applied were shown to align nanotubes during and after growth, though with low-linear densities. A global horizontal PE-CVD reactor was modelled, designed and fabricated. Langmuir probe characteristics clearly indicated that the

aligning sheath width can be appreciably extended within the practical limits of the growth conditions. Samples showed moderate alignment with a Str37 of 0.5. A mechanical peeling technique was developed and the photoresponse of truly pure, and substrate free MWCNTs was considered and is possibly the first study of its kind. The importance of surface bound oxygen was repeatedly implicated through FT-IR, *in-situ* heating and lasing EDX, pressure dependent conductivity measurements and low-temperature transport and transfer studies. Data irrefutably evidenced the photoconductivity of MWCNTs via the optical modulation of the surface bound oxygen and/or water. Devices were sufficiently large as to obviate any possible electrode interface effects and were free-standing to remove substrate related charge traps and heterojunctions. Finally, optical polarisers were developed that exploited the structural anisotropy of the MWCNT membranes. Broadband polarisation was evident and offered the promise of extremely wideband operation due to the lack of an often limiting substrate.

7.1 Future Work

The studies presented in this thesis have been exclusively concerned with understanding the growth, conduction mechanisms, dry-transfer and applications of graphene and MWCNT thin films, particularly with respect to field emission, optical sensors and optical polorisors. Each topic offered potentially useful insight into the development of fully flexible field emission display / environmental lighting platforms.

To achieve this modest adjustments to the technique developed previously must be made and incorporated with one another. Figure 7.1 illustrates the proposed device. Copper is patterned by either electro-deposition, thin film etching or precision tooled using high-precision cutting equipment. Graphene is CVD synthesised and laminated as before. The counter, electron extracting, electrode is fabricated from large-area graphene hot-press
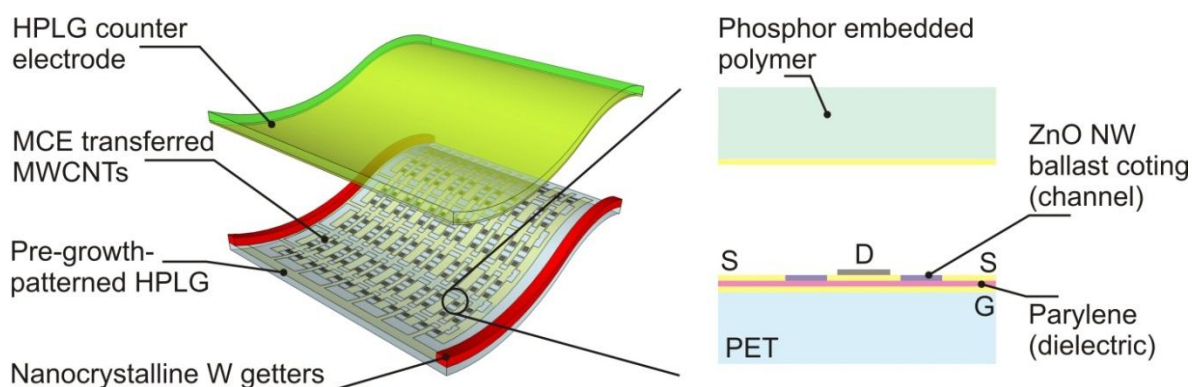
Figure 7.1 | **Future Work.** Proposed flexible field emission display / environmental lighting platform.

laminated to a phosphor embedded polymer. The electron emission sites are formed from transferred MWCNT/ZnO NW emitters as illustrated in Figure 7.1. Each emitter has an integrated ballast resistance (the ZnO NWs) and operates in a diode configuration. The HPLG substrate functions as the gate electrode and is coated, at low temperatures ($<50^{\circ}$C), with a 5 μm parylene dielectric that is then coated with a second, patterned, HPLG layer. This second layer forms independent source (S) and drain (D) electrodes (Figure 7.1) that electrically control the emission characteristics. MWCNTs are then deposited on the drain HPLG electrode by dry-transferred or solution processing (such as inkjet printing). A ZnO NW layer, hydrothermally grown, functions as the FET channel which optimises the emission characteristics of the MWCNT thin film. The ZnO ballasts the emission through both the channel and the emitter coating. Nanocrystalline W getters will be edge screen printed.

The proposed field emitter functions in a global sense (i.e. all pixels emit simultaneously) and as such is limited to applications such as environmental and flexible back lighting. Sub-pixel addressing is necessary for practical display applications and efforts have begun toward the development of CVD graphene all-carbon TFTs on polymer supports using

parylene-based dielectrics and the HPLG process. The HPLG processing is to be further optimised with experiments focusing on the pre-patterning of the Cu-catalyst prior to graphene growth and transfer as well further optimisation of the MWCNT transfer techniques developed – both of which will be instrumental in successful development of the proposed flexible field emitter.

With regards to understanding graphene CVD efforts are on-going in collaboration with the Chalmers University. Here we are focusing on the CVD of graphene on dielectric substrates by non-metallic catalysis. The author has also formed strong links with ETH Zurich regarding an experimental framework, developed by the author, to measure hitherto unmeasured activation energy of graphene catalysis across a variety of metallic catalysts and CVD growth conditions.

7.2 Summary

This thesis presented the development and use of various MWCNT and graphene dry-transfer, chemical vapour deposition and alignment techniques in applications such as field emitting sources and transparent flexible electrodes with enhance functionality, such as polarisation selective electrodes.